BEILSTEIN JOURNAL OF NANOTECHNOLOGY

New trends in nanobiotechnology

Edited by Pau-Loke Show, Wee-Jun Ong, Sunita Varjani and
Joon Ching Juan

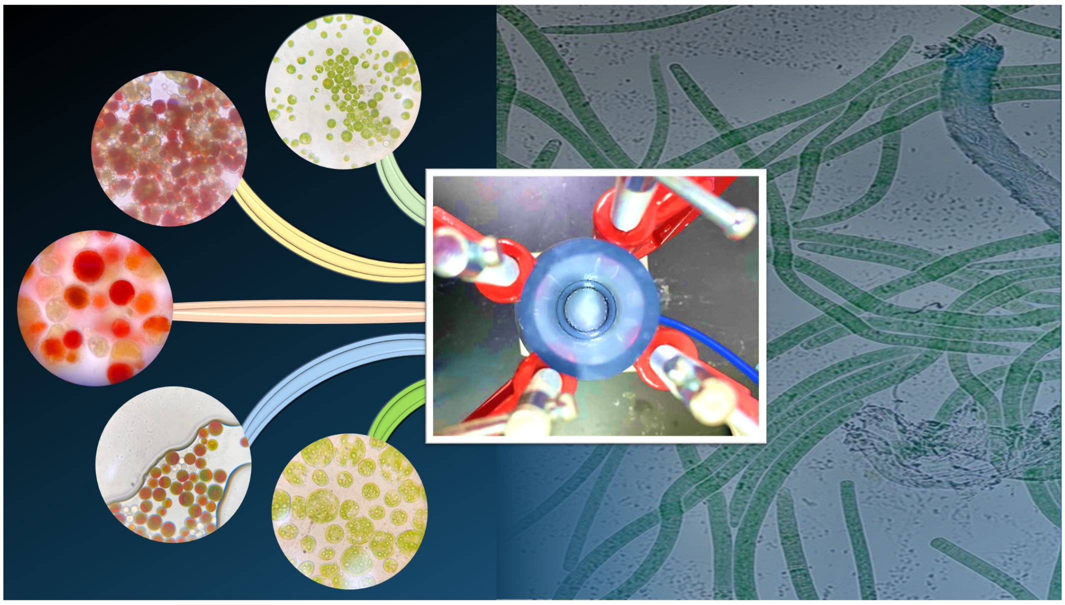

Imprint

Beilstein Journal of Nanotechnology
www.bjnano.org
ISSN 2190-4286
Email: journals-support@beilstein-institut.de

The *Beilstein Journal of Nanotechnology* is published by the Beilstein-Institut zur Förderung der Chemischen Wissenschaften.

Beilstein-Institut zur Förderung der
Chemischen Wissenschaften
Trakehner Straße 7–9
60487 Frankfurt am Main
Germany
www.beilstein-institut.de

BEILSTEIN JOURNAL OF NANOTECHNOLOGY

New trends in nanobiotechnology

Pau-Loke Show*[1,2,3,4], Kit Wayne Chew[5], Wee-Jun Ong[6,7], Sunita Varjani[8,9]
and Joon Ching Juan[10]

Editorial

Address:
[1]Department of Chemical Engineering, Khalifa University, P.O. Box 127788, Abu Dhabi, United Arab Emirates, [2]Zhejiang Provincial Key Laboratory for Subtropical Water Environment and Marine Biological Resources Protection, Wenzhou University, Wenzhou, 325035, China, [3]Department of Sustainable Engineering, Saveetha School of Engineering, SIMATS, Chennai, 602105, India, [4]Department of Chemical and Environmental Engineering, Faculty of Science and Engineering, University of Nottingham Malaysia, Jalan Broga, 43500, Semenyih, Selangor Darul Ehsan, Malaysia, [5]School of Chemistry, Chemical Engineering and Biotechnology, Nanyang Technological University, 62 Nanyang Drive, Singapore, 637459 Singapore, [6]School of Energy and Chemical Engineering, Xiamen University Malaysia, Selangor Darul Ehsan, Selangor, 43900, Malaysia, [7]Center of Excellence for NaNo Energy & Catalysis Technology (CONNECT), Xiamen University Malaysia, Selangor Darul Ehsan, Selangor, 43900, Malaysia, [8]School of Energy and Environment, City University of Hong Kong, Tat Chee Avenue, Kowloon, 999077, Hong Kong, [9]Centre for Energy and Environmental Sustainability, Lucknow, India and [10]Nanotechnology & Catalysis Research Centre (NanoCat), Institute of Postgraduate Studies, University Malaya, 50603, Kuala Lumpur, Malaysia

Email:
Pau-Loke Show* - showpauloke@gmail.com

* Corresponding author

Keywords:
biocompatible nanoparticles; cancer cells; carrageenan; cytotoxic selectivity; green synthesis methods; nanobiotechnology; SARS-CoV-2; self-assembly; wet chemical reduction

Beilstein J. Nanotechnol. **2023,** *14,* 377–379.
https://doi.org/10.3762/bjnano.14.32

Received: 22 February 2023
Accepted: 02 March 2023
Published: 27 March 2023

This article is part of the thematic issue "New trends in nanobiotechnology".

Editor-in-Chief: G. Wilde

The widespread use of nanotechnology has reached almost every sector in our daily lives and amazed the world by offering various potential applications in these sectors. The uprising wave of nanotechnology and its application are now prominent in the fields of chemistry and biomedicine, which are vital as these fields serve as a basis for the discovery of new molecules that may benefit humans. Nanotechnology contributed to the advancement of promising techniques either by the implementation of existing methods or by the establishment of new ones. Researchers in academia and industry sectors working in areas of biochemistry, chemical engineering, molecular biology, and genetics are likely to come across the advantages of applying nanobiotechnology tools in their studies. This profound technological advantage has brought many research laboratories to globally exchange ideas and promote intensive international scientific collaborations to further increase the level of understanding of applying nanotechnology to biological systems.

This thematic issue aims to provide vital findings to support new research and innovations utilizing recent trends in nanobiotechnological processes to encourage the development of these converging technologies for a sustainable economic growth.

The synthesis and the characterization of nanoscale biomaterials, the innovative applications of "smart nanoparticles", and the technological/biological impact of nanoscale systems are just some of the areas of focus in the field known as nanobiotechnology [1]. Nanobiotechnology has a wide array of applications: from organ-on-a-chip technologies to nanobiosensors and nanocatalysts for advanced characterisation and imaging tools, from intelligent drug delivery systems to artificial bioconstructs, and from functional nanostructured surfaces to smart materials and nanofluidics. In all these applications, it is important to consider the nanotoxicological and possible harmful impact of nanomaterials on living organisms [2]. In fact, the evaluation of the safety of a novel nanodevice is a process that should start at the very first step of concept and design. Particular attention should also be paid to the translational and regulatory aspects of nanobiomedical devices in order to enable them to be used in future clinical practice [3]. With proper consideration of these impacts, the implementation of nanotechnology tools can then be done in a safe manner.

In this thematic issue we invited many authors to contribute with manuscripts on novel concepts, ingenious designs, and promising applications in the field of nanobiotechnology. The submitted works were expected to feature innovative areas such as nanomaterials applied in biotechnology; nanoparticles used in environmental science and technology; nanosensors used in biosystems; nanomedicine in the context of biochemical engineering; micro- and nanofluidics; micro- and nano-electromechanical systems; nanoscience and nanotoxicology; nanotechnology applied in biology, medicine, food, environmental and agriculture sectors; environmental engineering and chemical engineering; nanoscale electrochemisty in biotechnology; computational nanochemistry in biotechnology; and life cycle assessment of nanobiotechnology.

The works presented in this thematic issue covered topics related to new concepts and ideas pertaining to the design and development of nanobiotechnology. These works include "The role of deep eutectic solvents and carrageenan in synthesizing biocompatible anisotropic metal nanoparticles" [4]. This review sheds light onto significant works involving the synthesis of metal nanoparticles using environmentally friendly wet chemical methods in which carrageenan is the main resource. The review summarises the possibility of creating a safe and nontoxic path to the synthesis of nanomaterials while maintaining its properties, such as morphology, yield and monodispersity. The introduction of a deep eutectic solvent as a cost-effective and green solvent was reviewed, where the usage of these solvents enabled the extraction and formation of desired nanostructures. The work also records the advantages and disadvantages of wet chemical reduction methods which use surfactants, and explores the in vitro and in vivo cytotoxicity of the synthesized anisotropic nanoparticles. A portion of the work looks into the possible integration of nanotechnology in deep eutectic solvent extractions and also the use of carrageenan as a safe stabilizing agent for nanomaterials synthesis. The review is concluded providing an outlook of these two components (i.e., deep eutectic solvents and carrageenan) as alternatives for the formation of plasmonic metal nanoparticles. The importance of applying these tools to improve the physicochemical properties and biocompatibility of the nanomaterials is also discussed.

The thematic issue also recorded a work on the topic of "Self-assembly of amino acids toward functional biomaterials" [5], where the role of biomaterials in nanobiotechnology is discussed. In this review, the latest advances in amino acid self-assembly and properties associated with the process and yielded products are highlighted. The self-assembly methods in focus included single amino acid self-assembly, functional amino acid self-assembly, amino acid and metal ion coordination self-assembly, and amino acid regulatory functional molecule self-assembly. Many works on self-assembly have shown low synthesis cost, ease of modelling, and good biocompatibility of the generated biomolecules. The review discusses the introduction and case studies of different types of self-assembly, applying examples on the application of the method. Finally, the review summarizes the use of nanotechnology in self-assembly methods and the challenges to adapt these nanomaterials to commercial applications.

Some other hot topics in the field of nanobiotechnology were also covered in the thematic issue. One of these topics is on the "Design and selection of peptides to block the SARS-CoV-2 receptor binding domain by molecular docking" [6]. This research work showcases peptides that are capable to bind and neutralize the SARS-CoV-2 virus through molecular docking. The latest developments of the molecular docking of peptides by molecular dynamics were investigated to understand the interaction between peptides with physiological proteins. Through the study, the selection and rapid design of peptides based on peptide binding sites, hydrogen bond number, and binding affinity were obtained. It was also concluded the potential role of these peptides in the prevention of infection caused by SARS-CoV-2. Another important topic covered in this thematic issue is presented in this article: "In search of cytotoxic selectivity on cancer cells with biogenically synthesized Ag/AgCl nanoparticles" [7]. This work explores the use of pineapple waste for the synthesis of silver and silver chloride nanoparticles, along with the analysis of the selective cytotoxicity of these nanoparticles on healthy and cancerous cells. The work aims to contribute to the production of alternative nanomaterials obtained from waste for therapeutic applications with emphasis on disease mitigation. Green synthesis methods were firstly applied for the biosynthesis of silver nanoparticles, along with silver chloride nanoparticles as there were chlorine salts in the pineapple peels which enable the formation of silver chloride. These nanoparticles were then characterized and tested regarding their cytotoxicity activity on cancer and healthy cells. The results showed a selective cytotoxicity of the nanoparticles towards cancer cell compared to that towards monocytes. This finding gives rise to the development of a new system where cytotoxicity can be selective. This may benefit future research in the field of nanoparticle synthesis for medical treatments.

The collection of comprehensive reviews and studies assembled in this thematic issue on nanobiotechnology trends provides useful and new scientific knowledge regarding the advancement of nanobiotechnology for science, technological, and engineering-related applications. A total of five high quality works were published within the thematic issue, with great support from researchers in various continents. The guest editors wish to express their gratitude to all the contributors, authors and reviewers, who have collectively ensured and maintained the standards of scientific quality within the works published. Finally, we also thank Dr. Wendy Patterson, Dr. Lasma Gailite, and Dr. Barbara Hissa for their support in the development of the "New Trends in Nanobiotechnology" thematic issue.

ORCID® iDs

Pau-Loke Show - https://orcid.org/0000-0002-0913-5409
Kit Wayne Chew - https://orcid.org/0000-0003-2622-6916

References

1. Koyande, A. K.; Chew, K. W.; Manickam, S.; Chang, J.-S.; Show, P.-L. *Trends Food Sci. Technol.* **2021,** *116,* 290–302. doi:10.1016/j.tifs.2021.07.026
2. Verma, S. K.; Suar, M.; Mishra, Y. K. *Front. Bioeng. Biotechnol.* **2022,** *10,* 919226. doi:10.3389/fbioe.2022.919226
3. Campora, S.; Ghersi, G. *Nanotechnol. Rev.* **2022,** *11,* 2595–2631. doi:10.1515/ntrev-2022-0148
4. Das, N.; Kumar, A.; Rayavarapu, R. G. *Beilstein J. Nanotechnol.* **2021,** *12,* 924–938. doi:10.3762/bjnano.12.69
5. Ren, H.; Wu, L.; Tan, L.; Bao, Y.; Ma, Y.; Jin, Y.; Zou, Q. *Beilstein J. Nanotechnol.* **2021,** *12,* 1140–1150. doi:10.3762/bjnano.12.85
6. Ramirez-Acosta, K.; Rosales-Fuerte, I. A.; Perez-Sanchez, J. E.; Nuñez-Rivera, A.; Juarez, J.; Cadena-Nava, R. D. *Beilstein J. Nanotechnol.* **2022,** *13,* 699–711. doi:10.3762/bjnano.13.62
7. Ramírez-Hernández, M. J.; Valera-Zaragoza, M.; Viñas-Bravo, O.; Huerta-Heredia, A. A.; Peña-Rico, M. A.; Juarez-Arellano, E. A.; Paniagua-Vega, D.; Ramírez-Vargas, E.; Sánchez-Valdes, S. *Beilstein J. Nanotechnol.* **2022,** *13,* 1505–1519. doi:10.3762/bjnano.13.124

License and Terms

BEILSTEIN JOURNAL OF NANOTECHNOLOGY

The role of deep eutectic solvents and carrageenan in synthesizing biocompatible anisotropic metal nanoparticles

Nabojit Das[1,2], Akash Kumar[1,2] and Raja Gopal Rayavarapu[*1,2]

Review

Open Access

Address:
[1]Nanomaterial Toxicology Laboratory, Nanomaterial Toxicology Group, CSIR-Indian Institute of Toxicology Research (CSIR-IITR), Vishvigyan Bhawan, 31 Mahatma Gandhi Marg, Lucknow 226001, India and [2]Academy of Scientific and Innovative Research (AcSIR), Ghaziabad 201002, India

Email:
Raja Gopal Rayavarapu[*] - rajagopal@iitr.res.in

* Corresponding author

Keywords:
anisotropic nanoparticles; carrageenan; cytotoxicity; eutectic solvents; surfactants

Beilstein J. Nanotechnol. **2021,** *12,* 924–938.
https://doi.org/10.3762/bjnano.12.69

Received: 23 March 2021
Accepted: 27 July 2021
Published: 18 August 2021

This article is part of the thematic issue "New trends in nano-biotechnology".

Guest Editor: P.-L. Show

Abstract

Plasmonic metal nanoparticles are widely used for many applications due to their unique optical and chemical properties. Over the past decade, anisotropic metal nanoparticles have been explored for imaging, sensing, and diagnostic applications. The variations and flexibility of tuning the size and shape of the metal nanoparticles at the nanoscale made them promising candidates for biomedical applications such as therapeutics, diagnostics, and drug delivery. However, safety and risk assessment of the nanomaterials for clinical purposes are yet to be made owing to their cytotoxicity. The toxicity concern is primarily due to the conventional synthesis route that involves surfactants as a structure-directing agent and as a capping agent for nanoparticles. Wet chemical methods employ toxic auxiliary chemicals. However, the approach yields monodispersed nanoparticles, an essential criterion for their intended application and a limitation of the green synthesis of nanoparticles using plant extracts. Several biocompatible counterparts such as polymers, lipids, and chitosan-based nanoparticles have been successfully used in the synthesis of safe nanomaterials, but there were issues regarding reproducibility and yield. Enzymatic degradation was one of the factors responsible for limiting the efficacy. Hence, it is necessary to develop a safer and nontoxic route towards synthesizing biocompatible nanomaterials while retaining morphology, high yield, and monodispersity. In this regard, deep eutectic solvents (DESs) and carrageenan as capping agent for nanoparticles can ensure the safety. Carrageenan has the potential to act as antibacterial and antiviral agent, and adds enhanced stability to the nanoparticles. This leads to a multidimensional approach for utilizing safe nanomaterials for advanced biomedical and clinical applications.

Review

Introduction

Plasmonic metals such as gold and silver, upon achieving nanoscale dimensions, exhibit unusual physicochemical characteristics, such as interesting plasmonic, optical and catalytic properties, and facile surface modification with tunable size and morphology [1]. Among these properties, the ability of surface plasmon resonance (SPR) at visible to near-infrared (NIR) wavelengths is the most striking characteristic feature of gold and silver nanoparticles. Surface plasmon resonance is an inherent property of plasmonic metal nanoparticles that is immensely employed as a tool for theranostics and is highly influenced by the size and shape of the nanoparticle [2]. The property of SPR has also been exploited for nanochips and smartphone-based sensing applications [3-5]. Several other advanced sensing applications have emerged, such as battery-free and wireless devices, providing on-site results [6,7]. NIR absorption is exclusively exhibited by plasmonic anisotropic nanoparticles, enabling diagnostic imaging within the optical therapeutic window. The realization of immense potential due to innate striking features of anisotropic nanoparticles has brought material and biological researchers under the same umbrella. The manifestation of NIR absorption in theranostic application is highly acknowledged due to the ability of NIR/IR rays to deeply penetrate tissues, enabling nanoparticle-mediated photothermal or contrast effects. However, the final purpose of these nanomaterials for biological applications is determined after successful toxicity assessment and stability evaluation in biological media [8]. Traditionally used stabilizing agents, such as surfactants and citrate, enable the synthesis of nanoparticles with high yield and monodispersity but also cause cytotoxicity and genotoxicity even at low concentrations [9,10]. Surfactants are known to act as a template for anisotropy in plasmonic metal nanoparticles, especially rod-shaped gold nanoparticles. The most approved and widely used surfactants for synthesizing anisotropic nanoparticles are quaternary ammonium surfactants with halides (bromide, chloride, or iodide) as counterions. Hexadecyltrimethylammonium bromide (CTAB) is the most commonly used surfactant for synthesizing anisotropic nanoparticles with high yield and monodispersity. The surfactant induces anisotropy during the growth of nanoparticles and enables NIR absorption capability due to longitudinal surface plasmon resonance (LSPR) [11]. However, despite the superior plasmonic properties, these nanomaterials are far away from a substantial use in biological applications due to toxic capping agents employed during synthesis.

Several counterparts such as polymers, lipids, and chitosan-based nanoparticles are extensively explored in drug delivery and therapeutic applications due to their biocompatible nature. Green synthesis of metal nanoparticles for biomedical applications has gained momentum recently due to their inherent nontoxicity. Although they are biocompatible, these metal nanoparticles lack monodispersity, high yield, and controlled morphology, which are essential criteria for the successful use in biological milieus. Recent studies indicated that the green synthesis of nanoparticles, such as zinc oxide nanoparticles and bimetallic copper–silver and nickel–cobalt nanoparticles, is preferred for catalytic, antibacterial, and therapeutic applications [12-14]. Several other synthesis methods have been developed for environmental applications, such as biohydrogen production and chromium deionization [15-18]. In addition, polymer-based nanoparticles showed low drug loading and encapsulation efficiency. The acidic nature of poly(lactic-*co*-glycolic acid) is not suitable for certain drugs and bioactive molecules and make the polymer prone to a higher enzymatic degradation rate [19]. This is why there is a need for novel synthetic routes for synthesizing safe plasmonic metal nanoparticles maintaining high yield and monodispersity with tunable size and morphology. Nontoxic, biocompatible, and sustainable solvents, such as deep eutectic solvents (DESs), and carrageenan as capping and reducing agent are gaining popularity in nanomaterial synthesis. Apart from potential tools for biomedical applications, recent studies have also shown the utilization of anisotropic nanomaterials in CO_2 mitigation and climate change control [20-22]. Several other studies reported novel environmental remediation approaches based on nanomaterials [23,24].

Deep eutectic solvents (DESs) are a class of nascent sustainable, non-aqueous solvents, comparable to room-temperature ionic liquids (RTILs). DESs fairly resemble the RTILs even though there are important differences regarding ecological footprint and price. One is that DESs are predominantly composed of molecules unlike RTILs, which predominantly contain ions. Also, DESs are fairly cheaper and easier to prepare, do not generate waste during preparation, and require no further purification, which gives them properties of a green solvent [25]. However, DESs share remarkable features with RTILs such as low vapor pressure, high tolerance to humidity, and high thermostability. The term “deep eutectic solvent” was first coined by Abbott in the year 2003 [26]. The first work on using DESs as a solvent in synthesizing anisotropic gold nanoparticles was reported in 2008 [27]. The synthesis involved no surfactant or seed in the reaction mixture. Later on, several studies were carried out to synthesize nanomaterials using DESs that embrace the principles of green chemistry. Despite extensive studies for more than a decade, DESs as solvents for nanomaterial synthesis yet awaits exploration regarding biological applications. In an interesting recently published work, a natural deep eutectic solvent (NADES) has been used to extract metal oxide nanoparticles [28]. Numerous indispensable parameters including surface tension, polarity, viscosity, and hydrogen bonding have an important influence on the reactivity of species. Also, the formation of nanostructures is governed by the mass transport properties of the DES components. It is also possible to modulate the viscosity of DESs, especially NADES, by varying the composition ratio of hydrogen bond donor and hydrogen bond acceptor components [29]. Also, the growth mechanisms and nucleation processes of nanoparticles are highly modulated by the components of DESs through modifying reduction potentials, neutralizing charge, and in particular, crystal face pacification, enabling preferential crystal growth. DESs are the medium where nanoparticle synthesis occurs in the presence of capping agent and reducing agents. Biocompatible capping and reducing agents, such as carbohydrates (i.e., carrageenan), are suitable for nanoparticle synthesis intended for biological applications.

Carrageenans are a group of oligosaccharides predominantly found in Rhodophyceae commonly known as red algae. They are sulfated linear oligosaccharides consisting of ᴅ-galactose residue units linked by (1→3)-linked β-ᴅ-galactopyranose (unit G) and (1→4)-linked α-ᴅ-galactopyranose (unit D) alternatively. Some of the reports in the literature showed that carrageenan has several pharmacological properties such as antiviral and antitumor activity that can add pharmaceutical value to the nanomaterials synthesized using them [30,31]. These additional properties enabled carrageenan to emerge as a suitable alternative for other biocompatible molecules and biopolymers. Similar to DESs, carrageenan is also biocompatible. A good understanding of its role as a green component for synthesizing nanomaterial for biological applications is only at the beginning. To be more specific, carrageenan was used in the synthesis of plasmonic metal nanomaterials much later than DESs. The excellent properties of carrageenan as a stabilizing/capping and a reducing agent was reported in a recent study for gold nanoparticles [32]. To understand the applicability of DESs and carrageenan in nanotechnology, a histogram with the number of publications (Scopus-indexed journals) for the past five years in shown in Figure 1. This shows the emerging potential of these novel materials for nanobiotechnology research.

The histogram shows an upward trend regarding the use of carrageenan in nanobiotechnology, indicating that it is a safe approach in synthesizing biocompatible nanomaterials. Carrageenans were either used in synthesis as a capping agent or as functional molecule for nanoparticle stabilization and targeted drug delivery. In contrast, nanomaterials synthesized using DESs received less interest, which is evident through a stagnant number of reports over the last five years. However, twenty reports have been published on using DESs for nanomaterial synthesis.

This review attempts to illuminate the works from the last decade that involved DESs and carrageenan in the synthesis of nanomaterials that are nontoxic. The review begins by discussing widely used wet chemical methods of synthesizing anisotropic plasmonic metal nanomaterials. We also give insight in growth mechanisms during the initiation of anisotropy in the presence of a surfactant. This review is a crisp overview of determining the anisotropy–cytotoxicity relationship due to

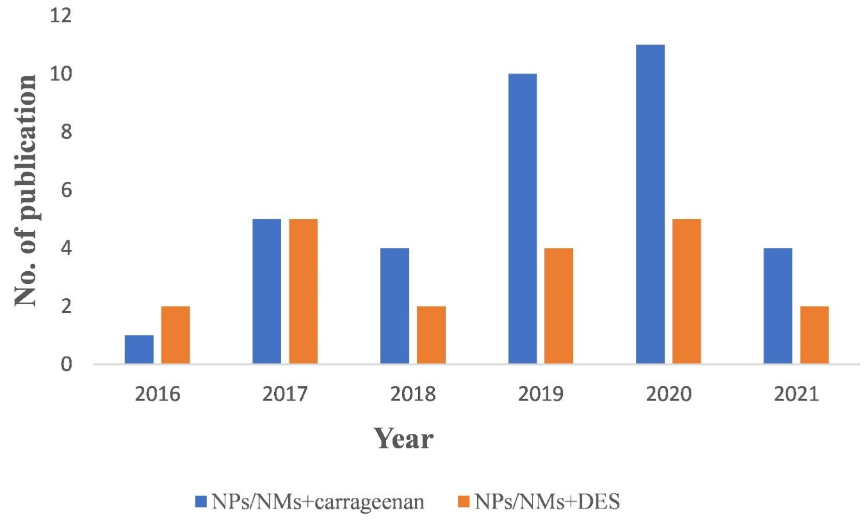

Figure 1: Number of publications over the last five years on the synthesis of nanoparticles (NPs)/nanomaterials (NMs) using carrageenan and a deep eutectic solvent (DES). The numbers have been obtained from SCOPUS-indexed journals using PubMed.

structure-directing agents and the role of DESs and carrageenan in alleviating toxicity of the synthesized nanomaterials. We conclude with an outlook towards the possible amalgamation of DESs and carrageenan creating a nontoxic platform for synthesizing nanomaterials with the potential for biological applications.

Wet chemical reduction method using surfactants: pros and cons

The widely used wet chemical approach for synthesizing nanomaterials is a facile reduction method involving a precursor metal salt and a reducing agent in the dispersion phase [33]. Furthermore, a stabilizing/capping agent is used for enhanced stability and functionalization for the intended application. The wet chemical route allows for a high degree of controllability and reproducibility in synthesizing anisotropic nanomaterials maintaining high yield and monodispersity. Initially, gold nanorods were synthesized using electrochemical methods using polycarbonate membrane templates or porous alumina for shape control in the presence of surfactants (mostly CTAB) [34,35]. Because of their optical properties, gold nanorods became increasingly popular between 1999 and 2003 and a laborious three-step seed-mediated synthesis via a wet chemical route was developed [36]. The emergence of seed-mediated synthesis provided chemists, for the first time, with a versatile and convenient wet chemistry of synthesizing nanorods and several other anisotropic shapes such as rhombic dodecahedrons, tadpoles, cubes, and tetrapods [37-39].

Seed-mediated synthesis via wet chemical routes is undoubtedly the most promising and accepted method to synthesize anisotropic nanoparticles exhibiting superior plasmonic characteristics. The route allows chemists to control the reaction parameters for synthesizing nanomaterials of desired sizes and shapes. The method employs a growth solution consisting of the respective metal salt, a weak reducing agent, a structure-directing agent (predominantly quaternary ammonium surfactants) and silver ions for preferential facet binding in the solution phase. The seed-mediated approach is a multistep controlled redox reaction utilizing metal seed nanocrystals of 1.5–4.0 nm. The seed particles are synthesized by reducing precursor gold salt using an excess amount of a strong reducing agent, such as sodium borohydride ($NaBH_4$). Although, seedless synthesis of anisotropic plasmonic metal nanoparticles has been reported, they involved binary surfactants for tuning the absorption spectrum [40].

Apart from CTAB, several other quaternary ammonium surfactants such as myristyltrimethylammonium bromide (MTAB), dodecyltrimethylammonium bromide (DTAB), hexadecyltrimethylammonium chloride (CTAC), and benzyldimethylhexadecylammonium chloride (BDAC) have been used as structure-directing agents for synthesizing gold nanorods [41-43]. Co-mixtures of these quaternary ammonium surfactants are also being used to synthesize anisotropic nanoparticles. Despite exhibiting such astonishing structure-directing features, surfactants are of limited use for the synthesis anisotropic nanoparticles for biomedical applications due to their cytotoxicity. The consequences, both in vitro and in vivo, are discussed in the following sections.

Anisotropic nanoparticles: cytotoxicity of structure-directing agents

The evolution of anisotropy through wet chemical methods (seed-mediated synthesis) using a surfactant (CTAB) has been discussed already. The function of surfactants as templates or matrices makes them an irreplaceable candidate for determining the controlled size/shape of anisotropic nanoparticles with excellent monodispersity. However, from the biological application point of view these nanomaterials could not achieve their potential despite acknowledgeable superior plasmonic properties. This is due to the toxic nature of surfactants adsorbed on the metal surface in a tightly packed bilayer structure. Among quaternary ammonium surfactants, CTAB has been extensively reported as cytotoxic even at low concentrations [44-46]. The positively charged CTAB interacts with the plasma membrane, which is negatively charged due to the asymmetric distribution of charged lipids between the two leaflets of the plasma membrane. This lead to a negative charged of the inner leaflet generating a surface potential and the binding affinity towards positively charged moieties. However, an interesting study revealed a structure-dependent cytotoxicity of quaternary ammonium surfactants in which cytotoxicity increased with the increase in carbon chain length of the surfactants [47]. Several reports have shown that the toxicity of CTAB-capped gold nanorods depends on nanoparticle size, shape, particle concentration, surface modification, and coating methods. There are contrasting results of toxicity based on various parameters conducted either in vitro or in vivo [48-53]. Gold is one of the most promising inert metals for synthesizing nanoparticles and is ideal for biomedical research. The safety and risk assessment of these nanoparticles are reported in the literature tabulated in Table 1. The cytotoxicity of nanoparticles is depicted based on several factors such as morphology, size and surface chemistry as shown in Table 1 and Figure 2.

In vitro cytotoxicity of anisotropic nanoparticles

The use of anisotropic metal nanoparticles in biomedical research is gaining attention due to their plasmonic/optical properties. However, in vitro cytotoxicity assessment of these nanomaterials is a prerequisite for further in vivo validation and

Table 1: In vitro and in vivo toxicity studies of gold nanoparticles of different shapes with different surface groups.

Nanoparticles	Morphology	Surface group	Model system	Remarks	Ref.
gold	spheres	PEG	in vivo	acute toxicity to liver and spleen	[53]
gold	spheres	citrate	in vitro	dose-dependent cytotoxicity	[49]
gold	nanospheres, nanostars, and nanorods	chitosan	in vitro	toxicity trend: nanorods > nanostars > nanospheres	[54]
gold	nanorods	CTAB	in vitro	cytotoxic	[60]
gold	spheres	citrate	in vivo	size-dependent toxicity	[65]
gold	spheres, triangles, rods, trigonal bipyramids	CTAB	in vivo	genotoxic	[67]

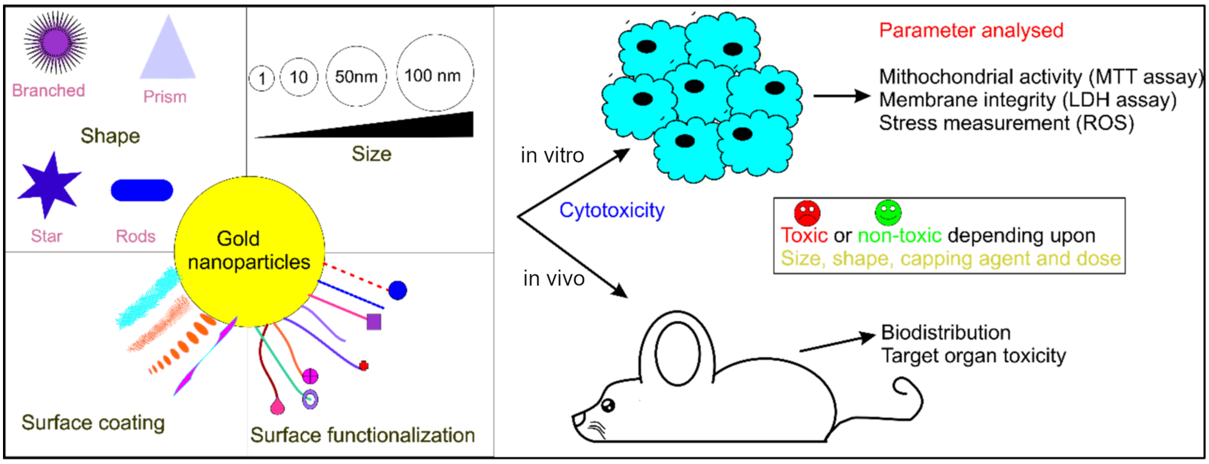

Figure 2: Cytotoxicity of anisotropic gold metal nanoparticles in vitro and in vivo.

subsequent clinical trials. The physicochemical properties of a nanoparticle such as size, shape, and surface chemistry, determine their cytotoxicity. For example, gold nanoparticles of different shapes, as shown in Figure 3, displayed morphology-dependent cytotoxicity. Rod-shaped gold nanoparticles were more toxic than nanostars and nanospheres [54]. The potential risk is higher for anisotropic nanoparticles than for spherical shapes. This is due to greater exposed surface area and more defects during crystal growth of anisotropic nanoparticles. Gold nanoparticles show tremendous potential in biomedical research due to unique optical and physicochemical properties and the inert nanoparticle core. The inertness is due to metallic gold formed upon reduction of Au^{3+} during nanoparticle formation. However, there is also the possibility of Au^0 oxidation that is influenced by size, shape, and stabilizing/capping agents. For instance, commonly used citrate and thiolate ligands result in a partial polarization of the nanoparticle core (Au^δ + O^δ and Au^δ + S^δ), which cannot be neglected following its subsequent leaching [55]. It is also well known that gold cations play a key role in oxidizing substrates in aerobic redox reactions catalyzed by gold nanoparticles [56]. Redox reactions are intrinsic in biological organisms and are mainly governed by cytochrome P450, which acts as a strong catalyst for oxidation. Hence, the gold nanoparticles can alter the cell metabolism, leading to toxicity. In vitro studies also confirmed that isotropic gold nanoparticles with core sizes of greater than 5 nm were less toxic and considered biologically inert [44,57,58].

Numerous in vitro studies carried out using high-throughput techniques such as microscopic techniques, TEM, and ICP-MS revealed the fate of nanoparticles and their interaction at the interface between the metal surface and cell membrane. Electron microscopy revealed fundamental and mechanistic information regarding nanoparticle–cell interactions and their uptake into cell organelles. The metal content within the cells was determined via ICP-MS. Cell toxicity of nanoparticles depends on their size, shape, surface chemistry (predominantly determined by the capping agent used) and the cell type used for toxicity assessment. Chan and co-workers reported that cell internalization is optimum for nanoparticles with a size of 40–50 nm [59].

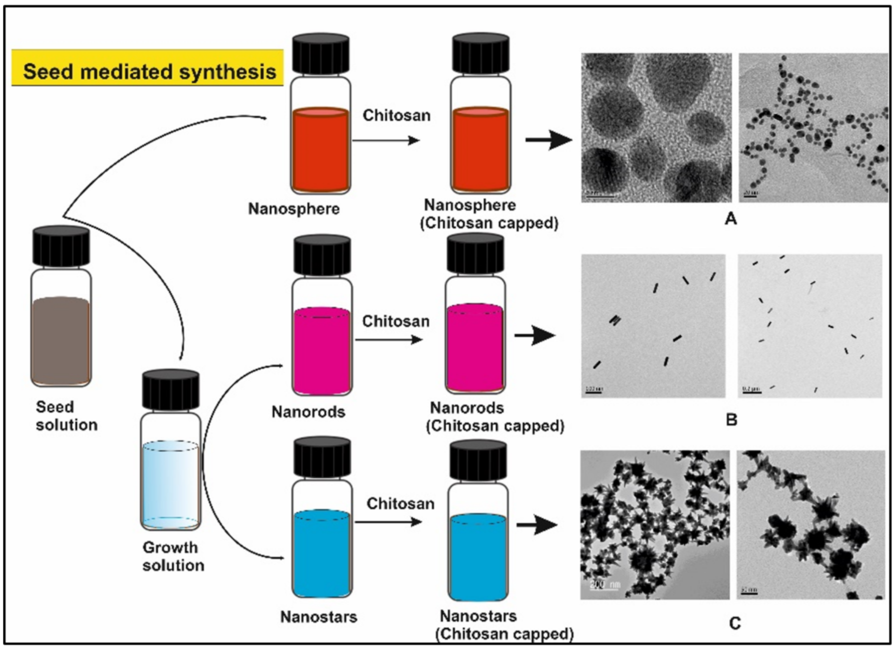

Figure 3: Synthesis of gold nanoparticles of different shapes using the seed-mediated approach. Chitosan was used for post functionalization of (A) gold nanospheres, (B) nanorods and (C) nanostars. Adapted from [54], © 2019 Y. J. Lee et al., distributed under the terms of the Creative Commons Attribution 4.0 International Licence, http://creativecommons.org/licenses/by/4.0/.

This is due to maximum interaction between antibody and receptor during receptor-mediated endocytosis. In vitro studies mostly involve a wide range of parameters, as highlighted by Murphy et al., but they do not provide all decisive aspects of toxicity [44]. John W. Stone and his group, in 2017, synthesized less toxic gold nanorods using dodecylethyldimethylammonium bromide (C_{12}EDMAB) as an alternative structure-directing surfactant [60]. They carried out an in vitro cytotoxicity study exposing Hep-G2 and A549 cells to CTAB- and C_{12}EDMAB-capped gold nanorods. The researchers observed a considerable difference in cell viability at the same concentration levels. Much earlier, a chemical method introduced by Chenxu Yu et al. illustrated the successful reduction of cytotoxicity of gold nanorods using organothiol compounds, namely 11-mercaptoundecaonic acid (MUDA) and 3-animo-5-mercapto-1,2,4-triazole (AMTAZ) [61]. PEGylation of gold nanorods is considered as a safe coating for alleviating the toxicity of CTAB adsorbed on the nanorod surface. The gold nanorods have excellent capability to be used in imaging as an optoacoustic contrast agent [62,63]. Poly(ethylene glycol) (PEG) is well known for reducing non-specific binding to biological molecules, rendering stealth character. This avoids macrophage recognition and phagocytosis and ultimately leads to prolonged blood circulation with enhanced retention and permeability of the nanorods. Apart from PEGylation, phosphatidylcholine has also been used as a coating agent for reducing the toxicity of CTAB-capped gold nanorods [64].

In vivo toxicity of anisotropic nanoparticles

In vivo toxicity validation of nanomaterials is an inevitable step before clinical trials. However, in vivo studies of nanoparticles are subtle and quite controversial when compared to in vitro studies. The most common citrate-capped gold nanoparticles proved to be non-cytotoxic in vitro and showed size-dependent toxicity in vivo. Chen et al. revealed that gold nanoparticles of smaller (3–5 nm) and larger (30 and 100 nm) sizes were nontoxic in vivo; however, nanoparticles of average sizes 8, 12, 13, 37 nm were found to be toxic, provoking drastic weight loss, sickness, and short life span in mice [65]. The deteriorating effect was due to systemic toxicity evident through liver, lung, and spleen injury. In contrast, the non-cytotoxic nature of 13 nm citrate-capped gold nanoparticles has been reported [66]. Another recent study on *Drosophila melanogaster* showed mutagenicity of isotropic and anisotropic gold nanoparticles through the process of proton transfer (PT) [67]. A 1-(2-hydroxy-5-chlorophenyl)-3,5-dioxo-1*H*-imidazo[3,4-*b*]isoindole (ADCL)-based PT process on anisotropic gold nanoparticles was found to be accelerated compared to isotropic gold nanoparticles. The role of surface chemistry in determining toxicity and cell internalization of nanoparticles due to capping agents is critical. It has been reported that glutathione-capped gold nanoparticles underwent efficient cell internalization and efficient renal clearance compared to PEGylated and citrate-capped gold nanoparticles [68,69]. This was observed due to the difference in the binding affinity of the capping agents toward serum proteins. Glutathione showed less affinity towards serum proteins than citric acid. In an exposure time duration study by Lopez-Chaves et al., size-dependent metabolic fate and deposit formation of gold nanoparticles in different biological systems (liver, spleen, and kidney) of Wistar rats was observed [70]. The study revealed that gold nanoparticles of 10 nm size exhibited an oxidation-induced deleterious effect evident through nuclear localization and greater DNA damage. Despite oxidative imbalance induced by the gold nanoparticles, no inflammatory responses or tissue damage was observed for shorter exposure time. Therefore, the study concluded by commencing short time clinical use of these gold nanoparticles and understanding their use for chronic treatments better. A study was reported on the effect of CTAB-capped gold nanorods on estuarine model systems (consisting of sediments, plants, microbial films, fish, and snails) for observing ecological and environmental impact [71]. The results showed that the biofilms were the primary route through which gold nanorods enters the food chain.

It is very evident from the discussed in vitro and in vivo studies that the root cause of cytotoxicity is the structure-directing agent. Therefore, green chemistry has been implemented in synthesizing nanoparticles without compromising the characteristics of anisotropic nanoparticles intended for biological application. The following section of the review focuses on DESs and carrageenan, a class of emerging green solvents and a carbohydrate polymer for synthesizing safe plasmonic nanomaterials.

Deep eutectic solvents in nanotechnology

The preparation of DESs involves mixing solid organic precursors with high melting points, which interact via hydrogen bond to form a fluid at room temperature with a freezing temperature much below that of the individual precursor components. These strong hydrogen bonds restrict the recrystallization of the parent compounds [72]. There are numerous reports on DESs from various combinations of compounds by self-association between hydrogen bond donors and acceptors. The most extensively studied to date involve mixtures of choline chloride (hydrogen bond acceptor) with urea, ethylene glycol, or glycerol (hydrogen bond donors) in a molar ratio of 1:2 [25]. However, more DESs can be synthesized through selecting different components using permutation and combination. The wide range of components available allowed the chemists to fundamentally research the application of DESs. DESs are environmentally friendly, bio-degradable, and nontoxic, as shown in Figure 4. DESs were used as solvents for metal cleaning before the extensive use in electroplating. Electrolytic decomposition is another appealing process for developing a microscale propulsion system. Recent reports on the electrolytic decompo-

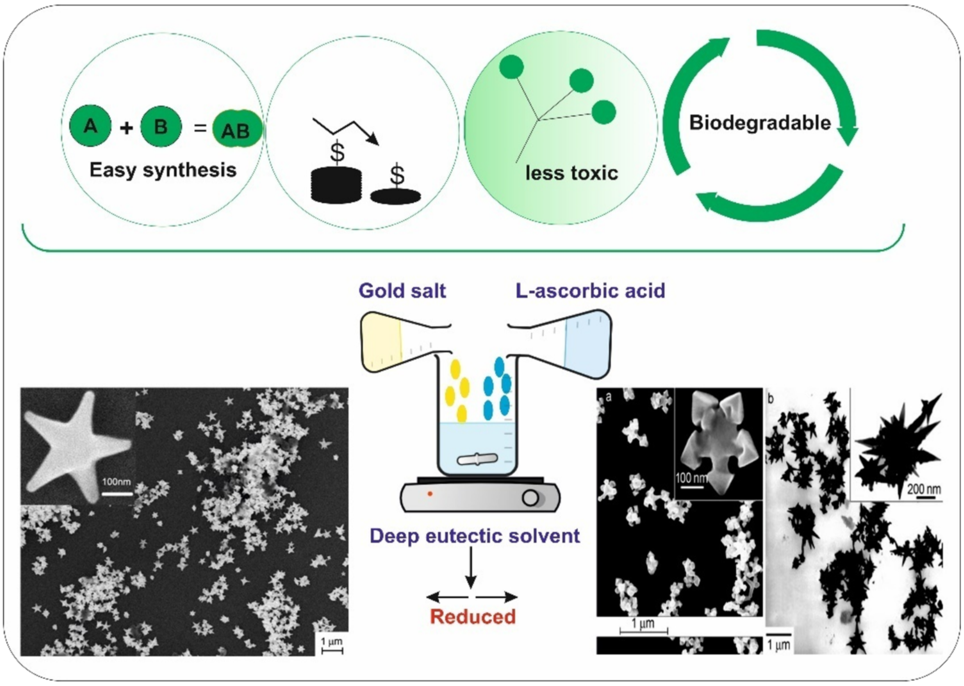

Figure 4: A deep eutectic solvent as green solvent in the synthesis of anisotropic nanoparticles (flower shape). All micrographs are adapted from [27], H. G. Liao et al., “Shape-Controlled Synthesis of Gold Nanoparticles in Deep Eutectic Solvents for Studies of Structure-Functionality Relationships in Electrocatalysis”, Angew. Chem. Int. Ed., with permission from John Wiley and Sons. Copyright © 2008 Wiley-VCH Verlag GmbH & Co. KGaA, Weinheim. This content is not subject to CC BY 4.0.

sition of hydroxylammonium nitrate (HAN) were demonstrated [73-75]. DESs are well known for dissolving many species of high polarity, for example, amino acids, metal salts, glycerol, benzoic acid, citric acid, and glucose [26,76]. They are also promising in the dissolution of different polymers, such as starch, cellulose, lignin, chitin, and are also used in the pretreatment of cellulose biomass [77]. Although the applications of DESs mentioned above lie at the interface of material and biological science, the following section will only discuss application of DESs in nanomaterial synthesis.

As mentioned earlier, the high solubility of metal salts in DESs makes them an ideal solvent. The solvation property determines the chemical (especially electrochemical) synthesis technology. Therefore, studying the solvation properties of a solvent is quite important for potential applications. DESs, due to their good solvation and electroconductivity properties, have been utilized in surface coating with nanoparticles through electrodeposition. A general electrodeposition setup consists of three electrodes, that is cathode, anode, and a reference electrode [78]. The solvation property and the conductivity of DESs also play a critical role in determining the physical structure, yield, and morphology of the products in chemical synthesis. This is also evident from the studies tabulated in Table 2, where the obtained shapes are given together with the eutectic mixture and precursor material used [79-87].

The aggregation/agglomeration of nanoparticles in the dispersion phase is a commonly encountered challenge. The stability of the nanoparticles is preserved by introducing various capping/stabilizing agents. The capping agent determines the surface chemistry of the nanoparticles deviating from the innate characteristics of the material. However, DESs when used as a solvent yield colloidally stable nanoparticles in the absence of capping/stabilizing agents. Also, the function of DESs is not limited to nanoparticle stabilization in their dispersion phase. They also act as a template, determining shape, size, and surface chemistry for the intended application. For example, Gutiérrez et al. synthesized porous carbon using *p*-toluenesulfonic acid and choline chloride in a molar ratio of 1:1 [88]. The DES used served as solvent and catalyst for the condensation of furfuryl alcohol, followed by carbonization resulting in the formation of pores. Oh et al. reported synthesizing highly monodispersed gold particles with a distinct rough surface and defined diameters using choline chloride and malonic acid [89]. The DES used served as reaction medium and structure-directing agent at the same time during synthesis. The synthesis did not require stabilizing or capping agents such as polymers

Table 2: Different DESs and their application in the synthesis of nanomaterials (NMs).

DESs	NM type	Surface group	Morphology	Role	Ref.
choline chloride/urea	alloys, iron	N/A, choline chloride-urea	dendrite-like and sharp-edged crystallites, nearly spherical	electrolyte for nanoparticle deposition, media for nanoparticle synthesis by a sputter deposition technique, solvent for chemical synthesis of nanomaterials	[79,80]
choline chloride/thiourea	chitin	acetic acid	whiskers	solvent for chemical synthesis of nanomaterials	[81]
choline chloride/ 1,3-dimethylurea	cobalt and nickel	N/A	coral-like	solvent for chemical synthesis of nanomaterials	[82]
choline chloride/malonic acid	cobalt	N/A	octahedral	solvent as well as structure-directing agent for chemical synthesis of nanomaterials	[83]
choline chloride/ethylene glycol	manganese	N/A	spherical	dispersant for nanoparticles and chemical synthesis of nanomaterials	[84]
choline chloride/acrylic acid	molybdenum, iron	poly(acrylic acid)	2D sheets	dispersant for nanoparticles and chemical synthesis of nanomaterials	[85]
choline chloride/*p*-toluenesulfonic acid	titanium	N/A	spherical	solvent as well as a structure-directing agent for chemical synthesis of nanomaterials	[86]
choline chloride/ tris(hydroxymethyl)propane	graphite	epoxy resin	platelets	dispersant for nanomaterials	[87]

or surfactants, highlighting the role of DES as a stabilizer and structure-directing agent. The work also illustrated temperature-dependent morphological differences between the nanostructures. Spherical sized small gold particles of nearly 100 nm were synthesized at 70 °C whereas network like nanostructures were observed when the synthesis temperature was 90 °C. Apart from nanomaterials, DESs are also being exploited for the electrodeposition of alloys for coating applications. For example, Bernasconi et al. developed a non-aqueous electrolyte using choline chloride and ethylene glycol in a molar ratio of 1:2 for electrodeposition of a zinc–nickel alloy to provide corrosion protection [90].

Due to the ever-rising interest in DESs for nanomaterial synthesis, a fundamental understanding regarding interfacial behavior and mass transport, such as ionic adsorption, surface wetting, double layered structure, and hydrogen bonding is needed as it will allow chemists to controllably manipulate the nanoscale growth [91]. While, in-depth studies (experimental and computational) regarding these aspects are yet to come, several significant preliminary studies have been reported. Much of the understanding of the interfacial behavior of DESs has been derived from electrodeposition studies. For example, Abbott et al. showed zinc electrodeposition in two different DESs (ethaline and reline in choline chloride), yielding respectively, “rice grains” and “platelets” morphologies [92]. The difference between the electrochemical double layers and a differential activity of chloride ions (i.e., preferential facet binding during crystal growth restricting the lattice growth in a particular direction) were responsible for the observed morphological difference. The lower surface tension of DESs facilitates rapid nucleation yielding tiny particles that undergo Ostwald ripening through a slow process, allowing for the manipulation on the nanoscale with controlled crystal growth.

Plasmonic metal nanoparticle synthesis using DESs

Plasmonic metal nanoparticles, such as gold, silver, and platinum, are showing excellent potential owing to their unique physicochemical properties. DESs were first used for synthesizing anisotropic gold nanoparticles with high monodispersity in a mixture of choline chloride and urea in 2008 by Sun and co-workers [27]. The anisotropy was driven using the mild reducing agent ascorbic acid and the DES. The result was remarkable as the synthesis involved no surfactant or seeds. The Sun group also synthesized platinum nanoflowers of ca. 200 nm size with high monodispersity using DESs [93]. The group also successfully synthesized triambic icosahedral (TIH) Pt nanocrystals with high-index {771} facets. The nanoparticles with high-index planes exhibited higher catalytic activity due to high density of atoms with low coordination number compared to nanoparticles with low-index facets such as {100}, {111}, or {110}. Chirea et al. synthesized polycrystalline gold nanowires through a $NaBH_4$-assisted rapid reduction of $HAuCl_4$ in a DES (mixture of reline and ethaline) [94]. The strong coordination of $[AuCl_4]^-$ in reline exhibited a sixfold enhanced catalytic activity.

Apart from the high catalytic activity, nanoparticles produced in DESs showed no cytotoxicity in vitro systems. Guar-gum-fabricated gold nanoparticles (GA-GNPs) in a DES were synthesized for the use as X-ray contrast agent. The precursors for the DES used were choline chloride, gallic acid and glycerol. The X-ray attenuation coefficient of GA-GNPs was three times higher than that of the clinically used contrast agent Visipaque [95]. The in vitro study of the synthesized GA-GNPs confirmed their high potential to replace conventional contrast agents. In another example, Mahyari et al. synthesized gold nanoflowers using a DES without using reducing agents [95]. The gold nanoflowers showed excellent surface-enhanced Raman scattering (SERS) when doped with rhodamine B (RhB). The enhancement factor produced by these gold nanoflowers was estimated to be 1.09×10^5 regarding pure RhB. The value of the enhancement factor is up to par with the intensively branched gold nanoparticles and is even greater than some of the reported gold nanostars and nanoflowers [96]. Concerning the biocompatibility of the nanomaterials synthesized using DESs, only a couple of studies has been carried out in vivo and in vitro. Mineral-substituted apatite nanoparticles synthesized using a choline chloride/thiourea mixture for prospective rejuvenation applications for bone tissues have shown no cytotoxicity in vivo [97]. The non-cytotoxic nature of fluorapatite nanoparticles synthesized using reline (choline chloride/urea) in vitro has been also reported [98]. However, with the rising popularity of DESs due to biodegradability, biocompatibility, sustainability, and low cost, achieving the real potential in nanobiotechnology is not far.

Carrageenan as green/safe stabilizing agent in nanomaterial synthesis

A stabilizing agent, often known as capping agent, is one of the vital components in the synthesis of nanomaterials. The colloidal stability of the nanoparticles is governed by the capping agent, which prevents the aggregation of nanoparticles. Several capping agents such as CTAB, citrate, polymers, and carbohydrates are extensively used to stabilize nanoparticles in their colloidal state [99]. The capping agents govern the stabilization of nanoparticles and determine morphological changes in a nanoparticle due to differential binding to crystal facets during the crystal growth phase of the nanoparticle during synthesis. However, there are reports on synthesizing nanomaterials without stabilizing agents but they were very definitive in size-shape tuning and storage conditions [100,101]. Figure 5 shows the synthesis of gold nanoparticles using carrageenan as a capping/stabilizing as well as a reducing agent. Furthermore, these carrageenan-capped gold nanoparticles showed promising antitumor activity in MDA-MB-231 and HCT-116 cell lines [32].

Carrageenans are sulfated oligosaccharides extracted from red algae. They are composed of galactose and anhydrogalactose sub-units linked through a glycosidic bond. They are mainly categorized into three types depending on the degree of sulfation. The three types are: kappa carrageenan (one sulfate group per disaccharide), iota carrageenan (two sulfate groups per disaccharide) and lambda carrageenan (three sulfate groups per disaccharide). Carrageenan forms highly flexible curly helical structures, which are responsible for their gelation property at room temperature. The number of sulfate groups with repeating galactose units determines the gelation properties of carrageenan [102]. The higher the number of sulfate groups, the lower is the solubility temperature of carrageenan. Therefore, kappa and iota carrageenan do gelate whereas lambda carrageenan does not form gels at room temperature due to higher number of sulfate groups. All three carrageenans are soluble in hot water while lambda carrageenan is also soluble in cold water. Carrageenan is mainly used as an additive in the food industry for thickening, emulsifying, and preserving food and drinks [103]. Carrageenan is FDA-approved and remarkably safe [104]. In vitro and in vivo studies involving carrageenan proved that it is safe for biological applications with negligible inflammatory responses [105-107]. A conclusive study for evaluating cytotoxicity, intestinal permeability, and induction of proinflammatory cytokines of carrageenan was carried out using human intestinal cells (HCT-8 and HT-29) [108]. Also, carrageenan, due to the SO_3^- groups, showed interaction with positively charged quaternary ammonium surfactants [109]. However, this sulfated oligosaccharide is yet to

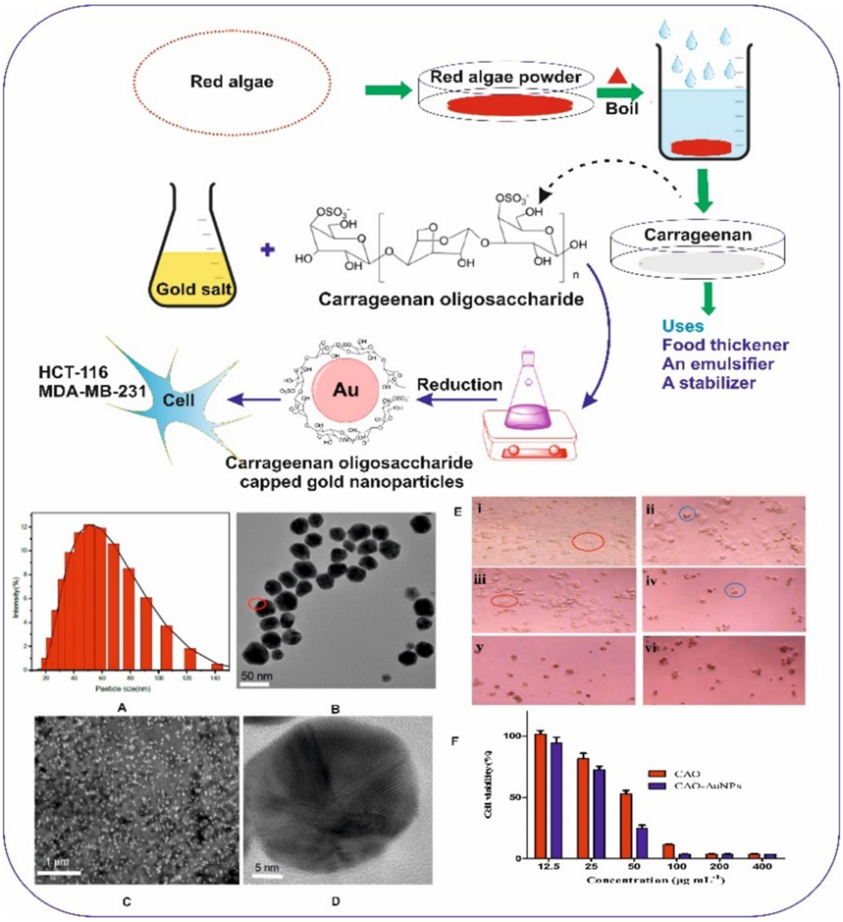

Figure 5: Carrageenan as capping and reducing agent for gold nanoparticle synthesis. (A) Histogram for the size distribution of nanoparticles. (B), (C) and (D) show TEM micrographs of the nanoparticles at different magnifications. (E) and (F) show the antitumor activity against MDA-MB-231 and HCT-116. Adapted from [32], © 2018 X. Chen et al., distributed under the terms of the Creative Commons Attribution 4.0 International Licence, http://creativecommons.org/licenses/by/4.0/.

realize its full potential in the field of nanotechnology. The use carrageenan in nanomaterial synthesis and application has been tabulated in Table 3 [32,110-115].

Carrageenan has been complexed with chitosan in a recent study, forming a composite for wound healing dressing. Silver nanoparticles, widely known for their antibacterial activity, are used in healthcare and the food industry, especially in manufacturing packaging materials. However, the cytotoxicity due to the release of the silver ions from AgNPs is a matter of concern. The cytotoxicity of micrometer-sized AgNPs was minimized by immobilizing them in carrageenan gel retaining the antibacterial property [85]. A study based on an injectable composite of carrageenan and nanoscale hydroxyapatite as an injectable bone substitute showed good adhesion properties with no cytotoxicity in vitro, as shown in Figure 6 [116]. The nanocomposite also

Table 3: The use of carrageenan in synthesizing various nanomaterials (NMs) for potential chemical and biological applications.

NMs type	Surface group	Morphology	Role	Ref.
silica	κ-carrageenan	2-dimensional	wound healing	[110]
silver	κ-carrageenan	spherical	catalytic degradation of dyes	[111]
chitosan	alginate, carrageenan	spherical	drug delivery	[112]
iron	κ-carrageenan, ι-carrageenan, λ-carrageenan	spherical	self-assembled nanoreactor yielding magnetite nanoparticles with polymer encapsulation	[113]
silver	κ-carrageenan	spherical	food packaging	[114]
silver	κ-carrageenan	spherical	antibacterial activity and low cytotoxicity	[115]
gold	κ-carrageenan	spherical	antitumor activity	[32]

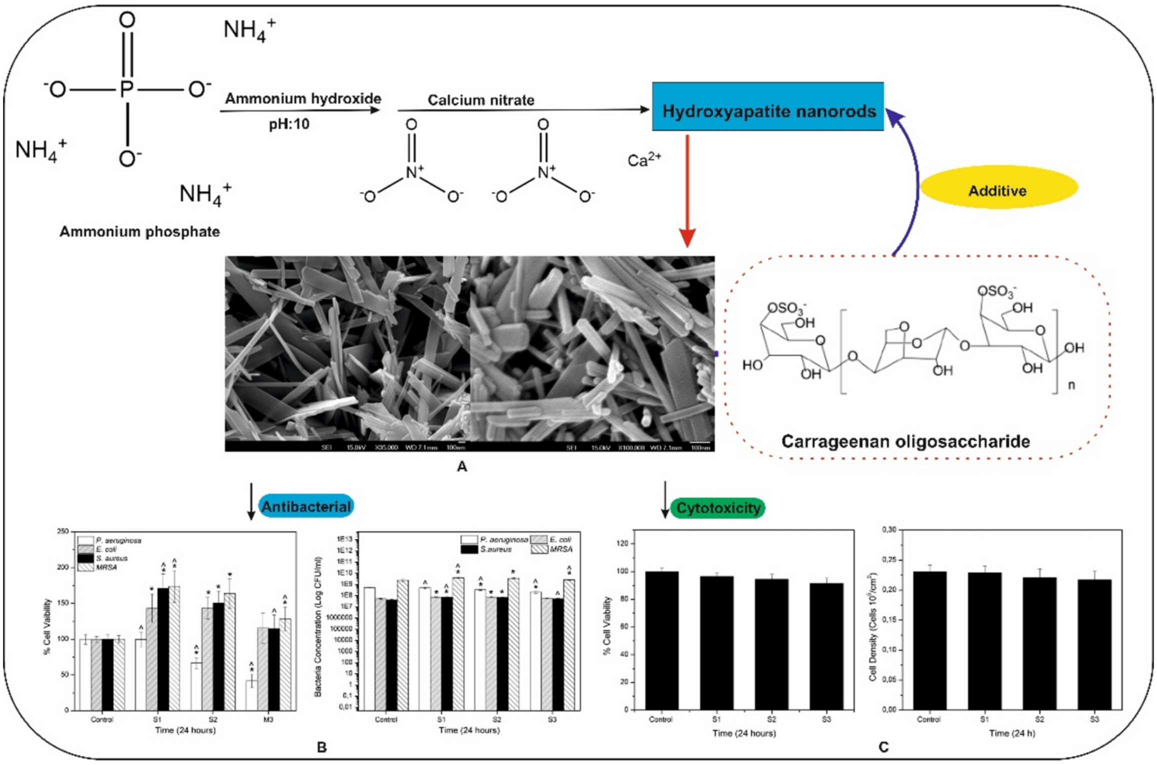

Figure 6: (A) A κ-carrageenan-stabilized hydroxyapatite rod-shaped nanocomposite. (B) Antibacterial study using *E. coli*, *S. aureus*, *B. subtilis*, *P. aeruginosa* showing the bactericidal properties of the nanocomposite. (C) The nanocomposite shows osteoblast cytotoxicity tests in cell lines (L02 and L929). Adapted from [116], J. I. González Ocampo et al., "Evaluation of cytotoxicity and antimicrobial activity of an injectable bone substitute of carrageenan and nano hydroxyapatite", J. Biomed. Mater. Res. A., with permission from John Wiley and Sons. Copyright © 2018 Wiley Periodicals, Inc. This content is not subject to CC BY 4.0.

exhibited antibacterial effect indicating its potential to restrict biofilm formation. Carrageenans are also being explored regarding the synthesis of polymeric nanoparticles complexed with other polymers such as chitosan and tripolyphosphate. The use of carrageenan is not only limited to biological applications, it also emerged as a promising candidate for industrial applications. Silver nanoparticles synthesized using carrageenan as a reducing and stabilizing agent showed promising results in removing organic dyes such as methylene blue and rhodamine B [111]. Magnetic iron nanoparticles were synthesized using κ-, ι-, or λ-carrageenan polysaccharides of different concentrations [113]. The particle size, morphology, and stability were predominantly determined by the concentration and the gelation properties of the used carrageenan. Another study involved stabilizing zein nanoparticles using ι-carrageenan to prevent aggregation and sedimentation above pH 5 [117]. The stability was enhanced upon adhesion of carrageenan to the nanoparticle surface rendering it negatively charged.

Although there are little reports on using carrageenan as a safe and sustainable component for synthesizing plasmonic metal nanomaterials, the works successfully illustrated the future endeavors for the oligosaccharide in the area of nanobiotechnology.

Conclusion

This mini-review described two alternative vital components, DESs and carrageenan, in the wet chemical synthesis of plasmonic metal nanoparticles. Both components embrace the principle of green chemistry generating safe nanomaterials for biological applications. The authors also discussed the importance of CTAB as a structure-directing agent for anisotropic nanoparticles and the concerns regarding toxicity. One of the works that has been mentioned above involved C_{12}EDMAB as an alternative to CTAB yielding less toxic nanorods. The lower toxicity can be attributed to the shorter carbon tail length of the surfactant compared to CTAB. Moreover, an excellent study reported the interaction between surfactants and carrageenan. The SO_3^- group present in carrageenan interacts with the positively charged head group of the surfactants in the solution phase.

The importance of using DESs and carrageenan is the fact that the biocompatible molecules already used in designing safe nanomaterials add no further improvement than just biocompatibility. Some are also prone to enzymatic degradation. In contrast, DESs and carrageenan exhibit properties that play a role in enhancing the physicochemical properties of metallic nanomaterials. Intrinsic properties, such as structure-directing ability, were observed when DESs were used as solvents during nanoparticle synthesis. Also, the antibacterial, antiviral, and stabilizing properties of carrageenan can lead to a multidimensional approach in synthesizing nanomaterials for advanced biomedical applications.

A synthetic system comprising DESs and carrageenan along with surfactants of different carbon tail length can pave a route towards synthesizing plasmonic metal nanomaterials with controlled size and shape for biological applications. In this way, the presence of the surfactant shall cause minimal or no cytotoxicity while maintaining the integrity of the nanoparticles. The higher degree of solvation observed in DESs leads to the complete dissolution of carrageenan and surfactants. The dissolution of several compounds would significantly contribute to a species-rich system with higher conductivity. This unique hybrid model will create a platform for synthesizing n different nanomaterials with combinatorial possibilities of 2^n since there are n possible ways of combining the components of DESs (hydrogen bridge donor and acceptor). Therefore, the authors believe that the combines use of the two components might allow for future endeavors towards synthesizing biocompatible plasmonic metal nanomaterials.

Acknowledgements

RRG is thankful to CSIR-Indian Institute of Toxicology Research, Lucknow for providing the infrastructure and support. The CSIR-IITR publication committee has approved this review article and the communication number is 3743.

Funding

ND and AK are thankful to the Council of Scientific and Industrial Research (CSIR) for the fellowship.

ORCID® iDs

Nabojit Das - https://orcid.org/0000-0001-8686-6400
Akash Kumar - https://orcid.org/0000-0002-0493-1991
Raja Gopal Rayavarapu - https://orcid.org/0000-0002-8769-4679

References

1. García-Lojo, D.; Núñez-Sánchez, S.; Gómez-Graña, S.; Grzelczak, M.; Pastoriza-Santos, I.; Pérez-Juste, J.; Liz-Marzán, L. M. *Acc. Chem. Res.* **2019,** *52,* 1855–1864. doi:10.1021/acs.accounts.9b00213
2. Jana, J.; Ganguly, M.; Pal, T. *RSC Adv.* **2016,** *6,* 86174–86211. doi:10.1039/c6ra14173k
3. Liu, J.; Xu, N.; Men, H.; Li, S.; Lu, Y.; Low, S. S.; Li, X.; Zhu, L.; Cheng, C.; Xu, G.; Liu, Q. *Sensors* **2020,** *20,* 1422. doi:10.3390/s20051422
4. Shin Low, S.; Pan, Y.; Ji, D.; Li, Y.; Lu, Y.; He, Y.; Chen, Q.; Liu, Q. *Sens. Actuators, B* **2020,** *308,* 127718. doi:10.1016/j.snb.2020.127718
5. Li, S.; Liu, J.; Lu, Y.; Zhu, L.; Li, C.; Hu, L.; Li, J.; Jiang, J.; Low, S.; Liu, Q. *Biosens. Bioelectron.* **2018,** *117,* 32–39. doi:10.1016/j.bios.2018.05.062

6. Cheng, C.; Li, X.; Xu, G.; Lu, Y.; Low, S. S.; Liu, G.; Zhu, L.; Li, C.; Liu, Q. *Biosens. Bioelectron.* **2021,** *172,* 112782. doi:10.1016/j.bios.2020.112782
7. Xu, G.; Li, X.; Cheng, C.; Yang, J.; Liu, Z.; Shi, Z.; Zhu, L.; Lu, Y.; Low, S. S.; Liu, Q. *Sens. Actuators, B* **2020,** *310,* 127809. doi:10.1016/j.snb.2020.127809
8. Kumar, A.; Das, N.; Satija, N. K.; Mandrah, K.; Roy, S. K.; Rayavarapu, R. G. *Nanomaterials* **2019,** *10,* 45. doi:10.3390/nano10010045
9. Bhamidipati, M.; Fabris, L. *Bioconjugate Chem.* **2017,** *28,* 449–460. doi:10.1021/acs.bioconjchem.6b00605
10. Fraga, S.; Faria, H.; Soares, M. E.; Duarte, J. A.; Soares, L.; Pereira, E.; Costa-Pereira, C.; Teixeira, J. P.; de Lourdes Bastos, M.; Carmo, H. *J. Appl. Toxicol.* **2013,** *33,* 1111–1119. doi:10.1002/jat.2865
11. Burrows, N. D.; Vartanian, A. M.; Abadeer, N. S.; Grzincic, E. M.; Jacob, L. M.; Lin, W.; Li, J.; Dennison, J. M.; Hinman, J. G.; Murphy, C. J. *J. Phys. Chem. Lett.* **2016,** *7,* 632–641. doi:10.1021/acs.jpclett.5b02205
12. Rambabu, K.; Bharath, G.; Banat, F.; Show, P. L. *J. Hazard. Mater.* **2021,** *402,* 123560. doi:10.1016/j.jhazmat.2020.123560
13. Al-Haddad, J.; Alzaabi, F.; Pal, P.; Rambabu, K.; Banat, F. *Clean Technol. Environ. Policy* **2020,** *22,* 269–277. doi:10.1007/s10098-019-01765-2
14. Bharath, G.; Rambabu, K.; Banat, F.; Ponpandian, N.; Alsharaeh, E.; Harrath, A. H.; Alrezaki, A.; Alwasel, S. *Mater. Res. Express* **2019,** *6,* 066104. doi:10.1088/2053-1591/ab0a85
15. Rambabu, K.; Bharath, G.; Thanigaivelan, A.; Das, D. B.; Show, P. L.; Banat, F. *Bioresour. Technol.* **2021,** *319,* 124243. doi:10.1016/j.biortech.2020.124243
16. Rambabu, K.; Bharath, G.; Banat, F.; Hai, A.; Show, P. L.; Phong Nguyen, T. H. *Int. J. Hydrogen Energy* **2021,** *46,* 16631–16643. doi:10.1016/j.ijhydene.2020.06.108
17. Rambabu, K.; Hai, A.; Bharath, G.; Banat, F.; Show, P. L. *Int. J. Hydrogen Energy* **2019,** *44,* 14406–14415. doi:10.1016/j.ijhydene.2019.03.085
18. Bharath, G.; Rambabu, K.; Banat, F.; Hai, A.; Arangadi, A. F.; Ponpandian, N. *Sci. Total Environ.* **2019,** *691,* 713–726. doi:10.1016/j.scitotenv.2019.07.069
19. Yoo, J.; Park, C.; Yi, G.; Lee, D.; Koo, H. *Cancers* **2019,** *11,* 640. doi:10.3390/cancers11050640
20. Bharath, G.; Rambabu, K.; Morajkar, P. P.; Jayaraman, R.; Theerthagiri, J.; Lee, S. J.; Choi, M. Y.; Banat, F. *J. Hazard. Mater.* **2021,** *409,* 124980. doi:10.1016/j.jhazmat.2020.124980
21. Bharath, G.; Prakash, J.; Rambabu, K.; Venkatasubbu, G. D.; Kumar, A.; Lee, S.; Theerthagiri, J.; Choi, M. Y.; Banat, F. *Environ. Pollut.* **2021,** *281,* 116990. doi:10.1016/j.envpol.2021.116990
22. Bharath, G.; Rambabu, K.; Hai, A.; Othman, I.; Ponpandian, N.; Banat, F.; Show, P. L. *Chem. Eng. J.* **2021,** *414,* 128869. doi:10.1016/j.cej.2021.128869
23. Chai, W. S.; Cheun, J. Y.; Kumar, P. S.; Mubashir, M.; Majeed, Z.; Banat, F.; Ho, S.-H.; Show, P. L. *J. Cleaner Prod.* **2021,** *296,* 126589. doi:10.1016/j.jclepro.2021.126589
24. Islam, M. A.; Jacob, M. V.; Antunes, E. *J. Environ. Manage.* **2021,** *281,* 111918. doi:10.1016/j.jenvman.2020.111918
25. Wagle, D. V.; Zhao, H.; Baker, G. A. *Acc. Chem. Res.* **2014,** *47,* 2299–2308. doi:10.1021/ar5000488
26. Abbott, A. P.; Capper, G.; Davies, D. L.; Rasheed, R. K.; Tambyrajah, V. *Chem. Commun.* **2003,** 70–71. doi:10.1039/b210714g
27. Liao, H.-G.; Jiang, Y.-X.; Zhou, Z.-Y.; Chen, S.-P.; Sun, S.-G. *Angew. Chem., Int. Ed.* **2008,** *47,* 9100–9103. doi:10.1002/anie.200803202
28. Jakubowska, M.; Ruzik, L. *Anal. Biochem.* **2021,** *617,* 114117. doi:10.1016/j.ab.2021.114117
29. Elhamarnah, Y. A.; Nasser, M.; Qiblawey, H.; Benamor, A.; Atilhan, M.; Aparicio, S. *J. Mol. Liq.* **2019,** *277,* 932–958. doi:10.1016/j.molliq.2019.01.002
30. Wang, W.; Wang, S.-X.; Guan, H.-S. *Mar. Drugs* **2012,** *10,* 2795–2816. doi:10.3390/md10122795
31. Kalitnik, A. A.; Byankina Barabanova, A. O.; Nagorskaya, V. P.; Reunov, A. V.; Glazunov, V. P.; Solov'eva, T. F.; Yermak, I. M. *J. Appl. Phycol.* **2013,** *25,* 65–72. doi:10.1007/s10811-012-9839-8
32. Chen, X.; Zhao, X.; Gao, Y.; Yin, J.; Bai, M.; Wang, F. *Mar. Drugs* **2018,** *16,* 277. doi:10.3390/md16080277
33. Chen, G.; Roy, I.; Yang, C.; Prasad, P. N. *Chem. Rev.* **2016,** *116,* 2826–2885. doi:10.1021/acs.chemrev.5b00148
34. Yu, Y.-Y.; Chang, S.-S.; Lee, C.-L.; Wang, C. C. *J. Phys. Chem. B* **1997,** *101,* 6661–6664. doi:10.1021/jp971656q
35. Chang, S.-S.; Shih, C.-W.; Chen, C.-D.; Lai, W.-C.; Wang, C. R. C. *Langmuir* **1999,** *15,* 701–709. doi:10.1021/la980929l
36. Nikoobakht, B.; El-Sayed, M. A. *Chem. Mater.* **2003,** *15,* 1957–1962. doi:10.1021/cm020732l
37. Personick, M. L.; Langille, M. R.; Zhang, J.; Harris, N.; Schatz, G. C.; Mirkin, C. A. *J. Am. Chem. Soc.* **2011,** *133,* 6170–6173. doi:10.1021/ja201826r
38. Li, F.; Tian, D.; Cui, H. *Luminescence* **2013,** *28,* 7–15. doi:10.1002/bio.1380
39. Murphy, C. J.; Sau, T. K.; Orendorff, C. J.; Gole, A. M. Surface enhanced Raman spectroscopy using shaped gold nanoparticles. U.S. Pat. Appl. 2011/0137062 A1 June 9, 2012.
40. Roach, L.; Ye, S.; Moorcroft, S. C. T.; Critchley, K.; Coletta, P. L.; Evans, S. D. *Nanotechnology* **2018,** *29,* 135601. doi:10.1088/1361-6528/aaa99d
41. Gao, J.; Bender, C. M.; Murphy, C. J. *Langmuir* **2003,** *19,* 9065–9070. doi:10.1021/la034919i
42. Agrahari, K.; Rayavarapu, R. G. *Vacuum* **2019,** *166,* 377–384. doi:10.1016/j.vacuum.2018.10.071
43. Shajari, D.; Bahari, A.; Gill, P.; Mohseni, M. *Opt. Mater. (Amsterdam, Neth.)* **2017,** *64,* 376–383. doi:10.1016/j.optmat.2017.01.004
44. Alkilany, A. M.; Murphy, C. J. *J. Nanopart. Res.* **2010,** *12,* 2313–2333. doi:10.1007/s11051-010-9911-8
45. Tarantola, M.; Pietuch, A.; Schneider, D.; Rother, J.; Sunnick, E.; Rosman, C.; Pierrat, S.; Sönnichsen, C.; Wegener, J.; Janshoff, A. *Nanotoxicology* **2011,** *5,* 254–268. doi:10.3109/17435390.2010.528847
46. Lau, I. P.; Chen, H.; Wang, J.; Ong, H. C.; Leung, K. C.-F.; Ho, H. P.; Kong, S. K. *Nanotoxicology* **2012,** *6,* 847–856. doi:10.3109/17435390.2011.625132
47. Zhang, Y.; Li, X.; Yu, H. *J. Environ. Sci. Health, Part C: Environ. Carcinog. Ecotoxicol. Rev.* **2016,** *34,* 204–215. doi:10.1080/10590501.2016.1202762
48. Patra, H. K.; Dasgupta, A. K. *Nanomedicine (N. Y., NY, U. S.)* **2012,** *8,* 842–852. doi:10.1016/j.nano.2011.10.009
49. Zhang, X.-D.; Guo, M.-L.; Wu, H.-Y.; Sun, Y.-M.; Ding, Y.-Q.; Feng, X.; Zhang, L.-A. *Int. J. Nanomed.* **2009,** *4,* 165. doi:10.2147/ijn.s6723

50. Sung, J.; Ji, J.; Park, J.; Song, M.; Song, K.; Ryu, H.; Yoon, J.; Jeon, K.; Jeong, J.; Han, B.; Chung, Y.; Chang, H.; Lee, J.; Kim, D.; Kelman, B. J.; Yu, I. *Part. Fibre Toxicol.* **2011,** *8,* 16. doi:10.1186/1743-8977-8-16
51. Yah, C. S. *Biomed. Res.* **2013,** *24,* 400–413. doi:10.1177/1049731513514116
52. Fratoddi, I.; Venditti, I.; Cametti, C.; Russo, M. V. *Nano Res.* **2015,** *8,* 1771–1799. doi:10.1007/s12274-014-0697-3
53. Cho, W.-S.; Cho, M.; Jeong, J.; Choi, M.; Cho, H.-Y.; Han, B. S.; Kim, S. H.; Kim, H. O.; Lim, Y. T.; Chung, B. H.; Jeong, J. *Toxicol. Appl. Pharmacol.* **2009,** *236,* 16–24. doi:10.1016/j.taap.2008.12.023
54. Lee, Y. J.; Ahn, E.-Y.; Park, Y. *Nanoscale Res. Lett.* **2019,** *14,* 129. doi:10.1186/s11671-019-2967-1
55. Perfilieva, O. A.; Pyshnyi, D. V.; Lomzov, A. A. *J. Chem. Theory Comput.* **2019,** *15,* 1278–1292. doi:10.1021/acs.jctc.8b00362
56. Mikami, Y.; Dhakshinamoorthy, A.; Alvaro, M.; García, H. *Catal. Sci. Technol.* **2013,** *3,* 58–69. doi:10.1039/c2cy20068f
57. Jia, Y.-P.; Ma, B.-Y.; Wei, X.-W.; Qian, Z.-Y. *Chin. Chem. Lett.* **2017,** *28,* 691–702. doi:10.1016/j.cclet.2017.01.021
58. Li, N.; Zhao, P.; Astruc, D. *Angew. Chem., Int. Ed.* **2014,** *53,* 1756–1789. doi:10.1002/anie.201300441
59. Jiang, W.; Kim, B. Y. S.; Rutka, J. T.; Chan, W. C. W. *Nat. Nanotechnol.* **2008,** *3,* 145–150. doi:10.1038/nnano.2008.30
60. Allen, J. M.; Xu, J.; Blahove, M.; Canonico-May, S. A.; Santaloci, T. J.; Braselton, M. E.; Stone, J. W. *J. Colloid Interface Sci.* **2017,** *505,* 1172–1176. doi:10.1016/j.jcis.2017.06.101
61. Yu, C.; Varghese, L.; Irudayaraj, J. *Langmuir* **2007,** *23,* 9114–9119. doi:10.1021/la701111e
62. Cox, B. T.; Laufer, J. G.; Beard, P. C. *Proc. SPIE* **2009,** *7177,* 717713. doi:10.1117/12.806788
63. Jia, Y. P.; Shi, K.; Liao, J. F.; Peng, J. R.; Hao, Y.; Qu, Y.; Chen, L. J.; Liu, L.; Yuan, X.; Qian, Z. Y. *Small Methods* **2020,** *4,* 1900799. doi:10.1002/smtd.201900799
64. Takahashi, H.; Niidome, Y.; Niidome, T.; Kaneko, K.; Kawasaki, H.; Yamada, S. *Langmuir* **2006,** *22,* 2–5. doi:10.1021/la0520029
65. Chen, Y.-S.; Hung, Y.-C.; Liau, I.; Huang, G. S. *Nanoscale Res. Lett.* **2009,** *4,* 858–864. doi:10.1007/s11671-009-9334-6
66. Lasagna-Reeves, C.; Gonzalez-Romero, D.; Barria, M. A.; Olmedo, I.; Clos, A.; Sadagopa Ramanujam, V. M.; Urayama, A.; Vergara, L.; Kogan, M. J.; Soto, C. *Biochem. Biophys. Res. Commun.* **2010,** *393,* 649–655. doi:10.1016/j.bbrc.2010.02.046
67. Ray, D.; Bhattacharyya, A.; Chandra Bhattacharya, S.; Guchhait, N. *J. Phys. Chem. C* **2018,** *122,* 17544–17551. doi:10.1021/acs.jpcc.8b05481
68. Simpson, C. A.; Salleng, K. J.; Cliffel, D. E.; Feldheim, D. L. *Nanomedicine (N. Y., NY, U. S.)* **2013,** *9,* 257–263. doi:10.1016/j.nano.2012.06.002
69. Li, B.; Lane, L. A. *Wiley Interdiscip. Rev.: Nanomed. Nanobiotechnol.* **2019,** *11,* e1542. doi:10.1002/wnan.1555
70. Lopez-Chaves, C.; Soto-Alvaredo, J.; Montes-Bayon, M.; Bettmer, J.; Llopis, J.; Sanchez-Gonzalez, C. *Nanomedicine (N. Y., NY, U. S.)* **2018,** *14,* 1–12. doi:10.1016/j.nano.2017.08.011
71. Dreaden, E. C.; Alkilany, A. M.; Huang, X.; Murphy, C. J.; El-Sayed, M. A. *Chem. Soc. Rev.* **2012,** *41,* 2740–2779. doi:10.1039/c1cs15237h
72. Stefanovic, R.; Ludwig, M.; Webber, G. B.; Atkin, R.; Page, A. J. *Phys. Chem. Chem. Phys.* **2017,** *19,* 3297–3306. doi:10.1039/c6cp07932f
73. Chai, W. S.; Chin, J.; Cheah, K. H.; Koh, K. S.; Ku Chik, T. F. W. *Acta Astronaut.* **2019,** *162,* 66–71. doi:10.1016/j.actaastro.2019.06.006
74. Chai, W. S.; Cheah, K. H.; Meng, H.; Li, G. *J. Mol. Liq.* **2019,** *293,* 111496. doi:10.1016/j.molliq.2019.111496
75. Chai, W. S.; Sun, D.; Cheah, K. H.; Li, G.; Meng, H. *ACS Omega* **2020,** *5,* 19525–19532. doi:10.1021/acsomega.0c01804
76. Abbott, A. P.; Boothby, D.; Capper, G.; Davies, D. L.; Rasheed, R. K. *J. Am. Chem. Soc.* **2004,** *126,* 9142–9147. doi:10.1021/ja048266j
77. Lynam, J. G.; Kumar, N.; Wong, M. J. *Bioresour. Technol.* **2017,** *238,* 684–689. doi:10.1016/j.biortech.2017.04.079
78. Bera, D.; Kuiry, S. C.; Seal, S. *JOM* **2004,** *56,* 49–53. doi:10.1007/s11837-004-0273-5
79. Manolova, M.; Böck, R.; Scharf, I.; Mehner, T.; Lampke, T. *J. Alloys Compd.* **2021,** *855,* 157462. doi:10.1016/j.jallcom.2020.157462
80. Tavakol, H.; Keshavarzipour, F. *Appl. Organomet. Chem.* **2017,** *31,* e3811. doi:10.1002/aoc.3811
81. Hong, S.; Yuan, Y.; Yang, Q.; Chen, L.; Deng, J.; Chen, W.; Lian, H.; Mota-Morales, J. D.; Liimatainen, H. *Carbohydr. Polym.* **2019,** *220,* 211–218. doi:10.1016/j.carbpol.2019.05.075
82. Söldner, A.; Zach, J.; Iwanow, M.; Gärtner, T.; Schlosser, M.; Pfitzner, A.; König, B. *Chem. – Eur. J.* **2016,** *22,* 13108–13113. doi:10.1002/chem.201602821
83. Thorat, G. M.; Jadhav, H. S.; Roy, A.; Chung, W.-J.; Seo, J. G. *ACS Sustainable Chem. Eng.* **2018,** *6,* 16255–16266. doi:10.1021/acssuschemeng.8b03119
84. Karimi, M.; Eshraghi, M. J. *J. Alloys Compd.* **2017,** *696,* 171–176. doi:10.1016/j.jallcom.2016.11.259
85. Fu, N.; Li, L.; Liu, K.; Kim, C. K.; Li, J.; Zhu, T.; Li, J.; Tang, B. *Talanta* **2019,** *197,* 567–577. doi:10.1016/j.talanta.2019.01.072
86. Shahi, S. K.; Kaur, N.; Sandhu, S.; Shahi, J. S.; Singh, V. *J. Sci.: Adv. Mater. Devices* **2017,** *2,* 347–353. doi:10.1016/j.jsamd.2017.07.006
87. Mąka, H.; Spychaj, T.; Kowalczyk, K. *J. Appl. Polym. Sci.* **2014,** *131,* 40401. doi:10.1002/app.40401
88. Gutiérrez, M. C.; Carriazo, D.; Tamayo, A.; Jiménez, R.; Picó, F.; Rojo, J. M.; Ferrer, M. L.; del Monte, F. *Chem. – Eur. J.* **2011,** *17,* 10533–10537. doi:10.1002/chem.201101679
89. Oh, J.-H.; Lee, J.-S. *J. Nanosci. Nanotechnol.* **2014,** *14,* 3753–3757. doi:10.1166/jnn.2014.8658
90. Bernasconi, R.; Panzeri, G.; Firtin, G.; Kahyaoglu, B.; Nobili, L.; Magagnin, L. *J. Phys. Chem. B* **2020,** *124,* 10739–10751. doi:10.1021/acs.jpcb.0c04784
91. Costa, R.; Figueiredo, M.; Pereira, C. M.; Silva, F. *Electrochim. Acta* **2010,** *55,* 8916–8920. doi:10.1016/j.electacta.2010.07.070
92. Abbott, A. P.; Barron, J. C.; Frisch, G.; Gurman, S.; Ryder, K. S.; Silva, A. F. *Phys. Chem. Chem. Phys.* **2011,** *13,* 10224–10231. doi:10.1039/c0cp02244f
93. Wei, L.; Zhou, Z.-Y.; Chen, S.-P.; Xu, C.-D.; Su, D.; Schuster, M. E.; Sun, S.-G. *Chem. Commun.* **2013,** *49,* 11152–11154. doi:10.1039/c3cc46473c
94. Chirea, M.; Freitas, A.; Vasile, B. S.; Ghitulica, C.; Pereira, C. M.; Silva, F. *Langmuir* **2011,** *27,* 3906–3913. doi:10.1021/la104092b
95. Shahidi, S.; Iranpour, S.; Iranpour, P.; Alavi, A. A.; Mahyari, F. A.; Tohidi, M.; Safavi, A. *J. Exp. Nanosci.* **2015,** *10,* 911–924. doi:10.1080/17458080.2014.933493
96. Mahyari, F. A.; Tohidi, M.; Safavi, A. *Mater. Res. Express* **2016,** *3,* 095006. doi:10.1088/2053-1591/3/9/095006

97. Govindaraj, D.; Rajan, M.; Munusamy, M. A.; Alarfaj, A. A.; Sadasivuni, K. K.; Kumar, S. S. *Nanomedicine (N. Y., NY, U. S.)* **2017,** *13,* 2661–2669. doi:10.1016/j.nano.2017.07.017
98. Karimi, M.; Ramsheh, M. R.; Ahmadi, S. M.; Madani, M. R.; Shamsi, M.; Reshadi, R.; Lotfi, F. *Mater. Sci. Eng., C* **2017,** *77,* 121–128. doi:10.1016/j.msec.2017.03.217
99. Guerrini, L.; Alvarez-Puebla, R. A.; Pazos-Perez, N. *Materials* **2018,** *11,* 1154. doi:10.3390/ma11071154
100. Deraedt, C.; Salmon, L.; Gatard, S.; Ciganda, R.; Hernandez, R.; Ruiz, J.; Astruc, D. *Chem. Commun.* **2014,** *50,* 14194–14196. doi:10.1039/c4cc05946h
101. Das, N.; Kumar, A.; Kumar Roy, S.; Kumar Satija, N.; Raja Gopal, R. *IET Nanobiotechnol.* **2020,** *14,* 851–857. doi:10.1049/iet-nbt.2020.0097
102. Cunha, L.; Grenha, A. *Mar. Drugs* **2016,** *14,* 42. doi:10.3390/md14030042
103. Melanie, H.; Taarji, N.; Zhao, Y.; Khalid, N.; Neves, M. A.; Kobayashi, I.; Tuwo, A.; Nakajima, M. *Int. J. Food Sci. Technol.* **2020,** *55,* 211–221. doi:10.1111/ijfs.14264
104. Burges Watson, D. *J. Appl. Phycol.* **2008,** *20,* 505–513. doi:10.1007/s10811-007-9252-x
105. McKim, J. M. *Crit. Rev. Toxicol.* **2014,** *44,* 211–243. doi:10.3109/10408444.2013.861797
106. Weiner, M. L. *Crit. Rev. Toxicol.* **2014,** *44,* 244–269. doi:10.3109/10408444.2013.861798
107. Popa, E. G.; Carvalho, P. P.; Dias, A. F.; Santos, T. C.; Santo, V. E.; Marques, A. P.; Viegas, C. A.; Dias, I. R.; Gomes, M. E.; Reis, R. L. *J. Biomed. Mater. Res., Part A* **2014,** *102,* 4087–4097. doi:10.1002/jbm.a.35081
108. McKim, J. M., Jr.; Baas, H.; Rice, G. P.; Willoughby, J. A., Sr.; Weiner, M. L.; Blakemore, W. *Food Chem. Toxicol.* **2016,** *96,* 1–10. doi:10.1016/j.fct.2016.07.006
109. Yin, T.; Qin, M.; Yang, Y.; Zheng, P.; Fan, D.; Shen, W. *Soft Matter* **2014,** *10,* 4126–4136. doi:10.1039/c4sm00322e
110. Lokhande, G.; Carrow, J. K.; Thakur, T.; Xavier, J. R.; Parani, M.; Bayless, K. J.; Gaharwar, A. K. *Acta Biomater.* **2018,** *70,* 35–47. doi:10.1016/j.actbio.2018.01.045
111. Pandey, S.; Do, J. Y.; Kim, J.; Kang, M. *Carbohydr. Polym.* **2020,** *230,* 115597. doi:10.1016/j.carbpol.2019.115597
112. Cheng, L.; Bulmer, C.; Margaritis, A. *Curr. Drug Delivery* **2015,** *12,* 351–357. doi:10.2174/1567201812666150114155948
113. Daniel-da-Silva, A. L.; Trindade, T.; Goodfellow, B. J.; Costa, B. F. O.; Correia, R. N.; Gil, A. M. *Biomacromolecules* **2007,** *8,* 2350–2357. doi:10.1021/bm070096q
114. Rhim, J.-W.; Wang, L.-F. *Appl. Clay Sci.* **2014,** *97-98,* 174–181. doi:10.1016/j.clay.2014.05.025
115. Zhu, M.; Li, X.; Ge, L.; Zi, Y.; Qi, M.; Li, Y.; Li, D.; Mu, C. *Mater. Sci. Eng., C* **2020,** *106,* 110185. doi:10.1016/j.msec.2019.110185
116. González Ocampo, J. I.; Bassous, N.; Ossa Orozco, C. P.; Webster, T. J. *J. Biomed. Mater. Res., Part A* **2018,** *106,* 2984–2993. doi:10.1002/jbm.a.36488
117. Cheng, C. J.; Jones, O. G. *Food Hydrocolloids* **2017,** *69,* 28–35. doi:10.1016/j.foodhyd.2017.01.022

License and Terms

BEILSTEIN JOURNAL OF NANOTECHNOLOGY

Self-assembly of amino acids toward functional biomaterials

Huan Ren, Lifang Wu, Lina Tan, Yanni Bao, Yuchen Ma, Yong Jin* and Qianli Zou*

Review

Open Access

Address:
School of Pharmacy, Anhui Medical University, Hefei 230032, China

Email:
Yong Jin* - jinyong@ahmu.edu.cn; Qianli Zou* - qlzou@ahmu.edu.cn

* Corresponding author

Keywords:
amino acids; functional biomaterials; intermolecular interactions; self-assembly

Beilstein J. Nanotechnol. **2021,** *12,* 1140–1150.
https://doi.org/10.3762/bjnano.12.85

Received: 23 July 2021
Accepted: 30 September 2021
Published: 12 October 2021

This article is part of the thematic issue "New trends in nano-biotechnology".

Guest Editor: P.-L. Show

Abstract

Biomolecules, such as proteins and peptides, can be self-assembled. They are widely distributed, easy to obtain, and biocompatible. However, the self-assembly of proteins and peptides has disadvantages, such as difficulty in obtaining high quantities of materials, high cost, polydispersity, and purification limitations. The difficulties in using proteins and peptides as functional materials make it more complicate to arrange assembled nanostructures at both microscopic and macroscopic scales. Amino acids, as the smallest constituent of proteins and the smallest constituent in the bottom-up approach, are the smallest building blocks that can be self-assembled. The self-assembly of single amino acids has the advantages of low synthesis cost, simple modeling, excellent biocompatibility and biodegradability in vivo. In addition, amino acids can be assembled with other components to meet multiple scientific needs. However, using these simple building blocks to design attractive materials remains a challenge due to the simplicity of the amino acids. Most of the review articles about self-assembly focus on large molecules, such as peptides and proteins. The preparation of complicated materials by self-assembly of amino acids has not yet been evaluated. Therefore, it is of great significance to systematically summarize the literature of amino acid self-assembly. This article reviews the recent advances in amino acid self-assembly regarding amino acid self-assembly, functional amino acid self-assembly, amino acid coordination self-assembly, and amino acid regulatory functional molecule self-assembly.

Review

Introduction

Biomaterials play a crucial role in the treatment of diseases and health care and have been widely used in prostheses and drug delivery devices [1]. Clinical applications of biomaterials include the use of metals, ceramics, and polymers to enhance, repair, or replace diseased, damaged, or defective tissue [2]. A few examples are tooth repair, peripheral nerve regeneration, nerve tissue engineering, bone and joint replacement and repair, and regeneration of bone defects, biological scaffolds, and wound healing [3-8]. Although traditional materials provide good structural analogues for native bone and surrounding tissue, they are difficult to mimic the dynamics and complexity of the natural environment [9]. Therefore, it is necessary to develop a new generation of biomaterials to improve strategies for natural tissue structure and functional reorganization.

Peptides and proteins are attractive candidates for functional biomedical materials [10] due to their extensive existence in nature, easy access, and good biocompatibility [11]. Self-assembly refers to the selective and spontaneous formation of one or more well-ordered structures from a complex mixture via noncovalent interactions, including van der Waals forces, electrostatic forces, hydrogen bonds, and stacking interactions [12,13]. Importantly, biomolecules, such as proteins, peptides, or biologically derived molecules, including de novo designed peptides or nucleotides, can be self-assembled [14]. Proteins are direct functional performers of countless interactions between living organisms and the outside world, and are susceptible to changes in pH value, ionic strength, and temperature [15]. Peptides have similar biocompatibility and diversity as proteins, but have better availability, can be obtained in a larger scale, and have higher stability and durability than proteins. Furthermore, some peptides may have the same function as proteins by retaining functional sequences [16]. Many studies have reported that proteins and peptides can be assembled into various nanostructures, such as nanowires [17], nanofibers [18], nanospheres [19], nanovesicles [20], nanogels [21], nanobelts [22], and nanotubes [23]. Self-assembly not only conveys higher stability and mechanical strength to proteins and peptides, but also further enhances their natural activity and function due to the collective behavior of aggregates [24]. However, protein and peptide assemblies exhibit disadvantages, such as difficulty in obtaining high quantities of materials, corresponding high costs, and in some cases polydispersity and purification limitations. When using proteins and peptides as functional materials it can be difficult to arrange assembled nanostructures at both microscopic and macroscopic scales [10]. Also, fine manipulation of noncovalent interactions and corresponding peptide and protein nanostructures remains a huge challenge [24].

Amino acids are the major components of all naturally occurring peptides and proteins [25]. Amino-acid-based nanostructures are self-assembled from the simplest building blocks in the biological system environment and are the smallest component of the bottom-up approach [26]. Amino acids and their derivatives can be self-assembled into ordered nanostructures through noncovalent interactions, including electrostatic, π–π stacking, van der Waals, and hydrophobic interactions. The self-assembly of single amino acids has the advantages of low synthesis cost, relatively easy modeling [27], and excellent biocompatibility and biodegradability in vivo [28] compared with the self-assembly of large molecules, such as proteins and peptides. Importantly, amino acids or amino acid derivatives may be self-assembled with other components to form functional architectures, such as drug delivery systems, light collection systems, and imaging systems. However, using these simple building blocks to design attractive materials remains a challenge due to the simplicity of the amino acids [26]. Most articles about self-assembly focus on peptide and protein self-assembly [15,29]. Therefore, it is of great significance to systematically summarize the latest advances in the field of amino acid self-assembly.

In this review, we highlight the latest advances in amino acid self-assembly. These self-assembly methods mainly focus on single amino acid self-assembly, modified amino acid self-assembly, amino acid and metal ion coordination self-assembly, and amino acid and functional molecule self-assembly (drug, photosensitizer) (Figure 1). In this paper, the self-assembly of single amino acids is discussed first. We then discuss the co-assembly of amino acids and their derivatives with functional components including metal ions, photosensitizers (PS), and pharmaceuticals. Finally, the applications of these assemblies in various systems are introduced.

Self-assembly of amino acids

Self-assembly is the process of creating high-level functional structures from simple building blocks, such as amino acids, peptides, proteins, and phospholipids [30]. Noncovalent bonds and molecular forces play a key role in self-assembly, including hydrogen bonds, hydrophobic bonds, van der Waals force, ionic bonds, π–π stacking, and electrostatic forces [31]. Importantly, amino acids are simple building blocks that provide relevant noncovalent interactions to construct complex supramolecular assemblies [32,33]. Twenty natural amino acids are used by cells to synthesize peptides and proteins.

A single amino acid can be self-assembled. For example, Adler-Abramovich et al. [34] showed for the first time that phenylalanine, a single aromatic amino acid, can form ordered fibrillar assemblies at the nanoscale. This component exhibits regular aggregate properties through hydrogen bonding and ion interaction, which are highly similar to those of amyloid components, suggesting that it may be associated with the etiology of amyloid-related diseases. Besides, the resulting structure is as toxic to cells as other amyloid structures. Their subsequent study continued to demonstrate that other single amino acids and metabolites, including cystine, tyrosine, and adenine, also self-assemble to form elongated and fibrillar structures at the nanoscale [35]. Likewise, the characteristics of these combina-

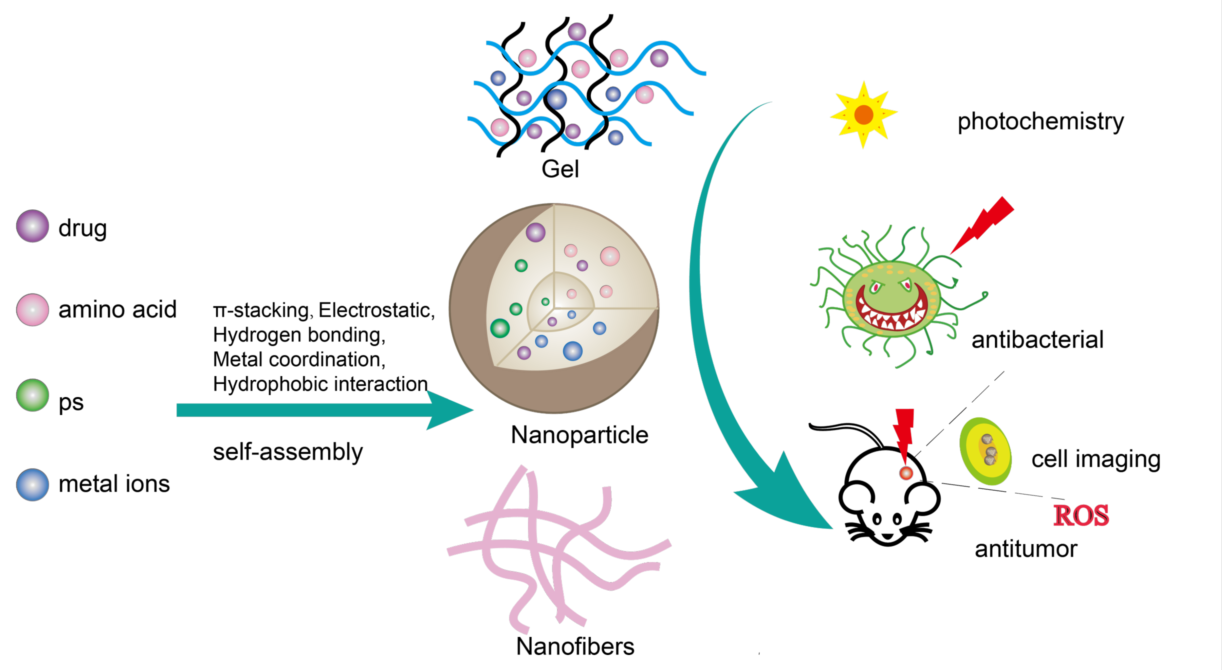

Figure 1: Schematic diagram of amino acid regulatory self-assembly (amino acid–drugs, amino acid–photosensitizers, amino acid–metal ions, multi-component collaborative self-assembly) as a general strategy for functional biomaterials research.

tions suggest that all assembled ultrastructures formed from various metabolites exhibit amyloidosis. These metabolites not only self-assemble into supramolecular amyloid fiber structures, but also have significant apoptotic effects on neuron model cells. Singh et al. [36] showed that the hydrophobic interaction between phenylalanine (Phe) rings may play a major role in the self-assembly process. Interestingly, their study also revealed that D-Phe changes L-Phe fibrous state to flakes, which do not propagate further and do not seed L-Phe, suggesting that D-Phe may be a potential therapeutic molecule for phenylketonuria. Bera et al. [37] studied the effect of chiral on aromatic amino acid self-assembly. They found that the hybrid DL system (racemate) alters the morphology and dynamics of the assemblies. For example, either L-phenylalanine or D-phenylalanine can form amyloid fibers, but the DL system shows a crystalline sheet-like assembly. Interestingly, their group also identified the optical properties of single amino acids during assembly, demonstrating the intrinsic fluorescence of amyloid structures of metabolites such as adenine, tryptophan, tyrosine, and phenylalanine which can be used to detect living cells [38]. Gour et al. explored the self-assembly of nonaromatic amino acids. They first reported the ability of nonaromatic single amino acids, cysteine and methionine, to spontaneously self-assemble to form protein-like aggregates, which are very long and fibrous and may be cytotoxic to human neuroblastoma cells [39]. These studies provide a new paradigm for metabolic disorders caused by single amino acids in amyloid-associated diseases.

Self-assembly of functionalized amino acids. There are only 20 natural amino acids, so it is very limited to rely on the self-assembly of natural amino acids. Self-assembly with modified amino acids is of great interest, most of which focuses on 9-fluorenylmethoxycarbonyl (Fmoc)-terminated materials [40-43]. Due to the inherent hydrophobicity and aromaticity of Fmoc, many Fmoc-modified amino acids exhibit relatively fast self-assembly kinetics, excellent physical and chemical properties, and great potential in cell culture, photocatalysis, drug delivery, and antibacterial applications [27].

The Fmoc modification of a single amino acid is the simplest building block, among which Fmoc-phenylalanine is the most studied due to its good hydrocoagulant properties [27] and good antibacterial activity [44]. Hydrogels of other amino acids modified by Fmoc, such as Fmoc-tryptophan, Fmoc-methionine, and Fmoc-tyrosine have also been shown to have antimicrobial activity and to be selectively resistant to Gram-positive bacteria [45].

The combined self-assembly strategy can provide different functions for amino acid assembly. Fmoc-phenylalanine and Fmoc-leucine were co-assembled, with Fmoc-phenylalanine as the hydrocoagulant and Fmoc-leucine as the antimicrobial unit. The resulting hydrogel selectively killed *Staphylococcus aureus* by breaking the cell wall and membrane and had good biocompatibility. After 20 h of incubation, approximately 95% of *Staphylococcus aureus* bacterial proliferation was effectively inhibited [46]. A novel supramolecular self-assembled hydrogel was prepared by mixing Fmoc-ʟ-phenylalanine (Fmoc-ʟ-Phe) with oligo(thiophene ethynylene)-ᴅ-phenylalanine (OTE-ᴅ-Phe), an amino-acid-modified conjugated oligomer [47]. Fmoc-ʟ-Phe/OTE-ᴅ-Phe formed yellow and transparent hydrogels through hydrogen bonding, van der Waals interactions, π–π interactions, and hydrophobic interactions, showing thicker and rougher nanofibers, which had obvious advantages in effectively capturing model bacteria methicillin-resistant *S. aureus* and *Escherichia coli*. When Fmoc-ʟ-Phe/OTE-ᴅ-Phe is coated on the surface, it also exhibits a strong ability to specifically kill methicillin-resistant *S. aureus*. In addition, Chakraborty et al. [43] designed a gelling agent containing two Fmoc groups, Fmoc-lysine and Fmoc-aspartic acid, by two-step self-assembly, which had an ultra-low critical gelling concentration and good mechanical properties and can be used for 2D/3D cell scaffolds and the production of conductive soft composites. In addition, Fmoc-amino acids can be co-assembled with drugs to play different therapeutic effects as drug delivery carriers. The encapsulation of the antibiotic aztreonam (ATZ) in the Fmoc-phenylalanine (Fmoc-F) hydrogel expands the antibacterial range of Fmoc-F, which can continuously release ATZ and Fmoc-F in the wound [48]. The AZT encapsulated Fmoc-F hydrogel was used in established wound infections, which slowly degraded within 24 h and were topically coated with AZT Fmoc-F hydrogel two days after infection, resulting in a 1000-fold reduction in bacterial load compared to untreated wounds. Aztreonam is specific against Gram-negative bacteria and aztreonam-encapsulated Fomc-F hydrogels antagonize *Pseudomonas aeruginosa* and enhance Fomc-F antimicrobial activity. Salicylic acid is loaded in Fmoc-ʟ-phenylalanine hydrogel, which can play a role against Gram-positive bacteria, and the drug release behavior changes at different temperature and pH values [49]. Rizzo et al. studied camptothecin loaded into Fmoc-F hydrogels in the presence of haloalkyl nanotubes. Importantly, this hybrid co-assembly method could not only control the release of camptothecin in the form of active lactone, but also showed significant inhibitory activity on cancer cells [50].

Furthermore, naphthalimide (NI) derivatives can also be used as end-capping materials for amino acids. Naphthalimide has unique photophysical properties and photostability as a luminescent material for aggregation-induced emission (AIE), which can display high emission properties in the aggregated state and can be used for imaging [51]. Importantly, NI exhibits hydrophobicity and π–π stacking due to the aromatic moieties, and is prone to dynamic aggregation, which can be used in self-assembled construction units [52]. For example, Hsu et al. [53] self-assembled NI and phenylalanine to produce hydrogels driven by hydrogen bonds and π–π interactions and to form microfiber three-dimensional networks at 1 wt % and pH 7.4. The microfibers have AIE properties and strong blue emission under an ultraviolet lamp. Ni-terminated hydrogels of NI-Phe exhibit viscoelasticity with a storage modulus (*G*') value of about 2000 Pa, and can be used for imaging three-dimensional cytoskeletal materials. After human mesenchymal stem cells (hMSCs) were cultured for 72 h in the 3D fiber hydrogel, the cell viability in the 3D gel was subsequently verified. Only a few dead cells were observed, indicating that hMSCs had a high viability in the supramolecular hydrogel formed by NI-Phe. Sarkar et al. synthesized amphiphilic molecules containing NI and histidine which formed fluorescent organic nanoparticles with J-aggregation in water/DMSO, exhibiting high emissivity upon aggregation. These particles were used for the selective sensing of Fe^{3+} within cancer cells and imaging of Fe^{3+} [54].

Amino-acid-coordinated self-assembly. Coordination-driven self-assembly is a supramolecular self-assembly method based on metal-coordination bond formation, which has the advantages of fewer steps, fast final product, easy assembly, self-calibration, and no defects [55]. The prepared components may further be used as modular “building blocks” for building higher-order upper structures with increased complexity and functionality [56]. Metal coordination can become a strong interaction due to its near-covalent characteristics compared to the common noncovalent interactions in self-assembly, such as hydrophobic interactions, van der Waals force, hydrogen bonds, ion attraction, and π–π stacking [57].

Cystine (Cys) can provide carboxyl and amino groups with which it can coordinate with equimolar amounts of cadmium ions (Cd^{2+}) to form a three-dimensional crystal of Cys/Cd nanorods. Then, upon the introduction of Na_2S, the Cys/Cd template mediates the mineralization of cadmium sulfide (CdS) into a layered CdS quantum dot structure, finally making a simple bionic daylight antenna with sustainable photocatalytic performance [58]. In addition, Liu et al. [59], inspired by the cystine pathological biomineralization process, developed a zinc-directed cystine assembly to mimic chloroplast photosynthesis. Zn^{2+} promotes rapid nucleation of cystine crystals and regulates crystal morphology through splitting growth mechanisms. Scanning electron microscopy and transmission electron microscopy images show that the assembly is layered and has a three-dimensional spherical structure with porous and stacked nanorods (width 50 nm, length 200 nm). During the self-assembly process, tetrakis(4-sulfonatophenyl)porphine and alcohol dehydrogenase may be incorporated into Cys microspheres, resulting in hybrid microspheres with photocatalytic and biocatalytic activities. In addition, Cys/Zn microspheres were modified with CO_3^{2-}-doped ZnS nanocrystals by a hydrothermal treatment, and then glutamic acid dehydrogenase was encapsulated in the Cys/Zn framework as a guest molecule to obtain the original pigment model, which can achieve methyl violet (MV^{2+}) photoreduction, CO_2 photoreduction, NADH formation, and hydrogen release [60]. In addition, histidine has site-specific metal ion coordination with an imidazole ring [61]. Han et al. [62] self-assembled metal nanoparticles with good catalytic activity by coordination of histidine derivatives *N*-(benzyloxycarbonyl)-ʟ-histidinohydrazide with zinc ions on a minimum design principle. The catalytic performance of *p*-nitrophenyl acetate hydrolysis to *p*-nitrophenol was evaluated by monitoring the absorbance of *p*-nitrophenol at 400 nm. The catalytic formation of *p*-nitrophenol started within the first three minutes and then gradually increased. The catalytic rate constant of metal nanoparticles was higher than that of lipase (6.00×10^{-2} and 6.95×10^{-3} s^{-1}, respectively). In addition, the substrate affinity of metal nanoparticles (1.53 mM) is comparable to that of natural lipase (1.27 mM).

Metal ions, especially silver ions (Ag^+), have been widely studied regarding antibacterial, antifungal, antiviral, anti-inflammatory, anti-angiogenic, and antitumor activities [63,64]. Silver nanoparticles (Ag NPs) hold great promise due to their broad-spectrum and robust antimicrobial properties [65]. The main mechanism is that Ag nanoparticles diffuse into cells and destroy cell walls [66]. However, Ag NPs are cytotoxic, which limits their application [67]. Song et al. [68] developed a broad-spectrum antimicrobial metallohydrogel based on Ag^+-coordinated Fmoc-amino acid self-assembly and local mineralization. The antibacterial activity of the amino acid metallohydrogel against *Escherichia coli and Staphylococcus aureus* was better than that of Ag^+ solution. In addition, Fmoc-amino acid metallohydrogels showed fewer toxicological side effects and were highly biocompatible than Ag^+ in the administered dosage range. Furthermore, Fmoc-amino acid metallohydrogels tested under the same conditions showed significantly better wound healing than silver sulfadiazine cream and the control group.

It has been shown that a novel protein-based nanoparticle with enhanced photothermal effect has been obtained for antitumor therapy using metal ions, proteins, and photosensitizers as building blocks [69]. The integration of metal ions significantly improved the structural stability and photothermal properties of the nanoparticles [69]. The use of amino acids coordinated with metal ions and the encapsulation of guest molecule photosensitizers have also achieved encouraging results. Zhang et al. [70] developed an antitumor photodynamic therapy (PDT) nanoparticle based on the coordination of modified amino acids and metal ions. The amphiphilic amino acid 9-fluorenylmethoxycarbonyl-ʟ-leucine (Fmoc-ʟ-L) and Mn^{2+} were coordinated to encapsulate the hydrophobic photosensitive drug chlorin e6 (Ce6) into a supramolecular system to obtain Fmoc-ʟ-L/Mn^{2+}/Ce6 nanoparticles (FMC NPs). Because of the strong coordination of Mn^{2+}, Fmoc-ʟ-L, and Ce6, a yield of 36 wt % can be obtained. After the uptake of FMC NPs by cancer cells, Mn^{2+} and Ce6 can be released in response to intracellular high levels of glutathione (GSH). Magnetic resonance imaging (MRI) results showed an almost complete elimination of the tumor three days after injection. At the same time, the formation of Mn^{2+} and GSH can decrease the level of intracellular GSH and promote the production of reactive oxygen species. In addition, Mn^{2+} combined with GSH can also be used for MRI diagnosis and treatment. By using these features, FMC NPs showed better antitumor PDT effects. In addition to Mn^{2+}, Li et al. [71] self-assembled Fmoc-L, Fmoc-H, and *N*-benzyloxycarbonyl-ʟ-histidine-ʟ-phenylalanine with zinc ions to form Fmoc-H/Zn^{2+} and Z-HF/Zn^{2+} nanoparticles (approx. 70 nm in size). Then, Ce6 was encapsulated and the Ce6 loading of Fmoc-H/Zn^{2+}/Ce6 and Z-HF/Zn^{2+}/Ce6 was greater than 50.0% in both cases, and the encapsulation efficiency was greater than 99.0%. The Fmoc-H/Zn^{2+}/Ce6 and Z-HF/Zn^{2+}/Ce6 nanoparticle assembly were based on coordination and other noncovalent interactions which are sensitive to environmental changes. They demonstrated the robustness of metal nanoparticles under physiological conditions and the abrupt responsive release upon pH and glutathione changes. The half-life of Ce6 in Fmoc-H/Zn^{2+}/Ce6 (8.71 h) and Z-HF/Zn^{2+}/Ce6 (6.33 h) was much longer than that of unencapsulated Ce6 (3.69 h), according to the fitting results of the pharmacokinetic model. To investigate the in vivo distribution of metal nanoparticles in tumor-bearing mice, mice injected with metal nanoparticles or unencapsulated Ce6 had strong fluorescence signals throughout the body 2 h after injection. Fmoc-H/Zn^{2+}/Ce6 or Z-HF/Zn^{2+}/Ce6 showed strong fluorescence at the tumor site 24 h after injection. In contrast, no significant fluorescence was observed in mice injected with unencapsulated Ce6 12 h after injection. In addition, metal nanoparticles induce an effective tumor ablation, while unencapsulated Ce6 only partially inhibits tumor growth.

Curcumin is a promising natural antitumor drug, which can inhibit the transformation, proliferation, and migration of tumor cells through various ways, and has anti-angiogenic activity and good biocompatibility [72]. However, the poor water solubility and low bioavailability of curcumin hinder its direct application [73]. Therefore, it is necessary to develop an encapsulation system to improve the bioavailability of curcumin in the tumor microenvironment in order to achieve effective delivery of curcumin and improve the therapeutic effect [74]. Li et al. [75] dissolved 9-Fmoc-ʟ-histidine (Fmoc-H) in hexafluoropropofol or dilute hydrochloric acid and self-assembled curcumin nanoparticles, B-Cur NPs (180 ± 25 nm in size) and S-Cur NPs

(80 ± 16 nm in size), by coordination with zinc chloride and curcumin, respectively, in combination with a variety of noncovalent interactions. The stability of curcumin increases with the formation of B-Cur NPs or S-Cur NPs. Even after an extended incubation time of 720 h, the curcumin content in B-Cur NPs and S-Cur NPs was approximately 67% and 77%, respectively. Furthermore, the release of curcumin from B-Cur NPs and S-Cur NPs can be effectively triggered by pH and redox stimulation, facilitating tumor therapy. Selective tumor accumulation was still observed up to 12 h in mice injected with fluorescently labeled (FL-labeled) B-Cur NPs or S-Cur NPs, while mice injected with FL-labeled curcumin showed no significant tumor accumulation after 4 h. In addition, antitumor activity experiments showed that the nanoparticles had higher cytotoxicity and better tumor inhibition than curcumin and did not decrease the biocompatibility of the drug. A tumor inhibition rate of 33.2% was observed in mice treated with curcumin (25 mg·kg^{-1}). In contrast, the tumor inhibition rate in mice treated with the corresponding concentration of S-Cur NP (25 mg·kg^{-1} of curcumin) reached 69.6%. Therefore, this method overcomes the obstacles of using pure curcumin in clinical applications and provides a new view for curcumin to effectively treat tumors.

Amino-acid-modulated self-assembly of functional molecule. Amino acids can be co-assembled with photosensitizers to form a variety of complex system structures, such as light collection systems, bionic systems, and delivery systems for PDT. Photodynamic therapy is a novel, noninvasive antitumor therapy based on photosensitizers, light, and oxygen [76]. However, the inherent disadvantages of PS, such as hydrophobicity and easy aggregation under physiological conditions, reduce its therapeutic efficiency [77]. Using nanotechnology to encapsulate PS in nanoparticles can effectively solve this problem, improve the bioavailability of PS, and achieve targeted delivery of PS to tumor tissues [76]. Liu et al. [78] designed photosensitizer delivery systems by self-assembling cationic diphenylalanine (H-Phe-Phe-NH_2 HCl, CDP) or 9-fluorenylmethoxycarbonyl-ʟ-lysine (Fmoc-ʟ-Lys) with Ce6 into nanoparticles (CCNPs and FCNPs, respectively). Intermolecular hydrophobic and π–π interactions contribute to co-assembly. FCNPs nanoparticles and free Ce6 were injected into the caudal vein of MCF7 tumor-bearing nude mice at different times. The assembled NPs selectively accumulated in the tumor. In addition, the fluorescence remained at the tumor site for 24 h, indicating a long residence time. However, a weak fluorescence signal was observed in the tumor site of the mice treated with free Ce6. Designing nanoplatforms responsive to pH, enzymes, and photothermal stimuli is critical to enhance cellular uptake and control PS release [79-81]. Nanoplatforms responsive to pH undergo conformational changes through various mechanisms, such as protonation, charge inversion, or chemical bond cleavage, promoting tumor-specific cellular uptake or drug release [82]. Sun et al. [83] coupled tryptophan-glycine (WG) to hydrophobic porphyrins (P) by an amidation reaction to obtain pH-responsive nanoparticles (PWG) capable of spontaneous assembly under physiological conditions. Interestingly, since glycine provides carboxyl groups and is acid-sensitive, when the nanoparticles reach the tumor site, the acidity increases and the protonation of PWG promotes the formation of intermolecular hydrogen bonds and induces the conversion of nanoparticles to nanofibers. In addition, the nanoparticles exhibited significant long-term fluorescence after intravenous injection, maintained for 168 h, and the fluorescence intensity in the tumor remained above 64% after 168 h, indicating that the PWG nanostructures exhibited high accumulation and ultra-long tumor retention effects. Importantly, animal experiments demonstrated complete eradication of tumor in mice after injection of PWG NPs and laser irradiation, demonstrating the efficacy of PWG nanoparticles in vivo.

Indocyanine green (ICG) is widely used in diagnosis and treatment because of its strong absorption ability in the near-infrared region [84]. However, ICG has poor stability and a short half-life, thus limiting its use in photothermal therapy. Liu et al. [85] developed a nanoparticle based on phenylalanine, geniposide, and ICG for antitumor photothermal therapy. Geniposide is a natural crosslinking agent that provides strong covalent interactions to enhance stability. In addition, they attached disulfide groups to phenylalanine in response to glutathione. The obtained nanoparticles (GDSP) have high stability and can improve the photostability and maintain the photothermal conversion efficiency up to 32.0%. After entering the tumor cells, the nanoparticles convert light into heat under a laser irradiation of 808 nm and effectively kill the tumor cells.

Inspired by natural photosynthesis, artificial light systems consisting of photosensitizers and biomolecules, such as proteins, peptides, and DNA have received extensive attention in recent years [86]. Liu et al. [87] used electrostatic force to adsorb tetrakis(4-sulfonatophenyl)porphine (TPPS) molecules on the surface of 9-fluorenylmethoxycarbonyl-ʟ-lysine (Fmoc-ʟ-Lys) self-assembled nanofibers such that the nanofibers were assembled into sea-urchin-like microspheres. Fmoc-ʟ-Lys nanofibers act as templates to regulate the self-assembly of pigments. Sea-urchin-like structures facilitate light collection due to enhanced absorption cross sections and exciton energy transfer. In addition, Liu et al. [88] combined chemical reactions and manufactured bionic photobacteria based on self-assembly of amino acids and porphyrins. First, Fmoc-ʟ-Lys was self-assembled into a nanofiber template, then the ε-amino group on the surface of the Fmoc-ʟ-Lys fiber reacted with 3,4-

dihydroxyphenylalanine (DOPA) melanin through a Schiff base reaction to form an adhesive layer, and Fmoc-ʟ-Lys/DOPA fiber simulated an antenna to capture light. As a photosensitizer, Sn(IV)tetrakis(4-pyridyl)porphyrin (SnTPyP) was combined with the photocatalyst Co_3O_4 NPs by coordination bonds and electrostatic interaction onto the adhesive fibers. Therefore, a simple and robust bionic cyanobacteria model with excellent catalytic activity and sustainability was obtained. In addition, amino acids were co-assembled with phthalocyanines to improve their functionality. Han et al. [89] used histidine derivatives, 9-fluorenylmethoxycarbonyl-ʟ-histidine, (Fmoc-His-OH) co-assembled with phthalocyanine tetrasulfonic acid to form nanocapsules to mimic the function of photooxidase. The synergistic effects of various molecular interactions are the cause of the formation of nanocapsules, which can precisely regulate the assembly of photosensitizers and limit their severe self-aggregation. Dopamine was chosen as the model substrate to illustrate the photooxidative properties of nanocapsules. After illumination, dopamine is converted to leucine on the nanocapsules. Hence, nanocapsules can be used as photocatalysts to improve the photosensitization activity and photostability of phthalocyanine.

Camptothecin can induce tumor apoptosis by inhibiting the activity of topoisomerase I [90]. However, camptothecin has some major limitations in therapeutic applications, such as poor water solubility and rapid lactone ring hydrolysis at physiological pH values, which leads to inactive carboxylate forms [91,92]. Guo et al. [93] obtained water-soluble spiral nanofibers by coupling hydrophilic arginine and camptothecin. Self-assembly behavior is achieved by intermolecular π–π stacking and hydrophilic–hydrophobic interactions. The conjugates are linked by ester bonds, which help to maintain the camptothecin ring stability. The assembly can effectively enhance blood circulation, tumor accumulation and cellular uptake. In addition, arginine-modified camptothecin can be combined with anionic cisplatin–polyglutamic acid through electrostatic interaction to construct a co-delivery system.

Conclusion

The self-assembly of biomolecules is based on the noncovalent interaction and the bottom-up combination of ordered 3D structures. Nanotechnology is the driving force of self-assembly, and it has made great contributions to the field of biology and biomedical science. The nanostructure of amino acids can be a good substitute for therapeutic delivery due to its good biocompatibility, functionalization, and ease of design/synthesis. Self-assembled nanostructures have become smart tools in the biomedical field, as demonstrated by the ability of self-assembled amino acid molecules to exhibit stimulation responsiveness to the environment, which has exciting prospects for use in drug delivery. The advantages of low production costs, easy dispersion in aqueous media, mild and rapid synthetic setup and simple functionality facilitate their use as future candidates for various applications such as drug delivery, imaging, diagnosis, and photochemistry. The morphology and structure of self-assembled nanomaterials can be flexibly adjusted by transforming the type, proportion, and concentration of the building blocks. This newer area of research is therefore accelerating. The assembly forms of amino acids include nanocapsules, nanoparticles, nanofibers, nanorods, nanoparticles, and hydrogels (Table 1). However, it is still a challenge to make these assemblies the preferred materials for scientific research and applications. The difficulties of controlling the size and composition of nanostructures, the assembling behavior and stability in aqueous solution, the loading/encapsulation ratio of drugs, and the toxicity of nanostructures to living organisms still need to be overcome by researchers. Moreover, little research has been done on the biocompatibility of these nanostructures. Therefore, as a new strategy, amino acid self-assembly needs further research to explore the biomimetic and biomedical applications of micro- and nanomaterials.

Table 1: Summary of amino acids/amino acid derivatives and their applications.

Amino acids	Derivative/co-assembly	Forms of assembly	Applications	Ref.
H-Phe-OH H-Leu-OH	Fmoc-Phe-OH; Fmoc-Leu-OH	hydrogel	antibacterial	[45]
H-Phe-OH	Fmoc-Phe-OH; oligo(thiophene ethynylene)-ᴅ-phenylalanine	hydrogel	antibacterial	[47]
—	Fmoc-Lys(Fmoc)-Asp	hydrogel	2D/3D cell scaffolding; conductive composite hydrogels	[43]
H-Phe-OH	Fmoc-Phe-OH; aztreonam, an antibiotic drug	hydrogel	antibacterial	[48]

Table 1: Summary of amino acids/amino acid derivatives and their applications. (continued)

H-Phe-OH	Fmoc-Phe-OH; salicylic acid, a model drug	hydrogel	antibacterial	[49]
H-Phe-OH	Fmoc-Phe-OH; camptothecin, an anticancer drug; functionalized halloysite nanotubes, carrier for the camptothecin	hydrogel	drug delivery; antitumor	[50]
H-Phe-OH	NI-Phe-OH	hydrogel	live cell imaging in 3D scaffolding materials	[53]
H-His-OH	NI-His-OH	nanoparticles	bioimaging of Fe^{3+} ions; a selective diagnostic probe for cancer cells	[54]
H-Cys-OH	H-Cys-OH/Cd^{2+}	nanorods	light harvesting, hydrogen evolution	[58]
H-Cys-OH	H-Cys-OH/Zn^{2+}; TPPS[a] and alcohol dehydrogenase, as model guest molecules	microspheres	biomimetic photosystems; chloroplast mimic	[59]
H-Cys-OH	H-Cys-OH/Zn^{2+}; glutamate dehydrogenase, a guest molecule	microspheres	pigment model	[60]
H-His-OH	(Z[b]-His-$NHNH_2$)/Zn^{2+}	metallo-nanozyme	catalytic hydrolyzation	[62]
H-His-OH, H-Pro-OH, H-Ala-OH, H-Leu-OH	Fmoc-His-OH/Ag^+, Fmoc-Pro-OH/Ag^+, Fmoc-Ala-OH/Ag^+, Fmoc-Leu-OH/Ag^+	hydrogel	antibacterial	[68]
H-Leu-OH	Fmoc-Leu-OH/Mn^{2+}; Ce6, a photosensitive drug	nanoparticles	drug delivery; antitumor; MRI	[70]
H-His-OH	Fmoc-His-OH/Zn^{2+}, (Z[b]-His-Phe)/Zn^{2+}; Ce6, a photosensitive drug	nanoparticles	drug delivery; antitumor	[71]
H-His-OH	Fmoc-His-OH/Zn^{2+}; curcumin, an anticancer drug	nanoparticles	drug delivery; antitumor	[75]
H-Lys-OH	Fmoc-Lys-OH; H-Phe-Phe-NH_2 HCl; Ce6, a photosensitive drug	nanoparticles	drug delivery; antitumor	[78]
H-Trp-OH; H-Gly-OH	tryptophan-glycine; porphyrin; a photosensitive drug	nanoparticles transform into nanofibers	drug delivery; antitumor	[83]
H-Phe-OH	*N,N′*-(disulfanediylbis(ethane-2,1-diyl))di-L-phenylalamide; genipin, as crosslinking agent; indocyanine green, a photosensitive drug	nanoparticles	drug delivery; antitumor	[85]
H-Lys-OH	Fmoc-Lys-OH; TPPS[a], model molecules of light-harvesting porphyrins	microspheres	light-harvesting, Hydrogen evolution	[87]
H-Lys-OH	Fmoc-Lys-OH; 3,4-dihydroxyphenylalanine; Sn(IV)tetrakis(4-pyridyl)porphyrin; Co_3O_4 NPs	nanofibers	oxygen evolution, biomimetic photosynthesis	[88]
H-His-OH	Fmoc-His-OH; phthalocyanine tetrasulfonic acid, a phthalocyanine model	nanovesicles	photocatalyst	[89]

Table 1: Summary of amino acids/amino acid derivatives and their applications. (continued)

H-Arg-OH	H-Arg-OH; camptothecin, an anticancer drug	nanofibers	drug delivery; antitumor	[93]

[a]Tetrakis(4-sulfonatophenyl) porphine; [b]*N*-benzyloxycarbonyl.

ORCID® iDs

Huan Ren - https://orcid.org/0000-0002-6782-5782

References

1. Langer, R.; Tirrell, D. A. *Nature* **2004,** *428,* 487–492. doi:10.1038/nature02388
2. Webber, M. J.; Appel, E. A.; Meijer, E. W.; Langer, R. *Nat. Mater.* **2016,** *15,* 13–26. doi:10.1038/nmat4474
3. Medina-Fernandez, I.; Celiz, A. D. *Biomater. Sci.* **2019,** *7,* 506–519. doi:10.1039/c8bm01296b
4. Gu, X.; Ding, F.; Williams, D. F. *Biomaterials* **2014,** *35,* 6143–6156. doi:10.1016/j.biomaterials.2014.04.064
5. Katti, K. S. *Colloids Surf., B* **2004,** *39,* 133–142. doi:10.1016/j.colsurfb.2003.12.002
6. Navarro, M.; Michiardi, A.; Castaño, O.; Planell, J. A. *J. R. Soc., Interface* **2008,** *5,* 1137–1158. doi:10.1098/rsif.2008.0151
7. Chung, L.; Maestas, D. R., Jr.; Housseau, F.; Elisseeff, J. H. *Adv. Drug Delivery Rev.* **2017,** *114,* 184–192. doi:10.1016/j.addr.2017.07.006
8. Singer, A. J.; Boyce, S. T. *J. Burn Care Res.* **2017,** *38,* e605–e613. doi:10.1097/bcr.0000000000000538
9. Mann, J. L.; Yu, A. C.; Agmon, G.; Appel, E. A. *Biomater. Sci.* **2017,** *6,* 10–37. doi:10.1039/c7bm00780a
10. Smith, K. H.; Tejeda-Montes, E.; Poch, M.; Mata, A. *Chem. Soc. Rev.* **2011,** *40,* 4563–4577. doi:10.1039/c1cs15064b
11. Okesola, B. O.; Mata, A. *Chem. Soc. Rev.* **2018,** *47,* 3721–3736. doi:10.1039/c8cs00121a
12. Mandal, D.; Nasrolahi Shirazi, A.; Parang, K. *Org. Biomol. Chem.* **2014,** *12,* 3544–3561. doi:10.1039/c4ob00447g
13. Northrop, B. H.; Zheng, Y.-R.; Chi, K.-W.; Stang, P. J. *Acc. Chem. Res.* **2009,** *42,* 1554–1563. doi:10.1021/ar900077c
14. Yang, B.; Adams, D. J.; Marlow, M.; Zelzer, M. *Langmuir* **2018,** *34,* 15109–15125. doi:10.1021/acs.langmuir.8b01165
15. Bai, Y.; Luo, Q.; Liu, J. *Chem. Soc. Rev.* **2016,** *45,* 2756–2767. doi:10.1039/c6cs00004e
16. Zou, Q.; Liu, K.; Abbas, M.; Yan, X. *Adv. Mater. (Weinheim, Ger.)* **2016,** *28,* 1031–1043. doi:10.1002/adma.201502454
17. Cosert, K. M.; Castro-Forero, A.; Steidl, R. J.; Worden, R. M.; Reguera, G. *mBio* **2019,** *10,* e02721–19. doi:10.1128/mbio.02721-19
18. Onur, T.; Yuca, E.; Olmez, T. T.; Seker, U. O. S. *J. Colloid Interface Sci.* **2018,** *520,* 145–154. doi:10.1016/j.jcis.2018.03.016
19. Pandit, G.; Roy, K.; Agarwal, U.; Chatterjee, S. *ACS Omega* **2018,** *3,* 3143–3155. doi:10.1021/acsomega.7b01871
20. Tagalakis, A. D.; Maeshima, R.; Yu-Wai-Man, C.; Meng, J.; Syed, F.; Wu, L.-P.; Aldossary, A. M.; McCarthy, D.; Moghimi, S. M.; Hart, S. L. *Acta Biomater.* **2017,** *51,* 351–362. doi:10.1016/j.actbio.2017.01.048
21. Purwada, A.; Tian, Y. F.; Huang, W.; Rohrbach, K. M.; Deol, S.; August, A.; Singh, A. *Adv. Healthcare Mater.* **2016,** *5,* 1413–1419. doi:10.1002/adhm.201501062
22. Li, Y.; Yan, L.; Liu, K.; Wang, J.; Wang, A.; Bai, S.; Yan, X. *Small* **2016,** *12,* 2575–2579. doi:10.1002/smll.201600230
23. Chen, J.; Zhang, B.; Xia, F.; Xie, Y.; Jiang, S.; Su, R.; Lu, Y.; Wu, W. *Nanoscale* **2016,** *8,* 7127–7136. doi:10.1039/c5nr06804e
24. Abbas, M.; Zou, Q.; Li, S.; Yan, X. *Adv. Mater. (Weinheim, Ger.)* **2017,** *29,* 1605021. doi:10.1002/adma.201605021
25. Zhang, H.; Guo, L.; Xie, Z.; Xin, X.; Sun, D.; Yuan, S. *Langmuir* **2016,** *32,* 13736–13745. doi:10.1021/acs.langmuir.6b03709
26. Chakraborty, P.; Gazit, E. *ChemNanoMat* **2018,** *4,* 730–740. doi:10.1002/cnma.201800147
27. Tao, K.; Levin, A.; Adler-Abramovich, L.; Gazit, E. *Chem. Soc. Rev.* **2016,** *45,* 3935–3953. doi:10.1039/c5cs00889a
28. Yuan, Y.; Zhao, L.; Shen, C.; He, Y.; Yang, F.; Zhang, G.; Jia, M.; Zeng, R.; Li, C.; Qiao, R. *Mater. Sci. Eng., C* **2020,** *106,* 110159. doi:10.1016/j.msec.2019.110159
29. Wang, Y.; Zhang, X.; Wan, K.; Zhou, N.; Wei, G.; Su, Z. *J. Nanobiotechnol.* **2021,** *19,* 253. doi:10.1186/s12951-021-00999-x
30. Zhang, Z.; Ma, R.; Shi, L. *Acc. Chem. Res.* **2014,** *47,* 1426–1437. doi:10.1021/ar5000264
31. Mendes, A. C.; Baran, E. T.; Reis, R. L.; Azevedo, H. S. *Wiley Interdiscip. Rev.: Nanomed. Nanobiotechnol.* **2013,** *5,* 582–612. doi:10.1002/wnan.1238
32. Stanković, I. M.; Niu, S.; Hall, M. B.; Zarić, S. D. *Int. J. Biol. Macromol.* **2020,** *156,* 949–959. doi:10.1016/j.ijbiomac.2020.03.064
33. Lee, J.; Ju, M.; Cho, O. H.; Kim, Y.; Nam, K. T. *Adv. Sci.* **2019,** *6,* 1801255. doi:10.1002/advs.201801255
34. Adler-Abramovich, L.; Vaks, L.; Carny, O.; Trudler, D.; Magno, A.; Caflisch, A.; Frenkel, D.; Gazit, E. *Nat. Chem. Biol.* **2012,** *8,* 701–706. doi:10.1038/nchembio.1002
35. Shaham-Niv, S.; Adler-Abramovich, L.; Schnaider, L.; Gazit, E. *Sci. Adv.* **2015,** *1,* e1500137. doi:10.1126/sciadv.1500137
36. Singh, V.; Rai, R. K.; Arora, A.; Sinha, N.; Thakur, A. K. *Sci. Rep.* **2015,** *4,* 3875. doi:10.1038/srep03875
37. Bera, S.; Xue, B.; Rehak, P.; Jacoby, G.; Ji, W.; Shimon, L. J. W.; Beck, R.; Král, P.; Cao, Y.; Gazit, E. *ACS Nano* **2020,** *14,* 1694–1706. doi:10.1021/acsnano.9b07307
38. Shaham-Niv, S.; Arnon, Z. A.; Sade, D.; Lichtenstein, A.; Shirshin, E. A.; Kolusheva, S.; Gazit, E. *Angew. Chem., Int. Ed.* **2018,** *57,* 12444–12447. doi:10.1002/anie.201806565
39. Gour, N.; Kanth P., C.; Koshti, B.; Kshtriya, V.; Shah, D.; Patel, S.; Agrawal-Rajput, R.; Pandey, M. K. *ACS Chem. Neurosci.* **2019,** *10,* 1230–1239. doi:10.1021/acschemneuro.8b00310
40. Martin, A. D.; Thordarson, P. *J. Mater. Chem. B* **2020,** *8,* 863–877. doi:10.1039/c9tb02539a
41. Diaferia, C.; Morelli, G.; Accardo, A. *J. Mater. Chem. B* **2019,** *7,* 5142–5155. doi:10.1039/c9tb01043b
42. Ryan, K.; Beirne, J.; Redmond, G.; Kilpatrick, J. I.; Guyonnet, J.; Buchete, N.-V.; Kholkin, A. L.; Rodriguez, B. J. *ACS Appl. Mater. Interfaces* **2015,** *7,* 12702–12707. doi:10.1021/acsami.5b01251

43. Chakraborty, P.; Tang, Y.; Yamamoto, T.; Yao, Y.; Guterman, T.; Zilberzwige-Tal, S.; Adadi, N.; Ji, W.; Dvir, T.; Ramamoorthy, A.; Wei, G.; Gazit, E. *Adv. Mater. (Weinheim, Ger.)* **2020,** *32,* 1906043. doi:10.1002/adma.201906043
44. Gahane, A. Y.; Ranjan, P.; Singh, V.; Sharma, R. K.; Sinha, N.; Sharma, M.; Chaudhry, R.; Thakur, A. K. *Soft Matter* **2018,** *14,* 2234–2244. doi:10.1039/c7sm02317k
45. Xie, Y.-Y.; Zhang, Y.-W.; Qin, X.-T.; Liu, L.-P.; Wahid, F.; Zhong, C.; Jia, S.-R. *Colloids Surf., B* **2020,** *193,* 111099. doi:10.1016/j.colsurfb.2020.111099
46. Irwansyah, I.; Li, Y.-Q.; Shi, W.; Qi, D.; Leow, W. R.; Tang, M. B. Y.; Li, S.; Chen, X. *Adv. Mater. (Weinheim, Ger.)* **2015,** *27,* 648–654. doi:10.1002/adma.201403339
47. Zhao, Q.; Zhao, Y.; Lu, Z.; Tang, Y. *ACS Appl. Mater. Interfaces* **2019,** *11,* 16320–16327. doi:10.1021/acsami.9b02643
48. Gahane, A. Y.; Singh, V.; Kumar, A.; Kumar Thakur, A. *Biomater. Sci.* **2020,** *8,* 1996–2006. doi:10.1039/c9bm01978b
49. Snigdha, K.; Singh, B. K.; Mehta, A. S.; Tewari, R. P.; Dutta, P. K. *Int. J. Biol. Macromol.* **2016,** *93,* 1639–1646. doi:10.1016/j.ijbiomac.2016.04.072
50. Rizzo, C.; Arrigo, R.; D'Anna, F.; Di Blasi, F.; Dintcheva, N. T.; Lazzara, G.; Parisi, F.; Riela, S.; Spinelli, G.; Massaro, M. *J. Mater. Chem. B* **2017,** *5,* 3217–3229. doi:10.1039/c7tb00297a
51. Gopikrishna, P.; Meher, N.; Iyer, P. K. *ACS Appl. Mater. Interfaces* **2018,** *10,* 12081–12111. doi:10.1021/acsami.7b14473
52. Chakravarthy, R. D.; Mohammed, M.; Lin, H.-C. *Chem. – Asian J.* **2020,** *15,* 2696–2705. doi:10.1002/asia.202000575
53. Hsu, S.-M.; Wu, F.-Y.; Cheng, H.; Huang, Y.-T.; Hsieh, Y.-R.; Tseng, D. T.-H.; Yeh, M.-Y.; Hung, S.-C.; Lin, H.-C. *Adv. Healthcare Mater.* **2016,** *5,* 2406–2412. doi:10.1002/adhm.201600342
54. Sarkar, D.; Chowdhury, M.; Das, P. K. *J. Mater. Chem. B* **2020,** *9,* 494–507. doi:10.1039/d0tb02450c
55. Chen, L.; Chen, Q.; Wu, M.; Jiang, F.; Hong, M. *Acc. Chem. Res.* **2015,** *48,* 201–210. doi:10.1021/ar5003076
56. Sun, Y.; Chen, C.; Stang, P. J. *Acc. Chem. Res.* **2019,** *52,* 802–817. doi:10.1021/acs.accounts.8b00663
57. Zou, Q.; Yan, X. *Chem. – Eur. J.* **2018,** *24,* 755–761. doi:10.1002/chem.201704032
58. Xie, Z.; Liu, K.; Ren, X.; Zhang, H.; Xin, X.; Zou, Q.; Yan, X. *ACS Appl. Bio Mater.* **2018,** *1,* 748–755. doi:10.1021/acsabm.8b00214
59. Liu, K.; Yuan, C.; Zou, Q.; Xie, Z.; Yan, X. *Angew. Chem., Int. Ed.* **2017,** *56,* 7876–7880. doi:10.1002/anie.201704678
60. Liu, K.; Ren, X.; Sun, J.; Zou, Q.; Yan, X. *Adv. Sci.* **2018,** *5,* 1701001. doi:10.1002/advs.201701001
61. Shao, T.; Falcone, N.; Kraatz, H.-B. *ACS Omega* **2020,** *5,* 1312–1317. doi:10.1021/acsomega.9b03939
62. Han, J.; Zou, Q.; Su, W.; Yan, X. *Chem. Eng. J.* **2020,** *394,* 124987. doi:10.1016/j.cej.2020.124987
63. Zhang, X.-F.; Liu, Z.-G.; Shen, W.; Gurunathan, S. *Int. J. Mol. Sci.* **2016,** *17,* 1534. doi:10.3390/ijms17091534
64. Nakamura, S.; Sato, M.; Sato, Y.; Ando, N.; Takayama, T.; Fujita, M.; Ishihara, M. *Int. J. Mol. Sci.* **2019,** *20,* 3620. doi:10.3390/ijms20153620
65. Tang, S.; Zheng, J. *Adv. Healthcare Mater.* **2018,** *7,* 1701503. doi:10.1002/adhm.201701503
66. Siddiqi, K. S.; Husen, A.; Rao, R. A. K. *J. Nanobiotechnol.* **2018,** *16,* 14. doi:10.1186/s12951-018-0334-5
67. Liao, C.; Li, Y.; Tjong, S. C. *Int. J. Mol. Sci.* **2019,** *20,* 449. doi:10.3390/ijms20020449
68. Song, J.; Yuan, C.; Jiao, T.; Xing, R.; Yang, M.; Adams, D. J.; Yan, X. *Small* **2020,** *16,* 1907309. doi:10.1002/smll.201907309
69. Sun, H.; Chang, R.; Zou, Q.; Xing, R.; Qi, W.; Yan, X. *Small* **2019,** *15,* 1905326. doi:10.1002/smll.201905326
70. Zhang, H.; Liu, K.; Li, S.; Xin, X.; Yuan, S.; Ma, G.; Yan, X. *ACS Nano* **2018,** *12,* 8266–8276. doi:10.1021/acsnano.8b03529
71. Li, S.; Zou, Q.; Li, Y.; Yuan, C.; Xing, R.; Yan, X. *J. Am. Chem. Soc.* **2018,** *140,* 10794–10802. doi:10.1021/jacs.8b04912
72. Hamzehzadeh, L.; Atkin, S. L.; Majeed, M.; Butler, A. E.; Sahebkar, A. *J. Cell. Physiol.* **2018,** *233,* 6530–6537. doi:10.1002/jcp.26620
73. Shishodia, S.; Chaturvedi, M. M.; Aggarwal, B. B. *Curr. Probl. Cancer* **2007,** *31,* 243–305. doi:10.1016/j.currproblcancer.2007.04.001
74. Ashrafizadeh, M.; Najafi, M.; Makvandi, P.; Zarrabi, A.; Farkhondeh, T.; Samarghandian, S. *J. Cell. Physiol.* **2020,** *235,* 9241–9268. doi:10.1002/jcp.29819
75. Li, Y.; Zou, Q.; Yuan, C.; Li, S.; Xing, R.; Yan, X. *Angew. Chem., Int. Ed.* **2018,** *57,* 17084–17088. doi:10.1002/anie.201810087
76. Kwiatkowski, S.; Knap, B.; Przystupski, D.; Saczko, J.; Kędzierska, E.; Knap-Czop, K.; Kotlińska, J.; Michel, O.; Kotowski, K.; Kulbacka, J. *Biomed. Pharmacother.* **2018,** *106,* 1098–1107. doi:10.1016/j.biopha.2018.07.049
77. Lim, C.-K.; Heo, J.; Shin, S.; Jeong, K.; Seo, Y. H.; Jang, W.-D.; Park, C. R.; Park, S. Y.; Kim, S.; Kwon, I. C. *Cancer Lett.* **2013,** *334,* 176–187. doi:10.1016/j.canlet.2012.09.012
78. Liu, K.; Xing, R.; Zou, Q.; Ma, G.; Möhwald, H.; Yan, X. *Angew. Chem., Int. Ed.* **2016,** *55,* 3036–3039. doi:10.1002/anie.201509810
79. Zhou, Y.; Zhou, C.; Zou, Y.; Jin, Y.; Han, S.; Liu, Q.; Hu, X.; Wang, L.; Ma, Y.; Liu, Y. *Biomater. Sci.* **2020,** *8,* 5029–5046. doi:10.1039/d0bm00840k
80. Zou, Q.; Abbas, M.; Zhao, L.; Li, S.; Shen, G.; Yan, X. *J. Am. Chem. Soc.* **2017,** *139,* 1921–1927. doi:10.1021/jacs.6b11382
81. Li, W.; Zheng, C.; Pan, Z.; Chen, C.; Hu, D.; Gao, G.; Kang, S.; Cui, H.; Gong, P.; Cai, L. *Biomaterials* **2016,** *101,* 10–19. doi:10.1016/j.biomaterials.2016.05.019
82. Yan, K.; Zhang, Y.; Mu, C.; Xu, Q.; Jing, X.; Wang, D.; Dang, D.; Meng, L.; Ma, J. *Theranostics* **2020,** *10,* 7287–7318. doi:10.7150/thno.46288
83. Sun, B.; Chang, R.; Cao, S.; Yuan, C.; Zhao, L.; Yang, H.; Li, J.; Yan, X.; Hest, J. C. M. *Angew. Chem., Int. Ed.* **2020,** *132,* 20763–20769. doi:10.1002/ange.202008708
84. Porcu, E. P.; Salis, A.; Gavini, E.; Rassu, G.; Maestri, M.; Giunchedi, P. *Biotechnol. Adv.* **2016,** *34,* 768–789. doi:10.1016/j.biotechadv.2016.04.001
85. Liu, Y.; Zhao, L.; Xing, R.; Jiao, T.; Song, W.; Yan, X. *Chem. – Asian J.* **2018,** *13,* 3526–3532. doi:10.1002/asia.201800825
86. Xiu, Y.; Zhang, D.; Xu, L.; Li, J.; Chen, Y.; Xia, Y.; Cao, M.; Wang, S. *J. Colloid Interface Sci.* **2021,** *587,* 550–560. doi:10.1016/j.jcis.2020.11.012
87. Liu, K.; Abass, M.; Zou, Q.; Yan, X. *Green Energy Environ.* **2017,** *2,* 58–63. doi:10.1016/j.gee.2016.12.005
88. Liu, K.; Zhang, H.; Xing, R.; Zou, Q.; Yan, X. *ACS Nano* **2017,** *11,* 12840–12848. doi:10.1021/acsnano.7b08215
89. Han, J.; Liu, K.; Chang, R.; Zhao, L.; Yan, X. *Angew. Chem., Int. Ed.* **2019,** *58,* 2000–2004. doi:10.1002/anie.201811478
90. Pommier, Y. *Nat. Rev. Cancer* **2006,** *6,* 789–802. doi:10.1038/nrc1977
91. Botella, P.; Rivero-Buceta, E. *J. Controlled Release* **2017,** *247,* 28–54. doi:10.1016/j.jconrel.2016.12.023

92. Lu, J.; Liu, C.; Wang, P.; Ghazwani, M.; Xu, J.; Huang, Y.; Ma, X.; Zhang, P.; Li, S. *Biomaterials* **2015,** *62,* 176–187. doi:10.1016/j.biomaterials.2015.05.046
93. Guo, Z.; Lin, L.; Hao, K.; Wang, D.; Liu, F.; Sun, P.; Yu, H.; Tang, Z.; Chen, M.; Tian, H.; Chen, X. *ACS Appl. Mater. Interfaces* **2020,** *12,* 7466–7476. doi:10.1021/acsami.9b21311

License and Terms

BEILSTEIN JOURNAL OF NANOTECHNOLOGY

Design and selection of peptides to block the SARS-CoV-2 receptor binding domain by molecular docking

Kendra Ramirez-Acosta[1,2], Ivan A. Rosales-Fuerte[1,2], J. Eduardo Perez-Sanchez[1,2], Alfredo Nuñez-Rivera[1,2], Josue Juarez[*3] and Ruben D. Cadena-Nava[*1]

Full Research Paper

Address:
[1]Centro de Nanociencias y Nanotecnología - Universidad Nacional Autónoma de México (UNAM) – Ensenada, Baja California, México, [2]Centro de Investigación Científica y de Educación Superior de Ensenada, Baja California, (CICESE), Ensenada, Baja California, México and [3]Departamento de Física, Universidad de Sonora, Blvd. Luis Encinas y Rosales, Hermosillo, Sonora, México

Email:
Josue Juarez[*] - josue.juarez@unison.mx; Ruben D. Cadena-Nava[*] - rcadena@cnyn.unam.mx

* Corresponding author

Keywords:
angiotensin converting enzyme-2 (ACE2); antiviral peptides; hydrogen bonds; molecular docking; SARS-CoV-2 RBD

Beilstein J. Nanotechnol. **2022,** *13,* 699–711.
https://doi.org/10.3762/bjnano.13.62

Received: 19 April 2022
Accepted: 12 July 2022
Published: 22 July 2022

This article is part of the thematic issue "New trends in nano-biotechnology".

Guest Editor: P.-L. Show

Abstract

The novel Severe Acute Respiratory Syndrome Coronavirus-2 (SARS-CoV-2) is currently one of the most contagious viruses in existence and the cause of the worst pandemic in this century, COVID-19. SARS-CoV-2 infection begins with the recognition of the cellular receptor angiotensin converting enzyme-2 by its spike glycoprotein receptor-binding domain (RBD). Thus, the use of small peptides to neutralize the infective mechanism of SARS-CoV-2 through the RBD is an interesting strategy. The binding ability of 104 peptides (University of Nebraska Medical Center's Antimicrobial Peptide Database) to the RBD was assessed using molecular docking. Based on the molecular docking results, peptides with great affinity to the RBD were selected. The most common amino acids involved in the recognition of the RBD were identified to design novel peptides based on the number of hydrogen bonds that were formed. At physiological pH, these peptides are almost neutral and soluble in aqueous media. Interestingly, several peptides showed the capability to bind to the active surface area of the RBD of the Wuhan strain, as well as to the RBD of the Delta variant and other SARS-Cov-2 variants. Therefore, these peptides have promising potential in the treatment of the COVID-19 disease caused by different variants of SARS-CoV-2. This research work will be focused on the molecular docking of peptides by molecular dynamics, in addition to an analysis of the possible interaction of these peptides with physiological proteins. This methodology could be extended to design peptides that are active against other viruses.

Introduction

The current pandemic due to coronavirus disease-19 (COVID-19), caused by the novel virus SARS-CoV-2, has over 533 million of confirmed cases and over 6.3 million fatalities over the five continents by June 15, 2022 [1]. It is known, that the entry of the SARS-CoV into the host cell begins with the binding of the RBD, which is part of the spike (S) glycoprotein, to the angiotensin converting enzyme-2 (ACE2) cellular receptor of the host cells [2-4]. Similarly, the entry of SARS-CoV-2 into cells is mediated by the interaction of the RBD with the host cell ACE2 receptor [2,3,5]. Figure 1 shows the RBD–ACE2 complex formed at the first stage of the cellular infection by SARS-CoV-2. The formation of the RBD–ACE2 complex is mediated by the amino acid residues F486, Y489, Q493, G496, T500, and N501 located on the active region of the SARS-CoV-2 RBD (Figure 1b, red rectangle) [6]. Therefore, the RBD has been proposed as one of therapeutic targets to block the infection mechanism of SARS-CoV-2. For instance, peptide analogues of the ACE2 receptor (I21 to S44) have been designed in silico to disrupt the formation of the RBD–ACE2 complex and to prevent the viral infection [7].

Small peptides (biological and synthetic) have been proposed as promising alternative drugs to block the SARS-CoV-2 RBD and to interrupt the infection [8]. Lactoferricin B, minidefensins, indolicidin, and dermaseptin peptides have been used to neutralize viruses such as human immunodeficiency virus, cytomegalovirus, herpes simplex virus, and hepatitis B virus [9-11]. In order to find an effective peptide, it is important to reduce secondary effects by avoiding the binding with the major histocompatibility complex (MHC). This is crucial to reduce any acute immunological responses [12,13]. Several suitable peptide candidates could be found to block the SARS-CoV-2 RBD. Natural antiviral and antimicrobial peptides and chimeric peptides with the capability to bind and neutralize viral proteins can be designed and selected by phage display or using in silico approaches [8,14]. Several peptides based on the ACE2 receptor have been designed by in silico approaches [5,15]. In silico approaches are commonly used to determine the capacity of small ligands (peptides and drugs) to bind to a particular target site of a given protein, due to the low cost, versatility, and ease to develop [16-18]. Current peptide design techniques involve the modification of peptides based on the ACE2 receptor to increase their binding affinity to the SARS-CoV-2 RBD and to prevent the virus from binding onto the ACE2 receptor [5,15].

Powerful computational programs, as local installations or on internet servers, can be used to perform molecular docking. These include DOCK, AutoDock, FlexX, SurFlex, GOLD, ICM, and AutoDock Vina [18-20]. AutoDock Vina (ADV), an open-source software with high docking power, is one of the most commonly used programs [16,17,21]. ADV provides theoretical information about hydrophobic interactions, electrostatic interactions, hydrogen bonds, and van der Waals interactions. It can also predict the binding pose and binding affinity [20]. Considering these important features, ADV was used to perform molecular docking of 104 biological peptides, selected from the University of Nebraska Medical Center’s Antimicrobial Peptide Database (APD) [22-24], and theoretical peptides with the region of the SARS-CoV-2 RBD that binds to the cellular receptor ACE2 (called the RBD active region). APD peptides were selected based on an already known antiviral activity (Table S1, Supporting Information File 1). ADV results showed that both peptides from the APD and theoretical peptides have the capability to dock on the RBD active region, blocking the amino acid residues related to the association of the Wuhan strain RBD (GenBank: MN908947.3) with ACE2 [6]. The number of hydrogen bonds between RBD and ACE2 influence the stability of the bound complex, which suggests

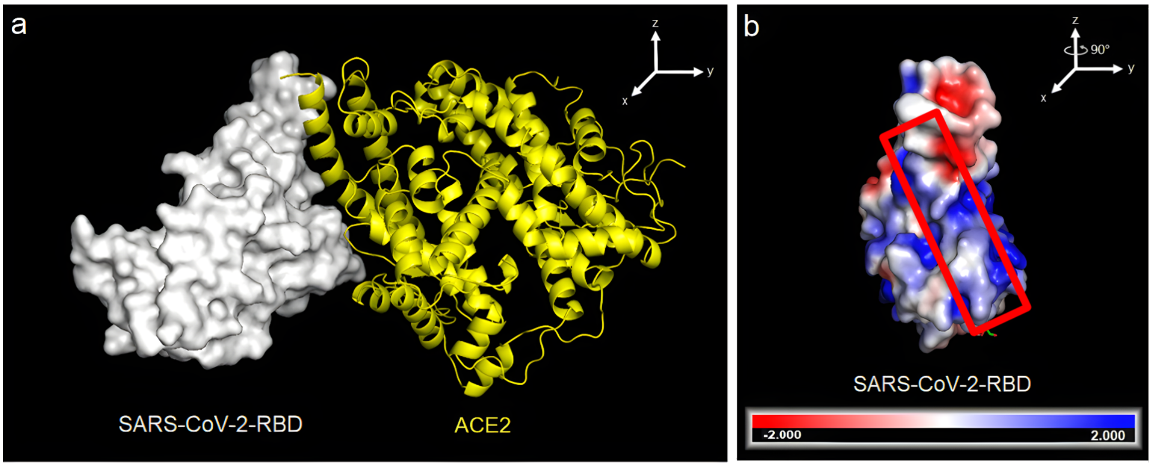

Figure 1: SARS-CoV-2 bound to the ACE2 receptor. (a) Crystallized complex between the RBD of the SARS-CoV-2 spike protein (white) and ACE2 (yellow) (PDB 6VYB). (b) Distribution of electrostatic potential on the surface of the SARS-CoV-2 spike protein. The electrostatic potential distribution was calculated using the adaptive Poisson–Boltzmann solver (APBS) module in PyMOL. The values range from −2 (red) over 0 (white) to +2 (blue). The orientation of the molecule is rotated by about 90° along the *z*-axis of image (a) to show the RBD surface that binds to the ACE2 cell receptor. Image modified from PDB 6VYB [3].

that designing peptides capable of forming several hydrogen bonds might prove useful for increasing the binding affinity [25]. From this, new theoretical peptides were designed, considering the most common amino acid residues involved in the formation of hydrogen bonds to the RBD active region of SARS-CoV-2. These small peptides may reinforce and enhance the effectiveness of the immune system response before and after the application of SARS-CoV-2 vaccines [26,27]. Furthermore, the proposed peptides may elude the immune system and bind effectively to SARS-CoV-2 RBD.

Materials and Methods

Ligand selection for screening

In total, 104 peptides were chosen from the University of Nebraska Medical Center's Antimicrobial Peptide Database [22-24]. The peptides were selected based on their previously reported antiviral activity in order to perform a massive docking experiment. PDB files were gathered for those peptides that possess a reported three-dimensional structure and a 3D structure was predicted through I-TASSER's and PEP-FOLD3.5's model prediction servers using the reported peptide sequence for those that lacked it [28-32]. All peptides analyzed were compared with the ACE2-derived peptide IEEQAKTFLDKFNHEAEDLFYQSS (I21 to S44 of ACE2) [7]. The electrostatic surface potential, hydrophobic interactions, hydrogen bonds, and interactions of the selected ligand and protein docked complexes were analyzed by PyMOL (version 2.4) and LigPlot+ (version 2.2) [33,34].

Protein and ligand preparation for AutoDock Vina

AutoDock Vina (1.1.2) software was employed for all docking experiments [21]. The X-ray diffraction crystal structure of SARS-CoV-2 RBD spike protein (PDB ID: 6VYB) was selected for this study. The molecules bound to the protein receptor molecule were removed. The RBD spike protein was prepared using AutoDock Tools to add polar hydrogen atoms, Kollman charges, and to remove water molecules. The active site grid was generated using a grid box (22 Å × 40 Å × 40 Å) centered at (11 Å, 90.5 Å, 57.5 Å). Docking was carried out with the 104 peptides from the APD as ligand molecules. The experiment was validated by comparing the position of the docked ACE2–RBD complex with the crystallized ACE2–RBD complex. The docked complex was superimposed onto the crystallized complex using PyMOL and an RMSD calculation was performed.

Proposing new peptides based on hydrogen-bond formation

Based on the selected APD peptides, new peptides were designed in order to improve the capability to block the SARS-CoV-2 RBD. The standard way to design novel peptides is by random sequences that can generate many peptides. However, this leads to an increase in computation time. To avoid this bottleneck, peptides were designed through the analysis of the APD–RBD active region docking, where the RBD amino acid residues able to form hydrogen bonds with the APD were considered. Five main regions (vertical, horizontal, left diagonal, right diagonal, center) in the RBD active region were selected to propose the sequence of amino acid residues of a theoretical peptide that could potentially form a great number of hydrogen bonds in these positions while docked to SARS-CoV-2 RBD. The proposed sequences of amino acid residues were modeled using PEP-FOLD 3.5 server. Then, theoretical peptides were submitted to molecular docking against the Wuhan strain (PDB ID: 6VYB), Delta variant (PDB ID: 7W92) and theoretical variants (K417N, Y453F, E484K, and N501Y), according to the B1.1.7, B.1.351, P.1, and Y453F SARS-CoV-2 variants.

Computing the radius of gyration

The radius of gyration (R_g) for the selected peptides against SARS-CoV-2 was determined using the WinHydroPro V10 software [35].

Immunogenicity analysis

Immunogenicity analysis of the selected peptides was carried out by the Tepitool software using specific alleles from the human major histocompatibility complex class I (MHC I) [36]. Peptides with low binding to MHC I molecules were considered ($50 \text{ nM} \leq IC_{50} \leq 500 \text{ nM}$) according to Calis and Adhikari [37,38]

Free energy of RBD–ligand by PRODIGY

The protein binding energy prediction (PRODIGY) web server is an effective predictive model based on intermolecular contacts in protein–protein complexes based on their 3D structure [39]. This tool predicts the binding free energy between protein complexes with great accuracy, which makes it an excellent complement to docking approaches. Thus, PRODIGY web server was used to predict the binding energy of the APD–RBD and theoretical peptide–RBD complexes [39-41]. The input files were acquired from ADT files in the PDB format.

Contact area analysis

PyMOL was used to compute the solvent-accessible surface area of SARS-CoV-2 RBD and the peptides that were docked to it. The surface area of the RBD–ligand complex was also calculated. The following equation was established to calculate the contact area between the RBD and each ligand analyzed:

$$A_c = \frac{A_{\text{RBD}} + A_{\text{ligand}} - A_{\text{complex}}}{2}, \qquad (1)$$

where A_c is the contact area of the ligand with the RBD, and A_{RBD} and A_{ligand} indicate the surface areas of RBD and ligand, respectively. A_{complex} corresponds to the surface area of the complex formed when the ligand binds to the SARS-CoV-2 RBD.

Results and Discussion

Initial virtual screening

Based on the binding affinity obtained through ADV, 69 of the 104 APD peptides bound stronger to the RBD active region than the ACE2 peptide (Table 1 and Table S2, Supporting Information File 1). Three peptides based on lysozyme were also designed for screening to compare with the APD peptides given the antimicrobial role of lysozyme as part of the innate immune system. The ADV results show that most of the APD peptides successfully docked on the active region of the RBD (Figure 1), suggesting that these APD peptides actually bind to the RBD active region, blocking the entry of SARS-CoV-2 to host cells. Additionally, according to Figure 1, peptides are posed in different ways on the RBD, covering different areas of the active surface of RBD. For instance, MVL (74–87), cyanovirin-N (70–80) and dermaseptin-S4 (Figure S2, Supporting Information File 1) are posed laterally to the RBD active surface. Similar results have been reported previously by Qiao & Olvera, who designed a negatively charged EELE tetrapeptide to neutralize the SARS-CoV-2-RBD–ACE2 binding [25]. It is important to note that the analyzed peptides have a nearly neutral charge, thus they have a low probability of unspecific interactions with other molecules, cellular uptake, or macrophage recognition [42-46].

It is important to note that RBD residues from Glu484 to Tyr505, Arg403 to Tyr421, and Tyr449 to Ala475 are involved in the docking of the APD peptides, as was previously reported by Othman and co-workers [6]. Figure 2 shows the mapping of these amino acid residues on the active region of RBD, suggesting that APD peptides are docking on five principal regions of the RBD. The center region of the RBD (Figure S4b and Figure S4c, Supporting Information File 1) is of particular interest because it binds directly to the ACE2 cellular receptor. After this analysis, the number of hydrogen bonds and hydrophobic interactions involved in the APD–RBD complexes was determined by the LigPlot+ software (Table 1) [35]. The numbers of hydrogen bonds per residue and hydrophobic interactions go from 0.25 to 0.95 and from 17 to 31, respectively. The binding affinity values are higher for those APD peptides bound to the RBD with a high number of hydrogen bonds and hydrophobic interactions [47]. Table 1 shows that twelve APD and three lysozyme peptides surpass the binding energy calculated for the ACE2 peptide to the RBD (−4.6 kcal/mol), indicating that these peptides bind to the RBD active region more strongly than the ACE2 peptide.

To validate the docking results for the APD peptides, the crystallized ACE2 peptide was tested using the same ADV parame-

Table 1: Potential peptide candidates against SARS-CoV-2 obtained by molecular docking. The table shows the physical and biochemical properties of the potential peptides.

Peptide	PDB/UNIPROT ID	Residues	Number of amino acids	H bonds/residue	Affinity (kcal/mol)
alpha basrubrin	P83186	1–20	20	0.95	−5.2
human beta defensin 3	1KJ6	27–44	19	0.95	−5.0
sesquin	P84868	1–10	10	0.80	−5.6
indolicidin	1G89	1–13	13	0.77	−8.0
GF-17	2L5M	1–17	17	0.76	−5.3
cyanovirin-N (70–80)	2EZM	70–80	10	0.73	−5.3
protegrin 5	2NC7	1–18	18	0.72	−7.2
MVL (94–110)	1ZHS	94–110	17	0.71	−5.0
temporin B	6GIL	1–13	13	0.69	−5.6
dermaseptin-S4	2DD6	1–13	13	0.69	−5.5
MVL (74–87)	1ZHS	74–87	14	0.64	−5.9
MVL (16–34)	1ZHS	16–34	19	0.63	−5.8
ACE2	6VYB	21–44	24	0.63	−4.6
lysozyme (1–20)	1REX	20	20	0.35	−4.9
lysozyme (61–80)	1REX	20	20	0.60	−5.7
lysozyme (111–130)	1REX	20	20	0.25	−5.2

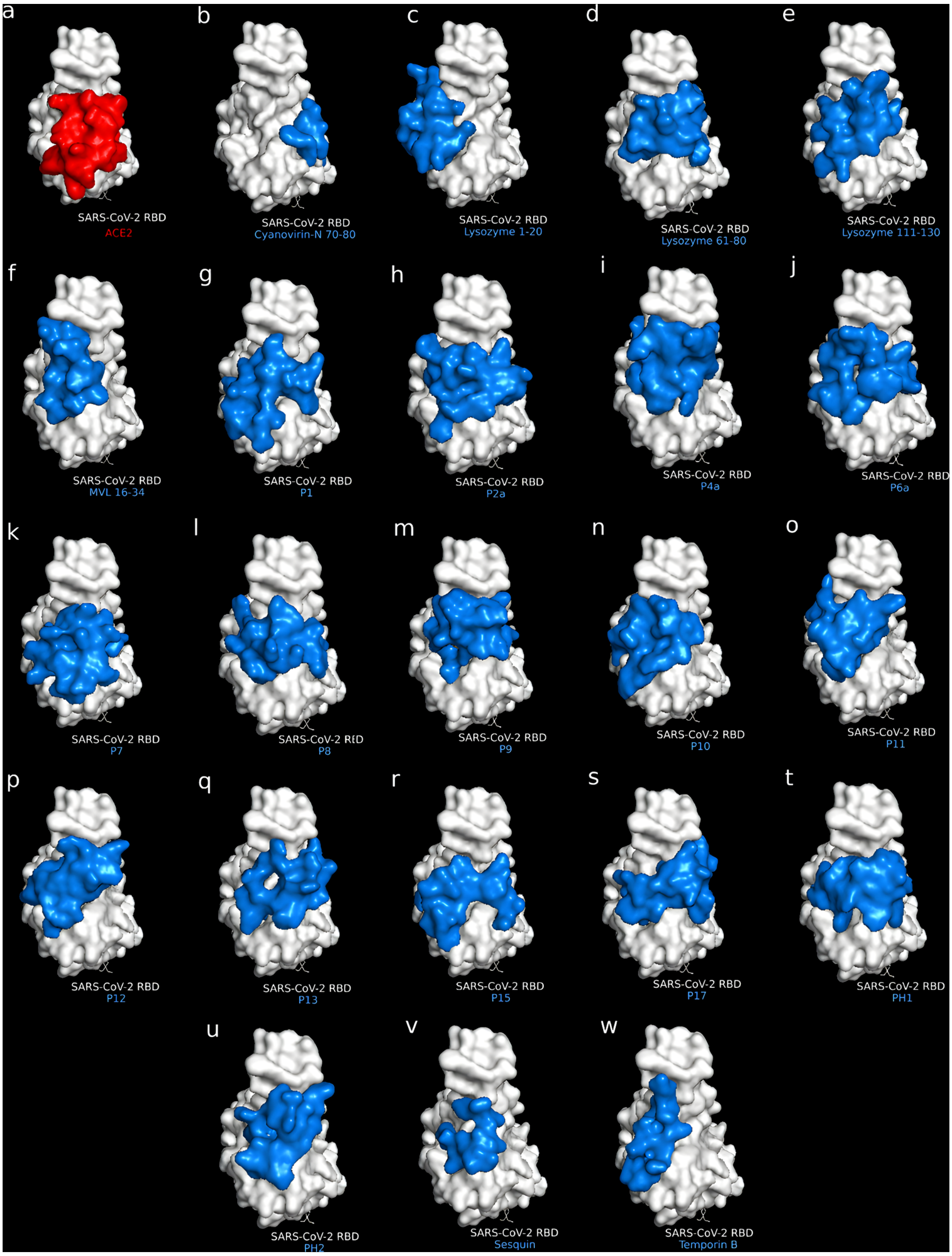

Figure 2: Peptide candidates (blue) docked to the SARS-CoV-2 RBD (white). (a) ACE2 control peptide (red), (b) cyanovirin-N (70–80), (c) lysozyme (1–20), (d) lysozyme (61–80), (e) lysozyme (111–130), (f) MVL (16–34), (g) P1, (h) P2a, (i) P4a, (j) P6a, (k) P7, (l) P8, (m) P9, (n) P10, (o) P11, (p) P12, (q) P13, (r) P15, (s) P17, (t) PH1, (u) PH2, (v) sesquin, and (w) temporin B.

ters. The peptide bound on the RBD active region, and superimposing the docked complex onto the crystallized complex showed a low RMSD of 0.31 Å (Figure 3). Generally, an RMSD value of 2 Å or lower is considered a good docking, thus confirming the validity of the protocol [48].

Proposing new peptides based on hydrogen-bond formation

Since hydrogen bonds play an important role in the formation and stabilization of the protein–ligand complex, novel peptides were designed considering the most common amino acid

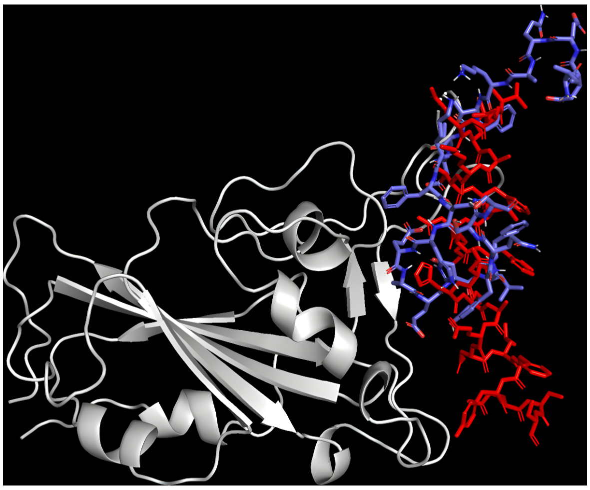

Figure 3: Superimposition of docked ACE2 (blue) onto the crystallized complex (red) in the active site using PyMOL (RMSD = 0.31 Å).

residues from the 13 APD and lysozyme peptides that bind to the RBD active region through hydrogen bonds [35]. This task is easy to develop in comparison to the typical procedures used in standard peptide design, in which complex algorithms are used to generate a large peptide library [49,50]. In contrast, designing peptides based on hydrogen bond interactions allows one to generate peptides that target specific sites while reducing computation time [51]. Figure 4 shows the most frequent amino acid residues binding to the RBD active region, together with the implicated amino acid residues in the formation of the RBD–ACE2 complex (Figure 4a) [34]. 41 theoretical peptides (denominated HB peptides) composed of 20 amino acid residues were designed, and from these, 23 HB peptides docked to the RBD.

In agreement with ADV analysis, the HB peptides docked laterally (left and right) and horizontally to the center region of the RBD. Furthermore, the number of hydrogen bonds formed between the amino acid residues from HB peptides and RBD as well as the binding energy between HB peptides and RBD were increased. These results support the success of the chosen strategy for designing peptides based on the hydrogen bond interactions in an easy way.

Immunogenicity

The immune system can recognize external molecules introduced into our body, which, in many cases, leads to the production of antibodies [12]. Specifically, during a viral infection,

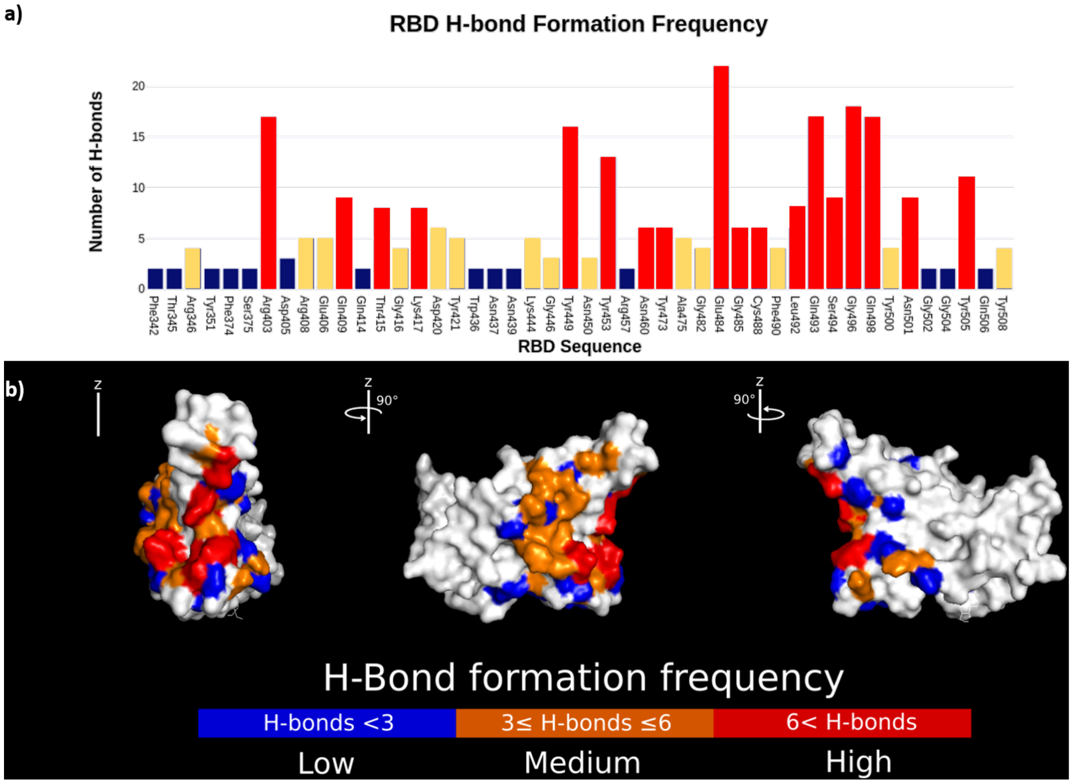

Figure 4: Mapping of the number of hydrogen bonds formed between APD and lysozyme peptide candidates to the SARS-CoV-2 RBD. (a) The graph depicts the residue location and frequency of hydrogen bonds formed with the SARS-CoV-2 RBD. (b) The location of the hydrogen bonds concentrates on the active region of SARS-CoV-2 RBD. The color coding differentiates the frequency of hydrogen bonds formed on each residue with blue being the lowest and red being the highest formation frequency.

viral antigens are presented by MHC I to be recognized by T cells, which, in turn, promote cytosine release and the cytotoxic activity of CD8+ T cells [12,52,53]. Due to the efficiency of this system, many biological therapeutics (proteins, peptides, nucleic acids, and even drugs) do not reach their target since they are eliminated by cells of the immune system, which limits their activity. Therefore, proposed peptides with antiviral activity must be evaluated from the immunological point of view. In this context, an immunogenicity prediction of the proposed peptides (APD, lysozyme, and HB peptides) was developed by the binding of the peptide candidates to MHC I. The final peptide selection was carried out using TepiTool to determine which peptides are capable of evading the immune system, in particular MHC I molecules. The TepiTool platform was used to select peptides of MHC I that do not bind to alleles with an IC_{50} value below 500 nM since, according to Calis and and Adhikari, binding to alleles with an IC_{50} above 500 nM would present low to zero immunogenic response [37,38]. From 55 peptides tested, including APD, lysozyme, and HB peptides, only 22 peptides (Table S4, Supporting Information File 1) had a low probability of being recognized by MHC I. This suggests that these peptides can be used to neutralize the SARS-CoV-2 virus without activating the immune system. These peptides, denominated here “OAPs”, optimally attached to the RBD, and their interaction with the RDB is discussed in the following section.

Physicochemical parameters and peptide–RBD interaction

Solubility, net charge, and size are important physical parameters that need to be considered in the design of novel drugs since these play a role in the distribution in the human body and in targeting specific cells, bacteria, viruses, or proteins. Therefore, the physicochemical parameters of the peptides and the peptide conformation after binding to RBD were obtained by using WinHydroPro software. The results are given in Table 2. The peptide net charge, isoelectric point, and water solubility for peptides were determined by the on-line software INNOVAGEN’s peptide calculator (PEPCALC). Almost all OAPs are soluble in aqueous media, independently on their isoelectric point, due to the high ratio between hydrophilic and hydrophobic amino acid residues, except the peptides temporin B and

Table 2: Summary of the physicochemical properties of the final peptide candidates.

Peptide	Residues	Number of amino acids	Affinity (kcal/mol)	H bonds/ residue	Water solubility	R_g (nm)	Net charge at pH 7	Isoelectric point	Molecular weight (kDa)
ACE2	21–44	24	−4.6	0.63	good	1.64	−3.9	4	2890.07
cyanovirin-N	70–80	10	−5.3	0.80	good	0.83	0.9	8.9	1252.40
lysozyme (1–20)	1–20	20	−4.9	0.35	good	0.98	1.9	9.5	2385.81
lysozyme (61–80)	61–80	20	−5.7	0.60	good	1.07	2.9	8.1	2408.69
lysozyme (111–130)	111–130	20	−5.2	0.25	poor	0.83	1.0	9.9	2179.40
MVL (16–34)	16–34	19	−5.8	0.63	good	0.91	0.1	7.9	1938.11
P1	1–20	20	−6.3	0.65	good	0.90	1.0	10	2394.64
P2a	1–20	20	−4.9	0.50	good	0.92	0.1	5.2	2463.58
P4a	1–20	20	−4.8	0.55	good	0.89	0.1	5.2	2463.58
P6a	1–20	20	−4.6	0.55	good	0.86	0.1	5.2	2463.58
P7	1–20	20	−5.0	0.45	good	0.89	0.1	9.5	2463.58
P8	1–20	20	−5.6	0.40	good	0.90	0.1	7.5	2463.58
P9	1–20	20	−5.2	0.50	good	0.87	0.1	7.5	2521.66
P10	1–20	20	−5.5	0.60	good	0.92	−0.9	7.5	2491.59
P11	1–20	20	−5.6	0.55	good	0.86	−0.9	7.5	2491.59
P12	1–20	20	−5.4	0.65	good	0.93	−0.9	7.5	2541.60
P13	1–20	20	−5.2	0.65	good	0.87	1.1	7.5	2532.69
P15	1–20	20	−4.9	0.55	good	0.87	0.1	7.5	2463.58
P17	1–20	20	−4.6	0.40	good	0.91	0.1	7.5	2463.58
PH1	1–20	20	−5.0	0.55	good	0.92	2.0	11.8	2379.51
PH2	1–20	20	−5.3	0.55	good	0.87	0	6.7	2338.41
sesquin	1–10	10	−5.6	0.80	good	0.70	−1.1	3.9	1157.25
temporin B	1–13	13	−5.6	0.69	poor	0.73	1	10.1	1392.77

lysozyme (61–80). The net charge calculated for the OAPs varies according to the number of negatively and positively charged amino acids present in the primary structure. The net charge values are in the range of −3.9 to 2.9 at pH 7. The OAPs were selected based on an absolute value of the electrical net charge smaller than 3.9 (|charge| ≤ 3.9, which is the net charge of ACE2), to avoid possible cytotoxic effects [54,55].

Given that, at physiological pH, the RBD active region is positively charged, it could be assumed that negatively charged peptides, such as sesquin and MVL (74–87) (Figure S3, panels 4a,b and 14a,b, Supporting Information File 1), would present a stronger binding to the RBD active region than those peptides with slightly positive charge or neutral charge (Figure S3, Supporting Information File 1) due to electrostatic repulsion [56]. However, as seen from the ADV results, cationic peptides, such as lysozyme (61–80) showed a higher binding affinity than the anionic peptides ACE2 and MVL (74–87). The higher binding affinity observed for positively charged peptides can be explained based on the distribution of the electrically charged patches located on the active surface of the RBD. Figure 1b shows the electrostatic surface potential of the RBD active region, in which negatively charged, neutral, and positively charged patches can be identified, depending on the amino acid residues. Therefore, it can be assumed that electrostatic repulsion forces are negligible. This suggests that the intermolecular interactions (hydrogen bonds and hydrophobic interactions) in the APD peptide–RBD complexes are favored. The secondary structure of the APDs changes and adopts a proper conformation to bind to the RBD protein.

An analysis of the secondary structure for free and docked OAPs was carried out using the PEP-FOLD 3.5 (RPBS Web) web server, while their surface area was analyzed using PyMol. Similar to previous results, the secondary structure of the OAPs changes from α-helices to random-coil conformations, when they docked to the RBD protein, as it is shown in Table 3 [57-59]. The secondary structure for free OAPs consists of α-helices and random coils at different fractions, except for P4a, P6a, temporin B, lysozyme (61–80), PH2, and sesquin, which adopt a fully random-coil conformation. Afterwards, the binding energy of the OAP–RBD complexes, as well as the contact area (A_c) with the RBD active region were determined using docking analysis. The secondary structure and net charge of the OAPs

Table 3: Secondary structure and contact area of peptides. The secondary structure is presented as the number of amino acids in each structure divided by the total number of amino acids of the peptide. A_0 represents the initial surface area, A_f corresponds to the final surface area, ΔA is the change in area (a positive value indicates an increase in area and a negative value indicates a decrease in peptide area), and A_c is the contact area of the peptide with the SARS-CoV-2 RBD.

OAP	α-Helix	Random coil	A_0 (Å^2)	A_f (Å^2)	ΔA (Å^2)	A_c (Å^2)
ACE2	0.25	0.75	3689.47	2544.86	−1144.61	929.92
lysozyme (111–130)	0.45	0.55	2316.07	2695.19	379.12	1113.77
MVL (16–34)	0.32	0.68	1955.31	1938.87	−16.44	449.73
P1	0.20	0.80	2146.66	2789.48	642.82	1092.27
P11	0.75	0.25	2107.56	2635.32	527.76	1078.03
P12	0.65	0.35	1961.34	2527.95	566.61	991.89
P4a	0.00	1.00	1900.02	2438.47	538.45	1019.92
P6a	0.00	1.00	2198.06	2484.03	285.97	962.49
temporin B	0.00	1.00	1444.79	1653.72	208.93	236.14
cyanovirin-N (70–80)	0.73	0.27	1456.50	1472.78	16.28	243.73
lysozyme (1–20)	0.55	0.45	2249.00	2326.36	77.36	907.99
lysozyme (61–80)	0.00	1.00	1737.46	2493.78	756.32	1021.43
P10	0.55	0.45	2104.89	2635.63	530.74	1031.17
P13	0.45	0.55	2071.74	2706.08	634.34	1046.71
P15	0.75	0.25	2064.25	2774.07	709.82	1139.50
P17	0.50	0.50	2035.18	2684.64	649.46	1053.52
P2a	0.55	0.45	2024.86	2416.36	391.50	940.54
P7	0.75	0.25	1963.84	2914.81	950.97	1113.68
P8	0.80	0.20	1935.11	2645.75	710.64	993.20
P9	0.75	0.25	2176.42	2592.66	416.24	983.47
PH1	0.15	0.85	2008.82	2483.21	474.39	1f007.82
PH2	0.00	1.00	2030.17	2509.95	479.78	987.57
sesquin	0.00	1.00	1212.56	1454.82	242.26	132.90

were plotted as functions of the binding energy (Figure 5) with the aim of understanding the relationship between these parameters. Figure 5 shows the secondary structure versus the binding energy of the OAP–RBD complexes (Figure 5a) and is divided into three regions. Region I shows the peptides that have binding energy values similar to the ACE2 binding energy (−4.6 kcal/mol), such as P9 (secondary structure composition 0.75 α-helix and 0.25 random coil) and P12 (fully random-coil conformation). In region II, several peptides present different conformations such as random coils (4), high α-helix-to-random-coil ratio (7), or high-random-coil-to-α-helix ratio (2) conformation. The binding energy in this second region is in the range of −4.8 to −5.6 kcal/mol. The OAPs included in region III are characterized by a high fraction of random-coil secondary structures with binding energies between −5.7 and −6.3 kcal/mol. Additionally, the final surface area (A_f) of peptides docked to the RBD increased, indicated by positive values of $\Delta A = A_\mathrm{f} - A_0$, where A_f and A_0 are the final and initial OAP surface area, respectively (Table 3). In contrast, ACE2 and MVL (16–34) show negative values of ΔA. The observed increase of A_f suggests that the OAPs have a large contact area (A_c) with the active surface area, blocking key amino acid residues involved in the association of RBD with ACE2 (Table 3 and Figure 5), as will be shown next. Figure 5b shows that the binding energy values vary independently of the net charge of the OAPs. This can be explained based on the electrostatic surface potential of the active region of the RBD (inset in Figure 5b), which can be divided into three characteristic regions: (i) The upper region is characterized by a negative potential (red ellipse). (ii) The middle region has neutral patches, slightly negative and positive patches (white ellipse); and (iii) the bottom region is characterized by a positive potential (blue ellipse). Recently, it has been reported that the residues Phe486, Tyr489 (located in the upper region), Gln493, Gly496 (located in the middle region), Thr500, and Asn501 (located in the bottom region), are involved in the association of RBD with the ACE2 protein [6,9]. Interestingly, OAPs were attached in different configurations around the active regions of the RBD (inset in Figure 4b), and those principally occupied the middle region of the active surface. These OAPs interact with residues Gln493, Gly496, Thr500, and Asn501, among others amino acidic residues located in the upper and bottom regions. Similar results have been reported by Debmalya and co-workers, who analyzed the potential of chimeric peptides to block the RBD using an in silico approach. They found that a peptide with 26 amino acids binds to the Thr500 and Asn501 residues of the RBD, while a peptide with 23 amino acids binds to the Tyr489 and Thr500 residues of the RBD, and a peptide with 20 amino acid binds to the Gln493 and Asn501 residues of the RBD. However, neither of these peptides was able to block the three regions of the RBD [8]. The results reported herein suggest that OAPs have a great potential as drug inhibitors of SAR-CoV2 and can block the entry of viruses to the cell host through the ACE2 cellular receptor.

Binding energy by protein binding energy prediction

ADV has been widely used to predict the alignment of small ligands within the binding cavity of a given protein and to evaluate the pose quality of the docked ligand in terms of binding energy. However, this computational tool gives comparably low binding energies of peptide–protein docking due to the molecular size, high flexibility, and complexing conformation of the peptide ligand, in addition to the simplification of the analysis of ADV (the electrostatic and solvation potentials are neglected, while van der Waals potential, the nondirectional hydrogen

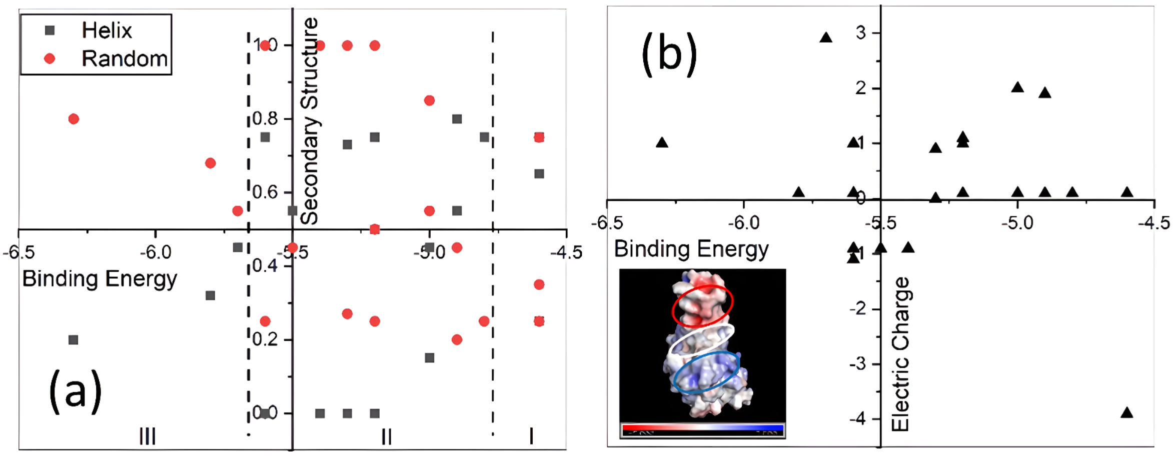

Figure 5: Plots of the peptide secondary structure and charge as functions of the binding energy. (a) Relationship between secondary structure and binding affinity of the peptides to SARS-CoV-2 RBD. (b) Relationship between charge and binding affinity of the peptides to SARS-CoV-2 RBD.

bond term, the hydrophobic term, and a conformational entropy penalty are considered) [20,21]. It can be observed that the binding energy values (Table 1 and Table 2) are significantly lower than the binding energies reported in similar works [6,60,61]. For instance, the experimental and theoretical values of the binding energy reported for ACE2–RBD is around −12.0 kcal/mol, which is higher than the binding energy of −4.6 kcal/mol given here [61]. Therefore, the PRODIGY web server was used to estimate the binding energy for peptide–RBD docking, since it has been demonstrated that PRODIGY can produce results comparable with those obtained experimentally and most standard in silico analyses [38-40,60]. To validate the PRODIGY results, the binding energy of the complex ACE2–RBD (6VYB) (Figure 6), acquired from the RCSB Protein Data Bank (https://www.rcsb.org/), was first tested. This value is similar to the binding energy previously reported for the crystalline complex [61].

Figure 6: Crystallized ACE2 peptide (I21 to S44) bound to the SARS-CoV-2 RBD.

The binding energy values for the OAP–RBD complexes vary from −9.2 kcal/mol to −13.3 kcal/mol (Figure 7). These results are similar to previous reports in which short peptides were docked to RBD [14]. However, the binding energy reported in the present research contrasts with several studies that reported higher binding energies between the theoretical peptides and RBD [62,63], probably due to the software used in the molecular docking calculations. However, these reports did not show the binding energy of the ACE2–RBD complex. 15 OAPs surpass the energy value registered for ACE2–RBD. It is important to recall that OAPs are attached to critical RBD amino acid residues (Phe486, Tyr489, Gln493, Gly496, Thr500, and Asn501) involved in the entry of SARS-CoV-2 into the host cell. These results indicate a possible application of these peptides in the prophylaxis of COVID-19 disease caused by different variants of SARS-CoV-2. In this regard, OAPs were also docked against two variants of RBD: a theoretical multimutation variant (RBDm), which encompasses the mutations found in Alpha, Beta, and Gamma SARS-CoV-2 variants, and the Delta variant (RBDδ).

The binding affinities of the OAPs with each RBD variant are shown in Figure 7. The binding affinities of the OAPs vary ac-

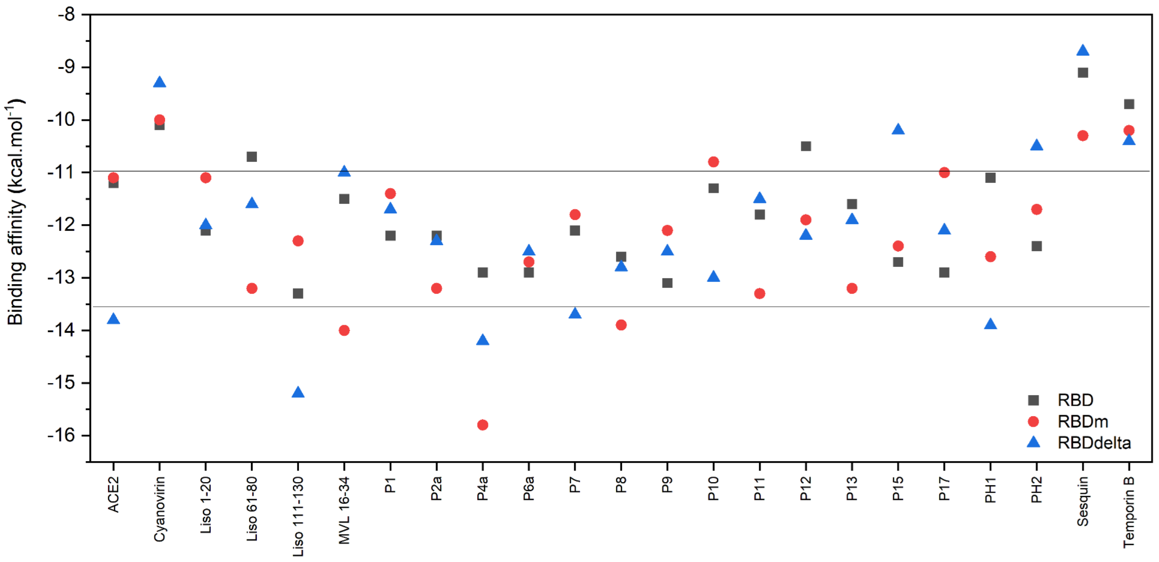

Figure 7: Binding affinity calculated using the PRODIGY server from ADV results. The binding affinities were calculated for different RBD variants: Wuhan strain RBD (black), RBDm (red), RBDδ (blue).

cording to the RBD variant. The binding affinity of sixteen OAPs is shown to be higher in comparison to ACE2 for RBDm, highlighting MVL (16–34), P2a, and P8 for their higher binding affinity to the RBDm. Four OAPs (lysozyme (111–130), P4a, P7, and PH1) showed a higher binding affinity to RBDδ than the ACE2 peptide, where the binding affinity of lysozyme (111–130) stands out compared to that of other OAPs. It important to note that lysozyme (111–130) and P4a consistently present a stronger binding affinity for all RBD variants than ACE2, making them the best candidates against all RBD variants.

Last, the radius of gyration of these peptides was determined to be in the range of 43% to 65% of the size of the ACE2 peptide. Therefore, the diffusion of these peptides is faster. These results show the potential of the selected peptides to inhibit SARS-CoV-2, considering that their smaller size and faster diffusion will allow them to find the virus faster and bind to the RBD, thus blocking its interaction with the ACE2 receptor.

Conclusion

Molecular docking was used to analyze the interaction of 104 peptides from the APD, recognized by their antimicrobial and antiviral activity, with the RBD of SARS-CoV-2. This analysis allowed for the selection (16 peptides) and faster design of peptides (41 peptides) based on the peptide binding site on the RBD, the number of hydrogen bonds, and the binding affinity. The peptide candidates have a nearly neutral charge at physiological pH and good solubility, which can benefit the diffusion of the molecules, allowing them to reach and efficiently bind to the RBD active region. After the immunogenicity analysis with MHC I, 22 peptides (15 theoretical peptides) were chosen because of their potential capability to inhibit the RBD of SARS-CoV-2. Since they interact with F486, Y489, Q493, G496, T500, and N501 residues present on the RBD, they play an important role in the infection mechanism of SARS-CoV-2. Also, these peptides showed a higher binding affinity for different RBD variants (Delta variant and a theoretical multimutation variant obtained from the combination of Alpha, Beta and Gamma SARS-CoV-2 variants), suggesting their potential use as therapeutic agents against COVID-19. Despite the fact that ADV analysis is a powerful tool, additional experimental and in silico assays are required to determine the preference of OAP peptides for binding to the RBD protein, instead of binding to other viral proteins or common proteins (salivary and plasmatic proteins) found in physiological fluids. The procedure described here for the design of antiviral molecules can be extended against other viruses, both in human and veterinary medicine.

Supporting Information

Supporting Information features previously reported antiviral activities of APD peptides (Table S1); molecular docking scores of the 104 peptides (Table S2); Ligplot+ diagrams of the hydrogen bonds and hydrophobic interactions between ACE2 and the SARS-CoV-2 RBD (Figure S1); distribution of electrostatic potential on the surface of APD peptide candidates docked to the SARS-CoV-2 RBD (Figure S2); secondary structure, docking, and distribution of electrostatic charges of aligned peptides (Figure S3); physicochemical properties, hydrogen bonds, and hydrophobic interactions of the peptide candidates against SARS-CoV-2 (Table S3); principal docking regions of screened APD and lysozyme peptides against the SARS-CoV-2 RBD (Figure S4); immunogenicity analysis of peptides against human MHC I to determine the number of alleles with IC_{50} < 50 nM and IC_{50} < 500 nM (Table S4); and the contact areas of peptides docked to SARS-CoV-2.

Supporting Information File 1

Additional experimental data.
[https://www.beilstein-journals.org/bjnano/content/supplementary/2190-4286-13-62-S1.pdf]

Acknowledgements

The authors thanks William Johnson Dawson for the English grammar review and edition.

Funding

RDCN acknowledges PASPA-DGAPA-UNAM for sabbatical support.

ORCID® iDs

Kendra Ramirez-Acosta - https://orcid.org/0000-0003-2228-2435
Josue Juarez - https://orcid.org/0000-0003-1801-0349
Ruben D. Cadena-Nava - https://orcid.org/0000-0001-8428-6701

References

1. Coronavirus Disease (COVID-19) Situation Reports. https://www.who.int/emergencies/diseases/novel-coronavirus-2019/situation-reports (accessed June 15, 2022).
2. Tortorici, M. A.; Veesler, D. *Adv. Virus Res.* **2019,** *105,* 93–116. doi:10.1016/bs.aivir.2019.08.002
3. Walls, A. C.; Park, Y.-J.; Tortorici, M. A.; Wall, A.; McGuire, A. T.; Veesler, D. *Cell* **2020,** *181,* 281–292.e6. doi:10.1016/j.cell.2020.02.058
4. He, Y.; Zhou, Y.; Liu, S.; Kou, Z.; Li, W.; Farzan, M.; Jiang, S. *Biochem. Biophys. Res. Commun.* **2004,** *324,* 773–781. doi:10.1016/j.bbrc.2004.09.106

5. Shang, J.; Ye, G.; Shi, K.; Wan, Y.; Luo, C.; Aihara, H.; Geng, Q.; Auerbach, A.; Li, F. *Nature* **2020,** *581,* 221–224. doi:10.1038/s41586-020-2179-y
6. Othman, H.; Bouslama, Z.; Brandenburg, J.-T.; da Rocha, J.; Hamdi, Y.; Ghedira, K.; Srairi-Abid, N.; Hazelhurst, S. *Biochem. Biophys. Res. Commun.* **2020,** *527,* 702–708. doi:10.1016/j.bbrc.2020.05.028
7. Morgan, D. C.; Morris, C.; Mahindra, A.; Blair, C. M.; Tejeda, G.; Herbert, I.; Turnbull, M. L.; Lieber, G.; Willett, B. J.; Logan, N.; Smith, B.; Tobin, A. B.; Bhella, D.; Baillie, G.; Jamieson, A. G. *Pept. Sci.* **2021,** *113,* e24217. doi:10.1002/pep2.24217
8. Barh, D.; Tiwari, S.; Silva Andrade, B.; Giovanetti, M.; Almeida Costa, E.; Kumavath, R.; Ghosh, P.; Góes-Neto, A.; Carlos Junior Alcantara, L.; Azevedo, V. *F1000Research* **2020,** *9,* 576. doi:10.12688/f1000research.24074.1
9. Berkhout, B.; van Wamel, J. L. B.; Beljaars, L.; Meijer, D. K. F.; Visser, S.; Floris, R. *Antiviral Res.* **2002,** *55,* 341–355. doi:10.1016/s0166-3542(02)00069-4
10. Cole, A. M. *Expert Opin. Ther. Targets* **2003,** *7,* 329–341. doi:10.1517/14728222.7.3.329
11. Ng, T. B.; Cheung, R. C. F.; Wong, J. H.; Wang, Y.; Ip, D. T. M.; Wan, D. C. C.; Xia, J. *Appl. Microbiol. Biotechnol.* **2015,** *99,* 6997–7008. doi:10.1007/s00253-015-6818-4
12. Shah, V. K.; Firmal, P.; Alam, A.; Ganguly, D.; Chattopadhyay, S. *Front. Immunol.* **2020,** *11,* 1949. doi:10.3389/fimmu.2020.01949
13. Doneva, N.; Doytchinova, I.; Dimitrov, I. *Symmetry* **2021,** *13,* 388. doi:10.3390/sym13030388
14. Basit, A.; Karim, A. M.; Asif, M.; Ali, T.; Lee, J. H.; Jeon, J. H.; Rehman, S. u.; Lee, S. H. *Front. Pharmacol.* **2021,** *12,* 731828. doi:10.3389/fphar.2021.731828
15. Han, Y.; Král, P. *ACS Nano* **2020,** *14,* 5143–5147. doi:10.1021/acsnano.0c02857
16. Roche, D. B.; McGuffin, L. J. In Silico Identification and Characterization of Protein-Ligand Binding Sites. In *Computational Design of Ligand Binding Proteins;* Stoddard, B. L., Ed.; Springer: New York, NY, USA, 2016; pp 1–21. doi:10.1007/978-1-4939-3569-7_1
17. Pagadala, N. S.; Syed, K.; Tuszynski, J. *Biophys. Rev.* **2017,** *9,* 91–102. doi:10.1007/s12551-016-0247-1
18. Hadley, E. B.; Hancock, R. E. W. *Curr. Top. Med. Chem.* **2010,** *10,* 1872–1881. doi:10.2174/156802610793176648
19. Morris, G. M.; Lim-Wilby, M. Molecular Docking. In *Molecular Modeling of Proteins;* Kukol, A., Ed.; Humana Press: Totowa, NJ, USA, 2008; pp 365–382. doi:10.1007/978-1-59745-177-2_19
20. Pantsar, T.; Poso, A. *Molecules* **2018,** *23,* 1899. doi:10.3390/molecules23081899
21. Eberhardt, J.; Santos-Martins, D.; Tillack, A. F.; Forli, S. *J. Chem. Inf. Model.* **2021,** *61,* 3891–3898. doi:10.1021/acs.jcim.1c00203
22. Wang, G.; Li, X.; Wang, Z. *Nucleic Acids Res.* **2016,** *44,* D1087–D1093. doi:10.1093/nar/gkv1278
23. Wang, G.; Li, X.; Wang, Z. *Nucleic Acids Res.* **2009,** *37* (Suppl. 1), D933–D937. doi:10.1093/nar/gkn823
24. Wang, Z. *Nucleic Acids Res.* **2004,** *32,* 590D–592. doi:10.1093/nar/gkh025
25. Qiao, B.; Olvera de la Cruz, M. *ACS Nano* **2020,** *14,* 10616–10623. doi:10.1021/acsnano.0c04798
26. Wiesner, J.; Vilcinskas, A. *Virulence* **2010,** *1,* 440–464. doi:10.4161/viru.1.5.12983
27. Mandal, S. M.; Silva, O. N.; Franco, O. L. *Drug Discovery Today* **2014,** *19,* 1045–1050. doi:10.1016/j.drudis.2014.05.019
28. Roy, A.; Kucukural, A.; Zhang, Y. *Nat. Protoc.* **2010,** *5,* 725–738. doi:10.1038/nprot.2010.5
29. Yang, J.; Zhang, Y. *Nucleic Acids Res.* **2015,** *43,* W174–W181. doi:10.1093/nar/gkv342
30. Lamiable, A.; Thévenet, P.; Rey, J.; Vavrusa, M.; Derreumaux, P.; Tufféry, P. *Nucleic Acids Res.* **2016,** *44,* W449–W454. doi:10.1093/nar/gkw329
31. Shen, Y.; Maupetit, J.; Derreumaux, P.; Tufféry, P. *J. Chem. Theory Comput.* **2014,** *10,* 4745–4758. doi:10.1021/ct500592m
32. Thévenet, P.; Shen, Y.; Maupetit, J.; Guyon, F.; Derreumaux, P.; Tufféry, P. *Nucleic Acids Res.* **2012,** *40,* W288–W293. doi:10.1093/nar/gks419
33. *The PyMOL Molecular Graphics System,* version 2.0; Schrödinger, LLC.
34. Wallace, A. C.; Laskowski, R. A.; Thornton, J. M. *Protein Eng., Des. Sel.* **1995,** *8,* 127–134. doi:10.1093/protein/8.2.127
35. Ortega, A.; Amorós, D.; García de la Torre, J. *Biophys. J.* **2011,** *101,* 892–898. doi:10.1016/j.bpj.2011.06.046
36. Paul, S.; Sidney, J.; Sette, A.; Peters, B. *Curr. Protoc. Immunol.* **2016,** *114,* 18.19.1–18.19.24. doi:10.1002/cpim.12
37. Calis, J. J. A.; Maybeno, M.; Greenbaum, J. A.; Weiskopf, D.; De Silva, A. D.; Sette, A.; Keşmir, C.; Peters, B. *PLoS Comput. Biol.* **2013,** *9,* e1003266. doi:10.1371/journal.pcbi.1003266
38. Adhikari, U. K.; Tayebi, M.; Rahman, M. M. *J. Immunol. Res.* **2018,** 6718083. doi:10.1155/2018/6718083
39. Xue, L. C.; Rodrigues, J. P.; Kastritis, P. L.; Bonvin, A. M.; Vangone, A. *Bioinformatics* **2016,** *32,* 3676–3678. doi:10.1093/bioinformatics/btw514
40. Vangone, A.; Bonvin, A. M. *eLife* **2015,** *4,* e07454. doi:10.7554/elife.07454
41. Honorato, R. V.; Koukos, P. I.; Jiménez-García, B.; Tsaregorodtsev, A.; Verlato, M.; Giachetti, A.; Rosato, A.; Bonvin, A. M. J. J. *Front. Mol. Biosci.* **2021,** *8,* 729513. doi:10.3389/fmolb.2021.729513
42. Tesauro, D.; Accardo, A.; Diaferia, C.; Milano, V.; Guillon, J.; Ronga, L.; Rossi, F. *Molecules* **2019,** *24,* 351. doi:10.3390/molecules24020351
43. Leal, J.; Liu, X.; Peng, X.; Mohanty, R. P.; Arasappan, D.; Wylie, D.; Schwartz, S. H.; Fullmer, J. J.; McWilliams, B. C.; Smyth, H. D. C.; Ghosh, D. *bioRxiv* **2019,** 659540. doi:10.1101/659540
44. Fei, L.; Ren, L.; Zaro, J. L.; Shen, W.-C. *J. Drug Targeting* **2011,** *19,* 675–680. doi:10.3109/1061186x.2010.531729
45. Arai, S.; Miyazaki, T. *Semin. Immunopathol.* **2018,** *40,* 567–575. doi:10.1007/s00281-018-0717-6
46. McNeil, P.; Hohman, T.; Muscatine, L. *J. Cell Sci.* **1981,** *52,* 243–269. doi:10.1242/jcs.52.1.243
47. Chen, D.; Oezguen, N.; Urvil, P.; Ferguson, C.; Dann, S. M.; Savidge, T. C. *Sci. Adv.* **2016,** *2,* e1501240. doi:10.1126/sciadv.1501240
48. C, S.; S., D. K.; Ragunathan, V.; Tiwari, P.; A., S.; P, B. D. *J. Biomol. Struct. Dyn.* **2022,** *40,* 585–611. doi:10.1080/07391102.2020.1815584
49. Kalafatovic, D.; Mauša, G.; Todorovski, T.; Giralt, E. *J. Cheminf.* **2019,** *11,* 25. doi:10.1186/s13321-019-0347-6
50. Bozovičar, K.; Bratkovič, T. *Int. J. Mol. Sci.* **2020,** *21,* 215. doi:10.3390/ijms21010215
51. Lesitha Jeeva Kumari, J.; Jesu Jaya Sudan, R.; Sudandiradoss, C. *PLoS One* **2017,** *12,* e0183041. doi:10.1371/journal.pone.0183041

52. Qin, C.; Zhou, L.; Hu, Z.; Zhang, S.; Yang, S.; Tao, Y.; Xie, C.; Ma, K.; Shang, K.; Wang, W.; Tian, D.-S. *Clin. Infect. Dis.* **2020,** *71,* 762–768. doi:10.1093/cid/ciaa248
53. Chiappelli, F.; Khakshooy, A.; Greenberg, G. *Bioinformation* **2020,** *16,* 219–222. doi:10.6026/97320630016219
54. Greco, I.; Molchanova, N.; Holmedal, E.; Jenssen, H.; Hummel, B. D.; Watts, J. L.; Håkansson, J.; Hansen, P. R.; Svenson, J. *Sci. Rep.* **2020,** *10,* 13206. doi:10.1038/s41598-020-69995-9
55. Laverty, G.; Gilmore, B. *Microbiol. Infect. Dis.* **2014,** *2,* 1–8. doi:10.15226/sojmid.2013.00112
56. Savjani, K. T.; Gajjar, A. K.; Savjani, J. K. *Int. Scholarly Res. Not.* **2012,** 195727. doi:10.5402/2012/195727
57. Ciemny, M.; Kurcinski, M.; Kamel, K.; Kolinski, A.; Alam, N.; Schueler-Furman, O.; Kmiecik, S. *Drug Discovery Today* **2018,** *23,* 1530–1537. doi:10.1016/j.drudis.2018.05.006
58. Sacquin-Mora, S.; Prévost, C. *Structure* **2015,** *23,* 1373–1374. doi:10.1016/j.str.2015.07.004
59. Verschueren, E.; Vanhee, P.; Rousseau, F.; Schymkowitz, J.; Serrano, L. *Structure* **2013,** *21,* 789–797. doi:10.1016/j.str.2013.02.023
60. Jawad, B.; Adhikari, P.; Podgornik, R.; Ching, W.-Y. *J. Chem. Inf. Model.* **2021,** *61,* 4425–4441. doi:10.1021/acs.jcim.1c00560
61. Buratto, D.; Saxena, A.; Ji, Q.; Yang, G.; Pantano, S.; Zonta, F. *Front. Immunol.* **2021,** *12,* 730099. doi:10.3389/fimmu.2021.730099
62. Stoddard, S. V.; Wallace, F. E.; Stoddard, S. D.; Cheng, Q.; Acosta, D.; Barzani, S.; Bobay, M.; Briant, J.; Cisneros, C.; Feinstein, S.; Glasper, K.; Hussain, M.; Lidoski, A.; Lingareddy, P.; Lovett, G.; Matherne, L.; McIntosh, J.; Moosani, N.; Nagge, L.; Nyamkondiwa, K.; Pratt, I.; Root, E.; Rutledge, M. R.; Sawyer, M.; Singh, Y.; Smith, K.; Tanveer, U.; Vaghela, S. *Biophysica* **2021,** *1,* 311–327. doi:10.3390/biophysica1030023
63. Baig, M. S.; Alagumuthu, M.; Rajpoot, S.; Saqib, U. *Drugs R&D* **2020,** *20,* 161–169. doi:10.1007/s40268-020-00312-5

License and Terms

The definitive version of this article is the electronic one which can be found at:
https://doi.org/10.3762/bjnano.13.62

BEILSTEIN JOURNAL OF NANOTECHNOLOGY

In search of cytotoxic selectivity on cancer cells with biogenically synthesized Ag/AgCl nanoparticles

Mitzi J. Ramírez-Hernández[1], Mario Valera-Zaragoza*[2], Omar Viñas-Bravo[2], Ariana A. Huerta-Heredia[3], Miguel A. Peña-Rico[4], Erick A. Juarez-Arellano[2], David Paniagua-Vega[5], Eduardo Ramírez-Vargas[6] and Saúl Sánchez-Valdes[6]

Full Research Paper

Open Access

Address:
[1]División de Estudios de Posgrado, Maestría en Ciencias Químicas, Universidad del Papaloapan, Tuxtepec Oaxaca 68301, México, [2]Centro de Investigaciones Científicas, Instituto de Química Aplicada, Universidad del Papaloapan, Tuxtepec Oaxaca, 68301, México, [3]CONACyT-UNPA, Centro de Investigaciones Científicas, Instituto de Biotecnología, Universidad del Papaloapan, Tuxtepec Oaxaca, 68301, México, [4]Centro de Investigaciones Científicas, Instituto de Biotecnología, Universidad del Papaloapan, Tuxtepec Oaxaca, 68301, México, [5]CONACyT-UANL, Departamento de Química Analítica, Facultad de Medicina, Universidad Autónoma de Nuevo León, Nuevo León, 64460, México and [6]Centro de Investigación en Química Aplicada, Saltillo Coahuila, 25294, México

Email:
Mario Valera-Zaragoza* - mvalera@unpa.edu.mx

* Corresponding author

Keywords:
cancer cells; cytotoxic behavior; green synthesis; pineapple extract; silver chloride nanoparticles; silver nanoparticles; structural characterization

Beilstein J. Nanotechnol. **2022,** *13,* 1505–1519.
https://doi.org/10.3762/bjnano.13.124

Received: 26 August 2022
Accepted: 25 November 2022
Published: 13 December 2022

This article is part of the thematic issue "New trends in nano-biotechnology".

Guest Editor: P.-L. Show

Abstract

Green synthesis may be a useful approach to achieve selective cytotoxicity of silver nanoparticles on cancer cells and healthy cells. In this study, the concomitant biosynthesis of silver (Ag)/silver chloride (AgCl) nanoparticles from pineapple peel extracts and their behavior on the breast cancer cell line MCF-7 is shown. Bioreactions were monitored at different temperatures. Fourier-transform infrared spectroscopy (FTIR), ultraviolet–visible spectroscopy (UV–vis), thermogravimetric analysis (TGA), X-ray diffraction (XRD), energy-dispersive X-ray spectroscopy (EDX), and transmission electron microscopy (TEM) techniques were used to characterize nanoparticle development. The breast cancer cell line MCF-7 was used as a test model to study the cytotoxic behavior of Ag/AgCl nanoparticles and, as a counterpart, the nanoparticles were also tested on mononuclear cells. Ag/AgCl nanoparticles with spherical and triangular morphology were obtained. The size of the nanoparticles (10–70 nm) and the size distribution depended on the reaction temperature. A dose close to 20 μg/mL of Ag/AgCl nanoparticles considerably decreased the cell viability of the MCF-7 line. The best cytotoxicity effects on cancer cells were obtained with nanoparticles at 60 and 80 °C where cell viability was reduced up to 80% at a concentration of 50 μg/mL. A significant preference was observed in the cytotoxic effect of Ag/AgCl nanoparticles against cancer cells in comparison to monocytes.

Introduction

The study of metallic nanoparticle synthesis by green methods is gaining importance, especially in cases where plant extracts are used to synthesize nanoparticles. The nanoparticles can be produced in a simple, inexpensive, and scalable way, with low reaction time and in aqueous media. Since no toxic by-products are generated, these methods are eco-friendly [1]. Silver nanoparticles (AgNPs) are commonly synthesized by green methods and, in some cases, are combined with other metals [2]. AgNPs have potential uses in biomedicine. Several authors have reported the ability of AgNPs to act as antibacterial [3,4] or as cytotoxic agents in certain cancer cell lines [5,6]. This type of application has attracted a lot of attention, given that cancer is a pathology with high incidence rates worldwide. In particular, breast cancer is highly aggressive and can metastasize, spreading to other organs through lymphatic and blood systems [7,8].

Several plant extract metabolites are known to have the ability to reduce the Ag^+ ion of the $AgNO_3$ salt to Ag^0. In this way, silver nuclei are generated and join to form nanoparticles, which are stabilized (via capping) by the same metabolites that are involved in the oxidation–reduction process [9]. Various plant parts have been used to generate AgNPs. Amongst these parts, agricultural residues, such as fruit peels, have the potential to be used for the development of nanoparticles [10-13].

Pineapple peel has also been valued as a good source of silver salt-reducing compounds. Pineapple peel extracts have been reported to contain polyphenols such as gallic acid, catechin, epicatechin, and ferulic acid [14]. These metabolites may be potential reducing agents for the formation of AgNPs. Until now, some studies have been reported on the use of pineapple peel for the generation of AgNPs [15-18]. For example, Agnihotri et al. [15] reported photocatalytic and antibacterial abilities of AgNPs synthesized from pineapple peel. They demonstrated the formation of spherical AgNPs with an average size of 14–20 nm by monitoring the pH values of the reaction and the concentration ratio between the precursor and the extract. Baran et al. [16] investigated the antibacterial and anticancer properties of AgNPs synthesized from pineapple peel. The authors reported a favorable antimicrobial activity at low concentrations of AgNPs. Das et al. [17] found that AgNPs synthesized in the same way have high antidiabetic potential and high cytotoxicity against $HepG_2$ cancer cells in a dose-dependent manner.

Based on the aforementioned findings, and considering the high content of phenolic compounds in the pineapple peel, which function as reducing agents of silver salt, the present study shows biosynthesis of Ag/AgCl nanoparticles using a pineapple peel extract. The study was conducted by monitoring biosynthesis temperature, considering that this variable has an important influence on the formation of nanoparticles. To verify the biological behavior of the obtained Ag/AgCl nanoparticles, their cytotoxic activity in the MCF-7 breast cancer cell line was investigated.

The novelty of this work is based on three major points. Firstly, by taking advantage of using pineapple waste, green synthesis methods were applied to obtain silver nanoparticles. In this way, an alternative use of agricultural residues was created, providing added value to fruit products. The second point is the obtaining of metallic Ag nanoparticles combined with AgCl, where AgNPs were formed by reducing compounds of the extract. Thus, the formation of AgCl was due to the availability of chlorine salts in pineapple peels. The third novelty shown in this work is that the cytotoxic activity of Ag/AgCl nanoparticles on breast cancer cells is dependent on the biosynthesis temperature. Consequently, its effect is different in cancer cells in comparison to healthy cells (monocytes). This result may give rise to a new system with cytotoxic selectivity. The goal of this study is to contribute to the generation of alternative materials for therapeutic applications, especially those that mitigate diseases.

Results and Discussion

Ag/AgCl biosynthesis

It has been reported in the literature that pineapple contains several phenolic compounds [14,19], which could act as reducing agents of silver salt. For this reason, the amount of phenolic compounds in the pineapple peel extract was quantified. The total phenolic content (TPC) in the pineapple peel extract was 24.66 ± 1.03 mg Catechin/g Ext, and the total flavonoid content (TFC) was 0.62 ± 0.21 mg Rutin/g Ext. The extract has a higher phenolic content in comparison to its flavonoid content. Li et al. [14] reported that some phenolic compounds, such as gallic acid, catechin, epicatechin, and ferulic acid are present in pineapple peel extracts. On the other hand, Steingass et al. [19] reported an extensive phytochemical study, by HPLC-DAD-ESI-MS^n and GM-MS, of pineapple phenolic compounds including those in pineapple peel.

Photographs of Ag/AgCl biosynthesis using pineapple peel are shown in Figure 1. Photographs were taken every 20 min up to 120 min for each reaction. The reaction temperatures are expressed as room temperature, 60, 80, and 100 °C, respectively. It can be clearly observed that as the reaction proceeds, a color change from yellow to reddish brown is produced, similar to that reported in the literature [20]. This behavior is the first evidence that the reaction between the biowaste and the silver

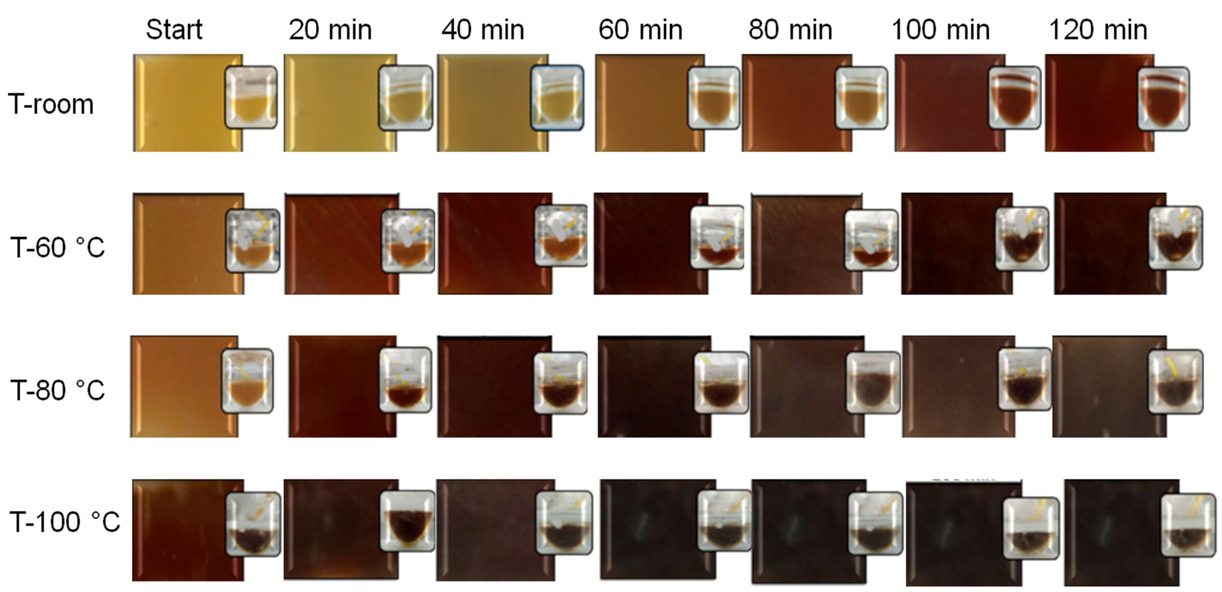

Figure 1: Photographs of Ag/AgCl nanoparticle biosynthesis from pineapple peel extracts. The photographs were taken at specified times and temperatures.

salt is taking place. In a previous report [21] these color changes were also observed during the formation of AgNPs from the *Stevia rebaudiana* extract. This behavior was attributed to the gradual formation of Ag nanoparticles, and the morphological changes that occur during biosynthesis. It is important to note that temperature has a considerable effect on biosynthesis. For example, based on its coloration, the reaction at room temperature after 120 min has a similar result as a reaction at a temperature of 60 °C or higher after only 20 min.

According to the literature, AgNPs synthesized from plant extracts can be directly produced at room temperature [22-24]. In this way, the ability of secondary metabolites of plant extracts to reduce precursor metal salts to particles with zero charge, and at the same time stabilize nanoparticles already formed, has been demonstrated. Despite this, the phenomenon of interaction of the chemical species of the extracts with the precursor salt could be enhanced depending on the temperature, since the kinetic and thermodynamic effects in the reaction system could be maximized [25]. Consequently, the formation of nanoparticles could be faster or more efficient in terms of size and shape of the nanoparticles.

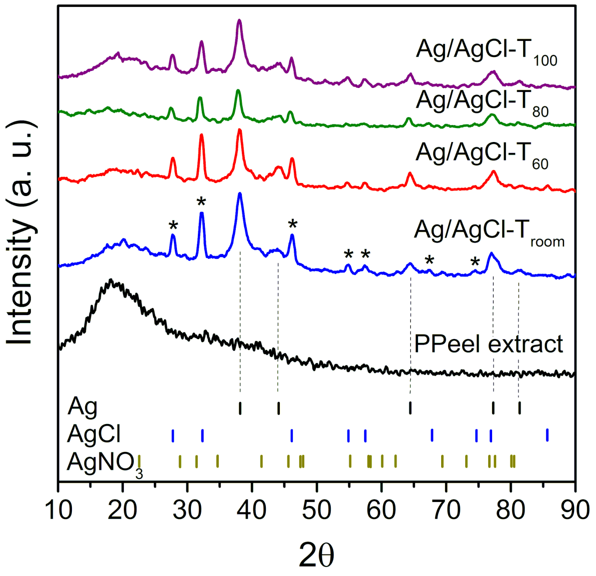

Figure 2: Diffraction patterns of the reaction products Ag/AgCl-T_{room}, Ag/AgCl-T_{60}, Ag/AgCl-T_{80}, and Ag/AgCl-T_{100}. Metallic Ag, AgCl, and $AgNO_3$ signals are set as references. The peaks marked with asterisks are related to the crystallographic planes of AgCl. The dashed lines represent the crystallographic signals of metallic Ag.

Crystalline behavior

In all of the reactions, the X-ray diffraction patterns shown in Figure 2 confirm the transformation of $AgNO_3$ into metallic Ag. The characteristic peaks of $AgNO_3$ salt and metallic Ag are indicated by short lines and can be used as a reference for comparison with the diffraction peaks obtained from the reaction products. In addition to the Ag reference pattern, an AgCl reference pattern is also attached. The latter was added because the experimental diffractograms of the reaction products showed characteristic peaks for Ag and AgCl. The Ag reference pattern was obtained from card number 00-04-0783 (Joint Committee on Powder Diffraction Standards, JCPDS). This pattern represents the peaks corresponding to the crystallographic planes (111), (200), (220), and (331) of the Cu-type face-centered cubic crystal structure of metallic Ag. The pattern for AgCl was taken from letter number 56540 (Inorganic Crystal Structure Database, ICSD). This pattern corresponds to the crystallographic planes (111), (200), (220), (311), and (222) of the NaCl-type face-centered cubic crystal structure.

According to the results, the pineapple peel extract (PPeel extract) is amorphous (i.e., does not show any signal of molecular order). The lack of $AgNO_3$ salt in the reaction products can also be observed. Hence, the diffraction patterns of the products obtained, regardless of the temperature used, show a combination of well-defined peaks of metallic Ag indicated with dashed lines and AgCl indicated with asterisks.

In an earlier work, the same combination of Ag and AgCl signals was obtained using extracts of *Stevia rebaudiana* [21]. In that report, the effect of the ratio between metallic AgNPs and AgClNPs on the morphology and dispersion in a thermoplastic starch matrix was demonstrated. At the same time, the nanodispersion behavior was related to the cytotoxic activity on cancer cells. The best results were obtained with the combination of nanoparticles mainly with AgCl. In other studies, the formation of Ag and AgCl signals has also been detected by XRD when using plant extracts [26-28].

As mentioned by Raven [29], Cl^- is an essential micronutrient for oxygenic photosynthetic organisms and is found in the environment in concentrations higher than those required by plants. Teixeira et al. [30] reported that the use of potassium chloride as a source of potassium for pineapple crops increases the availability of Cl^- in the soil and in the leaves of the plant. In this case, it is proposed that the synthesis of AgCl occurred by the interaction of the chloride ions present in the pineapple peel with the silver ions of $AgNO_3$ as other authors have pointed out [31,32]. The high concentration of chloride ions in pineapple peel may be due to the use of fertilizers with a high chloride content during pineapple cultivation. It is also considered that by adding silver salt to the extract, competitive reactions occur for the formation and stabilization of Ag or AgCl nanoparticles, giving rise to a concomitant generation of both silver species.

The crystallite size of Ag and AgCl was calculated from the XRD data and using the Scherrer equation, $D = (K\lambda)/(\beta\cos\theta)$, where D is the average crystallite size, K is the shape factor (a value of 0.94 was used for this analysis), λ is the wavelength of the X-ray radiation (which is 0.15418 nm), β is the full width at half maximum (FWHM) in radians, and θ is the Bragg angle. In addition, using the Match!® Software, the content of Ag and AgCl was also calculated, and the results are shown in Table 1.

Table 1: Content and crystallite size of Ag and AgCl calculated from XRD results.

Product	Crystallite size (nm)		Content (%)	
	Ag	AgCl	Ag	AgCl
Ag/AgCl-T_{room}	6.01	11.54	54.3	45.7
Ag/AgCl-T_{60}	7.32	11.70	46.3	53.7
Ag/AgCl-T_{80}	7.87	11.46	43.1	56.6
Ag/AgCl-T_{100}	6.32	10.67	52.1	47.9

According to Table 1, the change in crystallite size as a function of temperature is more noticeable for Ag than for AgCl, where an increasing trend in Ag crystallite size is observed up to 80 °C. It is speculated that at this temperature, the separation of salt ions and the interaction with reducing biological compounds are favorable, which enables the formation of a Ag nuclei and the growth of crystallites. In contrast, higher temperatures result in a higher reaction rate, causing a rapid conversion of Ag^+ into metallic Ag [33], as shown by the color change in Figure 1. This latter may be the cause of the impediment in the growth of crystallites at 100 °C. On the other hand, the different contents of Ag and AgCl depend on the presence of chloride ions in the extract and their ability to form AgCl instead of metallic Ag.

The qualitative and quantitative energy-dispersive X-ray (EDX) chemical analysis of Ag/AgCl products at different temperatures is shown in Figure 3. Consistently, the presence of Ag and Cl is evident. Likewise, characteristic elements of the compounds present in the pineapple peel extract are revealed, which act as capping agents for the nanoparticles. Silver is one of the most concentrated elements since it exists as metallic Ag and as an ion in AgCl. According to the quantitative results, Ag/AgCl-T_{room} and Ag/AgCl-T_{100} have the highest Ag content. In contrast, Ag/AgCl-T_{60} and Ag/AgCl-T_{80} have the lowest Ag concentrations. This result is consistent with the data determined from the XRD diffractograms shown in Table 1. Therefore, as mentioned before, the temperature affects the generation of AgNPs. However, for this particular case, the temperature also contributes to the formation of AgCl nanoparticles.

Spectroscopic characterization

It is known that the interaction of light with free electrons in an Ag nanoparticle can give rise to a collective oscillation known as surface plasmon effect [34]. This effect can be monitored by UV–vis spectroscopy, where metal nanoparticles absorb radiation at different wavelengths depending on their size [36]. The UV–vis absorption spectra of the reactions at different temperatures are shown in Figure 4. The absence of absorption of visible radiation is evident in the $AgNO_3$ salt and in the

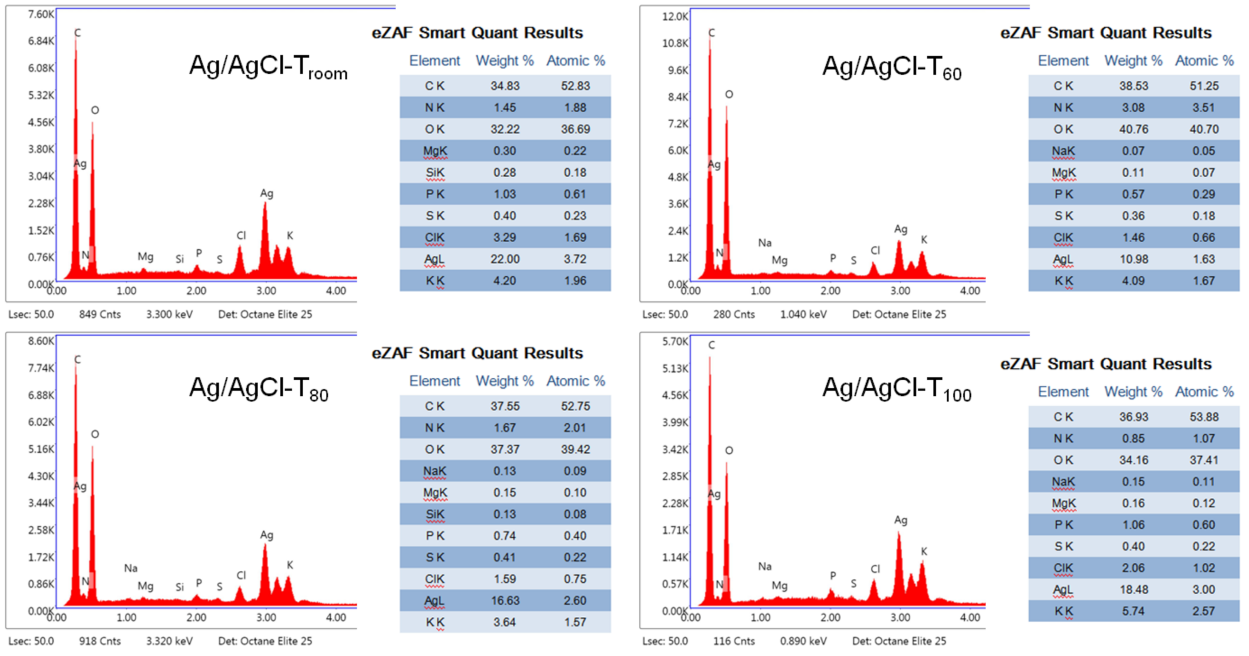

eZAF Smart Quant Results

Element	Weight %	Atomic %
C K	34.83	52.83
N K	1.45	1.88
O K	32.22	36.69
MgK	0.30	0.22
SiK	0.28	0.18
P K	1.03	0.61
S K	0.40	0.23
ClK	3.29	1.69
AgL	22.00	3.72
K K	4.20	1.96

eZAF Smart Quant Results

Element	Weight %	Atomic %
C K	38.53	51.25
N K	3.08	3.51
O K	40.76	40.70
NaK	0.07	0.05
MgK	0.11	0.07
P K	0.57	0.29
S K	0.36	0.18
ClK	1.46	0.66
AgL	10.98	1.63
K K	4.09	1.67

eZAF Smart Quant Results

Element	Weight %	Atomic %
C K	37.55	52.75
N K	1.67	2.01
O K	37.37	39.42
NaK	0.13	0.09
MgK	0.15	0.10
SiK	0.13	0.08
P K	0.74	0.40
S K	0.41	0.22
ClK	1.59	0.75
AgL	16.63	2.60
K K	3.64	1.57

eZAF Smart Quant Results

Element	Weight %	Atomic %
C K	36.93	53.88
N K	0.85	1.07
O K	34.16	37.41
NaK	0.15	0.11
MgK	0.16	0.12
P K	1.06	0.60
S K	0.40	0.22
ClK	2.06	1.02
AgL	18.48	3.00
K K	5.74	2.57

Figure 3: EDX analysis and quantification of Ag/AgCl products at different synthesis temperatures.

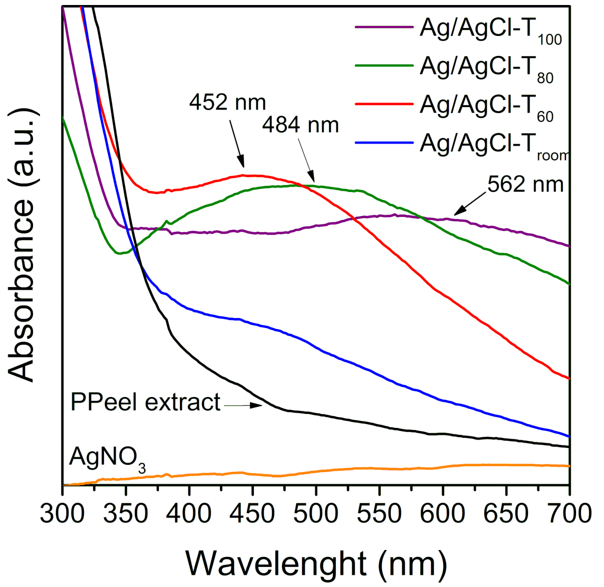

Figure 4: UV–visible spectroscopy of Ag/AgCl nanoparticle biosynthesis. The maximum absorption peaks are denoted by the arrows.

pineapple peel extract. Instead, reactions at different temperatures showed absorption in this region of the electromagnetic spectrum. Furthermore, differences in the maximum values of the absorption curves can be observed. Although in the reaction at room temperature (Ag/AgCl-T$_{room}$) the absorption maximum was not obvious, and it was in the case of the other reactions, the absorption maxima were easily identified. Ag/AgCl-T$_{60}$ shows absorption maximum at 452 nm, Ag/AgCl-T$_{80}$ at 484 nm, and Ag/AgCl-T$_{100}$ at 562 nm. For AgNPs, the maximum absorption signal is typically in the range of 400–500 nm [31]. Absorption trends at longer wavelengths are associated with increasing particle size [35,36]. It is also evident from Figure 4 that the absorption peak for the reaction at 100 °C (Ag/AgCl-T$_{100}$) is broader than that of the reactions at 60 and 80 °C. This behavior may be related to a larger size distribution of the nanoparticles. Hence, the uniformity of the nanoparticles is higher at 60 and 80 °C. This result is consistent with Nayak et al. [37], who reported an optimal temperature of 80 °C for Ag nanoparticle formation using extracts from *Cucurbita maxima*, *Moringa oleifera,* and *Acorus calamus*.

The FTIR results are shown in Figure 5. The spectra of the precursor salt and pineapple peel extract are shown for signal comparison. In the spectrum of the $AgNO_3$ salt, some signals were observed at (a) 1746 cm^{-1} corresponding to the symmetric tension and deformation in the N–O plane; (b) 1360 cm^{-1}, (c) 1284 cm^{-1}, and (d) 1230 cm^{-1} related to the asymmetric tension of N–O; (e) 800 and (f) 732 cm^{-1} related to the deformation and oscillation in the N–O plane. The following bands are found in the pineapple peel extract spectrum: 3300 cm^{-1} corresponds to O–H stretching in phenolic compounds; 2930 cm^{-1} is related to C–H stretching in any of the metabolites; 1737 cm^{-1} corresponds to C=O stretching in tannins; 1604 cm^{-1} and 1410 cm^{-1} are related to C=C stretching of aromatic rings in flavonoids, terpenes, tannins, and gallic acid;

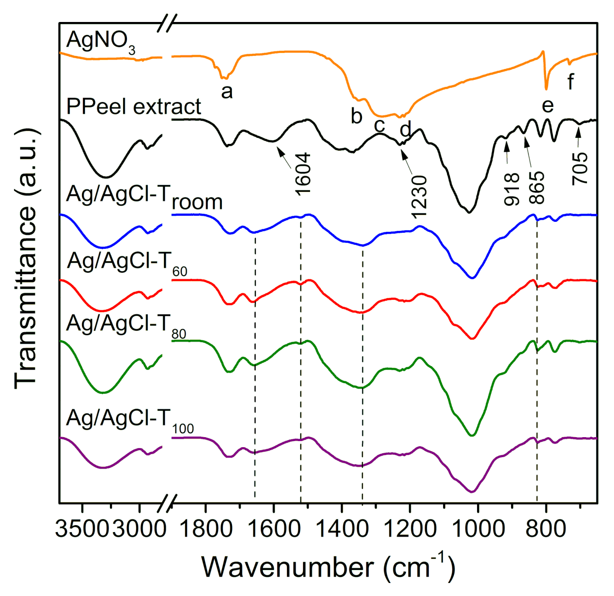

Figure 5: FTIR spectra of Ag/AgCl nanoparticles. The functional groups of the $AgNO_3$ salt are represented by the letters a–f. The wavenumber values of the functional groups of the pineapple peel extract which disappear in the reactions are denoted by arrows. New absorption peaks in the reaction products are shown by dashed lines.

1230 cm^{-1} corresponds to the tension of tertiary alcohols and flavonoids; 1026 cm^{-1} is related to C–O vibration in tannins and flavonoids; and 918 cm^{-1}, 865 cm^{-1}, and 705 cm^{-1} correspond to out-of-plane C–H vibration in gallic acid and catechin. According to the spectra shown in Figure 5, the formation of Ag/AgCl is evidenced by three phenomena. First, the $AgNO_3$ salt reacted completely as the characteristic absorption signals denoted by letters a–f in the $AgNO_3$ spectrum did not appear in the reaction products. Second, some of the absorption bands (indicated by arrows) of the pineapple peel extract disappeared. Third, new absorption bands are generated at 1663 cm^{-1}, 1522 cm^{-1}, 1340 cm^{-1}, and 825 cm^{-1} and are indicated by dashed lines in the spectra. This behavior occurs regardless of the reaction temperature used. According to the literature, pineapple peel contains several chemical species, especially phenolic and polyphenolic substances such as catechin, epicatechin, gallic acid, and ferulic acid [14]. These metabolites have reducing capacity, so it is hypothesized that this allows for the reduction of Ag^+ to Ag^0. The changes observed in the absorption bands of the reaction products are also a consequence of the capacity of the extract metabolites to act as capping agents for the formation of nanoparticles.

Morphological characterization

Although the data obtained by XRD and FTIR do not show significant differences in the formation of nanoparticles as a function of temperature, the micrographs obtained by TEM in Figure 6 show different behaviors both in size and shape of the nanoparticles with respect to temperature. These results are consistent with UV–vis spectra shown in Figure 4, where each curve has a different maximum depending on the reaction temperature. If the size of the nanoparticles is considered, as the reaction temperature increases, the nanoparticles become larger or the size distribution becomes broader. At room temperature and at 60 °C, the nanoparticles are less than 50 nm in size, but at 80 °C the nanoparticles reach a size of 70 nm. The shape of the nanoparticles is also modified, going from mostly spherical particles to a better defined morphology, as seen at 80 °C ($Ag/AgCl\text{-}T_{80}$). It is evident that at a temperature of 80 °C, in addition to spherical particles, triangular plate-like nanoparticles with well-defined and equal sides are obtained (see Figure $6C_1$). This result is consistent with Hyllested et al. [38] who also obtained AgNPs with triangular morphology using pineapple extract. The synthesis temperature plays an important role in the formation, growth, and size distribution of nanoparticles, as mentioned by Jiang et al. [39]. They reported the coexistence of triangular and spherical silver particles of different sizes obtained at temperatures ranging from 17 to 55 °C. According to the morphological results shown here, as the temperature increases the reaction rate also increases, favoring interactions between the reducing biocompounds and the precursor salt. Concomitantly, the particle size increases, as shown by the trend of images a_2–d_2 in Figure 6. However, the particle size distribution also increases because the higher the reaction rate, the greater the formation of silver crystals of different sizes. In the micrographs in Figure 6, it can be seen that the nanoparticles are embedded in a disordered system, with very low electron density. This system could be made of organic molecules that act as capping materials for nanoparticles, as described in the literature [24,40].

Thermal behavior

The weight loss curves and derivatives calculated from the thermogravimetric analysis data of the reaction products are shown in Figure 7a and Figure 7b, respectively. In the thermogram of the pineapple peel extract, denoted as PPeel extract, two stages of degradation of the metabolites were observed. The first degradation signal is very well defined and occurs at 202 °C, with an approximate mass loss of 35%. The second stage of degradation occurs in a temperature range of 277–395 °C, with an average temperature of 330 °C and an approximate mass loss of 15%. As the temperature increased, the sample continued to degrade such that at 750 °C, 36% of char residue remained (Table 2).

In the thermograms of the reaction products, two stages of degradation are also shown, except for $Ag/AgCl\text{-}T_{60}$, where a small additional peak appears at 163 °C, possibly from volatile organic molecules. The first degradation in the reaction prod-

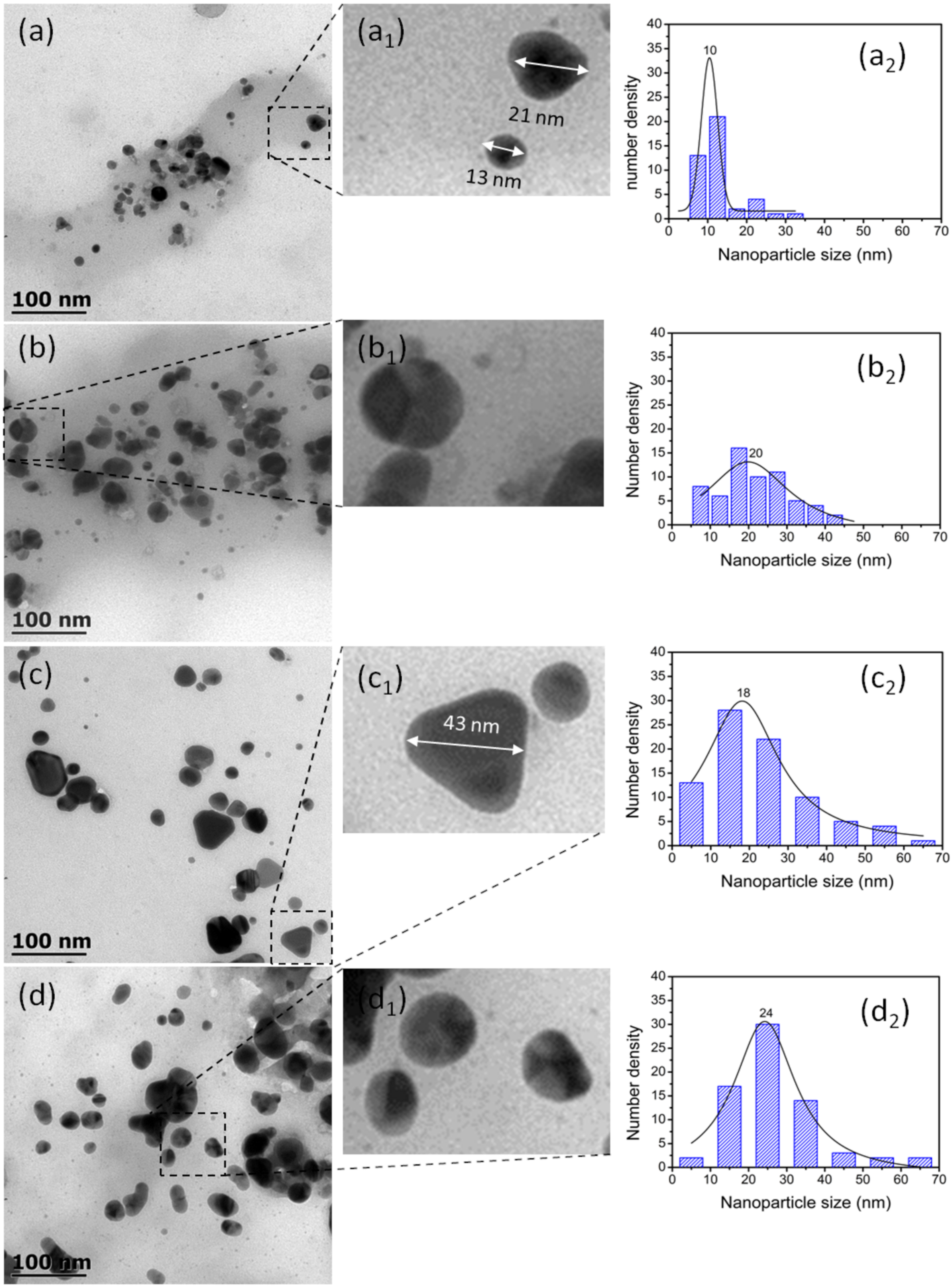

Figure 6: TEM micrographs of nanoparticles obtained at different temperatures. (a) Ag/AgCl-T_{room}, (b) Ag/AgCl-T_{60}, (c) Ag/AgCl-T_{80}, and (d) Ag/AgCl-T_{100}. Micrographs marked with subscript 1 are magnifications of some nanoparticles. In (a_1) and (c_1), sizes are indicated by double-headed arrows. The graphs with subscript 2 represent nanoparticle size distribution.

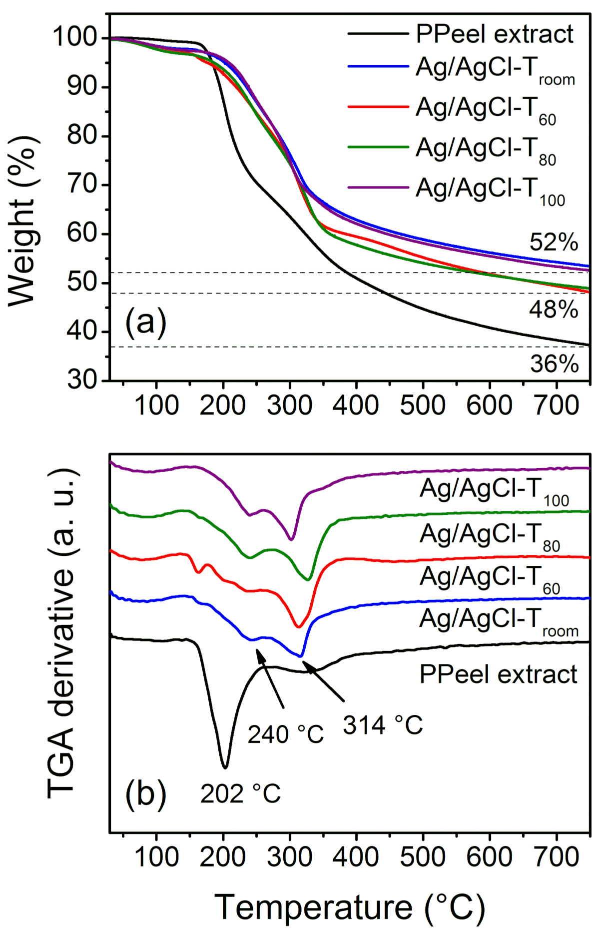

Figure 7: (a) TGA data and (b) weight loss derivatives of Ag/AgCl-T_{room}, Ag/AgCl-T_{60}, Ag/AgCl-T_{80}, and Ag/AgCl-T_{100}. The percentage of residual material after 700 °C is shown in (a). The average degradation temperature signals are indicated by the arrows in (b).

ucts is at 240 °C. The second degradation peak for both Ag/AgCl-T_{room} and Ag/AgCl-T_{60} is found at 314 °C. In the case of the Ag/AgCl-T_{80} reaction product, the degradation signal is at 326 °C and in Ag/AgCl-T_{100} the degradation temperature is 301 °C (Table 2).

Based on the results in Figure 7, it is remarkable that the reaction products have a higher thermal stability than that of the pineapple peel extract. This behavior can be attributed to two complementary situations. The first is a change in the chemical structure of the organic compounds used in the formation and capping of Ag/AgCl nanoparticles as observed by FTIR spectroscopy (Figure 5). The reducing species are oxidized and as a consequence have greater thermal stability. Hence, the higher temperature-shifted TGA curves show the thermal behavior of the modified metabolites during chemical reaction. The results are also consistent with Reddy et al. [41], who reported that phytochemicals capped on nanoparticles support thermal stability upon temperature changes. The second situation is the thermal barrier that Ag/AgCl nanoparticles themselves, based on their intrinsic characteristics, provide to the system. This last proposal is consistent with Rhim et al. [42], who stated that the increased thermal stability of the agar/AgNPs composite films is due to metallic silver being more thermally stable. On the other hand, throughout the thermal test, no evidence of decomposition of the $AgNO_3$ precursor salt (decomposition temperature is approx. 500 °C) is observed [43]. Hence, and as indicated by the FTIR and UV–vis results, the $AgNO_3$ salt was converted into Ag/AgCl nanoparticles. Furthermore, Figure 7 shows that the residual content in the reaction products is higher than that in the extract, illustrating the maximum percentage of biosynthesized Ag/AgCl nanoparticles (52% − 36% = 16%).

The degradation of the product with respect to temperature exhibited a behavior similar to that of nanoparticle biosynthesis, as shown by XRD, EDX, and TEM. That is, there is a difference in the degradation at intermediate temperatures (Ag/AgCl-T_{60} and Ag/AgCl-T_{80}) with respect to the products synthesized at room temperature and at 100 °C (Ag/AgCl-T_{room} and Ag/AgCl-T_{100}). This behavior particularly occurs in the second degradation and in the residual content. Therefore, this trend is probably related to the changes after the biological compounds act as reducing agents, as well as to changes in the shape, size, and size distribution of the resulting Ag nanoparticles.

Table 2: Thermal degradation data of pineapple peel extract and reaction products.

Sample	First weight loss			Second weight loss			Residual content (%)
	T_{deg} (°C)	Temperature range	Weight loss (%)	T_{deg} (°C)	Temperature range	Weight loss (%)	
PPeel extract	202	160–262	35	330	277–395	15	36
Ag/AgCl-T_{room}	240	175–269	20	314	274–339	13	52
Ag/AgCl-T_{60}	240	175–269	20	314	274–363	20	48
Ag/AgCl-T_{80}	240	175–269	20	326	274–368	21	48
Ag/AgCl-T_{100}	240	175–269	20	301	274–339	13	52

Cytotoxic behavior

It has been reported that several cytotoxic mechanisms of AgNPs can cause DNA, mitochondrial, and cell membrane damage as well as apoptosis [44]. Here, the cytotoxicity results of Ag/AgCl nanoparticles on MCF-7 breast cancer cells are shown in Figure 8. For each system of nanoparticles produced at different temperatures, cell viability is related to nanoparticle concentration. In all cases, cell viability decreased in a dose-dependent manner (i.e., cell death was progressive with increasing concentration). Cell viability was below 50% for Ag/AgCl-T_{room}, Ag/AgCl-T_{60}, and Ag/AgCl-T_{80} systems at concentrations below 25 µg/mL. Reactions at room temperature, 60, 80, and 100 °C achieved IC_{50} values of 24, 19, 17, and 36 µg/mL, respectively. Hence, the best behaviors occur with the nanoparticles formed at 60 and 80 °C. The results were favorable for all systems tested at 50 µg/mL. Here, the Ag/AgCl-T_{60} and Ag/AgCl-T_{80} systems also showed the best cytotoxic behavior, with cell viability of 21 and 20%, respectively. This response means that between 60 and 80 °C, it is beneficial to generate nanoparticles with a size and morphology suitable to induce cancer cell cytotoxicity.

According to the results obtained by TEM (Figure 6), at 60 °C spherical nanoparticles with a size range between 10 and 40 nm (size average of 20 nm) were obtained. At 80 °C, spherical nanoparticles and triangular plate-like nanoparticles were formed with a wider size range of 5–60 nm (size average of 18 nm). Even so, the size of the triangular plates is larger than 40 nm. Therefore, the morphology and size of nanoparticles are thought to have a great influence on the cytotoxicity of cancer cells. This result is consistent with Park et al. [45], who reported that the size of AgNPs is an important factor in cytotoxicity, inflammation, and genotoxicity. In this sense, AgNPs have been shown to induce cytotoxicity through apoptosis and necrosis in different cell lines [46].

Microscopic analysis (Figure 9) clearly shows that the morphological changes depend on the synthesis temperature and dosage of Ag/AgCl nanoparticles. The data show that the formation of apoptotic bodies (arrows) and the growth of cellular regions (black circles) are integral and characteristic of apoptosis. At high concentrations, however, necrosis (black box) predominates, where the formation of cellular debris and damage to the

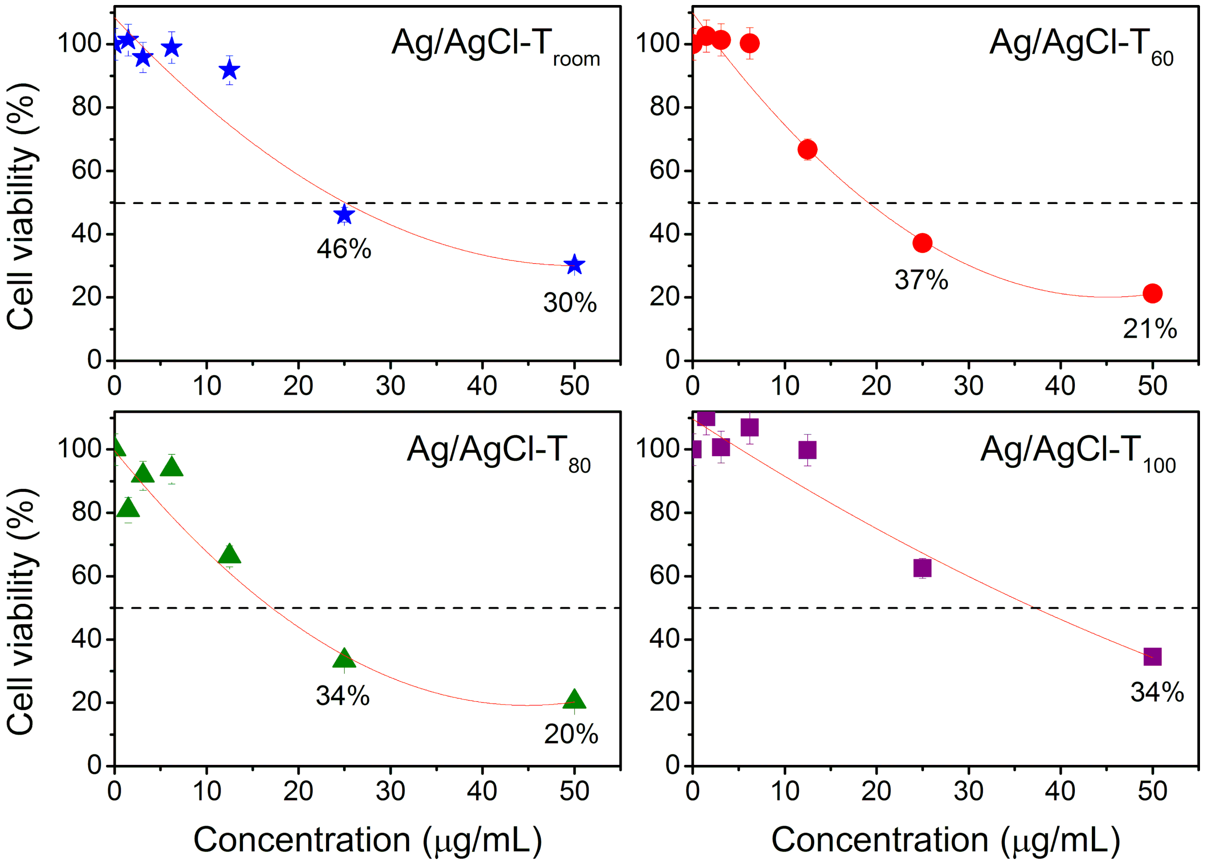

Figure 8: Cell viability assay of MCF-7 cells with Ag/AgCl nanoparticles obtained at room temperature, 60, 80, and 100 °C. The horizontal dashed line indicates 50% of cell viability. In all systems, cell viability at nanoparticle concentrations of 25 and 50 µg/mL is indicated, except for Ag/AgCl-T_{100}, since only cell viability at the concentration of 50 µg/mL is below 50%.

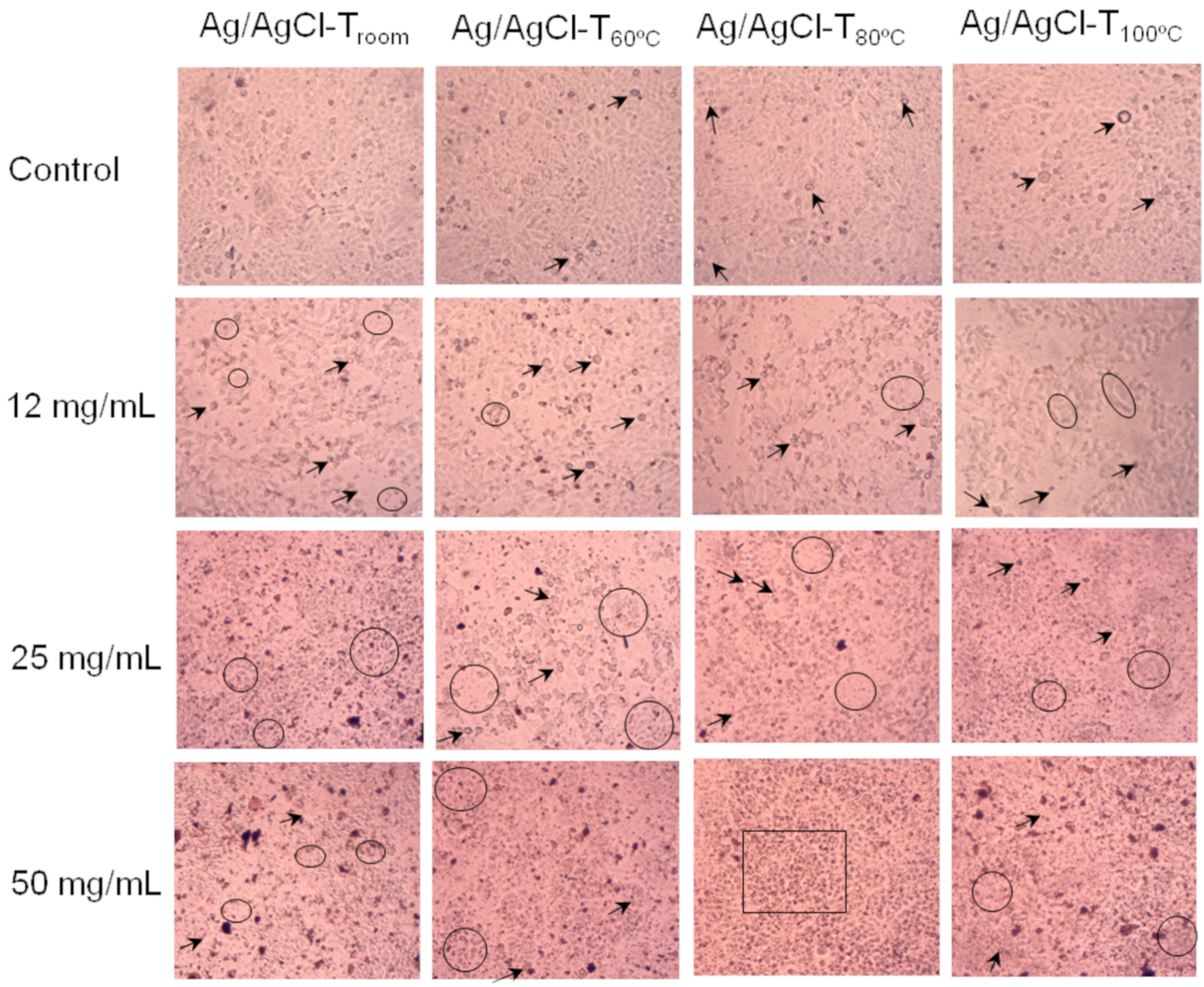

Figure 9: Microscopic observation of control MCF-7 cells and MCF-7 cells with Ag/AgCl nanoparticles after 24 hours of exposure. The MCF-7 cell line shows increased cell area or morphological changes (black circles) and formation of apoptotic bodies (arrows). At high concentrations, a large number of cells in a necrotic state were detected (black box).

cell membrane are detected. Depending on the level of stress exerted on the cell, this behavior will trigger cell death [47]. Çìftçì et al. [48] suggested that AgNPs induce apoptosis and necrosis in MCF-7 cells at lower concentrations, but induce necrosis only at higher concentrations.

Despite the strong cytotoxic activity of nanoparticles on MCF-7 cells, it was necessary to examine whether there is any effect on healthy cells. The systems with lower IC_{50} (Ag/AgCl-T_{60} and Ag/AgCl-T_{80}) were tested in mononuclear cells, particularly in monocytes. The results of the cytotoxic behavior of these systems are shown in Figure 10. It is evident that nanoparticles obtained at temperatures of 60 and 80 °C were also cytotoxic to monocytes at concentrations of 25 µg/mL. In fact, their IC_{50} was lower than that of MCF-7 cells at 13 and 12 µg/mL, respectively. Interestingly, an unexpected result was that for concentrations above 35 µg/mL, especially at 50 µg/mL, the cytotoxic effect of nanoparticles was more pronounced on cancer cells than on monocytes. The difference was 21% for AgNPs-T_{60} and 25% for AgNPs-T_{80}. In other words, at concentrations close to 50 µg/mL, the cytotoxic action of the nanoparticles becomes selective. This result is possibly due to the fact that a higher content of nanoparticles prevents cell proliferation in neoplastic cells. MCF-7 cells are known to overexpress matrix metalloproteinases (MMPs), the activity of which is favored by reactive species, and they have been shown to be directly involved in death mechanisms such as apoptosis, causing damage at the cell membrane level. In contrast, in monocytes, which are also high in MMPs, their activation mechanism is largely dependent on the production of NOs. Perhaps this fact is an explanation for the selectivity of the findings. However, a more in-depth study of this mechanism is necessary. These data have never been reported before, so their mechanistic interpretation and understanding requires further investigation.

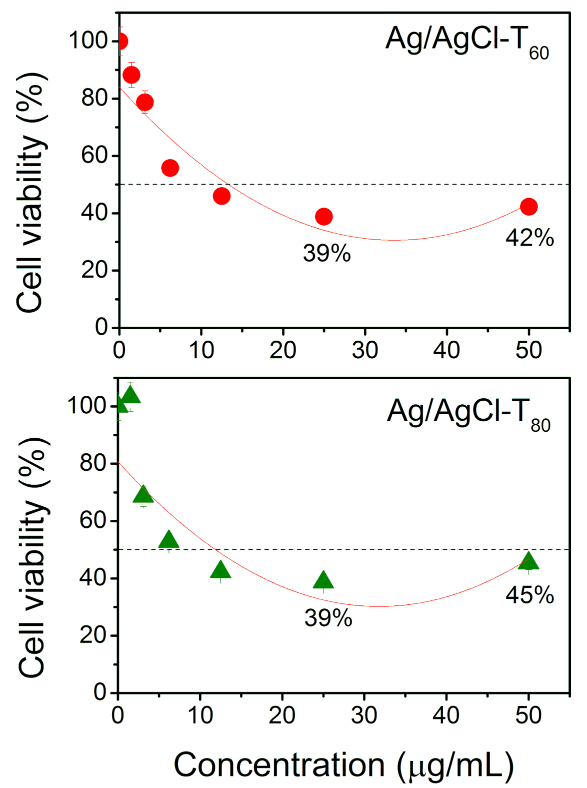

Figure 10: Cell viability tests on mononuclear cells (monocytes) with Ag/AgCl nanoparticles obtained at 60 and 80 °C. Cell viability at 50% is marked with a horizontal dashed line. Cell viability at 25 and 50 µg/mL is indicated.

In order to rule out whether the metabolites of the pineapple peel extract, necessary for the formation and stabilization of the nanoparticles, participate in the cytotoxic action, MCF-7 cell viability tests were performed on the extracts. The results are shown in Figure 11. In all cases, regardless of the temperature, there was no evidence that the extract had cytotoxic activity against MCF-7 cells. Therefore, the above cytotoxicity behavior can only be attributed to the Ag/AgCl nanoparticles obtained at different temperatures.

The results of the cytotoxic activity of $AgNO_3$ tested both in peripheral blood mononuclear cells (PBMC) and in breast cancer cells (MCF-7) are shown in Table 3. The maximum concentration of $AgNO_3$ tested was the one used to generate the Ag/AgCl nanoparticles. Even at the lowest concentrations, a significant decrease in cell viability was observed. The data indicated that $AgNO_3$ had strong cytotoxic activity in both PBMC and MCF-7 cells; however, no cytotoxic selectivity was observed.

Conclusion

This study demonstrates the combined production of Ag and AgCl nanoparticles obtained through a green synthesis method. Pineapple peel was used for the synthesis method, where phenolic compounds were found, whose reducing capacity allowed for the formation of Ag/AgCl nanoparticles. Four biosynthesis temperatures were tested (i.e., room temperature, 60, 80, and 100 °C). The size, shape, and size distribution of the nanoparticles were affected by the temperature. Preferably, spherical nanoparticles with a size between 10 and 70 nm were obtained. It was noticeable that at 80 °C, triangular plates were also formed. The cytotoxic activity of the biosynthesized products against the MCF-7 breast cancer cell line was tested. The results showed a high cytotoxicity in these cells, up to 80% of those with the products obtained at temperatures of 60 and 80 °C. In contrast, these products showed a lower cytotoxic activity in PBMC healthy cells. Hence, it is reported for the first time that with this combined system of Ag/AgCl nanoparticles synthesized at a controlled temperature, a cytotoxic selectivity between cancer cells and healthy cells can be achieved.

Experimental

Materials

MD2 hybrid pineapples (family: Bromeliaceae, genus: *Ananas* Mill, 1754, species: *comosus* (L.) Merr., 1917) were obtained from crops in the Tuxtepec region of the state of Oaxaca, Mexico. Silver nitrate (CAS 7761-88-8, ACS reagent, purity ≥99.0%, purchased from Sigma-Aldrich Co) was used as a silver nanoparticle precursor.

Aqueous extraction by infusion of pineapple peel

MD2 pineapples were peeled and used. The peel was cut into small pieces, and dried to a constant weight. Then, 100 g of dehydrated pineapple peel was weighed and put into a coffee filter. Subsequently, an infusion was made with 1 L of distilled water in a Oster® brand coffee maker. The solution obtained was vacuum filtered and concentrated in a rotary evaporator at 50 °C, 250 rpm, and 42 mbar.

Biosynthesis of Ag/AgCl nanoparticles

Quantification of phenolic and flavonoid compounds in the pineapple peel extract was performed before biosynthesis. Total phenolic content was performed using the method described by Singleton et al. [49], and the total flavonoid content was performed according to the method described by Dewanto et al. [50]. The biosynthesis of Ag/AgCl nanoparticles was carried out in a reflux system with a water bath at a controlled temperature. A proportion of 90% of $AgNO_3$ salt (at a concentration of 10 mM) and 10% of pineapple peel extract (at a concentration of 10% w/v) was used. The synthesis was performed under constant stirring at 500 rpm for 2 h. The temperature was established as the study variable: room temperature, 60, 80, and 100 °C were the temperatures studied. Finally, the synthesized

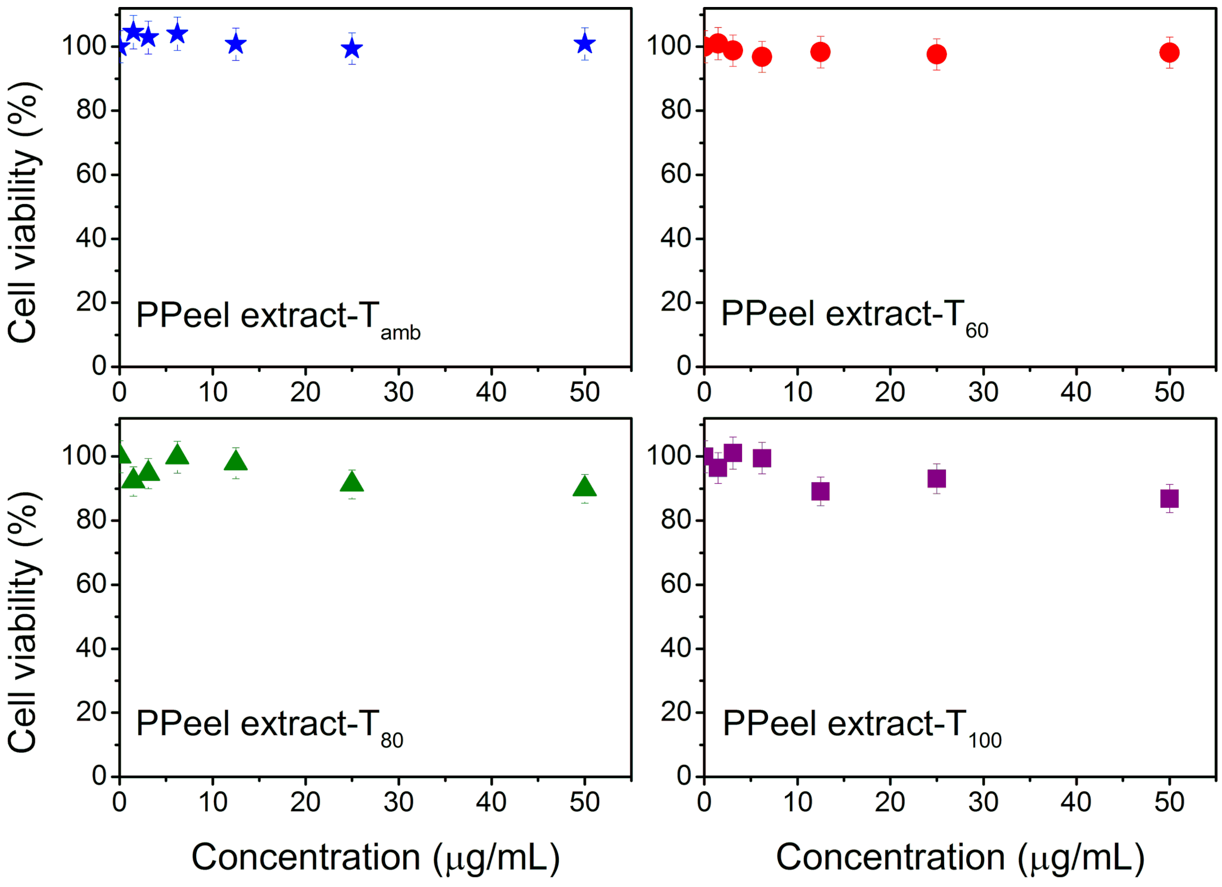

Figure 11: Cell viability assays on MCF-7 cells with pineapple peel extracts obtained at room temperature, 60, 80, and 100 °C.

Table 3: Data on the cytotoxic activity of $AgNO_3$ in peripheral blood mononuclear cells (PBMC) and in breast cancer cells (MCF-7).

$AgNO_3$ (mM)	PBMC viability (%)	MCF-7 cells viability (%)
0	94.4 ± 11.6^a	97.75 ± 12.12
0.031	29.1 ± 5.28^a	24.54 ± 5.67
0.070	24.8 ± 1.84^a	26.49 ± 2.31
0.150	27.2 ± 5.26^a	28.20 ± 5.88
0.312	27.1 ± 1.3^b	33.63 ± 5.82
0.620	27.8 ± 2.32^a	22.01 ± 2.13
1.250	6.92 ± 0.62^a	7.139 ± 0.44
2.500	6.86 ± 0.72^a	7.080 ± 0.64
5.000	8.07 ± 1.28^a	6.962 ± 0.20
10.000	7.55 ± 1.41^a	7.021 ± 0.41

Experimental data points are presented as the mean ± SD of three independent experiments, with three replicates. Significant differences are indicated by $^ap \leq 0.0001$ versus 0 mM and $^bp \leq 0.01$ versus 0 mM.

products were dried for 24 h for subsequent characterization. Some of the products of each reaction were kept at room temperature before drying to be characterized by UV–vis spectroscopy.

Characterization

X-ray diffraction patterns were obtained in a Bruker AXS D8 Advance diffractometer, at 30 mA and 40 kV, with a Ni filter and a Cu Kα radiation generator. Diffraction patterns were acquired at a scan rate of 1 °/min from 10 to 90° in 2θ. Quantitative chemical analysis was performed on a JEOL JSM-7401F field-emission scanning electron microscope (FE-SEM) using EDX. An acceleration voltage of 15 kV and a working distance of 8 mm were used. The samples were precoated with Au/Pd for 10 seconds. Ultraviolet–visible spectroscopy was obtained using a Perkin Elmer Lambda 25 spectrophotometer, operating in the range of 350 to 700 nm. Fourier-transform infrared spectra were obtained with a Perkin Elmer Dynascan Spectrum 100 spectrometer, using an attenuated total reflectance (ATR) interferometer, operating in the range of 4000–600 cm^{-1}. Transmission electron microscopy images were acquired on a JEOL 1010 microscope, with an accelerating voltage of 80 kV. For that, samples were pre-prepared in acetone and sonicated for 20 min, then dried at room temperature. Thermogravimetric analysis was performed on a Perkin Elmer STA 6000 simultaneous thermal analyzer, with a heating rate of 20 °C/min, under a nitrogen atmosphere, and a temperature range of 30–800 °C.

To carry out XRD, EDX, FTIR, and TGA analyses, the pineapple peel extract and the reaction products were previously dried at 110 °C for 24 h.

Cell culture

In a similar manner to [51], the MCF-7 human breast cell line was obtained from the American Type Culture Collection (ATCC®). This cell line was at passage 4 when used in the study and was routinely cultured on monolayers at 80% confluence in Dulbecco's modified Eagle's high glucose medium (DMEM), supplemented with 10% of fetal bovine serum, 100 U/mL of penicillin, 100 µg/mL of streptomycin, and 2 mM L-glutamine. The cells were kept at 37 °C with saturated humidity and 5% CO_2. The culture medium was removed to collect the human breast cancer cells, which were then washed with phosphate buffered saline (PBS). A cell dissociation solution made of trypsin-EDTA was added and incubated at 37 °C for 3 min in a humidified incubator with 5% CO_2 to produce a cell suspension. Trypsinized cells were reseeded in fresh medium at 10^5 cells/mL and incubated at 37 °C in a 5% CO_2 humidified incubator. All reagents were purchased from Biowest, Riverside, USA.

In a similar manner to [52], peripheral blood mononuclear cells were obtained from blood samples of healthy adult human volunteers, using standard Histopaque 1077 (Sigma-Aldrich, St. Louis, MO. USA) techniques and density gradient centrifugation. PBMCs were maintained in Roswell Park Memorial Institute medium at pH 7.4, supplemented with 10% of fetal bovine serum, 100 U/mL of penicillin, 100 µg/mL of streptomycin, and 2 mM of L-glutamine. All reagents were purchased from Biowest, Riverside, USA. PBMCs were kept at 37 ºC with saturated humidity and 5% CO_2. All procedures performed followed the ethical standards of the institutional and/or national research committee and the 1964 Declaration of Helsinki. According to the Ethics Committee on Human Beings of the Universidad del Papaloapan (signed informed consent was not needed).

Cell viability by MTT assay

The MTT assay is based on the ability of live cells to selectively reduce the yellow soluble salt MTT (3-(4,5-dimethylthiazol-2-yl)-2,5-diphenyl tetrazolium bromide, Sigma-Aldrich) to a purple/blue insoluble formazan crystal. For each sample, three independent experiments were performed in triplicates. Cell viability of control, Ag/AgCl-T_{room}, Ag/AgCl-T_{60}, Ag/AgCl-T_{80}, and Ag/AgCl-T_{100} samples were evaluated in 96-well flat-bottom culture plates (TPP). The MMT assay was performed on MCF-7 breast cancer cells and mononuclear cells. An amount of 2×10^4 MCF-7 cells and 2×10^5 PBMCs in 100 µL was seeded onto each well and incubated for 24 h at 37 °C, 5% CO_2. After this time, and starting from a stock of 10 mg/mL prepared in PBS with serial dilutions, 0.05 mg/mL of the study samples was added. Subsequently, they were incubated at 37 °C and 5% CO_2 for 24 h. Then, 10 µL of MTT solution prepared in PBS at a concentration of 5 mg/mL was added to MCF-7 cells, and an equal amount of MMT solution was added to monocytes. MCF-7 cells were incubated again for 4 h and mononuclear cells were incubated for 6 h, both at 37 °C and 5% CO_2. The media were removed and 100 µL of dimethyl sulfoxide (DMSO) was added. The samples were then incubated at room temperature until the formazan crystals were dissolved. Finally, the absorbance at 570 nm was measured.

Acknowledgements

We thank M. Lozano for his support in the EDX analysis. Thanks also to M. Roger for proofreading and correcting typos and grammatical errors in the manuscript.

Funding

M. J. Ramirez-Hernandez appreciates the scholarship granted by CONACyT Mexico for her master’s studies. This work was partially supported by PRODEP-SEP, Mexico, through Grant number DSA/103.5/15/11097. The support of Consejo Nacional de Ciencia y Tecnología (CONACyT) Mexico, through Grant INFRA-317225 is also acknowledged.

ORCID® iDs

Mario Valera-Zaragoza - https://orcid.org/0000-0003-4341-5997
Omar Viñas-Bravo - https://orcid.org/0000-0001-8345-2659
David Paniagua-Vega - https://orcid.org/0000-0002-2207-580X
Eduardo Ramírez-Vargas - https://orcid.org/0000-0001-8081-7384

References

1. Rambabu, K.; Bharath, G.; Banat, F.; Show, P. L. *J. Hazard. Mater.* **2021,** *402,* 123560. doi:10.1016/j.jhazmat.2020.123560
2. Al-Haddad, J.; Alzaabi, F.; Pal, P.; Rambabu, K.; Banat, F. *Clean Technol. Environ. Policy* **2020,** *22,* 269–277. doi:10.1007/s10098-019-01765-2
3. Bello, B. A.; Khan, S. A.; Khan, J. A.; Syed, F. Q.; Mirza, M. B.; Shah, L.; Khan, S. B. *Biochem. Biophys. Res. Commun.* **2017,** *490,* 889–894. doi:10.1016/j.bbrc.2017.06.136
4. Keshari, A. K.; Srivastava, R.; Singh, P.; Yadav, V. B.; Nath, G. *J. Ayurveda Integr. Med.* **2020,** *11,* 37–44. doi:10.1016/j.jaim.2017.11.003
5. M, J. F.; P, L. *Prog. Biomater.* **2015,** *4,* 113–121. doi:10.1007/s40204-015-0042-2
6. Vasanth, K.; Ilango, K.; MohanKumar, R.; Agrawal, A.; Dubey, G. P. *Colloids Surf., B* **2014,** *117,* 354–359. doi:10.1016/j.colsurfb.2014.02.052
7. Hunter, K. W.; Crawford, N. P. S.; Alsarraj, J. *Breast Cancer Res.* **2008,** *10,* S2. doi:10.1186/bcr1988
8. Jin, X.; Mu, P. *Breast Cancer: Basic Clin. Res.* **2015,** *9s1,* 23–34. doi:10.4137/bcbcr.s25460

9. Maddinedi, S. b.; Mandal, B. K.; Maddili, S. K. *J. Photochem. Photobiol., B* **2017,** *167,* 236–241. doi:10.1016/j.jphotobiol.2017.01.003
10. Ayinde, W. B.; Gitari, W. M.; Samie, A. *Green Chem. Lett. Rev.* **2019,** *12,* 225–234. doi:10.1080/17518253.2019.1627427
11. Kumar, R.; Roopan, S. M.; Prabhakarn, A.; Khanna, V. G.; Chakroborty, S. *Spectrochim. Acta, Part A* **2012,** *90,* 173–176. doi:10.1016/j.saa.2012.01.029
12. Skiba, M. I.; Vorobyova, V. I. *Adv. Mater. Sci. Eng.* **2019,** 8306015. doi:10.1155/2019/8306015
13. Yang, N.; Li, W.-H. *Ind. Crops Prod.* **2013,** *48,* 81–88. doi:10.1016/j.indcrop.2013.04.001
14. Li, T.; Shen, P.; Liu, W.; Liu, C.; Liang, R.; Yan, N.; Chen, J. *Int. J. Food Prop.* **2014,** *17,* 1805–1817. doi:10.1080/10942912.2012.732168
15. Agnihotri, S.; Sillu, D.; Sharma, G.; Arya, R. K. *Appl. Nanosci.* **2018,** *8,* 2077–2092. doi:10.1007/s13204-018-0883-9
16. Baran, A.; Keskin, C.; Baran, M. F.; Huseynova, I.; Khalilov, R.; Eftekhari, A.; Irtegun-Kandemir, S.; Kavak, D. E. *Bioinorg. Chem. Appl.* **2021,** *2021,* 2058149. doi:10.1155/2021/2058149
17. Das, G.; Patra, J. K.; Debnath, T.; Ansari, A.; Shin, H.-S. *PLoS One* **2019,** *14,* e0220950. doi:10.1371/journal.pone.0220950
18. Poadang, S.; Yongvanich, N.; Phongtongpasuk, S. *Chiang Mai Univ. J. Nat. Sci.* **2017,** *16,* 123–133. doi:10.12982/cmujns.2017.0010
19. Steingass, C. B.; Glock, M. P.; Schweiggert, R. M.; Carle, R. *Anal. Bioanal. Chem.* **2015,** *407,* 6463–6479. doi:10.1007/s00216-015-8811-2
20. Ahmed, S.; Saifullah; Ahmad, M.; Swami, B. L.; Ikram, S. *J. Radiat. Res. Appl. Sci.* **2016,** *9,* 1–7. doi:10.1016/j.jrras.2015.06.006
21. Valera-Zaragoza, M.; Huerta-Heredia, A. A.; Peña-Rico, M. A.; Juarez-Arellano, E. A.; Navarro-Mtz, A. K.; Ramírez-Vargas, E.; Sánchez-Valdes, S. *Polym. Bull.* **2021,** *78,* 1683–1701. doi:10.1007/s00289-020-03184-6
22. Chowdhury, I. H.; Ghosh, S.; Roy, M.; Naskar, M. K. *J. Sol-Gel Sci. Technol.* **2015,** *73,* 199–207. doi:10.1007/s10971-014-3515-1
23. Suman, T. Y.; Rajasree, S. R. R.; Jayaseelan, C.; Mary, R. R.; Gayathri, S.; Aranganathan, L.; Remya, R. R. *Environ. Sci. Pollut. Res.* **2016,** *23,* 2705–2714. doi:10.1007/s11356-015-5468-5
24. Yilmaz, M.; Turkdemir, H.; Kilic, M. A.; Bayram, E.; Cicek, A.; Mete, A.; Ulug, B. *Mater. Chem. Phys.* **2011,** *130,* 1195–1202. doi:10.1016/j.matchemphys.2011.08.068
25. Jurinjak Tušek, A.; Benković, M.; Belščak Cvitanović, A.; Valinger, D.; Jurina, T.; Gajdoš Kljusurić, J. *Ind. Crops Prod.* **2016,** *91,* 205–214. doi:10.1016/j.indcrop.2016.07.015
26. Patil, M. P.; Singh, R. D.; Koli, P. B.; Patil, K. T.; Jagdale, B. S.; Tipare, A. R.; Kim, G.-D. *Microb. Pathog.* **2018,** *121,* 184–189. doi:10.1016/j.micpath.2018.05.040
27. Alishah, H.; Pourseyedi, S.; Mahani, S. E.; Ebrahimipour, S. Y. *RSC Adv.* **2016,** *6,* 73197–73202. doi:10.1039/c6ra16127h
28. Villanueva-Ibáñez, M.; Yañez-Cruz, M. G.; Álvarez-García, R.; Hernández-Pérez, M. A.; Flores-González, M. A. *Mater. Lett.* **2015,** *152,* 166–169. doi:10.1016/j.matlet.2015.03.097
29. Raven, J. A. *J. Exp. Bot.* **2017,** *68,* 359–367. doi:10.1093/jxb/erw421
30. Teixeira, L. A. J.; Quaggio, J. A.; Cantarella, H.; Mellis, E. V. *Rev. Bras. Frutic.* **2011,** *33,* 627–636. doi:10.1590/s0100-29452011000200036
31. Gopinath, V.; Priyadarshini, S.; Meera Priyadharsshini, N.; Pandian, K.; Velusamy, P. *Mater. Lett.* **2013,** *91,* 224–227. doi:10.1016/j.matlet.2012.09.102
32. Ashok Kumar, D.; Palanichamy, V.; Roopan, S. M. *J. Photochem. Photobiol., B* **2014,** *138,* 302–306. doi:10.1016/j.jphotobiol.2014.06.011
33. Elemike, E. E.; Onwudiwe, D. C.; Arijeh, O.; Nwankwo, H. U. *Bull. Mater. Sci.* **2017,** *40,* 129–137. doi:10.1007/s12034-017-1362-8
34. Xia, Y.; Halas, N. J. *MRS Bull.* **2005,** *30,* 338–348. doi:10.1557/mrs2005.96
35. Amirjani, A.; Firouzi, F.; Haghshenas, D. F. *Plasmonics* **2020,** *15,* 1077–1082. doi:10.1007/s11468-020-01121-x
36. Ali, M.; Kim, B.; Belfield, K. D.; Norman, D.; Brennan, M.; Ali, G. S. *Mater. Sci. Eng., C* **2016,** *58,* 359–365. doi:10.1016/j.msec.2015.08.045
37. Nayak, D.; Pradhan, S.; Ashe, S.; Rauta, P. R.; Nayak, B. *J. Colloid Interface Sci.* **2015,** *457,* 329–338. doi:10.1016/j.jcis.2015.07.012
38. Ærøe Hyllested, J.; Espina Palanco, M.; Hagen, N.; Mogensen, K. B.; Kneipp, K. *Beilstein J. Nanotechnol.* **2015,** *6,* 293–299. doi:10.3762/bjnano.6.27
39. Jiang, X. C.; Chen, W. M.; Chen, C. Y.; Xiong, S. X.; Yu, A. B. *Nanoscale Res. Lett.* **2011,** *6,* 32. doi:10.1007/s11671-010-9780-1
40. Shankar, S. S.; Rai, A.; Ahmad, A.; Sastry, M. *J. Colloid Interface Sci.* **2004,** *275,* 496–502. doi:10.1016/j.jcis.2004.03.003
41. Reddy, N. V.; Li, H.; Hou, T.; Bethu, M. S.; Ren, Z.; Zhang, Z. *Int. J. Nanomed.* **2021,** *16,* 15–29. doi:10.2147/ijn.s265003
42. Rhim, J.-W.; Wang, L.-F.; Lee, Y.; Hong, S.-I. *Carbohydr. Polym.* **2014,** *103,* 456–465. doi:10.1016/j.carbpol.2013.12.075
43. Otto, K.; Oja Acik, I.; Krunks, M.; Tõnsuaadu, K.; Mere, A. *J. Therm. Anal. Calorim.* **2014,** *118,* 1065–1072. doi:10.1007/s10973-014-3814-3
44. Morais, M.; Teixeira, A. L.; Dias, F.; Machado, V.; Medeiros, R.; Prior, J. A. V. *J. Med. Chem.* **2020,** *63,* 14308–14335. doi:10.1021/acs.jmedchem.0c01055
45. Park, M. V. D. Z.; Neigh, A. M.; Vermeulen, J. P.; de la Fonteyne, L. J. J.; Verharen, H. W.; Briedé, J. J.; van Loveren, H.; de Jong, W. H. *Biomaterials* **2011,** *32,* 9810–9817. doi:10.1016/j.biomaterials.2011.08.085
46. Foldbjerg, R.; Olesen, P.; Hougaard, M.; Dang, D. A.; Hoffmann, H. J.; Autrup, H. *Toxicol. Lett.* **2009,** *190,* 156–162. doi:10.1016/j.toxlet.2009.07.009
47. Núñez, R.; Sancho-Martínez, S. M.; Novoa, J. M. L.; López-Hernández, F. J. *Cell Death Differ.* **2010,** *17,* 1665–1671. doi:10.1038/cdd.2010.96
48. Çìftçì, H.; Türk, M.; Tamer, U.; Karahan, S.; Menemen, Y. *Turk. J. Biol.* **2013,** *37,* 573–581. doi:10.3906/biy-1302-21
49. Singleton, V. L.; Orthofer, R.; Lamuela-Raventós, R. M. *Methods Enzymol.* **1999,** *299,* 152–178. doi:10.1016/s0076-6879(99)99017-1
50. Dewanto, V.; Wu, X.; Adom, K. K.; Liu, R. H. *J. Agric. Food Chem.* **2002,** *50,* 3010–3014. doi:10.1021/jf0115589
51. Borin, D. B.; Castrejón-Arroyo, K.; Cruz-Nolasco, A.; Peña-Rico, M.; Sagrillo, M. R.; Santos, R. C. V.; Silva de Baco, L.; Pérez-Picaso, L.; Camacho, L.; Navarro-Mtz, A. K. *Toxins* **2021,** *13,* 476. doi:10.3390/toxins13070476
52. Lissette Mora-Medina, T.; Martínez-Pascual, R.; Ángel Peña-Rico, M.; Viñas-Bravo, O.; Montiel-Smith, S.; Pérez-Picaso, L.; Moreno-Díaz, H. *Steroids* **2022,** *182,* 109012. doi:10.1016/j.steroids.2022.109012

License and Terms

The definitive version of this article is the electronic one which can be found at:
https://doi.org/10.3762/bjnano.13.124

BEILSTEIN JOURNAL OF NANOTECHNOLOGY

Nanotechnology – a robust tool for fighting the challenges of drug resistance in non-small cell lung cancer

Filip Gorachinov*[1], Fatima Mraiche*[2,3], Diala Alhaj Moustafa[2], Ola Hishari[2], Yomna Ismail[2], Jensa Joseph[2], Maja Simonoska Crcarevska[1], Marija Glavas Dodov[1], Nikola Geskovski[1] and Katerina Goracinova*[1]

Review

Open Access

Address:
[1]Institute of Pharmaceutical Technology, Faculty of Pharmacy, University of Ss. Cyril and Methodius in Skopje, 1000 Skopje, North Macedonia, [2]College of Pharmacy, QU Health, Qatar University, PO Box 2713, Doha, Qatar and [3]Department of Pharmacology, Faculty of Medicine and Dentistry, University of Alberta, T6G 2R3 Edmonton, Canada

Email:
Filip Gorachinov* - filip.gorachinov@gmail.com; Fatima Mraiche* - mraiche1@ualberta.ca; Katerina Goracinova* - kago@ff.ukim.edu.mk

* Corresponding author

Keywords:
co-delivery nanoparticles; combinatorial therapy; EGFR TKI resistance; non-small cell lung cancer (NSCLC); overcoming and preventing resistance

Beilstein J. Nanotechnol. **2023,** *14,* 240–261.
https://doi.org/10.3762/bjnano.14.23

Received: 09 November 2022
Accepted: 01 February 2023
Published: 22 February 2023

This article is part of the thematic issue "New trends in nano-biotechnology".

Guest Editor: P.-L. Show

Abstract

Genomic and proteomic mutation analysis is the standard of care for selecting candidates for therapies with tyrosine kinase inhibitors against the human epidermal growth factor receptor (EGFR TKI therapies) and further monitoring cancer treatment efficacy and cancer development. Acquired resistance due to various genetic aberrations is an unavoidable problem during EGFR TKI therapy, leading to the rapid exhaustion of standard molecularly targeted therapeutic options against mutant variants. Attacking multiple molecular targets within one or several signaling pathways by co-delivery of multiple agents is a viable strategy for overcoming and preventing resistance to EGFR TKIs. However, because of the difference in pharmacokinetics among agents, combined therapies may not effectively reach their targets. The obstacles regarding the simultaneous co-delivery of therapeutic agents at the site of action can be overcome using nanomedicine as a platform and nanotools as delivery agents. Precision oncology research to identify targetable biomarkers and optimize tumor homing agents, hand in hand with designing multifunctional and multistage nanocarriers that respond to the inherent heterogeneity of the tumors, may resolve the challenges of inadequate tumor localization, improve intracellular internalization, and bring advantages over conventional nanocarriers.

Introduction

Among the malignant diseases, lung cancer takes the lead in mortality. Also, it is the second most frequently diagnosed cancer (11.4% of the total cases), surpassed only by female breast cancer (11.7%) [1-3]. According to the WHO International Agency for Research on Cancer in 2020 (GLOBOCAN database), around 1.8 million new lung mortalities were recorded worldwide for both genders, representing 18% of all cancer deaths [4]. There are two main classes of lung cancer based on histological appearance, namely small-cell lung cancer (SCLC), which is highly aggressive, and non-small cell lung cancer (NSCLC), which is more prevalent (85% of all diagnosed lung cancer cases) [5]. NSCLC can be further categorized into histologically different subtypes. that is, adenocarcinomas (45%), squamous cell carcinoma (23%), and large cell carcinoma (3%), leaving approximately 28% for all other subtypes and making adenocarcinomas the most prevalent among the subtypes. Recently, based on the progress in cancer genomics, a new classification based on the clinical, histological, radiological, and molecular subtypes of lung adenocarcinoma has been proposed as a result of a joined effort of the International Association for the Study of Lung Cancer (IASLC), the American Thoracic Society (ATS), and the European Respiratory Society (ERS), with the intention of improving diagnostic, prognostic, and therapeutic approaches for different subtypes of lung cancers [6,7]. Moreover, advances in histological, genomic, and proteomic studies of cancer have had a significant impact on the discovery of novel therapies based on specific histological types and molecular signatures of cancer. Molecularly targeted therapies that have been developed for a subgroup of non-small cell lung cancer (NSCLC) with endothelial growth factor receptor (EGFR) activating mutations firmly underlined the importance of an improved classification of lung cancer into specific subtypes that qualify for specialized therapeutic strategies. Tyrosine kinase inhibitors (TKIs) have demonstrated enhanced efficacy and reduced toxicity in EGFR-sensitive patients compared to classical chemotherapy treatments because of their ability to target specific molecular abnormalities associated with NSCLC cells [8-13].

Unlike traditional chemotherapy, which interferes with cell division and kills rapidly dividing cells, molecularly targeted therapy is directed towards somatic genome mutations. Along with the well-established EGFR, Kirsten rat sarcoma viral oncogene homolog (KRAS) oncogene mutations and concurrent anaplastic lymphoma kinase (ALK) and proto-oncogene tyrosine-protein kinase (ROS1) rearrangements, other gene mutations in the context of NSCLC tumorigenesis biomarkers and targets for new clinical therapies include fusions of echinoderm microtubule-associated protein-like 4 and anaplastic lymphoma kinase (EML4-ALK) and mutations of human epidermal growth factor receptor 2 (HER2), phosphatidylinositol 3-kinase (PIK3CA), protein kinase B (AKT), v-raf murine sarcoma viral oncogene homolog B1 (BRAF), mitogen-activated protein kinase 1 (MAP2K1), and mesenchymal-epithelial transition factor (MET). An improved understanding of EGFR driver mutations leads the way to the establishment of personalized clinical therapy based on genomic and proteomic testing, which is becoming a standard of care for patients with advanced NSCLC [13-15].

This review article briefly covers some of the advances in therapeutic protocols based on the novel discoveries in molecular profiles and mutational diagnostics of NSCLC, which harbor activating and resistance EGFR mutations along with corresponding genetic alterations leading to drug resistance. Further, an emphasis will be put on the developmental challenges of targeted nanomedicines for the co-delivery of therapeutic agents to lung tumors. Finally, current approaches in literature used to design nanotools loaded with logical combinations of different drugs and inhibitors of various oncogenic pathways to fight NSCLC resistance are covered.

Review

EGFR mutations and current problems in NSCLC treatment

The main reasons behind the limited success of TKI monotherapy in the suppression of lung cancer growth for an extended period are tumor heterogeneity, key signaling pathway alteration, and activation of alternate signaling, which effectively rescue the main inhibited pathway. The oncogenic significance of EGFR and the weak response to TKIs have been the focus of clinical interest for more than a decade, motivating the research community to look deeper into relevant explanations for therapeutic failure and suggest smart solutions for overcoming resistance.

There are five selective EGFR TKIs approved for the treatment of EGFR-mutated NSCLC, namely, gefitinib (GEF) and erlotinib (ERL) (first-generation reversible EGFR TKIs), afatinib (AF) and dacomitinib (DAC) (second-generation irreversible EGFR TKIs), and osimertinib (OS) (third-generation irreversible EGFR TKI). All of these drugs act as therapies of choice for NSCLC with EGFR-activating mutations [16-19].

First-generation EGFR TKIs are well-established molecularly driven therapies for lung cancer harboring specific types of activating EGFR mutations involved in the development of NSCLC (classical sensitive EGFR mutations, i.e., deletions in exon 19 and the single-point substitution mutation L858R in exon 21) [8,9]. Not all tumors with activating EGFR mutations will respond to EGFR TKI treatment. A subgroup of around 20–30% of patients harboring an activating mutation is intrinsically resistant to TKIs and shows weak clinical response, including those with wild-type EGFR NSCLC cancer. The establishment of clinical criteria for intrinsic resistance is still ongoing, and considerable efforts are made toward the estimation of the efficacy and optimal sequence of administration of different EGFR TKIs across TKI-sensitive patients with common and uncommon EGFR mutations [20]. The type of EGFR mutation influences the effectiveness of gefitinib and erlotinib across NSCLC tumors. For example, gefitinib is more efficient in treating NSCLC harboring the L858R mutation than in NSCLC expressing the G719S mutation [21]. Further, an approved treatment with EGFR TKIs for NSCLC with defined but uncommon mutations such as G719X, S768I, and L861Q is the second-generation TKI afatinib. Lastly, osimertinib is a third-generation TKI that is approved for EGFR T790M positive NSCLC with acquired resistance to first- and second-generation drugs [12,22,23]. Similar to traditional cytotoxic agents, acquired resistance to TKIs and early relapse are still significant limitations of this therapeutic approach. Following the initial pronounced response, after only 9 to 14 months around 50% of patients develop resistance to therapy with first- and second-generation TKIs as a result of T790M secondary mutation in exon 20 of EGFR [24]. Acquired resistance to TKIs is unavoidable and has already been documented even for the third generation of TKIs (target-dependent and target-independent molecular mechanisms of resistance to TKIs are presented in Table 1). Target-independent acquired resistance driven by cMET amplification after EGFR TKI treatment may be treated with crizotinib, a dual inhibitor of ALK and cMET, and brigatinib (multi-kinase inhibitor of EGFR, ALK, FLT3, and other kinases). This therapy shows effectiveness against mutant variants of EGFR and ALK that are resistant to common types of EGFR and ALK inhibitors [25].

However, only a limited number of mutations are covered by clinical therapy. In addition, some novel therapeutic approaches against resistant tumors have failed due to the heterogeneity of the progression of genetic alteration and the resulting complexity of resistance mechanisms [23]. Enormous efforts have been made in finding a way forward from this standstill, and evidence has been derived that no single drug can treat the broad spectrum of molecular alterations in NSCLC. Considering the fact that multiple mechanisms are involved in the reactivation of the EGFR signaling pathway, targeting multiple constituents within the EGFR cascade or targeting parallel pathways to prevent cross talk between multiple growth factor receptors have emerged as valid approaches that could be used to tackle cancer resistance and maximize the efficacy of EGFR inhibition. Presently, a combinatorial therapeutic strategy is believed to be a rational approach to combat the complexity of resistance and continuous cancer mutations. Co-delivery of TK inhibitors with anticancer drugs, immunotherapy, or gene-specific therapeutics to disrupt key resistance pathways, reactivate p53-mediated apoptosis, or inhibit cellular drug efflux are only a few examples of strategies used to fight cancer resistance mechanisms successfully [23,24]. In addition, co-delivery of anticancer therapy using surface-engineered nanoparticles for tumor targeting may alleviate some of the unwanted effects on off-site targets and increase the therapeutic concentration at the site of action as well as efficacy and safety of the current therapy for lung cancer treatment. Co-delivery of combined therapeutic agents at the right time and at the right place using

Table 1: Molecular mechanisms of resistance to EGFR TKIs.

Target-dependent		
Secondary exon 20 mutation: EGFR T790 (40–55% of EGFR resistance cases) and EGFR amplification **Secondary mutations with low occurrence**: D761Y (exon 19), L747S (exon 19), and T854A (exon 21)	**Tertiary mutation**: EGFR C797S; L798I Other tertiary mutations: WZ4002, L718Q, and L844V	
Secondary (T790M gatekeeper residue) and tertiary kinase domain (C797S) resistance mutation in the targeted kinase reduces drug affinity or prevents access of the TKI to the active site and reduces its efficacy. Resistance to gefitinib and erlotinib is evident when the T790 mutation is present, and the C797S mutation induces resistance to osimertinib.		
Target independent		
Bypass resistance (bypass the EGFR blockade) **MET gene amplification:** Amplified MET causes phosphorylation of ERBB3. Even when phosphorylation of EGFR is inhibited by an EGFR TKI, activation of the PI3K/AKT pathway is maintained through ERBB3 or the ERBB3/ERBB2 duet. **HGF overexpression:** HGF induces activation of the PI3K/AKT pathway through MET; this activation is independent of ERBB3 or EGFR). **HER2 amplification:** HER2 forms heterodimers with EGFR to activate downstream signaling.	Downstream signaling mutations in BRAF and PI3K, KRAS, PTEN loss, NF-1 loss, and CRKL amplification, MAPK pathway activation by mutated KRAS or MEK (less frequent events)	Phenotypic alterations epithelial-mesenchymal transition (EMT), or small cell histologic transformation

smart nanotools to exert a simultaneous effect on multiple signaling pathways, leading to the avoidance or combating of resistance as well as the prevention of side effects, is the theoretical rationale behind the use of designed nanoparticles (NPs) [26-28].

Advances in the therapeutic approaches used for overcoming NSCLC resistance

Combinatorial treatments are designed with the goal of exerting additive or synergistic inhibitory effects on the proliferation and survival mechanisms on which the cancer cells are heavily dependent. The efficacy of existing small molecules in synergistic combinations for relevant genetic mutations in resistant cancers has been evaluated in many research and clinical studies, with promising results in some types of mutant lung cancers. A plethora of multimodal treatments for the co-administration of: (i) conventional cytotoxic agents with signaling pathway inhibitor/s, (ii) inhibitors of two or more signaling pathways within a signaling network, (iii) inhibitors of multiple targets within a single pathway exerting synergistic effects, and (iv) cytotoxic or molecular targeting agents with small interfering RNA (siRNA) for silencing the mutating genes at protein and messenger RNA (mRNA) level, have made their way to clinical therapy or are under evaluation for their efficacy and safety in many research studies and several clinical trials. The synergistic effects of combination therapy depend on the status and the type of genetic alteration; as such, the most potent will be the one showing synergistic or additive effects on oncogene pathways essential for cell survival.

Conventional cytotoxic agents with signaling pathway inhibitor/s

EGFR signal transduction pathways can be roughly divided into a pro-survival arm with the PI3K-mTOR-AKT cascade and a proliferative arm with the Ras-Raf-Mek-Erk cascade. Enhanced kinase activity on mutated EGFR with exon 19 deletion is associated with upregulated c-MYC levels through the Ras-Raf-Erk pathway, promoting angiogenesis via hypoxia-inducible factor 1α (HIF-1α) and vascular endothelial growth factor (VEGF) signaling [29-31]. According to preclinical data, a combination therapy consisting of erlotinib and cisplatin targets angiogenesis and manifests synergistic and additive antitumor activity via downregulation of the c-MYC–HIF-1α–VEGF signaling pathway in mutated NSCLC with exon 19 deletions (Figure 1) [32-34]. Several randomized clinical studies have also reported on the increased effectiveness of combined chemotherapy/EGFR TKI treatments in patients with NSCLC bearing an EGFR mutation. Therefore, to prevent or delay the emergence

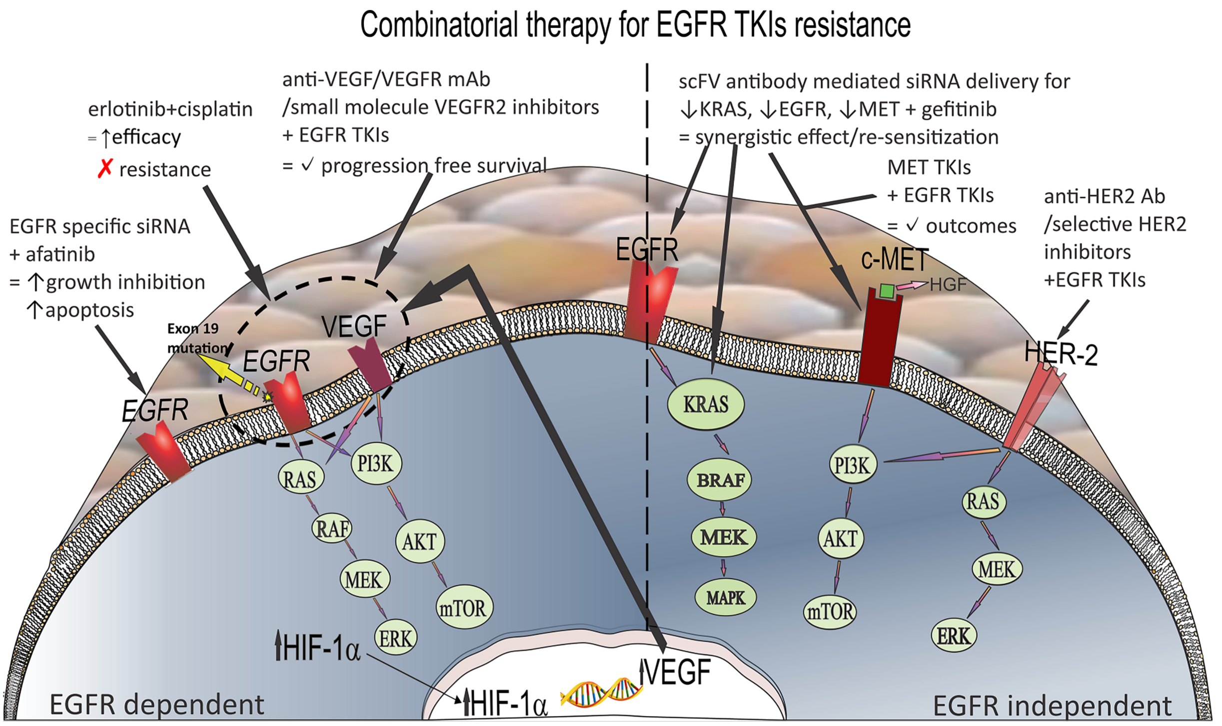

Figure 1: Examples of combinatorial therapy for (left) EGFR-dependent and (right) EGFR-independent TKI resistance. The upward-pointing black arrows indicate upregulation/increase, while the downward-pointing black arrows indicate inhibition/decrease. The black tick marks indicate a beneficial effect. The red x mark indicates a delayed or prevented event.

of acquired resistance to EGFR TKIs, adding carboplatin and pemetrexed to gefitinib is recommended as a first-line option in patients with EGFR-mutated tumors [35-40].

Inhibitors of two or more signaling pathways within a signaling network

EGFR and VEGF share common downstream signaling, although they may function independently during oncogenesis. Increased VEGF levels, which have been confirmed in cancers with acquired resistance, lead to the preservation of tumor growth when the tumor is under attack from EGFR TKIs. Because of the interplay of mechanisms, combining EGFR TKIs and VEGF inhibitors seems to be a rational approach to combat tumor resistance and increase the efficacy of anti-tumor therapy [41-45]. Several trials that compared the efficacy and safety of EGFR TKIs from the first, second or third generation combined with anti-angiogenic therapy, such as small-molecule inhibitors of VEGFR-2 (vandetanib, nintedanib, axitinib, and cediranib) or anti-VEGF/VEGFR monoclonal antibodies (ramucirumab, which is specific for the VEGFR-2 extracellular domain, or bevacizumab, a VEGF-A inhibitor), have been conducted to evaluate the efficacy of combination therapy in mutated NSCLC (Figure 1). Results from preclinical and clinical trials point to substantially improved progression-free survival in patients with EGFR-mutant NSCLC receiving combined EGFR TKIs and angiogenic therapy. However, this combined therapeutic approach has been characterized by an increased incidence of adverse reactions of grades 3–5 [41,46-53]. Nanomedicines can be used as tools for improved localization of combination therapy at the site of action, improving the outcome and decreasing the adverse effects.

Inhibitors of multiple targets within a single pathway exerting synergistic effects

Amplification, overexpression, and mutation of MET and HER2 are heavily involved in EGFR TKI resistance development, and the cross talk of these receptors is a way to avoid TK inhibition in many cancers (Figure 1). Hence, these oncogenic drivers are legitimate therapeutic targets in NSCLC with off-target mechanisms of acquired resistance to first- and second-generation TKIs. Various MET TKIs, among them crizotinib and the more selective savolitinib, tepotinib, and capmatinib, may be good candidates for EGFR TKI/MET TKI combination therapy (Figure 1). This approach shows improved clinical outcomes over chemotherapy or MET TKI monotherapy in patients with advanced EGFR-mutant NSCLC who acquired MET amplification or MET overexpression during EGFR TKI treatment [54-62].

Further, substantial evidence for the efficacy of EGFR TKIs combined with HER2-targeted therapy in patients with developed EGFR TKI resistance due to HER2 amplification can be found in the literature [63-65]. Patients with HER2 gene mutations showing resistance to EGFR TKIs may be sensitive to novel, more selective HER2 inhibitors (poziotinib and pyrotinib), HER2 targeting agents such as anti-HER2 antibodies, and small-molecule EGFR tyrosine kinase inhibitor dual therapy (Figure 1). The administration of target-specific antibody–drug conjugates (cytotoxic chemotherapy) has also been characterized by positive responses regardless of HER2-specific mutation sites. In oncogene-addicted cancers (HER2-mutant cancer, oncogene-driven EGFR-positive, ALK-positive, or RET-positive NSCLC), current studies do not encourage the use of immune checkpoint inhibitors, with the exception of KRAS-mutated cancers [61,64,65].

Despite the encouraging results of antibody–drug conjugates, acquired resistance to these agents might eventually develop following the initial positive response. Various mechanisms of acquired resistance in patients with HER2-positive locally advanced breast cancer or metastatic breast cancer involving factors crucial for their mechanism of action are reported across the literature [66,67]. This suggests that such acquired resistance might also become a common problem in advanced NSCLC treatment [68]. Some of the potential factors of resistance, such as poor internalization, defective intracellular trafficking of the HER2 antibody–drug conjugates, masking of the HER2 epitope, high rate of recycling, and the effect of upregulated drug efflux pumps, may be resolved by novel nanomedicines designed to interact with the tumor cells in a variety of ways with the goal of overcoming the limitations of the conjugates [68,69].

Cytotoxic or molecular targeting agents with siRNA

Targeting homologous mRNA sequences in cells and knockdown of receptors involved in cell survival and proliferation using RNA interference downregulates receptor protein expression, inhibits cell growth, and induces apoptosis. The effect obtained by siRNA is not influenced by the receptor alteration status and significantly decreases the gene's oncogenic potential. Chen et al. compared the efficacy of TKIs in NSCLC cells harboring different mutations with combined therapy consisting of TKIs (gefitinib, erlotinib, and afatinib) and EGFR-specific siRNA. The authors noted that combined therapy with the potent irreversible EGFR/HER TKI afatinib and EGFR-specific siRNA resulted in enhanced growth inhibition and apoptosis due to the inhibitory effect of the EGFR-specific siRNA on the overall EGFR oncogenic activity, including the downstream TKI resistance mutations (Figure 1) [70]. Lu et al. tested the efficacy of combined siRNA treatment with gefitinib in several NSCLC cell lines (A549, H1975, and H1993). The A549 cell line carried wild-type EGFR and KRAS mutations, H1975 cells expressed L858R/T790M EGFR, and H1993 cells harbored MET amplification. Therefore, three types of siRNA were used as EGFR–scFv–arginine nonamer peptide fusion protein complexes, namely siRNA for KRAS, EGFR, and MET gene expression silencing (Figure 1). The synergistic effect of gefitinib and scFv antibody-mediated siRNA delivery for silencing the expression of resistance-related genes was evidenced by a significant reduction in cell growth and increased rate of apoptosis compared to the cells treated with siRNA only. Furthermore, considering that these cell lines are EGFR-positive TKI-resistant NSCLC cells, a synergistic effect of gefitinib and siRNA may be regarded as proof of restored sensitivity of EGFR-positive NSCLC to gefitinib as a result of silencing the expression of resistance-related genes [71]. Therapy consisting of EGFR siRNA combined with EGFR TKIs and anti-EGFR monoclonal antibodies can additively enhance growth factor inhibition in vitro, maintaining its biological efficacy in cells and xenograft models with different mutation statuses [70,72-74].

Further advances in the multimodal combination therapy approach

KRAS proteins operate as guanosine diphosphate (GDP)/guanosine triphosphate (GTP) molecular switches in response to activated transmembrane receptors such as EGFR. The KRAS mutation occurs at a frequency of around 30% in NSCLC, with the KRAS p.G_{12}C mutation being the most frequent variant. Mutated KRAS cannot return to its inactive GDP form, which triggers EGFR-independent activation of several downstream effectors [75-77]. The binding of KRAS-GTP to several effectors, among them PIK3K and RAF kinases, triggers activation of downstream AKT and mTOR (PIK3K), which regulates apoptosis, metabolism, and translation, as well as MEK and ERK signaling (RAF kinases), which influences cell cycle progression and proliferation [78]. Therefore, it is expected that KRAS-mutated tumors would not respond to EGFR TKIs. Patients with KRAS-mutant NSCLC can benefit from direct KRAS inhibitors, such as sotorasib, which lock KRAS in its inactive GDP-bound form. However, a heterogeneous resistance pattern during KRASG_{12}C inhibitor treatment has been noticed after an initial positive response [78-80]. Co-targeting of upstream signaling (suppression of receptor tyrosine kinases) and downstream signal inhibition by targeting the RAF-MEK-ERK signaling cascade are tested in clinical studies as relevant approaches to delay resistance and improve KRASG_{12}C inhibitor efficacy [81,82]. Clinical data from CodeBreak 100/101 revealed promising efficacy with long-lasting anti-tumor effects when a programmed cell death protein 1 (PD-1) antibody was administered alongside a KRASG_{12}C inhibitor, suggesting that PD-1 inhibition produces a synergistic effect with sotorasib and enhances CD8-positive T-cell infiltration, which causes an inhibition of tumor growth [83-87]. In addition, there is substantial evidence that the co-delivery of siRNA that shows specific binding to mRNA of the most commonly occurring KRAS missense mutations together with a chemical EGFR inhibitor may efficiently reduce mutant KRAS-induced effects and may contribute to overcoming resistance in the treatment of NSCLC [72,88,89].

Many of the obstacles to the co-delivery of combined therapies can be resolved by nanomedicines as tools for the targeted delivery of high concentrations of anticancer drugs at their site of action. Although designated as molecularly targeted therapies, the targeting of receptors by EGFR TKIs and other receptor inhibitors is not absolute. Once the EGFR TKIs are absorbed from the gastrointestinal tract and distributed in the body, they interact with EGFR signaling pathways of many normal cells influencing their proliferation, differentiation, migration, and apoptosis. This leads to side effects, including rash, erythema, diarrhea, gastrointestinal perforations, ocular lesions, and hematological disorders. Using nanomedicines as a vehicle for the administration of TKIs may alleviate the aforementioned problems of conventional administration and (i) improve their pharmacokinetic profile, (ii) increase tumor targeting potential and localization at the tumor site, (iii) decrease the exposure of healthy tissues to the drug, (iv) minimize off-site targets and side effects, (v) even bypass, reduce, or reverse the multidrug resistance mechanisms, and/or (vi) overcome acquired resistance and sensitize mutant NSCLC cells to EGFR TKIs through the synergistic action of combined therapy against various multiple anti-tumor targets [20,22,90].

Surface-engineered nanoparticles for lung tumor targeting and co-delivery of combinatorial therapy

Simultaneous delivery of combinatorial inhibitors with the goal of targeting multiple constituents within a single pathway or different oncogenic pathways in therapeutic concentrations at the tumor site, preferentially in the tumor cell, is essential for the efficacy of the therapy. Adequate concentrations might not be achieved with conventional dosage forms mainly due to the poor localization of the free drug molecules at the site of action and the differences in bioavailability and pharmacokinetic parameters. Notably, the failure of delivery at the right time and at the right place contributes to severe systemic toxicities and ineffectiveness. Successful translation of scientific knowledge of the mechanisms of resistance combined with nanotechnology as a tool for targeted delivery may bring improvements in the efficacy of anticancer drugs and may aid in elucidating the beneficial synergistic combinations regarding lung cancer subtype treatment. Nanomedicines have the potential for (i) multivalent targeting and co-delivery of agents to endothelial cells, tumor microenvironment, and tumor cells, (ii) delivering large payloads of active substances with different physicochemical properties, such as small-molecular drugs and siRNA, to the site of action, and (iii) limiting drug resistance [91]. Nanotherapy can change the landscape of clinical lung cancer treatment by mitigating the risk of therapeutic failure due to the non-coordinated co-delivery of therapeutic agents and off-target side effects. However, despite substantial progress, a precise control of the in vivo trajectories of the nanosystems is still beyond our reach. Some of the promising approaches and design considerations in the engineering of tumor-homing nanoparticles will be discussed below with an emphasis on increased lung tumor tissue localization.

Current approaches for overcoming biological barriers and improved drug targeting

Looking back at almost half a century of research on drug targeting, experimental evidence shows that efficient tumor localization and intracellular delivery may still be very challenging. However, an improved understanding of the mechanisms involved in angiogenesis, tumor–stroma interactions, molecular heterogeneity between cancers, genetic and epigenetic alterations, and cancer marker expression has not only improved current therapeutic plans for cancer patients but has had an impact on the design approaches of the nanotools for cancer imaging and anticancer drug delivery. In recent years, new platforms to enhance the low tumor targeting capacity of nanomedicines using biomimetic targeting motifs, multifunctional and multistage nanomicelles and polymer nanoparticles, and nanostructured lipid nanocarriers, combined with precision oncology research to identify additional targetable biomarkers, have emerged. Some have been applied in the co-delivery of clinically relevant combinations of molecularly targeted drugs, chemotherapeutic agents, and siRNA.

Historically, the most promising first-generation, passive targeting, stealth polymer NPs for anticancer drug/gene delivery are hydrophobic core–hydrophilic shell NPs including (i) self-assembled kinetically stable amphiphilic block copolymer core–shell NPs, (ii) polymer–polypeptide hybrid core–shell NPs, and (iii) polymer–lipid hybrid core–shell NPs additionally decorated with ligands for overexpressed receptors on cancer cells [92]. Traditionally selected overexpressed cancer cell surface markers for the active targeting of NPs include αvβ3 integrin, aminopeptidase N (CD13), lymphocyte homing receptor (CD44), programmed death ligand-1 (CD274), folate receptor protein, nucleolin receptor, epidermal growth factor receptor (EGFR), vascular endothelial growth factor receptor (VEGFR), human epidermal growth factor receptor 2 (HER2), luteinizing hormone-releasing hormone (LHRH) receptor, and somatostatin receptors (SSTRs) [93].

Due to the complexity of the problem of specific targeting, secondary to the many different types of barriers in the body, incorporating several functionalities to address diverse barriers might improve the targeting efficacy of nanomedicines. Various solutions have been proposed to improve mononuclear phagocytic system (MPS) evasion, extravasation at the tumor site, and diffusion through the dense collagen matrix of the solid tumors. Biomimetic, multifunctional, and multistage targeted nanoscale delivery systems with improved potential for intratumor and intracellular localization, as well as sub-cellular targeting, capable of tackling several body barriers and tumor heterogeneity more efficiently, have been designed to address the problems of efficient targeting [94].

Multifunctional stimuli-responsive nanosized drug delivery carriers: Mixed-layer and multilayered nanocarriers with bioresponsive and cleavable layers, possessing different functional properties for improving the enhanced permeability and retention (EPR) effect, diffusion in the tumor microenvironment, cellular internalization and subcellular targeting, were synthesized by click coupling reactions or arranged by self-assembly and co-assembly of block copolymers. These carriers may challenge different barriers after bioresponsive cleavage of the above functionalities. One recently published example involves a micellar structure composed of a polycaprolactone (PCL) core, a mixed poly(2-dimethylamino)ethyl methacrylate/poly(ethylene oxide) (PDMAEMA$^{(TPP+)}$/PEO) middle layer, and a PEO corona. The system was self-assembled using poly(ethylene oxide)-poly(ε-caprolactone)-*b*-poly(ethylene oxide) (PEO$_{113}$-*b*-PCL$_{70}$-*b*-PEO$_{113}$) and poly(2-(dimethylamino)ethyl methacrylate)-*b*-poly(ε-caprolactone)-*b*-poly(2-(dimethylamino)ethyl methacrylate (PDMAEMA$_{20}$$^{(TPP+)}$-*b*-PCL$_{70}$-*b*-PDMAEMA$_{20}$$^{(TPP+)}$) block copolymers. PEO-PCL blocks were linked using acetal groups to enable the cleavage of the PEO blocks from the NP surface in the acidic environment of a tumor and the lysosomes, exposing the PDMAEMA layer decorated with triphenylphosphonium (TPP) ligand to the environment. The TPP lipophilic cation is characterized by a large hydrophobic surface area, which facilitates its permeation throughout phospholipid bilayers, lysosomal escape due to the proton sponge effect, and further accumulation within mitochondria [95]. Barthel et al. developed mixed-layer ABC triblock terpolymer mixed PEO shell nanomicelles of a size below 30 nm, based on poly(ethylene oxide)-*b*-poly(allyl glycidyl ether)-*b*-poly(*tert*-butyl glycidyl ether) (PEO-*b*-PAGE-*b*-PtBGE). The PAGE segment can be subsequently modified using thiolene chemistry to introduce positive charges [$-NH_2$ (cysteamine, ENT)], negative charges [−COOH (3-mercaptopropionic acid, ECT)], and active targeting ligands [thiogalactose residues (EGT)] for fine-tuning the charges in the shell in different biological environments either for higher uptake or reduced toxicity. In brief, the ABC triblock terpolymers comprised identical A and C segments. Yet, different functionalities in the middle PAGE block (B) are directly correlated to the combination and the number of functionalities and, therefore, easily adjusted to optimize the systems for different target sites, which is especially promising for nucleic acid delivery [96]. One example of multifunctional, multilayer, bioresponsive lipid polymer nanoparticles with a cleavable layer as a vessel for the co-delivery of erlotinib and bevacizumab was recently published by Pang and co-workers. Clinical studies point to the serious toxicity of conventional application, which might be mitigated with nanotools for co-delivery of therapy for the dual inhibition of VEGF and EGFR pathways. The designed nanocarrier was composed of a polycaprolactone core with bevacizumab and erlotinib, coated with a phospholipid layer, with anchors composed of hyaluronic acid–adipic acid hydralazide–poly(ethylene glycol) (HA-ADH-PEG). Hyaluronic acid-decorated lipid polymer hybrid nanoparticles (LPH NPs) specifically target overexpressed CD44 at the NSCLC cells. In the acidic tumor environment, the pH-responsive linker between HA and PEG is hydrolyzed, leading to the cleavage of the HA layer. This, in turn, decreases the NP size and enables faster tumor diffusion, improved internalization, and drug release at the site of action. These nanocarriers exhibited a high degree of tumor homing, low toxicity, and efficient tumor inhibition in vitro and in a tumor mouse model [97]. An additional example of multilayered cleavable pH-responsive nanoparticles for KRAS mutated cancer is described in Table 2.

Multistage drug delivery systems: Multistage nanocarriers address the issue of heterogenous barriers by the use of different groups of particles carrying various functional modalities. Tasciotti et al. proposed a multistage delivery system composed of stage-1 mesoporous silica particles with improved deposition in the vascular endothelium, optimized for crossing the endothelial barrier through intravascular gaps or fenestrations or actively by a transcytotic mechanism, loaded with one or more types of stage-2 nanoparticles. The payload of drug/diagnostic agent-loaded nanoparticles optimized for improved interaction with various cancer cells, including lung cancer cells, is released over time at the tumor site, showing facilitated diffusion through tumor tissue due to their smaller size and specific surface engineering [111]. Wong et al. developed a multistage system with facilitated tumor diffusive transport composed of 100 nm gelatin nanoparticles, capable of releasing 10 nm NPs from their surface, triggered by protease degradation after tumor homing by the EPR effect [112]. Mesoporous silica vesicles (MSVs; d_{av} = 3 µm) with high affinity to tumor vasculature were also described by Blanco et al. as a platform for the triggered release of various therapeutic nanoscale vectors (liposomes, gold nanoshells, and microbots) and imaging contrast nanoparticles (quantum dots and iron oxide), after homing into the tumor environment [113]. Xu et al. described an injectable nanoparticle generator (iNPG) showing substantial natural tumor tropism designed as aminopropyltriethoxysilane (APTES)-functionalized nanoporous silica particles loaded with a poly(L-glutamic acid) pH-cleavable linker–doxorubicin conjugate, which self-assembles into NPs after its release from the iNPG [114]. Li et al. designed a multistage nanocarrier for NSCLC targeting, composed of icotinib-loaded amphiphilic chitosan micelles with hyaluronic acid–doxorubicin NPs layered by electrostatic adsorption upon the micelle surface. Hyaluronic acid was used for CD44 targeting (a receptor that is often overexpressed on the surface of lung tumor cells), as well as for the optimization of biodistribution, improved tumor homing potential, and cell internalization of the nanocarriers. Due to the enhanced tumor accumulation, reduced accumulation at the off-site targets, and same-place/same-time delivery of therapeutic concentrations of both drugs at the site of action, an optimal synergistic effect of the active substances and efficient tumor inhibition was achieved [115]. Lv et al. prepared multifunctional dendrimer nanoscale complexes composed of anti-EGFR aptamer-modified poly(amidoamine) (PAMAM) loaded with erlotinib and chloroquine (CQ) for NSCLC treatment. These cationic nanoparticles showed high condensation capacity for survivin-small hairpin RNA (survivin-shRNA), which was trapped by electrostatic interactions in the cavity between several assembled nanoparticles (AP/ES+CQ NPs; AP = amine-terminated PAMAM dendrimers modified with anti-EGFR aptamer; ES = erlotinib and survivin-shRNA; Figure 2, Figure 3). The nanocomplexes demonstrated pH-dependent selective survivin-shRNA release in the acidic environment after endosomal escape and disassembly to single PAMAM nanoparticles showing continuous release of erlotinib and chloroquine. Chloroquine has a dual effect on the efficacy. It improves vascular barrier integrity and together with PAMAM, facilitates endosomal escape. Down-regulation of survivin reverses EGFR TKI resistance in T790M mutant NSCLC cells and sensitizes the tumor to erlotinib. The synergy of survivin and EGFR downregulation coupled with decreased angiogenesis results in significant inhibition of proliferation and improved induction of apoptosis [116].

Biomimetic drug delivery systems: The natural tropism of biomimetic materials for improved tissue localization has been proven to be a valuable tool in lung cancer targeting. Anselmo et al. evaluated the cell hitchhiking approach in targeting using red blood cell–polystyrene NP (200 and 500 nm) complexes (RBCsNP complexes) [119]. Compared to the free NPs, the delivery of RBCsNP complexes to the lungs, that is, the first capillary bed downstream of the IV injection of the NPs, was five-fold increased, which makes RBCsNP complexes very use-

Table 2: Examples of various nanoparticles for the co-delivery of combinatorial therapy for resistant lung tumor treatment.

Type	Co-delivered agents	Description and outcome	Ref.
polymer NPs (PLGA-PEI[a])	paclitaxel (PTX) + Stat3 siRNA	increased sensitivity of NSCLC cells to paclitaxel due to the silencing of STAT3	[98]
polymer NPs (MPEG-PLA[b])	ERL + cilengitide (Cilen; integrin αvβ3 inhibitor)	Cilen reversed EGFR resistance to ERL by inhibition of integrin αvβ3, the activator of galectin-3/KRAS/RalB/TBK1/NF-κB	[99]
polymer NPs (PEG-PLA[c])	ERL + fedratinib (FDTN; JAK2 inhibitor)	re-sensitization of EGFR resistant cancer to ERL due to suppression of JAK2/STAT3 and disruption of EGFR/JAK2/STAT3 axis	[100]
pH-responsive polymer NPs (DOX-PEI+Bcl2 siRNA[d])	doxorubicin (DOX) + Bcl2 siRNA	suppression of Bcl2 (a key regulator among the anti-apoptotic proteins) resulted in DOX enhanced antitumor efficacy	[101]
complex polymer micelles (P85-PEI/TPGS[e])	paclitaxel (PTX) + survivin shRNA (shSur)	down-regulation of survivin, enhanced paclitaxel-induced apoptosis and cell arrest in the G2/M phase	[102]
micelleplexes (pH-responsive cationic micellar nanoparticles; PDMA-*b*-PDPA[f])	paclitaxel (PTX) + Bcl-2 siRNA	suppression of Bcl2 (a key regulator among the anti-apoptotic proteins) resulted in enhanced antitumor efficacy of PTX	[103]
multilayered PAA cleavable pH-responsive nanoceria (FA-PAA-PNC[g])	doxorubicin + ganetespib	ganatespib synergizes and accelerates therapeutic efficacy of DOX via ROS production	[104]
multistage solid lipid NPs (SLNs) loaded in microspheres	afatinib (AFT) + paclitaxel (PTX)	synergistic effect of afatinib and PTX due to inactivation of p70 s6 kinase by PTX and inactivation of PI3K/AKT/mTOR	[105]
liposomes (PEGylated lipo-DTX/siRNA NPs[h])	docetaxel (DTX) + Bcl-2 siRNA	suppression of Bcl2 (a key regulator among the anti-apoptotic proteins) resulted in enhanced DTX antitumor efficacy	[106]
nanostructured lipid carriers (LHRH-decorated NLC-PTX-siRNA[i])	paclitaxel (PTX) + gefitinib (GEF) + siRNA targeted to EGFR	i) suppression of EGF tyrosine kinase signaling pathways, ii) prevention of EGF receptor protein synthesis, and iii) induction of cell death by the microtubule-stabilizing drug paclitaxel lead to an enhanced therapeutic effect in EGFR TKI resistant cancer	[107]
polymer-coated magnetic NPs (FA-PAA-Pt(MCO)$_2$(Pt) + ganetespib[j])	platinum cyanoximate complex + ganetespib	ganetespib effectively suppressed KRAS mutated cancer cells when co-delivered with Pt-agents and prevented multidrug resistance	[108]
PEG-modified metallic NPs (IR780@INPs-CTX[k])	cetuximab + IR780 (sonodynamic therapy)	combinatorial treatment compensates for cetuximab-resistant mutations due to the ROS-generating potential of IR780, which promotes cell apoptosis and inhibits proliferation	[109]
PEG-modified photoresponsive metallic nanocarriers	gefitinib + CuS (photodynamic switching)	re-sensitization to gefintinib as a result of the inactivation of bypass signaling in gefitinib resistant tumors due to increased ROS levels which downregulate expression of IGF1R and its downstream AKT/ERK/NF-kB signaling	[110]

[a]PLGA-PEI NPs covered with a PEI corona; [b]methoxy poly(ethylene glycol)–poly(ʟ-lactide) NPs; [c]poly(ethylene glycol)–poly(lactic acid) NPs; [d]doxorubicin–polyethyleneimine conjugate via a pH-sensitive linker mixed with Bcl2 siRNA; [e]Pluronic P85–polyethyleneimine conjugate and ᴅ-α-tocopheryl–polyethylene glycol 1000 succinate complex NPs; [f]pH-responsive poly(2-(dimethylamino) ethyl methacrylate)-*b*-poly(2-(diisopropylamino) ethyl methacrylate) NPs; [g]folic acid-decorated polyacrylic acid-coated pH-responsive cerium oxide NPs; [h]PEGylated cationic liposome complex with Bcl-2 siRNA; [i]luteinizing hormone-releasing hormone decapeptide-decorated multifunctional nanostructured carriers prepared by self-assembly of liquid/solid lipids, surfactants, and cationic lipids; [j]folate-ligated PEGylated polyacrylic acid-coated magnetic NPs with encapsulated platinum cyanoximate complex and ganetespib; [k]PEG-modified (distearoyl-glycero-phosphorylethanolamine-PEG-COOH) iron tetroxide core nanoparticles loaded with IR780 and decorated with cetuximab.

ful for lung tissue targeting. Once in the lung microcirculation, the RBC-bound NPs are mechanically detached from the RBCs when the RBCs are squeezed through the tiny capillaries of the air–blood barrier and transferred to the endothelium by nonspecific interactions. When decorated with vascular endothelium-specific ligands, as in the case of RBCs anti-PECAM mAb-coated polystyrene NPs, the complex showed a 760-fold increase in the lung-to-liver distribution ratio compared to non-specific NPs. Different studies envision RBCsNPs complexes as a highly performant platform for augmented NP localization, which can be easily translated to drug delivery systems for lung and brain targeting [119-122].

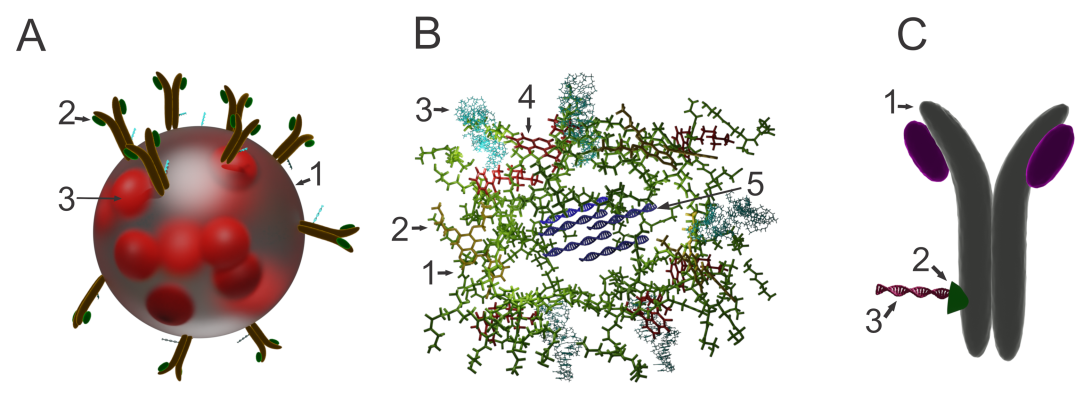

Figure 2: (A) Gefitinib-loaded gelatin-A NPs functionalized with a cetuximab-siRNA conjugate (Ab-SiRNA-GelGEF NPs). 1: Gelatin-A nanoparticle, 2: cetuximab–KRASG12C-specific siRNA conjugate, and 3: gefitinib [117]. (B) Multifunctional dendrimer nanocomplex. 1: poly(amidoamine) (PAMAM) nanoparticle, 2: erlotinib, 3: anti-EGFR aptamer, 4: chloroquine, and 5: survivin sh-RNA trapped in the cavity between PAMAM nanoparticles structured together in a dendrimer nanocomplex (AP/ES+CQ NPs; AP = amine-terminated PAMAM dendrimers modified with anti-EGFR aptamer; ES = erlotinib, and survivin-shRNA) [116]. (C) Cetuximab–cationic gelatin–specific siRNA delivery system (CTB-cGel-siRNA conjugate). 1: Cetuximab, 2: cationic gelatin, and 3: KRASG12C-specific siRNA [118].

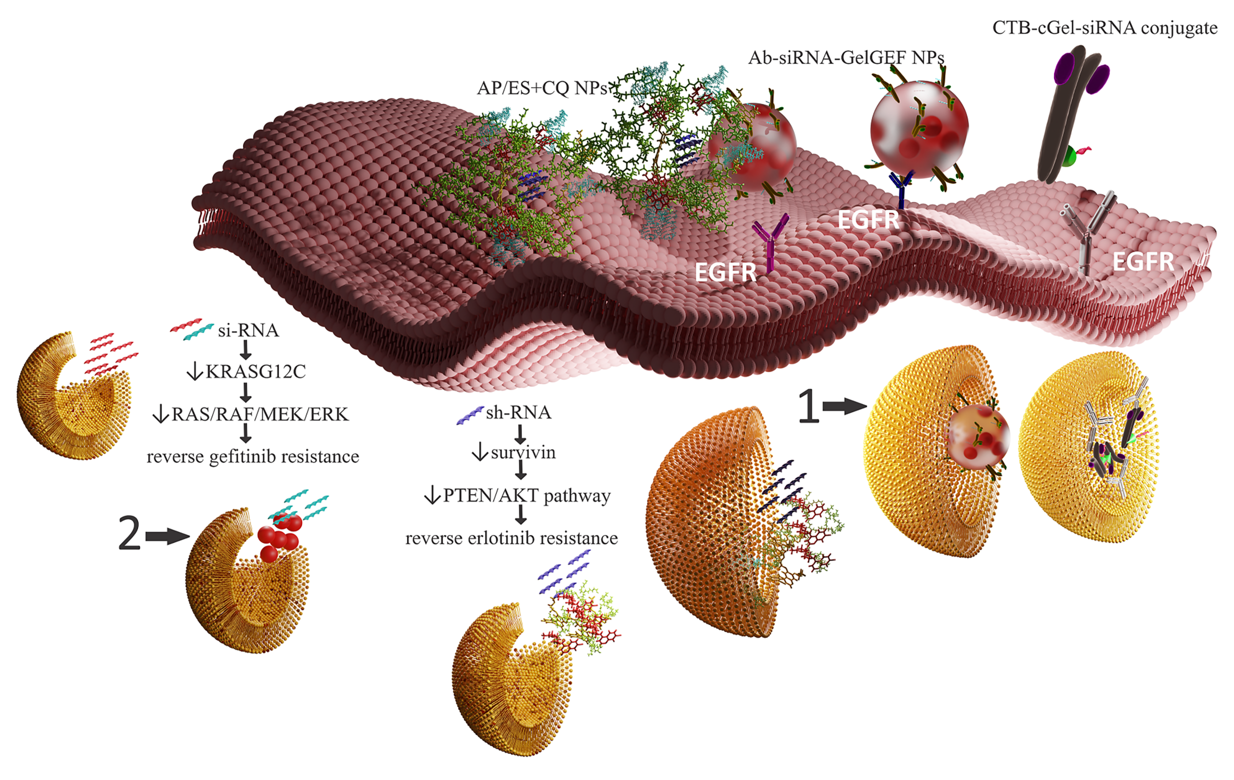

Figure 3: Nanotools for reversal of EGFR TKI resistance by RNAi. Favorable cell internalization was mediated by anti-EGFR aptamer/EGFR interaction (AP/ES+CQ) and cetuximab–EGFR interaction (Ab-siRNA-GelGEF NPs; CTB-cGel-siRNA conjugate). Efficient transfection was enabled by endosomal escape facilitated by (i) endosomal buffering and the proton sponge effect of chloroquine and PAMAM dendrimer (AP/ES+CQ), (ii) proton sponge effect of Ab-siRNA-GelGEF NPs, and (iii) proton sponge effect the CTB–cationic gelatin–siRNA conjugate. 1: Early endosome and 2: late endosome. This figure contains a modified version of “Liposome” by rafeequemv1 CC BY 3.0. This figure contains a modified version of "Antibodies IgG" by LucasPresoto is licensed under CC BY 4.0.

Biomimetic cell membrane protein-decorated NPs successfully mitigate immune system recognition, increase blood circulation time, improve nonspecific tumor targeting, and increase tumor homing potential. NPs with red blood cell-like (RBC) surfaces, a “do not eat me” CD47 cell signal, and an immuno-suppressive protein shell instead of, or combined with, a PEG corona are among the most common biomimetic cell membrane-based NP examples in literature. So-called red blood cell vesicle shell nanoparticles (RVPNs), or RBC-mimetic NPs, showed significant retention in the systemic circulation and significantly decreased macrophage uptake compared to the conventional NPs with PEG corona [123]. Improved targeting may be achieved by RVPNs coupled with the tumor-penetrating peptide iRGD specific to αv integrins and neuropilin-1 receptors. After binding to αvβ3 and αvβ5 integrin receptors in the tumor vasculature, iRDG is subsequently cleaved by cellular proteases to a fragment with a stronger affinity for the neuropilin-1 receptor. Neuropilin-1 receptor binding triggers extravasation and initiates deep tissue penetration, intratumoral dissemination, and infiltration into the tumor parenchyma [123-125]. RVPNs decorated with a composite of an anti-EGFR single-domain antibody and iRGD provided long circulation time, improved extravasation and tumor localization, enhanced parenchymal penetration, as well as increased interaction with the overexpressed EGFR receptors [126]. Such multifunctional nanocarriers with multistage targeting hold promise for improved efficacy of treatment and increased the intracellular availability of anticancer agents for solid tumors with EGFR overexpression, among them lung cancer.

Leuko-like membrane-decorated NPs, platelet membrane-coated core–shell nanovesicles, and cancer cell membrane-coated nanoparticles are also versatile biomimetic nanocarriers showing improved biodistribution and increased tumor-homing potential [127-130]. Among them, cancer cell membrane biomimetic NPs may demonstrate specific homologous targeting to cancer cells [131]. In addition, hybrid cell membrane biomimetic shells composed of fused red blood cell membrane and homotypic cancer membrane materials may significantly contribute to personalized nanomedicine design for targeting various tumors [132].

One example of biomimetic NPs was described designed by Wang and co-workers. They used the natural tropism of mouse bone marrow mesenchymal cells (MSCs) for lung tumors for improved targeting of docetaxel (DTX) NPs (DTX-loaded polylactide-*co*-glycolide-*b*-poly(ethylene glycol); PLGA-*b*-PEG) loaded into the MSCs. The authors used animal models to show predominant lung trapping of MSCs in both rabbit and monkey. In vitro experiments in A549 NSCLC cells pointed to the release of the DTX-loaded PLGA-*b*-PEG NPs from the MSCs and their subsequent internalization. Efficient internalization and tumor inhibition were also confirmed in an in vivo lung cancer mouse model [133].

Models for drug targeting via nanocarriers and ideas for the resolution of the main drawbacks regarding their performance are numerous. Only a choice of approaches was discussed in this section giving rational solutions for improving the homing potential and decreasing off-site targets, which is one of the major issues in targeted system design. Experimental options are endless, but experience from clinical studies is still insufficient when it comes to the clinical development of nanosystems with high homing potential and acceptable toxicological profiles [134]. A systematic approach in synthesizing statistical copolymer libraries, fine-tuning nanoparticle biointeractions, and polymer bioresponsiveness, hand in hand with cell culture experiments for fast screening and dynamic cell culture models, may greatly improve the successful outcomes in the engagement of nanotools in clinical treatments in the future [135]. Recently, lipid nanocarriers gained a lot of attention owing to their ability to carry and efficiently deliver gene therapy materials and antigens. Some of the approaches for their fine-tuning for lung cancer targeting and nucleic acid co-delivery for the treatment of resistant lung cancer will be discussed below.

The challenge of nucleic acid tumor targeting

Silencing target genes using siRNA is an attractive therapeutic approach with significant translational potential in lung cancer treatment. The high specificity of siRNA in the downregulation of oncogenes offers numerous advantages in combinatorial lung cancer treatment for targeting mutations that contribute to the resistance to cancer therapy. Synthetic siRNA can be designed to inhibit any target gene expression and consequently prevent or decrease target protein expression, thus, altering the proliferation of cancer cells. Separate transcripts or mutations may also be specifically targeted using siRNA according to the genetic tumor profiling of resistant tumors. The increase in understanding of driver mutations of oncogenes and molecular mechanisms that contribute to cancer therapy resistance encouraged the therapeutic application of RNA interference as a powerful tool to fight resistant tumors. Knockdown of oncogenic genes involved in drug resistance combined with traditional therapy or molecularly targeted agents for subsequent tumor killing may alleviate the issue of resistance. Some of the recent approaches in the design of nanocarriers for overcoming the challenges of siRNA delivery and therapeutic nanosystems for combined RNAi treatments of resistant NSCLC will be discussed below.

The delivery of siRNA therapy to its targets in vivo is a demanding task limited by extracellular and intracellular challenges. Combinatorial therapy further complicates the right-time, right-place co-delivery of siRNA with other active ingredients due to the differences in the physicochemical properties, delivery, and stability problems. The nanoparticle core for siRNA delivery should generally be positively charged to facilitate siRNA loading by electrostatic interactions. Frequently used traditional polymer materials as nonviral vectors for siRNA encapsulation are polyethyleneimine (PEI), cationic dendrimers, phospholipids, cationic lipids, polysaccharides such as cyclodextrin, inulin, and chitosan. These polymers are used alone or combined with amphiphilic polymers for core–shell nanoparticles such as the triblock polymer poly(L-lactide)-poly(ethylene glycol)-poly(L-lactide) (PLLA-PEG-PLLA) to increase the stability and decrease the immunogenicity of the nanosystems [136,137].

Lipid nanoparticles (LNPs) in clinical trials are mainly composed of ionizable cationic lipids, amphipathic phospholipids, cholesterol, diffusible PEG lipids (for transient protection), and a targeting ligand [138]. After IV administration, lung capillaries receive the entire cardiac output, but successful lung localization of nanocarriers depends upon NP interaction with the endothelial cells. Lung endothelial cells are an important target for drugs and gene delivery as they are involved in processes such as inflammation, vascular permeability, and tumor growth. Also, they play an important role in cancer development [139,140]. However, efficacy or functional delivery cannot be predicted by solely considering the biodistribution. Endothelial transcytosis and improved tropism to tumor tissue/cells, internalization rate, intracellular trafficking, and endosomal release are crucial to maximize the delivery or co-delivery of active agents to the site of action in the cell [141].

State-of-the-art LNPs for siRNA gene silencing, that is, stable antisense–lipid particles (SALPs) and stable nucleic acid–lipid particles (SNALPs), were recently developed as PEGylated lipid carriers based on ionizable lipids with pKa values between 6 and 7. Onpattro^{TM} is the first RNAi therapy used for liver-based gene silencing approved by the FDA and EC and is a SNALP transfection system based on transient PEGylation. The lipid components of these benchmark LNPs for siRNA and mRNA delivery to the liver are: (i) DLin-MC3-DMA (an ionizable cationic lipid that contains amine functions with an acid dissociation constant of ca. 6.5, neutral at physiological pH and relatively non-toxic and non-immunogenic because of a low surface charge in the physiological environment), (ii) distearoyl phosphatidylcholine (DSPC), (iii) cholesterol, and (iv) PEG$_{2000}$-C-DMG (PEGylated myristoyl glyceride, a lipid with C_{14} acyl chains). The PEGylated lipids (PEG$_{2000}$-C-DMG) are conjugated with short anchors to the NP lipid membrane, which allows for their redistribution from the NP surface in the surrounding environment and exposure of the ionizable lipids at the surface of the LNPs. After dissociation of the PEGylated lipids, the naked surface of the particles containing the ionizable DLin-KC2-DMA, which is neutral in a biological environment, interacts with apolipoprotein E (ApoE), enabling ApoE liver-mediated targeting. Transient PEGylation facilitates not only the localization and interaction with the target cell but also improves ion pair formation between the ionizable lipid (which will become cationic at pH 4) and the anionic endogenous endosomal phospholipids. This will enable the fast release of the payload into the cytoplasm and efficacious transfection [142-148]. Besides the efforts for liver and liver hepatocyte targeting, different research groups are working on the challenge of developing lipid nanoparticles for specific organ targeting after IV administration, including lipid nanoparticles for lung targeting or targeting relevant cell types, that is, epithelial cells, endothelial cells, immune cells of the lungs, B cells, and T cells. Data regarding the biodistribution of polymers, polymer lipids, and lipid nanoparticles indicate that the internal and external nanoparticle charges are one of the most influential factors for selective organ and tissue tropism of nanostructured LNPs [149-153]. Cheng et al. added 1,2-dioleoyl-3-(trimethylammonium) propane (DOTAP), a permanently charged quaternary amino lipid, to SNALPs used for Onpattro^{TM}. They reported a shift of the protein expression profile from liver to spleen and lungs. The authors also pointed to charge-mediated changes in organ distribution, depending on the type of lipid, upon IV injection of LNPs fine-tuned for organ tropism with increasing DOTAP concentration. Components of the NPs fine-tuned with DOTAP were 5A2-SC8 (a degradable dendrimer ionizable cationic lipid with $pK_a < 8$), 1,2-dioleoyl-*sn*-glycero-3-phosphoethanolamine (DOPE), cholesterol, 1,2-dimyristoyl-*rac*-glycerol-methoxy(poly(ethylene glycol)) (DMG-PEG; 15/15/30/3, mol/mol), and mRNA (5A2-SC8/mRNA, 20/1, wt/wt) [154,155]. Although it is still a challenge to design SNALPs for efficient tumor cell targeting, the design of lung-, spleen- and liver-specific mRNA LNPs for selective organ targeting (SORT) is evidence that there is a light at the end of the tunnel and a solution for nucleic acid delivery problems for cancer and gene therapy. Additional findings in the field emerged with the combinatorial synthesis of SORT lipid libraries, which improved screening, selection, and optimization of ionizable SORT lipids for exclusive organ/tissue localization.

Considerable effort has also been made to understand the influence of the chemical properties (head structure, tail length, degree of unsaturation, and degree of branching) of lipidoids (i.e., above cationic lipid-like materials) and the lipidoid tail structure on biodistribution and efficacy of the NPs. It has been found that imidazole-based synthetic lipidoids preferentially target the spleen, the amide-containing lipidoids contribute to increased lung targeting, and lipidoids with ester bonds in the tail tend to deliver mRNA into the liver [156]. Rational design of LNPs by in vitro and in vivo optimization of morphology and ratio of the lipid components and their physicochemical properties (polar headgroup, linker region, and type and length of hydrophobic domain), PEG amount, PEG lipid alkyl length, as well as the physicochemical properties of the LNPs (zeta potential, pK_a value, and structure and conformation of the lipid bilayer) will result in improved targeting, localization, internalization, and endosomal escape. This will increase the potency of the NPs. The FIND project is a high-throughput approach to identify and define the rational design of LNPs for functional delivery of mRNA to the liver and non-liver tissues and targeted gene editing. Structure–activity relationships of the LNPs are discovered by building and evaluating different LNP libraries [153]. Studies should also intensify in the area of nanoscale biointerface interactions and their influence on specific targeting and internalization, improved tolerability, and the reduction of immunogenicity and off-target effects that may generate systemic cytokines, activate complements, and intensify the frequency of the side effects.

A multifunctional envelope-type nanodevice (MEND), inspired by the influenza virus, for lung endothelial cell siRNA targeting was recently reported in the literature. The authors discussed that the developed Glu-Ala-Leu-Ala peptid (GALA)-MEND NPs could be clearly distinguished from conventional cationic lipoplexes and polyplexes, which are known for their high frequency and magnitude of coagulant, inflammatory, and hemolytic side effects. Conventional cationic complexes may form large aggregates with erythrocytes, which will drive lung accumulation, induce microinfarctions and ischemia and cause possible myocardial damage. The GALA-MEND structure consists of a complex of siRNA and PEI, encapsulated in a cationic liposomal envelope (di-octadecenyl-trimethylammoniumpropane (DOTMA)/egg phosphatidylcholine (EPC)/cholesterol), the surface of which was modified with cholesteryl GALA (Chol-GALA) and stearylpolyethylene glycol 2000 (STR-mPEG2000). GALA is a synthetic pH-sensitive peptide inspired by the envelope-type influenza virus. GALA improves siRNA delivery to endothelial cells after its structural transformation in the acidic environment of the endosomes, which facilitates endosomal membrane fusion and endosomal escape. This artificial virus-like vector and nucleic acid carrier showed high efficacy in targeting the lung endothelium because of lectin receptor recognition by the GALA protein. When intravenously administered to mice, due to the high targeting potential and efficacious siRNA delivery, GALA-MEND induced more than 80% gene knockdown compared to the non-treated group and successfully suppressed lung metastasis by approximately 50% compared with the control groups [157,158]. Santiwarangkool et al. tried to improve the lung-targeting potential of GALA peptide-decorated liposomes by adding a polyethylene glycol linker between GALA and the lipid surface. Liposomes modified with GALA/PEG2000 showed increased lung accumulation after IV administration in mice and were internalized more efficiently by human lung endothelial cells (HMVEC-L) compared with GALA/Chol-modified liposomes [159]. Targeting and functional efficacy of siRNA-loaded GALA/PEG2000-MENDssPalmE NPs modified with an intracellular environment-responsive lipid-like material (i.e., pH-activated ssPalmE) resulted in highly efficient knockdown of a lung endothelium specific gene in a mice model. Compared to GALA-modified NPs, GALA/PEG2000 as a ligand resulted in a more efficient gene knockdown. Abd Elwakil et al. further investigated the possibilities for improvement of gene silencing efficacy and targeting potential of GALA-MEND for siRNA delivery to the lung endothelium. They replaced DOTMA with a pH-sensitive lipid (YSK05) in the LNPs. The incorporation induced a dramatic improvement in silencing efficiency by enhancing endosomal escape. However, this also caused a reduction in lung selectivity, raising the awareness that not only the targeting ligand but also the composition of the nanosystem itself heavily influences the nanoscale biointeractions and the organ selectivity. GALA/YSK05-MEND NPs were more efficient than a previously developed MEND with a robust lung endothelium gene knockdown at small doses of 0.01 mg siRNA·kg^{-1} [160]. Hagino et al. optimized GALA/YSK05-MEND-modified LNPs for pDNA delivery to the lungs. They prepared a double-coated MEND composed of DOPE/STR-R8 (9.55:0.45) as the inner coating, while the outer coating was composed of DOTMA/YSK05/Chol/DMG-PEG/CholGALA (4:4:2:0.3:0.4). The MEND showed a higher lung/liver ratio and efficient gene expression in the lung [161].

Co-delivery of cytotoxic agents, chemical inhibitors, and nucleic acids using nanocarriers

Garbuzenko et al. designed LHRH decapeptide-decorated multifunctional nanostructured lipid carriers (NLCs) for co-delivery of siRNA and paclitaxel as combined therapy for resistant NSCLC. Suppression of four types of EGFR tyrosine kinases (TKs) by a pool of siRNAs resulted in a three- to sevenfold greater in vitro efficacy of the LHRH-NLC-siRNAs-PTX combined therapy compared to gefitinib in three cell lines with decreasing order of gefitinib sensitivities, H3255, A549, and H1781, regardless of the EGFR TK mutation status. LHRH peptide may influence biodistribution and cell internalization as it is overexpressed in many types of cancer cells, including human lung cancer cells. In contrast, no detectable levels can be found in liver, kidney, spleen, heart, muscle, and lung. The LHRH-decorated nanomedicines showed a favorable lung distribution after IV and pulmonary administration in a mouse model and superior anticancer effect in a human lung orthotopic A549 mouse model compared to the treatment with a local inhalation with gefitinib [162]. Another example of LHRH-decorated multifunctional nanostructured lipid nanocarriers for EGFR-resistant cancer is described in Table 2.

Aiming to improve tumor response and regression, Xue et al. proposed lipid/polymer nanocarriers composed of 7C1 (i.e., PEI-C_{15} carbon lipid) mixed with C_{14}PEG2000 for concurrent delivery of miR-34a and siKRAS, to restore the p53-regulated tumor suppressor mRNA levels in lung tumor and reduce KRAS gene expression. Restored miR-34a levels accompanied with KRAS gene knockdown and reduced MAPK signaling in KRAS-mutant cancers, increased apoptosis, and reduced tumor growth in a physiologically relevant mouse model of human lung adenocarcinoma. Multigene therapy proved to be more efficient compared to single-RNA treatment and, when combined with chemotherapy (cisplatin), further improved survival. Considering novel achievements in the field of design of LNPs with specific organ/tissue/cell tropism, combined siRNA/microRNA treatments may be used for personalized therapies targeting primary and metastatic cancer sites [163].

Kim et al. demonstrated that single or combined (Vim and/or JAK3) siRNA delivery to EGFR-overexpressing tumor cells using anti-EGFR immunolipoplexes coupled with cetuximab or immunoviroplexes decorated with fusogenic viral envelope proteins resulted in efficient reduction of cell viability and a potent anticancer effect [164].

Li et al. designed self-assembled lipid prodrugs for the delivery of therapeutic concentrations of two chemotherapeutic agents at the same time and the same place in order to avoid differences in pharmacokinetic profiles and optimize combination synergy in the treatment of NSCLC. The study highlighted the superiority of the co-delivery of PUFAylated (polyunsaturated fatty acid) cisplatin and SN38 chemotherapeutic agents assembled in PEGylated lipid nanomedicines using 1,2-distearoyl-*sn*-glycero-3-phosphoethanolamine-*N*-[methoxy-(polyethyleneglycol)2000] (DSPE-PEG2k), in comparison to single-drug therapy. The remarkable increase in the efficacy in mice harboring a cisplatin-resistant lung tumor xenograft was due to the SN38-altered DNA repair combined with the inhibition of ATM/Chk2/p53-mediated pathway, which imposes additional DNA damage. Therefore SN38, when acting at the same time as cisplatin, augments its efficacy and prevents cisplatin resistance [165].

Polymer–lipid hybrid systems or polymer systems are also described as carriers for the co-delivery of siRNA. Gao et al. suggested a combined immunotherapeutic approach involving PD-L1-siRNA and IL-2 pDNA delivered to NSCLC using PEI lipid nanoparticles (PEI-stearic acid/dipalmitoyl phosphatidylcholine/cholesterol NPs) [166]. The co-delivery of IL-2, a key regulator of T-cell activation, with PD-L1 siRNA for immune checkpoint blockade, contributes to the appropriate immune cell equilibrium and optimizes long-term anti-PD-L1/IL-2 immunotherapy [166,167]. The authors argue that the combination of PD-L1 knockdown siRNA and immunostimulatory pDNA/IL-2 delivered using LNPs reduces the drug resistance rate and leads to enhanced anti-tumor activity while also providing tumor-selective therapeutic properties [166].

Ultrasmall, less than 30 nm, theranostic micelles with a magnetic core surrounded by a DSPE-PEG2000 phospholipid layer, loaded with erlotinib and decorated with bevacizumab (Bev + Erl@MNPs) were developed by Wang et al. for the treatment of refractory NSCLCs expressing EGFR wild-type (EGFR-wt) genes. Their aim was to evaluate the capacity of the actively targeted erlotinib-based nanoscale agent to sensitize wild-type EGFR to TKIs. The authors pointed to a dual effect involving the successful sensitization of EGFR-wt to erlotinib, potent tumor inhibition, and bevacizumab-induced normalization of the tumor-embedded vessels in a mouse model. Vascular normalization as an additional effect to the co-regulatory relationship and dual inhibition of VEGF and EGFR pathways was proven to be a promising strategy to enhance cell apoptosis of NSCLC cells in vivo [168]. Such combination therapies, including the co-delivery of cetuximab and afatinib, are useful in restoring the sensitivity towards third-generation specific mutation inhibitors in tumors with acquired resistance, including Src-AKT pathway activation and the recently reported EGFR wild-type allele amplification [169].

Recently, two cetuximab-decorated gelatin-based KRASG$_{12}$C-specific siRNA delivery systems showing successful KRAS oncogene knockdown leading to sensitization of the cancer cells to gefitinib were described in the literature. In the cetuximab–cationic gelatin–KRASG12C-specific siRNA gelatin antibody delivery system (GADS; CTB-cGel-siRNA conjugate), positively charged gelatin had a dual role. It acted as a linker between the antibody and the siRNA and as an endosomal escape agent for efficient delivery of the siRNA in the cell cytoplasm due to its charge reversal properties (Figure 2, Figure 3) [118]. The second system composed of gefitinib-loaded gelatin-A NPs functionalized with a cetuximab-siRNA conjugate (Ab-siRNA-GelGEF NPs) also efficiently delivered stable siRNA to the cell cytoplasm in vitro and in vivo in a mouse model (Figure 2, Figure 3). This successfully sensitized the cancer cells to gefitinib through GAB1-SHP2 dissociation, disabling the feedback loop between Ras and AKT pathways and causing 70% loss in cell viability of KRAS-mutant NCI-H23 NSCLC cancer cells [117].

Conclusion

A rigorous understanding of the challenges regarding efficient cancer cell targeting and the engineering of corresponding nanosystems is relevant to attack multiple molecular targets simultaneously, overcoming acquired drug resistance, and increasing the therapeutic potential of molecularly targeted agents, anticancer drugs and immunotherapy. Experimental options for nanomedicines with improved targeting and homing potential are endless. However, clinical studies have often resulted in dubious results and are often accompanied by an unacceptable toxicological profile. The recent focus on large-scale screening and optimization of tumor homing agent libraries for the fine-tuning of polymer NPs and the synthesis of statistical libraries of lipid NPs with balanced biointeractions and bioresponsiveness may significantly improve the outcomes of clinical treatments based on actively targeted nanotools with improved cell internalization and selective intracellular delivery. Multifunctional and multistage nanocarriers designed to overcome different barriers, to interact with the environment, and to respond to the inherent heterogeneity of the tumors should yield advantages over conventional nanocarriers. Novel strategies for precise delivery to specific intracellular targets may resolve cancer resistance issues. They may also increase the efficacy of co-delivery of combined therapy to block or knockout oncogenic genes using RNAi, reverse drug resistance, and subsequently kill the tumor using molecularly targeted or anticancer agents. Knockout of overexpressed resistance genes or removal of the functional regions of drug resistance genes to reverse the resistance of NSCLC can be performed by gene editing and CRISPR/Cas9 technology. However, additional conclusive data to ensure the feasibility of the approach are still needed.

Appendix

Table 3 shows all abbreviations and their meanings/explantions used in the text.

Table 3: List of abbreviations.

Abbreviation	Meaning/explanation
Ab-siRNA-GelGEF	gefitinib loaded gelatin-A NPs functionalized with a cetuximab-siRNA conjugate
ADH	adipic acid hydralazide
AF	afatinib
AKT	protein kinase B
ALK	anaplastic lymphoma kinase
AP	amine-terminated PAMAM dendrimers modified with anti-EGFR aptamer
AP/ES+CQ	anti-EGFR aptamer modified poly(amidoamine) (PAMAM) nano complexes loaded with erlotinib/chloroquine and electrostatic interaction trapped survivin-shRNA
ApoE	apolipoprotein E
APTES	aminopropyltriethoxysilane
ATS	American Thoracic Society
Bev + Erl@MNPs	theranostic micelles with a magnetic core surrounded by a DSPE-PEG2000 phospholipid layer, loaded with erlotinib and decorated with bevacizumab
BRAF	v-raf murine sarcoma viral oncogene homolog B1
CD8	cluster of differentiation 8
CD13	aminopeptidase N
CD44	lymphocyte homing receptor
CD47	integrin-associated protein
CD274	programmed death ligand-1
Chol-GALA	cholesteryl GALA
cMET	mesenchymal-epidermal transition factor
c-MYC	cellular myelocytomatosis protein
CQ	chloroquine
CRKL	CRK like proto-oncogene, adaptor protein
CTB-cGel-siRNA conjugate	cetuximab-cationic gelatin-specific siRNA delivery system
DAC	dacomitinib
DLin-KC2-DMA	2,2-dilinoleyl-4-dimethylaminoethyl-[1,3]-dioxolane
DLin-MC3-DMA	(6*Z*,9*Z*,28*Z*,31*Z*)-heptatriaconta-6,9,28,31-tetraen-19-yl 4-(dimethylamino)butanoate
DOPE	1,2-dioleoyl-*sn*-glycero-3-phosphoethanolamine
DOTAP	1,2-dioleoyl-3-(trimethylammonium)propane
DOTMA	dioctadecenyl-trimethylammoniumpropane
DSPC	distearoyl phosphatidylcholine
DSPE	1,2-distearoyl-*sn*-glycero-3-phosphoethanolamine

Table 3: List of abbreviations. (continued)

DSPE-PEG2000	1,2-distearoyl-*sn*-glycero-3-phosphoethanolamine-*N*-[amino(polyethylene glycol)-2000]
DTX	docetaxel
ECT	3-mercaptopropionic acid
EGFR	epidermal growth factor receptor
EGT	thiogalactose residues
EML4-ALK -ALK	echinoderm microtubule-associated protein like 4 and anaplastic lymphoma kinase
EMT	epithelial-mesenchymal transition
ENT	cysteamine
EPC	egg phosphatidylcholine
EPR	enhanced permeability and retention
ERBB2	receptor tyrosine-protein kinase erbB-2
ERBB3	receptor tyrosine-protein kinase erbB-3
ERK	extracellular signal-regulated kinase
ERL	erlotinib
ERS	European Respiratory Society
ES	erlotinib and Survivin-shRNA
FLT3	fms-related receptor tyrosine kinase 3
GADS	gelatin antibody delivery system
GALA	peptide with glutamic acid-alanine-leucine-alanine repeats
GDP	guanosine diphosphate
GEF	gefitinib
GTP	guanosine triphosphate
HA	hyaluronic acid
HER2	human epidermal growth factor receptor 2
HGF	hepatocyte growth factor
HIF-1α	hypoxia inducible factor 1α
HMVEC-L	human lung endothelial cells
IASLC	International Association for the Study of Lung Cancer
iNPG	injectable nanoparticle generator
iRGD	red blood cell vesicle shell nanoparticles coupled with tumor penetrating peptide
JAK3	Janus kinase 3
KRAS	Kirsten rat sarcoma viral oncogene homologue
LHRH	luteinizing hormone-releasing hormone
LNP	lipid nanoparticles
LPH NPs	lipid polymer hybrid nanoparticles
MAPK	mitogen activated protein kinase
MAP2K1	mitogen-activated protein kinase 1
MEK	mitogen activated protein kinase kinase
MEND	multifunctional envelope-type nano device
MET	mesenchymal-epitehelial transition factor
MPS	mononuclear phagocytic system
mRNA	messenger RNA
MSC	mouse bone marrow mesenchymal cells
MSVs	mesoporous silica vesicles
mTOR	mammalian target of rapamycin
NF-1	neurofibromin 1
NLC	nanostructured lipid carriers
NPs	nanoparticles
NSCLC	non-small cell lung cancer
OS	osimertinib
PAGE	poly(allyl glycidyl ether)

Table 3: List of abbreviations. (continued)

PAMAM	poly(amidoamine)
PCL	polycaprolactone
PD-1	programmed cell death protein 1
PD-L1	programmed death-ligand 1
PDMAEMA	poly(2-dimethylamino)ethyl methacrylate
pDNA	plasmid DNA
PECAM	platelet/endothelial cell adhesion molecule 1
PEG	poly(ethylene glycol)
PEG2000-C-DMG	PEGylated myristoyl glyceride, lipid with relatively short C14 acyl chains
PEI	polyethyleneimine
PIK3CA	phosphatidylinositol 3 kinase, catalytic subunit alpha
PI3K	phosphoinositide 3-kinase
PLGA	poly lactic-*co*-glycolic acid
PLLA	poly(ʟ-lactide)
PtBGE	poly(*tert*-butyl glycidyl ether)
PTEN	phosphatase and tensin homologue
PTX	paclitaxel
PUFA	polyunsaturated fatty acid
RAF	rapidly accelerated fibrosarcoma
RBC	red blood cells
RBCsNPs complexes	red blood cell nanoparticle complexes
RET	rearranged during transfection proto-oncogene gene
ROS1	proto-oncogen tyrosine protein kinase
RTKs	receptor tyrosine kinases
RVPNs	red blood cell vesicle shell nanoparticles
SALPs	stable antisense–lipid particles
SCLC	small cell lung cancer
shRNA	short hairpin RNA
siRNA	short interfering RNA
SNALPs	stable nucleic acid–lipid particles
SORT	selective organ targeting
ssPalmE	vitamin E scaffolded SS-cleavable and pH-activated lipid-like material
SSTRs	somatostatin receptors
STR-mPEG2000	stearylpolyethylene glycol 2000
TKIs	tyrosine kinase inhibitors
TPP	triphenylphosphonium
VEGFR	vascular endothelial growth factor receptor
YSK05	1-methyl-4,4-bis[(9*Z*,12*Z*)-9,12-octadecadien-1-yloxy]piperidine

ORCID® iDs

Fatima Mraiche - https://orcid.org/0000-0001-6188-1145
Diala Alhaj Moustafa - https://orcid.org/0000-0002-6251-394X
Maja Simonoska Crcarevska - https://orcid.org/0000-0002-1927-7101
Nikola Geskovski - https://orcid.org/0000-0002-2073-5632
Katerina Goracinova - https://orcid.org/0000-0002-8101-6359

References

1. Bray, F.; Ferlay, J.; Soerjomataram, I.; Siegel, R. L.; Torre, L. A.; Jemal, A. *Ca-Cancer J. Clin.* **2018,** *68,* 394–424. doi:10.3322/caac.21492
2. Ferlay, J.; Colombet, M.; Soerjomataram, I.; Mathers, C.; Parkin, D. M.; Piñeros, M.; Znaor, A.; Bray, F. *Int. J. Cancer* **2019,** *144,* 1941–1953. doi:10.1002/ijc.31937
3. Ferlay, J.; Colombet, M.; Soerjomataram, I.; Dyba, T.; Randi, G.; Bettio, M.; Gavin, A.; Visser, O.; Bray, F. *Eur. J. Cancer* **2018,** *103,* 356–387. doi:10.1016/j.ejca.2018.07.005
4. Sung, H.; Ferlay, J.; Siegel, R. L.; Laversanne, M.; Soerjomataram, I.; Jemal, A.; Bray, F. *Ca-Cancer J. Clin.* **2021,** *71,* 209–249. doi:10.3322/caac.21660
5. Ke, X.; Shen, L. *Front. Lab. Med.* **2017,** *1,* 69–75. doi:10.1016/j.flm.2017.06.001
6. Fang, W.; Xiang, Y.; Zhong, C.; Chen, Q. *J. Thorac. Dis.* **2014,** *6* (Suppl. 5), S552–S560. doi:10.3978/j.issn.2072-1439.2014.06.09

7. Travis, W. D.; Brambilla, E.; Nicholson, A. G.; Yatabe, Y.; Austin, J. H. M.; Beasley, M. B.; Chirieac, L. R.; Dacic, S.; Duhig, E.; Flieder, D. B.; Geisinger, K.; Hirsch, F. R.; Ishikawa, Y.; Kerr, K. M.; Noguchi, M.; Pelosi, G.; Powell, C. A.; Tsao, M. S.; Wistuba, I. *J. Thorac. Oncol.* **2015,** *10,* 1243–1260. doi:10.1097/jto.0000000000000630
8. Vijayalakshmi, R.; Krishnamurthy, A. *Ind. J. Surg. Oncol.* **2011,** *2,* 178–188. doi:10.1007/s13193-011-0108-0
9. Park, J.; Kobayashi, Y.; Urayama, K. Y.; Yamaura, H.; Yatabe, Y.; Hida, T. *PLoS One* **2016,** *11,* e0161081. doi:10.1371/journal.pone.0161081
10. Yao, Y.; Peng, M.; Shen, Q.; Hu, Q.; Gong, H.; Li, Q.; Zheng, Z.; Xu, B.; Li, Y.; Dong, Y. *Thorac. Cancer* **2019,** *10,* 193–202. doi:10.1111/1759-7714.12932
11. Zhu, Y.-c.; Lin, X.-p.; Li, X.-f.; Wu, L.-x.; Chen, H.-f.; Wang, W.-x.; Xu, C.-w.; Shen, J.-f.; Wei, J.-g.; Du, K.-q. *Thorac. Cancer* **2018,** *9,* 159–163. doi:10.1111/1759-7714.12518
12. Masood, A.; Kancha, R. K.; Subramanian, J. *Semin. Oncol.* **2019,** *46,* 271–283. doi:10.1053/j.seminoncol.2019.08.004
13. Mohammed, A. A.; El-Tanni, H.; Alsakkaf, M. A.; Mirza, A. A.; Atiah, T. A.-M.; Atiah, A. A.-M. *J. Cancer Res. Ther. (Mumbai, India)* **2017,** *13,* 9–15.
14. Salgia, R. *Expert Rev. Mol. Diagn.* **2016,** *16,* 737–749. doi:10.1080/14737159.2016.1181545
15. Mok, T. S.; Carbone, D. P.; Hirsch, F. R., Eds. *IASLC Atlas of EGFR Testing in Lung Cancer;* Editorial Rx Press: North Fort Myers, FL, USA, 2017.
16. Solassol, I.; Pinguet, F.; Quantin, X. *Biomolecules* **2019,** *9,* 668. doi:10.3390/biom9110668
17. Bergonzini, C.; Leonetti, A.; Tiseo, M.; Giovannetti, E.; Peters, G. J. *Expert Opin. Pharmacother.* **2020,** *21,* 1287–1298. doi:10.1080/14656566.2020.1746269
18. Reungwetwattana, T.; Rohatgi, N.; Mok, T. S.; Prabhash, K. *Expert Rev. Precis. Med. Drug Dev.* **2021,** *6,* 161–171. doi:10.1080/23808993.2021.1909420
19. Liao, B.-C.; Griesing, S.; Yang, J. C.-H. *Ther. Adv. Med. Oncol.* **2019,** *11,* 175883591989028. doi:10.1177/1758835919890286
20. Zhong, W.-Z.; Zhou, Q.; Wu, Y.-L. *Oncotarget* **2017,** *8,* 71358–71370. doi:10.18632/oncotarget.20311
21. Gazdar, A. F. *Oncogene* **2009,** *28* (Suppl. 1), S24–S31. doi:10.1038/onc.2009.198
22. Zhang, T.; Wan, B.; Zhao, Y.; Li, C.; Liu, H.; Lv, T.; Zhan, P.; Song, Y. *Transl. Lung Cancer Res.* **2019,** *8,* 302–316. doi:10.21037/tlcr.2019.04.12
23. Harrison, P. T.; Vyse, S.; Huang, P. H. *Semin. Cancer Biol.* **2020,** *61,* 167–179. doi:10.1016/j.semcancer.2019.09.015
24. Takeda, M.; Nakagawa, K. *Int. J. Mol. Sci.* **2019,** *20,* 146. doi:10.3390/ijms20010146
25. Du, X.; Yang, B.; An, Q.; Assaraf, Y. G.; Cao, X.; Xia, J. *Innovation* **2021,** *2,* 100103. doi:10.1016/j.xinn.2021.100103
26. Zhou, X.; Shi, K.; Hao, Y.; Yang, C.; Zha, R.; Yi, C.; Qian, Z. *Asian J. Pharm. Sci. (Amsterdam, Neth.)* **2020,** *15,* 26–41. doi:10.1016/j.ajps.2019.06.001
27. Gurunathan, S.; Kang, M.-H.; Qasim, M.; Kim, J.-H. *Int. J. Mol. Sci.* **2018,** *19,* 3264. doi:10.3390/ijms19103264
28. Uchibori, K.; Inase, N.; Araki, M.; Kamada, M.; Sato, S.; Okuno, Y.; Fujita, N.; Katayama, R. *Nat. Commun.* **2017,** *8,* 14768. doi:10.1038/ncomms14768
29. Hartl, M. *Front. Oncol.* **2016,** *6,* 132. doi:10.3389/fonc.2016.00132
30. Brand, T. M.; Iida, M.; Li, C.; Wheeler, D. L. *Discovery Med.* **2011,** *12,* 419–432.
31. Jaganathan, S.; Yue, P.; Turkson, J. *J. Pharmacol. Exp. Ther.* **2010,** *333,* 373–381. doi:10.1124/jpet.109.162669
32. Lee, J. G.; Wu, R. *Neoplasia (Ann Arbor, MI, U. S.)* **2015,** *17,* 190–200. doi:10.1016/j.neo.2014.12.008
33. Moore, S.; Wheatley-Price, P. *J. Thorac. Oncol.* **2021,** *16,* 1788–1792. doi:10.1016/j.jtho.2021.06.004
34. Pore, N.; Jiang, Z.; Gupta, A.; Cerniglia, G.; Kao, G. D.; Maity, A. *Cancer Res.* **2006,** *66,* 3197–3204. doi:10.1158/0008-5472.can-05-3090
35. Wen, M.; Xia, J.; Sun, Y.; Wang, X.; Fu, X.; Zhang, Y.; Zhang, Z.; Zhou, Y.; Li, X. *Biologics* **2018,** *12,* 183–190. doi:10.2147/btt.s169305
36. Rossi, A. *Transl. Cancer Res.* **2016,** *5* (Suppl. 2), S166–S169. doi:10.21037/tcr.2016.08.04
37. Wu, Q.; Luo, W.; Li, W.; Wang, T.; Huang, L.; Xu, F. *Front. Oncol.* **2021,** *11,* 598265. doi:10.3389/fonc.2021.598265
38. Wu, Y.-L.; Planchard, D.; Lu, S.; Sun, H.; Yamamoto, N.; Kim, D.-W.; Tan, D. S. W.; Yang, J. C.-H.; Azrif, M.; Mitsudomi, T.; Park, K.; Soo, R. A.; Chang, J. W. C.; Alip, A.; Peters, S.; Douillard, J.-Y. *Ann. Oncol.* **2019,** *30,* 171–210. doi:10.1093/annonc/mdy554
39. Zhang, Z.; Zeng, K.; Zhao, S.; Zhao, Y.; Hou, X.; Luo, F.; Lu, F.; Zhang, Y.; Zhou, T.; Ma, Y.; Yang, Y.; Fang, W.; Huang, Y.; Zhang, L.; Zhao, H. *Ther. Adv. Med. Oncol.* **2019,** *11,* 1758835919891652. doi:10.1177/1758835919891652
40. Yoon, S.; Lee, D. H.; Kim, S.-W. *Ann. Transl. Med.* **2017,** *5,* 11. doi:10.21037/atm.2016.12.64
41. Chen, F.; Chen, N.; Yu, Y.; Cui, J. *Front. Oncol.* **2020,** *10,* 904. doi:10.3389/fonc.2020.00904
42. Le, X.; Nilsson, M.; Goldman, J.; Reck, M.; Nakagawa, K.; Kato, T.; Ares, L. P.; Frimodt-Moller, B.; Wolff, K.; Visseren-Grul, C.; Heymach, J. V.; Garon, E. B. *J. Thorac. Oncol.* **2021,** *16,* 205–215. doi:10.1016/j.jtho.2020.10.006
43. Masuda, C.; Yanagisawa, M.; Yorozu, K.; Kurasawa, M.; Furugaki, K.; Ishikura, N.; Iwai, T.; Sugimoto, M.; Yamamoto, K. *Int. J. Oncol.* **2017,** *51,* 425–434. doi:10.3892/ijo.2017.4036
44. Comunanza, V.; Bussolino, F. *Front. Cell Dev. Biol.* **2017,** *5,* 101. doi:10.3389/fcell.2017.00101
45. Iwama, E.; Nakanishi, Y.; Okamoto, I. *Expert Rev. Anticancer Ther.* **2018,** *18,* 267–276. doi:10.1080/14737140.2018.1432356
46. Naumov, G. N.; Nilsson, M. B.; Cascone, T.; Briggs, A.; Straume, O.; Akslen, L. A.; Lifshits, E.; Byers, L. A.; Xu, L.; Wu, H.-k.; Jänne, P.; Kobayashi, S.; Halmos, B.; Tenen, D.; Tang, X. M.; Engelman, J.; Yeap, B.; Folkman, J.; Johnson, B. E.; Heymach, J. V. *Clin. Cancer Res.* **2009,** *15,* 3484–3494. doi:10.1158/1078-0432.ccr-08-2904
47. Herbst, R. S.; Ansari, R.; Bustin, F.; Flynn, P.; Hart, L.; Otterson, G. A.; Vlahovic, G.; Soh, C.-H.; O'Connor, P.; Hainsworth, J. *Lancet* **2011,** *377,* 1846–1854. doi:10.1016/s0140-6736(11)60545-x
48. Johnson, B. E.; Kabbinavar, F.; Fehrenbacher, L.; Hainsworth, J.; Kasubhai, S.; Kressel, B.; Lin, C.-Y.; Marsland, T.; Patel, T.; Polikoff, J.; Rubin, M.; White, L.; Yang, J. C.-H.; Bowden, C.; Miller, V. *J. Clin. Oncol.* **2013,** *31,* 3926–3934. doi:10.1200/jco.2012.47.3983
49. Seto, T.; Kato, T.; Nishio, M.; Goto, K.; Atagi, S.; Hosomi, Y.; Yamamoto, N.; Hida, T.; Maemondo, M.; Nakagawa, K.; Nagase, S.; Okamoto, I.; Yamanaka, T.; Tajima, K.; Harada, R.; Fukuoka, M.; Yamamoto, N. *Lancet Oncol.* **2014,** *15,* 1236–1244. doi:10.1016/s1470-2045(14)70381-x

50. Stinchcombe, T. E.; Jänne, P. A.; Wang, X.; Bertino, E. M.; Weiss, J.; Bazhenova, L.; Gu, L.; Lau, C.; Paweletz, C.; Jaslowski, A.; Gerstner, G. J.; Baggstrom, M. Q.; Graziano, S.; Bearden, J., III; Vokes, E. E. *JAMA Oncol.* **2019,** *5,* 1448–1455. doi:10.1001/jamaoncol.2019.1847
51. Saito, H.; Fukuhara, T.; Furuya, N.; Watanabe, K.; Sugawara, S.; Iwasawa, S.; Tsunezuka, Y.; Yamaguchi, O.; Okada, M.; Yoshimori, K.; Nakachi, I.; Gemma, A.; Azuma, K.; Kurimoto, F.; Tsubata, Y.; Fujita, Y.; Nagashima, H.; Asai, G.; Watanabe, S.; Miyazaki, M.; Hagiwara, K.; Nukiwa, T.; Morita, S.; Kobayashi, K.; Maemondo, M. *Lancet Oncol.* **2019,** *20,* 625–635. doi:10.1016/s1470-2045(19)30035-x
52. Rosell, R.; Dafni, U.; Felip, E.; Curioni-Fontecedro, A.; Gautschi, O.; Peters, S.; Massutí, B.; Palmero, R.; Aix, S. P.; Carcereny, E.; Früh, M.; Pless, M.; Popat, S.; Kotsakis, A.; Cuffe, S.; Bidoli, P.; Favaretto, A.; Froesch, P.; Reguart, N.; Puente, J.; Coate, L.; Barlesi, F.; Rauch, D.; Thomas, M.; Camps, C.; Gómez-Codina, J.; Majem, M.; Porta, R.; Shah, R.; Hanrahan, E.; Kammler, R.; Ruepp, B.; Rabaglio, M.; Kassapian, M.; Karachaliou, N.; Tam, R.; Shames, D. S.; Molina-Vila, M. A.; Stahel, R. A. *Lancet Respir. Med.* **2017,** *5,* 435–444. doi:10.1016/s2213-2600(17)30129-7
53. Ichihara, E.; Hotta, K.; Nogami, N.; Kuyama, S.; Kishino, D.; Fujii, M.; Kozuki, T.; Tabata, M.; Harada, D.; Chikamori, K.; Aoe, K.; Ueoka, H.; Hosokawa, S.; Bessho, A.; Hisamoto-Sato, A.; Kubo, T.; Oze, I.; Takigawa, N.; Tanimoto, M.; Kiura, K. *J. Thorac. Oncol.* **2015,** *10,* 486–491. doi:10.1097/jto.0000000000000434
54. Liu, L.; Qu, J.; Heng, J.; Zhou, C.; Xiong, Y.; Yang, H.; Jiang, W.; Zeng, L.; Zhu, S.; Zhang, Y.; Tan, J.; Hu, C.; Deng, P.; Yang, N. *Front. Oncol.* **2021,** *11,* 722039. doi:10.3389/fonc.2021.722039
55. Wang, W.; Wang, H.; Lu, P.; Yu, Z.; Xu, C.; Zhuang, W.; Song, Z. *J. Transl. Med.* **2019,** *17,* 52. doi:10.1186/s12967-019-1803-9
56. Wang, Y.; Tian, P.; Xia, L.; Li, L.; Han, R.; Zhu, M.; Lizaso, A.; Qin, T.; Li, M.; Yu, B.; Mao, X.; Han-Zhang, H.; He, Y. *Lung Cancer* **2020,** *146,* 165–173. doi:10.1016/j.lungcan.2020.06.003
57. Gainor, J. F.; Niederst, M. J.; Lennerz, J. K.; Dagogo-Jack, I.; Stevens, S.; Shaw, A. T.; Sequist, L. V.; Engelman, J. A. *J. Thorac. Oncol.* **2016,** *11,* e83–e85. doi:10.1016/j.jtho.2016.02.021
58. Sequist, L. V.; Han, J.-Y.; Ahn, M.-J.; Cho, B. C.; Yu, H.; Kim, S.-W.; Yang, J. C.-H.; Lee, J. S.; Su, W.-C.; Kowalski, D.; Orlov, S.; Cantarini, M.; Verheijen, R. B.; Mellemgaard, A.; Ottesen, L.; Frewer, P.; Ou, X.; Oxnard, G. *Lancet Oncol.* **2020,** *21,* 373–386. doi:10.1016/s1470-2045(19)30785-5
59. Wu, Y.-L.; Cheng, Y.; Zhou, J.; Lu, S.; Zhang, Y.; Zhao, J.; Kim, D.-W.; Soo, R. A.; Kim, S.-W.; Pan, H.; Chen, Y.-M.; Chian, C.-F.; Liu, X.; Tan, D. S. W.; Bruns, R.; Straub, J.; Johne, A.; Scheele, J.; Park, K.; Yang, J. C.-H.; Wu, Y.-L.; Liu, X.; Liu, Z.; Lu, S.; Chen, X.; Pan, H.; Wang, M.; Yu, S.; Zhang, H.; Zhang, Y.; Fang, J.; Li, W.; Zhou, J.; Zhao, J.; Cheng, Y.; Yang, C.-H.; Chang, G.-C.; Chen, Y.-M.; Hsia, T.-C.; Chian, C.-F.; Yang, C.-T.; Wang, C.-C.; Kim, S.-W.; Park, K.; Kim, D.-W.; Cho, B. C.; Lee, K. H.; Kim, Y.-C.; An, H. J.; Woo, I. S.; Cho, J. Y.; Shin, S. W.; Lee, J.-S.; Kim, J.-H.; Yoo, S. S.; Kato, T.; Shinagawa, N.; Soo, R. A.; Tan, S. W. D.; Ngo, L. S.-M.; Ratnavelu, K.; Ahmad, A. R.; Liam, C. K.; de Marinis, F.; Tassone, P.; Molla, A. I.; Calles Blanco, A.; Lazaro Quintela, M. E.; Felip Font, E.; Dingemans, A.-M.; Bui, L. *Lancet Respir. Med.* **2020,** *8,* 1132–1143. doi:10.1016/s2213-2600(20)30154-5
60. Riudavets, M.; Sullivan, I.; Abdayem, P.; Planchard, D. *ESMO Open* **2021,** *6,* 100260. doi:10.1016/j.esmoop.2021.100260
61. Gan, J.; Huang, Y.; Liao, J.; Pang, L.; Fang, W. *OncoTargets Ther.* **2021,** *14,* 5297–5307. doi:10.2147/ott.s335217
62. Ruiz-Saenz, A.; Dreyer, C.; Campbell, M. R.; Steri, V.; Gulizia, N.; Moasser, M. M. *Cancer Res.* **2018,** *78,* 3645–3658. doi:10.1158/0008-5472.can-18-0430
63. Westover, D.; Zugazagoitia, J.; Cho, B. C.; Lovly, C. M.; Paz-Ares, L. *Ann. Oncol.* **2018,** *29* (Suppl. 1), I10–I19. doi:10.1093/annonc/mdx703
64. Passaro, A.; Peters, S. *N. Engl. J. Med.* **2022,** *386,* 286–289. doi:10.1056/nejme2119442
65. Zhang, X.; Lv, J.; Wu, Y.; Qin, N.; Ma, L.; Li, X.; Nong, J.; Zhang, H.; Zhang, Q.; Yang, X.; Shi, H.; Wang, J.; Zhang, S. *Front. Oncol.* **2020,** *10,* 1162. doi:10.3389/fonc.2020.01162
66. Verma, S.; Miles, D.; Gianni, L.; Krop, I. E.; Welslau, M.; Baselga, J.; Pegram, M.; Oh, D.-Y.; Diéras, V.; Guardino, E.; Fang, L.; Lu, M. W.; Olsen, S.; Blackwell, K. *N. Engl. J. Med.* **2012,** *367,* 1783–1791. doi:10.1056/nejmoa1209124
67. Hurvitz, S. A.; Dirix, L.; Kocsis, J.; Bianchi, G. V.; Lu, J.; Vinholes, J.; Guardino, E.; Song, C.; Tong, B.; Ng, V.; Chu, Y.-W.; Perez, E. A. *J. Clin. Oncol.* **2013,** *31,* 1157–1163. doi:10.1200/jco.2012.44.9694
68. Barok, M.; Joensuu, H.; Isola, J. *Breast Cancer Res.* **2014,** *16,* 209. doi:10.1186/bcr3621
69. White, B. E.; White, M. K.; Adhvaryu, H.; Makhoul, I.; Nima, Z. A.; Biris, A. S.; Ali, N. *Cancer Nanotechnol.* **2020,** *11,* 1–26. doi:10.1186/s12645-020-00068-2
70. Chen, G.; Kronenberger, P.; Teugels, E.; Umelo, I. A.; De Grève, J. *BMC Med.* **2012,** *10,* 28. doi:10.1186/1741-7015-10-28
71. Lu, Y.; Liu, L.; Wang, Y.; Li, F.; Zhang, J.; Ye, M.; Zhao, H.; Zhang, X.; Zhang, M.; Zhao, J.; Yan, B.; Yang, A.; Feng, H.; Zhang, R.; Ren, X. *Biomaterials* **2016,** *76,* 196–207. doi:10.1016/j.biomaterials.2015.10.036
72. Zarredar, H.; Pashapour, S.; Ansarin, K.; Khalili, M.; Baghban, R.; Farajnia, S. *J. Cell. Physiol.* **2019,** *234,* 1560–1566. doi:10.1002/jcp.27021
73. Xue, L.; Maihle, N. J.; Yu, X.; Tang, S.-C.; Liu, H. Y. *Mol. Pharmaceutics* **2018,** *15,* 4801–4813. doi:10.1021/acs.molpharmaceut.8b00388
74. Perepelyuk, M.; Shoyele, O.; Birbe, R.; Thangavel, C.; Liu, Y.; Den, R. B.; Snook, A. E.; Lu, B.; Shoyele, S. A. *Mol. Ther.–Nucleic Acids* **2017,** *6,* 259–268. doi:10.1016/j.omtn.2016.12.009
75. Skoulidis, F.; Li, B. T.; Dy, G. K.; Price, T. J.; Falchook, G. S.; Wolf, J.; Italiano, A.; Schuler, M.; Borghaei, H.; Barlesi, F.; Kato, T.; Curioni-Fontecedro, A.; Sacher, A.; Spira, A.; Ramalingam, S. S.; Takahashi, T.; Besse, B.; Anderson, A.; Ang, A.; Tran, Q.; Mather, O.; Henary, H.; Ngarmchamnanrith, G.; Friberg, G.; Velcheti, V.; Govindan, R. *N. Engl. J. Med.* **2021,** *384,* 2371–2381. doi:10.1056/nejmoa2103695
76. Hong, D. S.; Fakih, M. G.; Strickler, J. H.; Desai, J.; Durm, G. A.; Shapiro, G. I.; Falchook, G. S.; Price, T. J.; Sacher, A.; Denlinger, C. S.; Bang, Y.-J.; Dy, G. K.; Krauss, J. C.; Kuboki, Y.; Kuo, J. C.; Coveler, A. L.; Park, K.; Kim, T. W.; Barlesi, F.; Munster, P. N.; Ramalingam, S. S.; Burns, T. F.; Meric-Bernstam, F.; Henary, H.; Ngang, J.; Ngarmchamnanrith, G.; Kim, J.; Houk, B. E.; Canon, J.; Lipford, J. R.; Friberg, G.; Lito, P.; Govindan, R.; Li, B. T. *N. Engl. J. Med.* **2020,** *383,* 1207–1217. doi:10.1056/nejmoa1917239
77. Blair, H. A. *Drugs* **2021,** *81,* 1573–1579. doi:10.1007/s40265-021-01574-2
78. Kim, D.; Xue, J. Y.; Lito, P. *Cell* **2020,** *183,* 850–859. doi:10.1016/j.cell.2020.09.044

79. Awad, M. M.; Liu, S.; Rybkin, I. I.; Arbour, K. C.; Dilly, J.; Zhu, V. W.; Johnson, M. L.; Heist, R. S.; Patil, T.; Riely, G. J.; Jacobson, J. O.; Yang, X.; Persky, N. S.; Root, D. E.; Lowder, K. E.; Feng, H.; Zhang, S. S.; Haigis, K. M.; Hung, Y. P.; Sholl, L. M.; Wolpin, B. M.; Wiese, J.; Christiansen, J.; Lee, J.; Schrock, A. B.; Lim, L. P.; Garg, K.; Li, M.; Engstrom, L. D.; Waters, L.; Lawson, J. D.; Olson, P.; Lito, P.; Ou, S.-H. I.; Christensen, J. G.; Jänne, P. A.; Aguirre, A. J. *N. Engl. J. Med.* **2021,** *384,* 2382–2393. doi:10.1056/nejmoa2105281
80. Zhao, Y.; Murciano-Goroff, Y. R.; Xue, J. Y.; Ang, A.; Lucas, J.; Mai, T. T.; Da Cruz Paula, A. F.; Saiki, A. Y.; Mohn, D.; Achanta, P.; Sisk, A. E.; Arora, K. S.; Roy, R. S.; Kim, D.; Li, C.; Lim, L. P.; Li, M.; Bahr, A.; Loomis, B. R.; de Stanchina, E.; Reis-Filho, J. S.; Weigelt, B.; Berger, M.; Riely, G.; Arbour, K. C.; Lipford, J. R.; Li, B. T.; Lito, P. *Nature* **2021,** *599,* 679–683. doi:10.1038/s41586-021-04065-2
81. Lito, P.; Solomon, M.; Li, L.-S.; Hansen, R.; Rosen, N. *Science* **2016,** *351,* 604–608. doi:10.1126/science.aad6204
82. Patricelli, M. P.; Janes, M. R.; Li, L.-S.; Hansen, R.; Peters, U.; Kessler, L. V.; Chen, Y.; Kucharski, J. M.; Feng, J.; Ely, T.; Chen, J. H.; Firdaus, S. J.; Babbar, A.; Ren, P.; Liu, Y. *Cancer Discovery* **2016,** *6,* 316–329. doi:10.1158/2159-8290.cd-15-1105
83. Rothschild, S. I. *J. Thorac. Oncol.* **2019,** *14,* 951–954. doi:10.1016/j.jtho.2019.03.004
84. CodeBreaK 100/101: First Report of Safety/Efficacy of Sotorasib in Combination with Pembrolizumab or Atezolizumab in Advanced KRAS p.G12C NSCLC | IASLC. https://www.iaslc.org/iaslc-news/press-release/codebreak-100/101-first-report-safety/efficacy-sotorasib-combination (accessed Nov 1, 2022).
85. FDA grants accelerated approval to sotorasib for KRAS G12C mutated NSCLC | FDA. https://www.fda.gov/drugs/resources-information-approved-drugs/fda-grants-accelerated-approval-sotorasib-kras-g12c-mutated-nsclc (accessed Nov 1, 2022).
86. Canon, J.; Rex, K.; Saiki, A. Y.; Mohr, C.; Cooke, K.; Bagal, D.; Gaida, K.; Holt, T.; Knutson, C. G.; Koppada, N.; Lanman, B. A.; Werner, J.; Rapaport, A. S.; San Miguel, T.; Ortiz, R.; Osgood, T.; Sun, J.-R.; Zhu, X.; McCarter, J. D.; Volak, L. P.; Houk, B. E.; Fakih, M. G.; O'Neil, B. H.; Price, T. J.; Falchook, G. S.; Desai, J.; Kuo, J.; Govindan, R.; Hong, D. S.; Ouyang, W.; Henary, H.; Arvedson, T.; Cee, V. J.; Lipford, J. R. *Nature* **2019,** *575,* 217–223. doi:10.1038/s41586-019-1694-1
87. Punekar, S. R.; Velcheti, V.; Neel, B. G.; Wong, K.-K. *Nat. Rev. Clin. Oncol.* **2022,** *19,* 637–655. doi:10.1038/s41571-022-00671-9
88. Papke, B.; Azam, S. H.; Feng, A. Y.; Gutierrez-Ford, C.; Huggins, H.; Pallan, P. S.; Van Swearingen, A. E. D.; Egli, M.; Cox, A. D.; Der, C. J.; Pecot, C. V. *ACS Pharmacol. Transl. Sci.* **2021,** *4,* 703–712. doi:10.1021/acsptsci.0c00165
89. Zarredar, H.; Pashapour, S.; Farajnia, S.; Ansarin, K.; Baradaran, B.; Ahmadzadeh, V.; Safari, F. *J. Cell. Biochem.* **2019,** *120,* 10670–10677. doi:10.1002/jcb.28357
90. Han, W.; Shi, L.; Ren, L.; Zhou, L.; Li, T.; Qiao, Y.; Wang, H. *Signal Transduction Targeted Ther.* **2018,** *3,* 16. doi:10.1038/s41392-018-0019-4
91. In, G. K.; Nieva, J. *Transl. Cancer Res.* **2015,** *4,* 340–355. doi:10.3978/j.issn.2218-676x.2015.08.05
92. Goracinova, K.; Geskovski, N.; Dimchevska, S.; Li, X.; Gref, R. Multifunctional Core-Shell Polymeric and Hybrid Nanoparticles as Anticancer Nanomedicines. In *Design of Nanostructures for Theranostics Applications;* Grumezescu, A. M., Ed.; William Andrew: Oxford, UK, 2018; pp 109–160. doi:10.1016/b978-0-12-813669-0.00004-x
93. Nag, O. K.; Delehanty, J. B. *Pharmaceutics* **2019,** *11,* 543. doi:10.3390/pharmaceutics11100543
94. Haynes, M. T.; Huang, L. *Mol. Ther.* **2016,** *24,* 849–851. doi:10.1038/mt.2016.75
95. Grancharov, G.; Gancheva, V.; Kyulavska, M.; Momekova, D.; Momekov, G.; Petrov, P. *Polymer* **2016,** *84,* 27–37. doi:10.1016/j.polymer.2015.12.040
96. Barthel, M. J.; Rinkenauer, A. C.; Wagner, M.; Mansfeld, U.; Hoeppener, S.; Czaplewska, J. A.; Gottschaldt, M.; Träger, A.; Schacher, F. H.; Schubert, U. S. *Biomacromolecules* **2014,** *15,* 2426–2439. doi:10.1021/bm5002894
97. Pang, J.; Xing, H.; Sun, Y.; Feng, S.; Wang, S. *Biomed. Pharmacother.* **2020,** *125,* 109861. doi:10.1016/j.biopha.2020.109861
98. Su, W.-P.; Cheng, F.-Y.; Shieh, D.-B.; Yeh, C.-S.; Su, W.-C. *Int. J. Nanomed.* **2012,** *7,* 4269–4283. doi:10.2147/ijn.s33666
99. He, F.; Wang, Y.; Cai, W.; Li, M.; Dong, L. *Biosci. Rep.* **2019,** *39,* BSR20181259. doi:10.1042/bsr20181259
100. Chen, D.; Zhang, F.; Wang, J.; He, H.; Duan, S.; Zhu, R.; Chen, C.; Yin, L.; Chen, Y. *Front. Pharmacol.* **2018,** *9,* 1214. doi:10.3389/fphar.2018.01214
101. Xu, C.; Wang, P.; Zhang, J.; Tian, H.; Park, K.; Chen, X. *Small* **2015,** *11,* 4321–4333. doi:10.1002/smll.201501034
102. Shen, J.; Yin, Q.; Chen, L.; Zhang, Z.; Li, Y. *Biomaterials* **2012,** *33,* 8613–8624. doi:10.1016/j.biomaterials.2012.08.007
103. Yu, H.; Xu, Z.; Chen, X.; Xu, L.; Yin, Q.; Zhang, Z.; Li, Y. *Macromol. Biosci.* **2014,** *14,* 100–109. doi:10.1002/mabi.201300282
104. Sulthana, S.; Banerjee, T.; Kallu, J.; Vuppala, S. R.; Heckert, B.; Naz, S.; Shelby, T.; Yambem, O.; Santra, S. *Mol. Pharmaceutics* **2017,** *14,* 875–884. doi:10.1021/acs.molpharmaceut.6b01076
105. Yang, Y.; Huang, Z.; Li, J.; Mo, Z.; Huang, Y.; Ma, C.; Wang, W.; Pan, X.; Wu, C. *Adv. Healthcare Mater.* **2019,** *8,* 1900965. doi:10.1002/adhm.201900965
106. Qu, M.-H.; Zeng, R.-F.; Fang, S.; Dai, Q.-S.; Li, H.-P.; Long, J.-T. *Int. J. Pharm.* **2014,** *474,* 112–122. doi:10.1016/j.ijpharm.2014.08.019
107. Majumder, J.; Minko, T. *Pharmaceutics* **2021,** *13,* 1063. doi:10.3390/pharmaceutics13071063
108. Kallu, J.; Banerjee, T.; Sulthana, S.; Darji, S.; Higginbotham, R.; Fletcher, C.; Gerasimchuk, N. N.; Santra, S. *Nanotheranostics* **2019,** *3,* 120–134. doi:10.7150/ntno.28468
109. Qiu, G.; Xue, L.; Zhu, X.; Lu, X.; Liu, L.; Wang, Z.; Li, X.; Huang, C.; Liu, J. *Front. Oncol.* **2022,** *12,* 756489. doi:10.3389/fonc.2022.756489
110. Gu, X.; Qiu, Y.; Lin, M.; Cui, K.; Chen, G.; Chen, Y.; Fan, C.; Zhang, Y.; Xu, L.; Chen, H.; Wan, J.-B.; Lu, W.; Xiao, Z. *Nano Lett.* **2019,** *19,* 3344–3352. doi:10.1021/acs.nanolett.9b01065
111. Tasciotti, E.; Liu, X.; Bhavane, R.; Plant, K.; Leonard, A. D.; Price, B. K.; Cheng, M. M.-C.; Decuzzi, P.; Tour, J. M.; Robertson, F.; Ferrari, M. *Nat. Nanotechnol.* **2008,** *3,* 151–157. doi:10.1038/nnano.2008.34
112. Wong, C.; Stylianopoulos, T.; Cui, J.; Martin, J.; Chauhan, V. P.; Jiang, W.; Popović, Z.; Jain, R. K.; Bawendi, M. G.; Fukumura, D. *Proc. Natl. Acad. Sci. U. S. A.* **2011,** *108,* 2426–2431. doi:10.1073/pnas.1018382108

113. Blanco, E.; Sangai, T.; Hsiao, A.; Ferrati, S.; Bai, L.; Liu, X.; Meric-Bernstam, F.; Ferrari, M. *Cancer Lett.* **2013,** *334,* 245–252. doi:10.1016/j.canlet.2012.07.027
114. Xu, R.; Zhang, G.; Mai, J.; Deng, X.; Segura-Ibarra, V.; Wu, S.; Shen, J.; Liu, H.; Hu, Z.; Chen, L.; Huang, Y.; Koay, E.; Huang, Y.; Liu, J.; Ensor, J. E.; Blanco, E.; Liu, X.; Ferrari, M.; Shen, H. *Nat. Biotechnol.* **2016,** *34,* 414–418. doi:10.1038/nbt.3506
115. Li, K.; Zhan, W.; Jia, M.; Zhao, Y.; Liu, Y.; Jha, R. K.; Zhou, L. *Int. J. Med. Sci.* **2020,** *17,* 390–402. doi:10.7150/ijms.39172
116. Lv, T.; Li, Z.; Xu, L.; Zhang, Y.; Chen, H.; Gao, Y. *Acta Biomater.* **2018,** *76,* 257–274. doi:10.1016/j.actbio.2018.06.034
117. Srikar, R.; Suresh, D.; Zambre, A.; Taylor, K.; Chapman, S.; Leevy, M.; Upendran, A.; Kannan, R. *Sci. Rep.* **2016,** *6,* 30245. doi:10.1038/srep30245
118. Sreedurgalakshmi, K.; Srikar, R.; Harikrishnan, K.; Srinivasan, L.; Rajkumari, R. *Technol. Cancer Res. Treat.* **2021,** *20,* 153303382110414. doi:10.1177/15330338211041453
119. Anselmo, A. C.; Gupta, V.; Zern, B. J.; Pan, D.; Zakrewsky, M.; Muzykantov, V.; Mitragotri, S. *ACS Nano* **2013,** *7,* 11129–11137. doi:10.1021/nn404853z
120. Brenner, J. S.; Pan, D. C.; Myerson, J. W.; Marcos-Contreras, O. A.; Villa, C. H.; Patel, P.; Hekierski, H.; Chatterjee, S.; Tao, J.-Q.; Parhiz, H.; Bhamidipati, K.; Uhler, T. G.; Hood, E. D.; Kiseleva, R. Y.; Shuvaev, V. S.; Shuvaeva, T.; Khoshnejad, M.; Johnston, I.; Gregory, J. V.; Lahann, J.; Wang, T.; Cantu, E.; Armstead, W. M.; Mitragotri, S.; Muzykantov, V. *Nat. Commun.* **2018,** *9,* 2684. doi:10.1038/s41467-018-05079-7
121. Zelepukin, I. V.; Yaremenko, A. V.; Shipunova, V. O.; Babenyshev, A. V.; Balalaeva, I. V.; Nikitin, P. I.; Deyev, S. M.; Nikitin, M. P. *Nanoscale* **2019,** *11,* 1636–1646. doi:10.1039/c8nr07730d
122. Zhuang, X.; Herbert, J. M. J.; Lodhia, P.; Bradford, J.; Turner, A. M.; Newby, P. M.; Thickett, D.; Naidu, U.; Blakey, D.; Barry, S.; Cross, D. A. E.; Bicknell, R. *Br. J. Cancer* **2015,** *112,* 485–494. doi:10.1038/bjc.2014.626
123. Pasto, A.; Giordano, F.; Evangelopoulos, M.; Amadori, A.; Tasciotti, E. *Clin. Transl. Med.* **2019,** *8,* e8. doi:10.1186/s40169-019-0224-y
124. Yin, H.; Yang, J.; Zhang, Q.; Yang, J.; Wang, H.; Xu, J.; Zheng, J. *Mol. Med. Rep.* **2017,** *15,* 2925–2930. doi:10.3892/mmr.2017.6419
125. Zuo, H. *J. Oncol.* **2019,** 9367845. doi:10.1155/2019/9367845
126. Zhang, Z.; Qian, H.; Huang, J.; Sha, H.; Zhang, H.; Yu, L.; Liu, B.; Hua, D.; Qian, X. *Int. J. Nanomed.* **2018,** *13,* 4961–4975. doi:10.2147/ijn.s170148
127. Wu, M.; Le, W.; Mei, T.; Wang, Y.; Chen, B.; Liu, Z.; Xue, C. *Int. J. Nanomed.* **2019,** *14,* 4431–4448. doi:10.2147/ijn.s200284
128. Xuan, M.; Shao, J.; Dai, L.; Li, J.; He, Q. *ACS Appl. Mater. Interfaces* **2016,** *8,* 9610–9618. doi:10.1021/acsami.6b00853
129. Li, R.; He, Y.; Zhang, S.; Qin, J.; Wang, J. *Acta Pharm. Sin. B* **2018,** *8,* 14–22. doi:10.1016/j.apsb.2017.11.009
130. Rao, L.; He, Z.; Meng, Q.-F.; Zhou, Z.; Bu, L.-L.; Guo, S.-S.; Liu, W.; Zhao, X.-Z. *J. Biomed. Mater. Res., Part A* **2017,** *105,* 521–530. doi:10.1002/jbm.a.35927
131. Chen, Z.; Zhao, P.; Luo, Z.; Zheng, M.; Tian, H.; Gong, P.; Gao, G.; Pan, H.; Liu, L.; Ma, A.; Cui, H.; Ma, Y.; Cai, L. *ACS Nano* **2016,** *10,* 10049–10057. doi:10.1021/acsnano.6b04695
132. Wang, D.; Dong, H.; Li, M.; Cao, Y.; Yang, F.; Zhang, K.; Dai, W.; Wang, C.; Zhang, X. *ACS Nano* **2018,** *12,* 5241–5252. doi:10.1021/acsnano.7b08355
133. Wang, X.; Chen, H.; Zeng, X.; Guo, W.; Jin, Y.; Wang, S.; Tian, R.; Han, Y.; Guo, L.; Han, J.; Wu, Y.; Mei, L. *Acta Pharm. Sin. B* **2019,** *9,* 167–176. doi:10.1016/j.apsb.2018.08.006
134. Yildirimer, L.; Thanh, N. T. K.; Loizidou, M.; Seifalian, A. M. *Nano Today* **2011,** *6,* 585–607. doi:10.1016/j.nantod.2011.10.001
135. Bajracharya, R.; Song, J. G.; Patil, B. R.; Lee, S. H.; Noh, H.-M.; Kim, D.-H.; Kim, G.-L.; Seo, S.-H.; Park, J.-W.; Jeong, S. H.; Lee, C. H.; Han, H.-K. *Drug Delivery* **2022,** *29,* 1959–1970. doi:10.1080/10717544.2022.2089296
136. Kozielski, K. L.; Tzeng, S. Y.; Green, J. J. *Wiley Interdiscip. Rev.: Nanomed. Nanobiotechnol.* **2013,** *5,* 449–468. doi:10.1002/wnan.1233
137. Mahmoodi Chalbatani, G.; Dana, H.; Gharagouzloo, E.; Grijalvo, S.; Eritja, R.; Logsdon, C. D.; Memari, F.; Miri, S. R.; Rad, M. R.; Marmari, V. *Int. J. Nanomed.* **2019,** *14,* 3111–3128. doi:10.2147/ijn.s200253
138. Algarni, A.; Pilkington, E. H.; Suys, E. J. A.; Al-Wassiti, H.; Pouton, C. W.; Truong, N. P. *Biomater. Sci.* **2022,** *10,* 2940–2952. doi:10.1039/d2bm00168c
139. Srikar, R.; Suresh, D.; Zambre, A.; Taylor, K.; Chapman, S.; Leevy, M.; Upendran, A.; Kannan, R. *Sci. Rep.* **2016,** *6,* 30245. doi:10.1038/srep30245
140. Deng, Z.; Kalin, G. T.; Shi, D.; Kalinichenko, V. V. *Am. J. Respir. Cell Mol. Biol.* **2021,** *64,* 292–307. doi:10.1165/rcmb.2020-0306tr
141. Blanco, E.; Shen, H.; Ferrari, M. *Nat. Biotechnol.* **2015,** *33,* 941–951. doi:10.1038/nbt.3330
142. Akinc, A.; Maier, M. A.; Manoharan, M.; Fitzgerald, K.; Jayaraman, M.; Barros, S.; Ansell, S.; Du, X.; Hope, M. J.; Madden, T. D.; Mui, B. L.; Semple, S. C.; Tam, Y. K.; Ciufolini, M.; Witzigmann, D.; Kulkarni, J. A.; van der Meel, R.; Cullis, P. R. *Nat. Nanotechnol.* **2019,** *14,* 1084–1087. doi:10.1038/s41565-019-0591-y
143. Carrasco, M. J.; Alishetty, S.; Alameh, M.-G.; Said, H.; Wright, L.; Paige, M.; Soliman, O.; Weissman, D.; Cleveland, T. E., IV; Grishaev, A.; Buschmann, M. D. *Commun. Biol.* **2021,** *4,* 956. doi:10.1038/s42003-021-02441-2
144. Kulkarni, J. A.; Witzigmann, D.; Chen, S.; Cullis, P. R.; van der Meel, R. *Acc. Chem. Res.* **2019,** *52,* 2435–2444. doi:10.1021/acs.accounts.9b00368
145. Akinc, A.; Zumbuehl, A.; Goldberg, M.; Leshchiner, E. S.; Busini, V.; Hossain, N.; Bacallado, S. A.; Nguyen, D. N.; Fuller, J.; Alvarez, R.; Borodovsky, A.; Borland, T.; Constien, R.; de Fougerolles, A.; Dorkin, J. R.; Narayanannair Jayaprakash, K.; Jayaraman, M.; John, M.; Koteliansky, V.; Manoharan, M.; Nechev, L.; Qin, J.; Racie, T.; Raitcheva, D.; Rajeev, K. G.; Sah, D. W. Y.; Soutschek, J.; Toudjarska, I.; Vornlocher, H.-P.; Zimmermann, T. S.; Langer, R.; Anderson, D. G. *Nat. Biotechnol.* **2008,** *26,* 561–569. doi:10.1038/nbt1402
146. Kulkarni, J. A.; Darjuan, M. M.; Mercer, J. E.; Chen, S.; van der Meel, R.; Thewalt, J. L.; Tam, Y. Y. C.; Cullis, P. R. *ACS Nano* **2018,** *12,* 4787–4795. doi:10.1021/acsnano.8b01516
147. van der Meel, R.; Sulheim, E.; Shi, Y.; Kiessling, F.; Mulder, W. J. M.; Lammers, T. *Nat. Nanotechnol.* **2019,** *14,* 1007–1017. doi:10.1038/s41565-019-0567-y
148. Jayaraman, M.; Ansell, S. M.; Mui, B. L.; Tam, Y. K.; Chen, J.; Du, X.; Butler, D.; Eltepu, L.; Matsuda, S.; Narayanannair, J. K.; Rajeev, K. G.; Hafez, I. M.; Akinc, A.; Maier, M. A.; Tracy, M. A.; Cullis, P. R.; Madden, T. D.; Manoharan, M.; Hope, M. J. *Angew. Chem., Int. Ed.* **2012,** *51,* 8529–8533. doi:10.1002/anie.201203263

149. Yan, Y.; Xiong, H.; Zhang, X.; Cheng, Q.; Siegwart, D. J. *Biomacromolecules* **2017,** *18,* 4307–4315. doi:10.1021/acs.biomac.7b01356
150. Fehring, V.; Schaeper, U.; Ahrens, K.; Santel, A.; Keil, O.; Eisermann, M.; Giese, K.; Kaufmann, J. *Mol. Ther.* **2014,** *22,* 811–820. doi:10.1038/mt.2013.291
151. Fenton, O. S.; Kauffman, K. J.; Kaczmarek, J. C.; McClellan, R. L.; Jhunjhunwala, S.; Tibbitt, M. W.; Zeng, M. D.; Appel, E. A.; Dorkin, J. R.; Mir, F. F.; Yang, J. H.; Oberli, M. A.; Heartlein, M. W.; DeRosa, F.; Langer, R.; Anderson, D. G. *Adv. Mater. (Weinheim, Ger.)* **2017,** *29,* 1606944. doi:10.1002/adma.201606944
152. Kowalski, P. S.; Capasso Palmiero, U.; Huang, Y.; Rudra, A.; Langer, R.; Anderson, D. G. *Adv. Mater. (Weinheim, Ger.)* **2018,** *30,* 1801151. doi:10.1002/adma.201801151
153. Sago, C. D.; Lokugamage, M. P.; Paunovska, K.; Vanover, D. A.; Monaco, C. M.; Shah, N. N.; Gamboa Castro, M.; Anderson, S. E.; Rudoltz, T. G.; Lando, G. N.; Munnilal Tiwari, P.; Kirschman, J. L.; Willett, N.; Jang, Y. C.; Santangelo, P. J.; Bryksin, A. V.; Dahlman, J. E. *Proc. Natl. Acad. Sci. U. S. A.* **2018,** *115,* E9944–E9952. doi:10.1073/pnas.1811276115
154. Cheng, Q.; Wei, T.; Farbiak, L.; Johnson, L. T.; Dilliard, S. A.; Siegwart, D. J. *Nat. Nanotechnol.* **2020,** *15,* 313–320. doi:10.1038/s41565-020-0669-6
155. van der Meel, R. *Nat. Nanotechnol.* **2020,** *15,* 253–255. doi:10.1038/s41565-020-0666-9
156. Qiu, M.; Tang, Y.; Chen, J.; Muriph, R.; Ye, Z.; Huang, C.; Evans, J.; Henske, E. P.; Xu, Q. *Proc. Natl. Acad. Sci. U. S. A.* **2022,** *119,* e2116271119. doi:10.1073/pnas.2116271119
157. Li, W.; Nicol, F.; Szoka, F. C., Jr. *Adv. Drug Delivery Rev.* **2004,** *56,* 967–985. doi:10.1016/j.addr.2003.10.041
158. Kusumoto, K.; Akita, H.; Ishitsuka, T.; Matsumoto, Y.; Nomoto, T.; Furukawa, R.; El-Sayed, A.; Hatakeyama, H.; Kajimoto, K.; Yamada, Y.; Kataoka, K.; Harashima, H. *ACS Nano* **2013,** *7,* 7534–7541. doi:10.1021/nn401317t
159. Santiwarangkool, S.; Akita, H.; Nakatani, T.; Kusumoto, K.; Kimura, H.; Suzuki, M.; Nishimura, M.; Sato, Y.; Harashima, H. *J. Pharm. Sci.* **2017,** *106,* 2420–2427. doi:10.1016/j.xphs.2017.04.075
160. Abd Elwakil, M. M.; Khalil, I. A.; Elewa, Y. H. A.; Kusumoto, K.; Sato, Y.; Shobaki, N.; Kon, Y.; Harashima, H. *Adv. Funct. Mater.* **2019,** *29,* 1807677. doi:10.1002/adfm.201807677
161. Hagino, Y.; Khalil, I. A.; Kimura, S.; Kusumoto, K.; Harashima, H. *Mol. Pharmaceutics* **2021,** *18,* 878–888. doi:10.1021/acs.molpharmaceut.0c00854
162. Garbuzenko, O. B.; Kuzmov, A.; Taratula, O.; Pine, S. R.; Minko, T. *Theranostics* **2019,** *9,* 8362–8376. doi:10.7150/thno.39816
163. Xue, W.; Dahlman, J. E.; Tammela, T.; Khan, O. F.; Sood, S.; Dave, A.; Cai, W.; Chirino, L. M.; Yang, G. R.; Bronson, R.; Crowley, D. G.; Sahay, G.; Schroeder, A.; Langer, R.; Anderson, D. G.; Jacks, T. *Proc. Natl. Acad. Sci. U. S. A.* **2014,** *111,* E3553–E3561. doi:10.1073/pnas.1412686111
164. Kim, J. S.; Kim, M. W.; Kang, S. J.; Jeong, H. Y.; Park, S. I.; Lee, Y. K.; Kim, H. S.; Kim, K. S.; Park, Y. S. *Int. J. Nanomed.* **2018,** *13,* 4817–4830. doi:10.2147/ijn.s161932
165. Li, T.; Shi, W.; Yao, J.; Hu, J.; Sun, Q.; Meng, J.; Wan, J.; Song, H.; Wang, H. *Biomater. Res.* **2022,** *26,* 3. doi:10.1186/s40824-022-00249-7
166. Gao, L.; Yu, S.; Lin, J.; Chen, S.; Shen, Z.; Kang, M. *AIP Adv.* **2021,** *11,* 045201. doi:10.1063/5.0041311
167. Alvarez, M.; Simonetta, F.; Baker, J.; Morrison, A. R.; Wenokur, A. S.; Pierini, A.; Berraondo, P.; Negrin, R. S. *Front. Immunol.* **2020,** *11,* 7. doi:10.3389/fimmu.2020.00007
168. Wang, D.; Zhou, J.; Fang, W.; Huang, C.; Chen, Z.; Fan, M.; Zhang, M.-R.; Xiao, Z.; Hu, K.; Luo, L. *Bioact. Mater.* **2022,** *13,* 312–323. doi:10.1016/j.bioactmat.2021.10.046
169. Nukaga, S.; Yasuda, H.; Tsuchihara, K.; Hamamoto, J.; Masuzawa, K.; Kawada, I.; Naoki, K.; Matsumoto, S.; Mimaki, S.; Ikemura, S.; Goto, K.; Betsuyaku, T.; Soejima, K. *Cancer Res.* **2017,** *77,* 2078–2089. doi:10.1158/0008-5472.can-16-2359

License and Terms

The definitive version of this article is the electronic one which can be found at:
https://doi.org/10.3762/bjnano.14.23